Mathematical Models of Glacier Sliding and Drumlin Formation

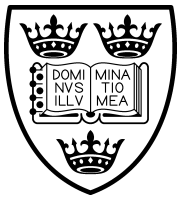

Christian Schoof

Corpus Christi College

University of Oxford

A thesis submitted for the degree of

Doctor of Philiosphy

Michaelmas Term 2002

To Vikki and Oliver

Acknowledgements

I would like to express my thanks

to Andrew Fowler, my long-suffering supervisor, who had to endure the abduction of many of his books and journals (all safely returned now), as well as my teutonic writing style, and still provided all the help and advice I could have hoped for,

also, to Felix Ng, for his help and advice, as well as for an introduction to the joys of climbing loose shale, for wild goat chases (!) and a week's board and lodging in Seattle,

to Alexandra Guerrero, Ivana Drobnjak and Rob Hinch, for putting up with me in the same office,

to Bernard Hallet, for the hospitality of the Quaternary Resaerch Centre at the University of Washington,

to the EPSRC and Corpus Christi College for their financial support,

to my parents, for their support throughout my education,

but above all, to Vikki and Oliver, for putting up with all the hardships and uncertainties, and for still supporting me all along.

Abstract

One of the central difficulties in many models of glacier and ice sheet flow lies in the prescription of boundary conditions at the bed. Often, processes which occur there dominate the evolution of the ice mass as they control the speed at which the ice is able to slide over the bed. In part I of this thesis, we study two complications to classical models of glacier and ice sheet sliding. First, we focus on the effect of cavity formation on the sliding of a glacier over an undeformable, impermeable bed. Our results do not support the widely used sliding law $u_b = C\tau_b^p N^{-q}$, but indicate that τ_b/N actually decreases with u_b/N at high values of the latter, as suggested previously for simple periodic beds by Fowler (1986). The second problem studied is that of an ice stream whose motion is controlled by bed obstacles with wavelengths comparable to the thickness of ice. By contrast with classical sliding theory for ice of constant viscosity, the bulk flow velocity does not depend linearly on the driving stress. Indeed, the bulk flow velocity may even be a multi-valued function of driving stress and ice thickness. In the second part of the thesis, attention is turned to the formation of drumlins. The viscous till model of Hindmarsh (1998) and Fowler (2000) is analysed in some detail. It is shown that the model does not predict the formation of three-dimensional drumlins, but only that of two-dimensional features, which may be interpreted as Rogen moraines. A non-linear model allows the simulation of the predicted bedforms at finite amplitude. Results obtained indicate that the growth of bedforms invariably leads to cavitation. A model for travelling waves in the presence of cavitation is also developed, which shows that such travelling waves can indeed exist. Their shape is, however, unlike that of real bedforms, with a steep downstream face and no internal stratification. These results indicate that Hindmarsh and Fowler's model is probably not successful at describing the processes which lead to the formation of streamlined subglacial bedforms.

Contents

List of Figures

Chapter 1

Introduction

1.1 Ice Sheets and Glaciers

Around 90 % of the world's land ice is concentrated in the two Antarctic ice sheets, which form an almost continuous cover of ice above the Antarctic land mass, occupying over 13 million square kilometres. Only in a few places do mountain ranges and isolated peaks penetrate through the ice, and over most of the continent the ice sheets reach thicknesses in excess of 1000 m. The underlying bedrock is generally low-lying and of low relief by comparison with the mountainous areas with which the much smaller ice masses of temperate regions are associated; in fact, especially in West Antarctica, the bedrock often lies below sea level.

Ice flows as a highly viscous solid from the central parts of the continent, where ice thickness is greatest, towards the margins, which are either at or near the coast or take the form of floating ice shelves. This gravity-driven flow is maintained by snow fall over the continent, while mass loss from the ice sheets occurs mostly through the calving of icebergs at its margins.

At 1.7 million square kilometres, the only other present-day ice sheet, in Greenland, is much smaller than its Antarctic counterparts. In contrast to Antarctica, Greenland does not possess extensive ice shelves, and a considerable proportion of its mass loss occurs through surface melting as well as through iceberg formation. Apart from these differences, Greenland shares many of the general characteristics of the Antarctic ice sheets.

Geological evidence suggests that at least three more major ice sheets were formed repeatedly over the last two million years, two in North America and one in Europe, while smaller ice sheets and ice caps existed in all the major mid-latitude mountain ranges. At their maximum extent, these ice sheets, together with those remaining in

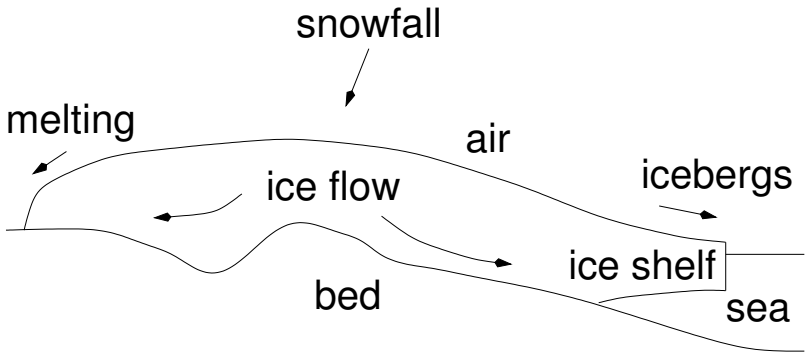

Figure 1.1: Sketch of a typical ice sheet.

Greenland and Antarctica, are believed to have occupied 30 % of the world's land surface.

The existence of cool periods in the Earth's recent geological history, during which lower than average temperatures led to the formation of these ancient ice sheets, is supported by other, climatological evidence, such as that contained in deep seabed cores and ice cores from the surviving ice sheets (Embleton and King, 1975). The concept of a succession of Ice Ages separated by warmer climatic conditions during which the American and Scandinavian ice sheets would have melted, is well established.

In fact, the formation and disintegration of these mid-latitude ice sheets is believed to have played an active part in causing the cycle of Ice Ages. Ice reflects a much greater proportion of incoming solar radiation than other types of land surface. Consequently, the growth of an ice sheet decreases the energy budget of the Earth. In turn, the resultant lowering of surface temperatures may lead to increased snowfall and suppress snowmelt, thus contributing to the growth of the ice sheet. Conversely, the melting of an ice sheet allows more radiation to be absorbed and can thus lead to further temperature increases and accelerated melting. Far from being static elements of the Earth's surface, ice sheets are thus dynamic features with potentially significant climatic impact.

The response of an ice sheet to changes in snowfall and melt patterns is mediated through the flow of ice from areas with higher snowfall or *accumulation* rates to areas where ice is lost from the ice sheet, which may either be regions of net melt or coastal regions where icebergs can break away from the ice sheet. Such flow occurs essentially as a result of the ice sheet spreading under its own weight. At the centre of the ice sheet, its surface elevation is greatest and decreases towards the margins. This causes a lateral pressure gradient which drives the flow.

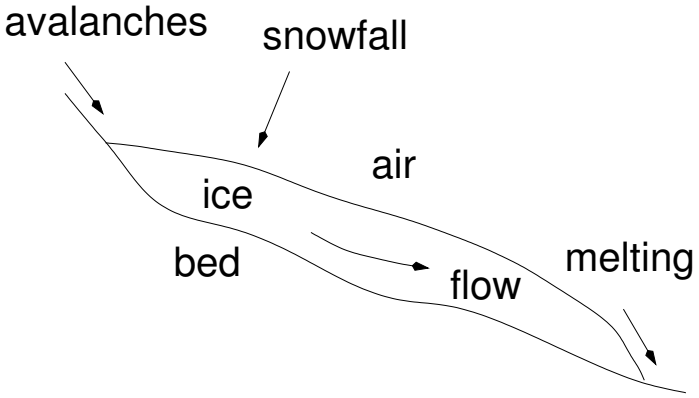

Figure 1.2: Sketch of a typical glacier.

On sufficiently long time scales, ice behaves essentially as a highly viscous solid, and can thus flow by creep deformation. In addition, where the base of an ice sheet approaches the pressure melting point, a thin and possibly patchy film of water can form at the interface between the ice and its bed. Such a water film weakens the contact between ice and bed and is thought to allow for a finite interfacial or 'sliding' velocity. Similarly, an unfrozen layer of soft sediment—also known as ground moraine—separating the ice sheet from underlying bedrock can itself deform and thus contribute to the flow of the ice sheet.

The precise nature of the sliding process is of great interest in predicting the behaviour of ice sheets. For instance, some parts of the Antarctic ice sheets called *ice streams* are found to move at much higher speeds than the surrounding parts of the ice sheets, and therefore to carry much higher ice fluxes. The observed high speeds generally cannot be explained by creep deformation alone, and sliding must contribute significantly to the motion of ice streams.

By contrast with ice sheets, glaciers are rather smaller ice masses which typically occupy mountainous terrain. Like ice sheets, most glaciers are fed by snowfall in their upper reaches (some receive significant mass input through avalanches); mass loss occurs either through melting and sublimation at their lower end, or through the calving of icebergs if the glacier ends in the sea. Crucially, the flow of a glacier differs from that of an ice sheet because it usually occurs as a result of a significant bedrock slope, while ice sheets essentially spread under their own weight in the same way a drop of oil spreads on a flat surface (see fig. 1.1). Moreover, many glaciers are confined in relatively narrow valleys and thus their flow is essentially two-dimensional, following the direction of the valley, while ice sheets can spread in all directions.

While ice sheets have received considerable scientific attention in large part due

to their climatic importance, glaciers exhibit other phenomena which make them of interest in their own right. In particular, glaciers can *surge*. A glacier surge is a periodic rapid advance of a glacier lasting months to years, followed by a long period of retreat usually lasting tens of years. Where surging glaciers exist, they can present serious environmental hazards. For instance, shipping lanes to the Alaskan oil port of Valdez have in the past been affected by iceberg discharge from nearby Columbia Glacier, a fast-flowing glacier which terminates in a fjord. Other hazards associated with surging glaciers include the blocking of side valleys, which can lead to the formation of ice-dammed lakes. The sudden drainage of such lakes can then lead to catastrophic floods.

Surge-type glaciers are also of particular interest because their rapid motion, like that of ice streams, cannot be explained by the deformation of glacier ice alone; in addition there must be significant sliding at the glacier bed. Whether the mechanisms for rapid glacier sliding and ice stream behaviour are related is, at present, unclear, but much of the research on surging glaciers is motivated by the possible analogy with ice streams.

1.2 Glacial Geomorphology

Much of the evidence for the existence of mid-latitude ice sheets and ice caps during the Ice Ages is geological in nature. Familiar examples include corries and glacial valleys left behind by extensive mountain glaciations in areas such as the Scottish Highlands, where there are no surviving glaciers. Possibly less well-known are the landforms and sediment deposits which indicate the former presence of large ice sheets in low-lying areas such as the Canadian Shield or the Baltic.

Such landforms and deposits may be associated with the margins of former ice sheets; typical examples include the lakebed deposits of former ice-dammed lakes, and ridges of sediment dumped by a melting ice sheet at its margins, known as end moraines. Here, we will be mostly concerned with landforms which originated underneath former ice sheets, and in particular with *drumlins*. Drumlins are elongated hills, typically several hundred metres to a few kilometres long, a few hundred metres wide and tens of metres high. The shape of a classical drumlin is often described as resembling the inverted bowl of a spoon, symmetrical about the ice flow direction with a steep upstream face and a tapered downstream side. Notably, drumlins occur in swarms or *drumlin fields*, where many individual hills of similar shapes and sizes are clustered together with their long axes aligned (fig. 1.3). This, along with the

observation that drumlins occur exclusively in areas formerly covered by ice sheets, has led to the conclusion that drumlins originate underneath ice sheets (Gravenor, 1953). The direction of their long axes is then usually taken to indicate the direction of ice flow at the time when the drumlin field was formed. Other indicators of ice flow direction, such as scratch marks or *striae* on exposed bedrock usually corroborate this assumption (e.g. Alden, 1905).

Drumlins and other subglacial landforms are of particular interest because they may yield important clues about processes which act at the base of ice sheets, where direct observation is notoriously difficult. Such processes are of great interest in glaciology because they may control how glaciers and ice sheets are able to slide. Conversely, the origin of drumlins at the base of ice sheets does make them very difficult to interpret, precisely because so little is known about subglacial processes which might be used to constrain theories for drumlin formation. From a mathematical point of view, the appearance of drumlins in quasi-regular swarms suggests that they originate by some kind of instability mechanism (Fowler, 2000), but little else can be said with any certainty.

There are many processes by which the bedrock and soft sediments which underlie an ice sheet can be altered and shaped into the different landforms we see in deglaciated areas today. We will only present a short review of these processes here. More comprehensive accounts can be found in the books by Coates (1974), Sugden and John (1976), Eyles (1983) and Menzies (1995), as well as in the review article by Alley and others (1997).

When sliding occurs over exposed bedrock and the interface between ice and bedrock is not free from debris, the glacier or ice sheet will erode the underlying bedrock by dragging debris across it; the result are fragments of bedrock which add to the debris load of the basal ice. Boulton (1974) estimates typical rates of erosion of exposed bedrock as 1 mm a^{-1}; during a typical ice age lasting 10^5 years, bedrock erosion can generate vast amounts of glacial debris. This partly explains why formerly glaciated areas often have a cover of soft glacial sediments or *drift*. Frequently, drift takes the form of *till*, which is a blanket term used to describe unstratified, highly mixed (i.e. containing many different grain sizes) glacial sediment.

Where a glacier or ice sheet overrides soft sediments, these can be affected in a number of ways. Firstly, they can become incorporated or *entrained* in basal ice, usually as the result of liquid water freezing onto the base of the ice sheet (Alley and others, 1997, 1998), or as a result of the creep deformation of ice forming debris-filled thrusts and folds (Murray, 1997). The entrained sediment is then transported in

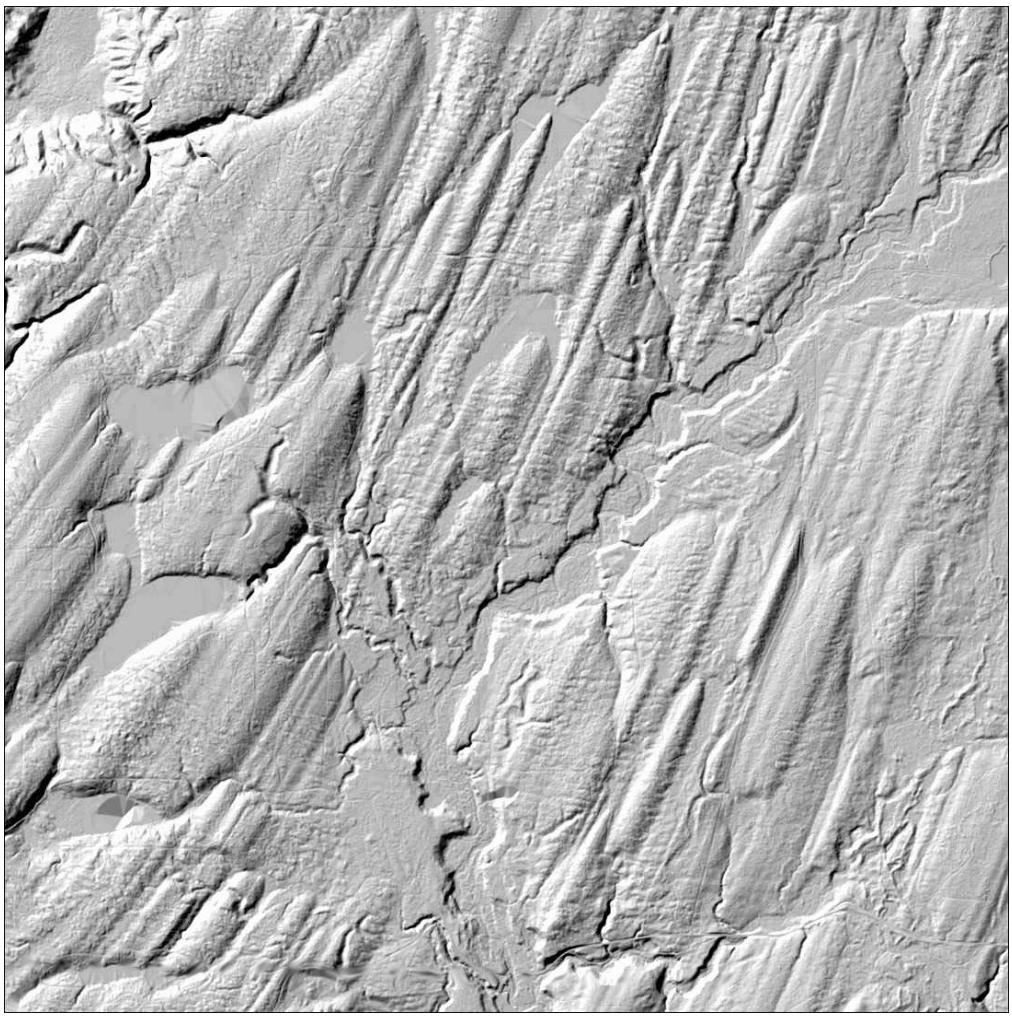

Figure 1.3: 6 × 6 km close-up of a digital elevation model of the Puget Sound drumlin field, Washington State, U.S.A. Ice flow direction is from top right to bottom left. Note that the Puget Sound drumlin field is underlain by hundreds of metres of unlithified sediment (B. Hallet, personal communication), which may be contrasted with other drumlin fields where there are frequent bedrock exposures and the cover of soft sediment is thin (e.g. Shaw and Kvill, 1984) — the occurrence of drumlins does not appear to be affected by this. Image courtesy of Ralph Haugerud, U.S. Geological Survey.

the basal ice and deposited again when the ice melts. Depending on the conditions under which the ice melts, different types of till deposits result: if deposition is by melt-out from moving ice, the resulting sediment is referred to as *lodgement till*, while *melt-out till* results if the ice is no longer moving when melting occurs. Entrained material can also reach the surface of a glacier or ice sheet, particularly near the margins. Till which results from surficial melting is usually known as *ablation till*. As ablation till is frequently subject to landslides and a variety of other processes which change its composition and structure (Goldthwait, 1974; Eyles, 1983), it can often be distinguished from subglacial tills by the presence of so-called 'flow structures'.

Where soft sediment underlying a glacier or ice sheet is unfrozen and water-saturated at sufficiently high pore pressures, at least a certain thickness of the sediment immediately below the ice may become mobile and deform continuously under the flow of basal ice (Boulton and Hindmarsh, 1987). The sediment which results is usually highly mixed and described as *deformation till*. Deformation till is frequently underlain by more consolidated soft sediments, which do not deform continuously but may show some signs of 'tectonic' deformation such as folds or faults (Krüger and Thomsen, 1984; Boulton, 1987).

Lastly, meltwater draining through a network of subglacial channels can also transport large quantities of sediment (Alley and others, 1997), often beyond the margins of a glacier or ice sheet, where they form 'outwash' deposits. As the ability of flowing water to transport sediment depends on grain size, deposits resulting from water-borne transport tend to be much less mixed than tills and are often stratified.

In order to understand which of the processes above was involved in the formation of drumlins, many different aspects of drumlins have been considered, such as their location, their shapes and their internal composition.

Drumlins appear to be ubiquitous in formerly glaciated areas of low relief, as the glaciological map of Canada by Prest and others (1968) shows; some drumlin fields are clearly associated with the margins of former ice sheets (Alden, 1905; Whittecar and Mickelson, 1979; Harry and Trenhaile, 1987), whereas others bear no obvious relation to former ice margins (Shaw, 1983; Shaw and Kvill, 1984). Although drumlins frequently consist of soft sediment, the thickness of available drift does not seem to be a factor in drumlin formation. Thus, drumlin fields occur in areas with a thin drift cover and frequent bedrock exposure (e.g. Lundqvist, 1970; Shaw and Kvill, 1984), as well as in areas underlain by thick sequences of soft sediments (Alden, 1905; Harry and Trenhaile, 1987, see also fig. 1.3).

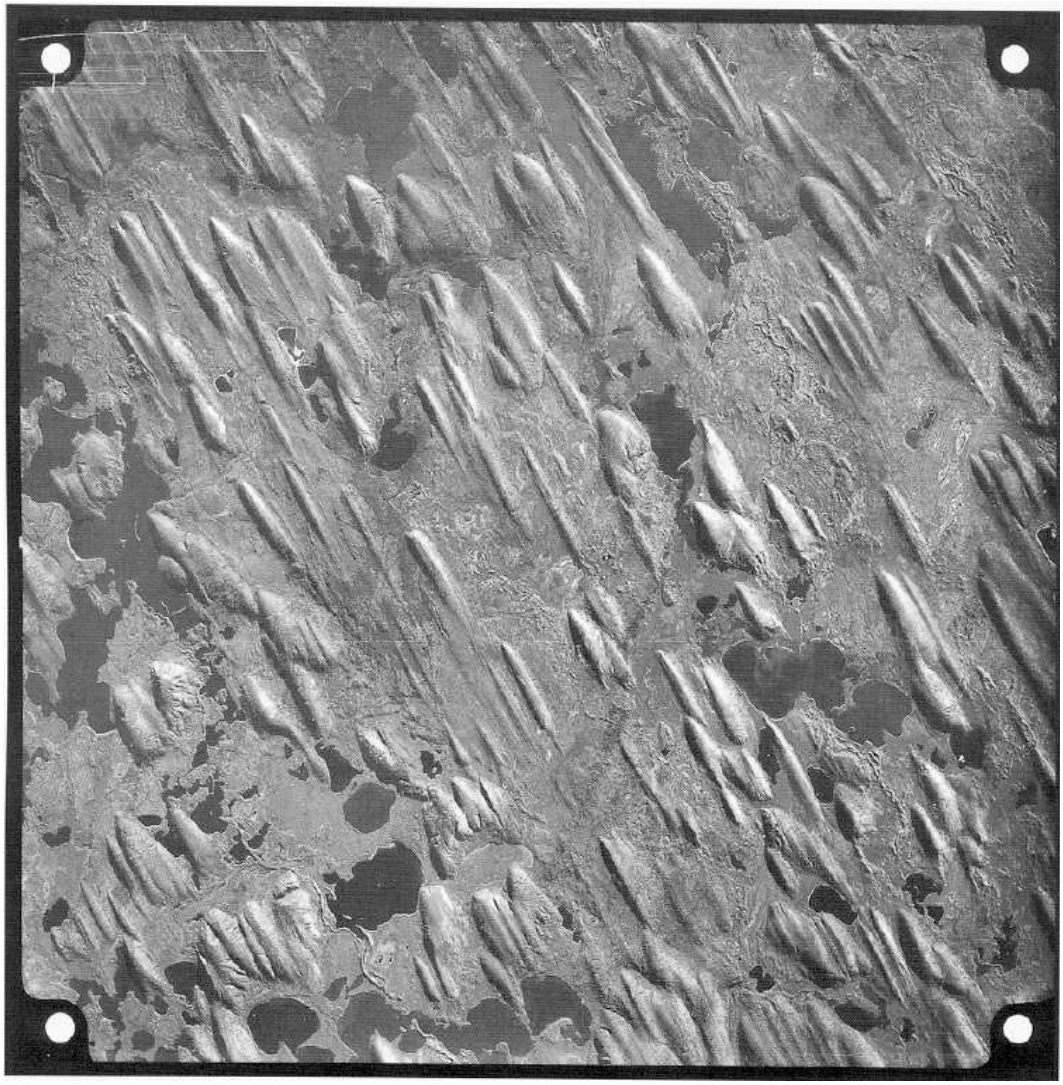

Figure 1.4: Aerial photograph of a drumlin field in Saskatchewan, Canada. Ice flow direction is from top left to bottom right. Reproduced from Hindmarsh (1998b).

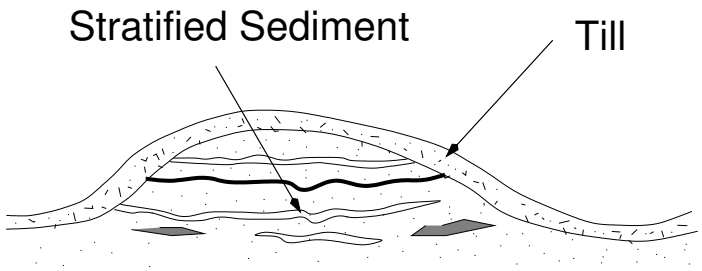

Figure 1.5: A sketch of a stratified drumlin core in cross-section.

The observations above make it difficult to associate drumlins with particular conditions which must have prevailed at the base of the ice sheet during their formation. We may suppose that they must have formed under ice which was able to slide at least to some extent over its bed; if this had not been the case, the interpretation of drumlin orientation as an indicator of ice flow direction seems questionable, as ice near the base of the ice sheet would have had no appreciable velocity.

Much attention in the study of drumlins has been focussed on their internal composition. If an individual drumlin is somehow 'built up' on a pre-existing flat surface, then one would expect the internal structure of the drumlin, and in particular the type of deposits found in them, to reflect this. However, field observations of the interiors or *cores* of different drumlins reveal a bewildering variety of materials. Thus, drumlins may be composed partly or almost entirely of bedrock (Tarr, 1894; Glückert, 1973), they may consist of stratified soft sediments indicative of deposition under water (Whittecar and Mickelson, 1979; Shaw, 1983; Sharpe, 1987; Harry and Trenhaile, 1987), or entirely of till (Alden, 1905). The internal composition of drumlins varies between different drumlin fields as well as within the same drumlin field. For instance, Alden (1905) finds drumlins consisting of stratified sediment and drumlins made entirely of till co-existing in the same drumlin field. Moreover, some drumlin cores contain materials which could not have originated under an ice sheet, such as peat (Schaeffer, 1969), tree stumps (Goldthwait, 1974) or soil (Krüger and Thomsen, 1984). This wide range of internal structures suggests that the material found in drumlins pre-dates their formation and that drumlin cores are not altered significantly during the formation process. A certain amount of alteration through deformation is sometimes evident in drumlin cores, for instance through the presence of folds or faults (Alden, 1905; Whittecar and Mickelson, 1979; Krüger and Thomsen, 1984). However, not all drumlin cores show such signs of deformation (Sharpe, 1987), and where deformation occurs, it usually does not obliterate internal structure entirely,

as one might expect if deformation resulted in core material being transported over long distances (Boulton, 1987).

One of the few features which most drumlins appear to share is a cover or *sheath* of till, i.e. of highly mixed, unstratified sediment of a glacial origin. This cover is usually between 0.5 and 3 m thick (Alden, 1905; Goldthwait, 1974; Shaw, 1983; Sharpe, 1987; Harry and Trenhaile, 1987), but may merge with underlying till to form a much thicker deposit (Whittecar and Mickelson, 1979). The till cover found on many drumlins is of particular interest to us because some of the theories which have been suggested for drumlin formation — and in particular, the model which we shall study in part II of this thesis — involve the notion that the deformation of subglacial sediment is responsible for the formation of drumlins (Boulton, 1987; Hindmarsh, 1998a,b; Fowler, 2000). As we have already explained, the cores of many drumlins do not exhibit signs of widespread deformation, and any deformation which resulted in significant transport of sediment must have been confined to a thin layer at the top of the drumlin — namely the till sheath. In many cases, the nature of the till sheath is consistent with an origin by subglacial deformation (Boulton, 1987), though there is some evidence that some till sheaths are the result of ablation (Aario, 1987; Karczewski, 1987).

In addition to drumlins, there are other, related subglacial landforms which differ from drumlins in shape. At one extreme, there are ridges transverse to the ice flow direction known as *Rogen moraines* (e.g. Lundqvist, 1969; Aario, 1977, 1987), while at the other end of the spectrum, *megaflutes* (e.g. Smith, 1948; Gravenor and Meneley, 1958; Shaw and Freschauf, 1973) are ridges which are highly elongated in the former direction of ice flow. Their connection with drumlins is based on the observation that there appears to exist a continuous 'spectrum' of shapes. Thus, some Rogen moraines do not form continuous transverse ridges, but are broken in places; where such breaks occur, the ends of the ridge curve in the downstream direction, leading to a crescentic appearance. This makes them similar in appearance to certain types of drumlins which have a horseshoe-type plan shape (the bottom right-hand corner of fig. 1.4 provides an example). At the other extreme, very elongated drumlins can be similar in appearance to megaflutes. Furthermore, all of these landforms occur in swarms, and drumlin fields can appear to merge continuously into Rogen moraine or megaflute topography (Lundqvist, 1969; Glückert, 1973; Aario, 1977, 1987). Collectively, drumlins, Rogen moraines and megaflutes are often referred to as 'streamlined bedforms'. Whilst geographical proximity and similarities in appearance suggest that these diverse features may be formed by similar processes (cf. Fowler, 2001a), there

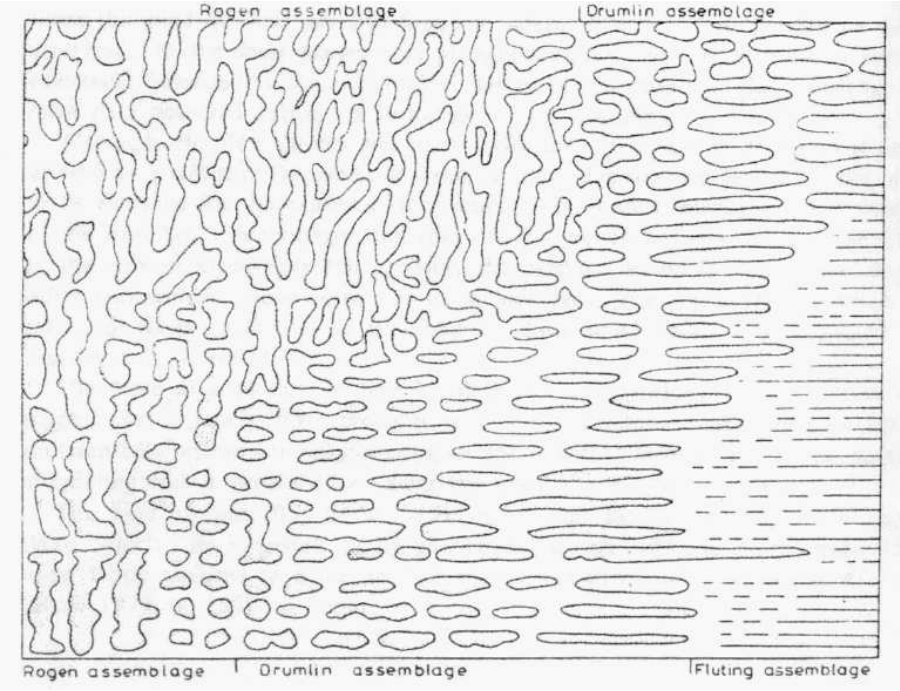

Figure 1.6: A sketch of the different plan shapes of streamlined subglacial bedforms and their relation to one another. Ice flow is from left to right. Reproduced from Aario (1977).

is as yet no universally accepted theory for the formation of any of these landforms (Gravenor, 1953; Smalley and Unwin, 1968; Shaw and Freschauf, 1973; Whittecar and Mickelson, 1979; Shaw, 1983; Shaw and Kvill, 1984; Aario, 1987; Boulton, 1987; Everett, 1987).

1.3 Outline of the Thesis

In chapter 2, we first review some of the basic models which have been constructed elsewhere to study the behaviour of ice sheets and glaciers and their interactions with the underlying bedrock or unconsolidated sediment. In particular, we consider how ice sheets and glaciers flow, and how conditions at their base can contribute to ice flux through the process of glacier sliding. We also review present models for the deformation of subglacial sediment, as these will be relevant for the model of drumlin formation studied later in the thesis. In part I we then address several complications to the classical models of glacier and ice sheet mechanics. In part II of the thesis, we focus on a model for the evolution of an ice sheet bed into drumlins through the process of subglacial deformation.

1.4 Statement of Originality

The material presented in chapter 2 and appendix A is based entirely on the work of other authors, who are acknowledged in the appropriate places. The bound for basal shear stress in section 3.2 is based on Iken's (1981) paper, but the generalised derivation is new. Similarly, the model for sliding in the presence of cavitation in section 3.4 is based on Fowler's (1986a) paper, but the method of solution in the subsequent sections is new. The material in chapter 4 is new. The basic model for drumlin formation in section 5 is due to Hindmarsh (1998b) and Fowler (2000, 2001a); the subsequent reduction of the model and the work in chapter 6 and appendix C is new.

Chapter 2

Review of Classical Models

2.1 A Simple Model for Ice Flow

If the basal temperature of an ice sheet or glacier is sufficiently below the pressure melting point and sliding is suppressed, then ice flow occurs entirely through creep deformation of the polycrystalline ice which makes up the ice sheet or glacier. This creep deformation is usually modelled as a slow, incompressible viscous flow (see e.g. Paterson, 1994, chapter 5).

Given a Cartesian coordinate system $(x, y, z) = (x_1, x_2, x_3)$ and a velocity field $\mathbf{u} = (u, v, w) = (u_1, u_2, u_3)$, the usual strain rate tensor $\dot{\boldsymbol{\varepsilon}}$ can be defined as

$$\dot{\varepsilon}_{ij} = \frac{1}{2}\left(\frac{\partial u_i}{\partial x_j} + \frac{\partial u_j}{\partial x_i}\right), \tag{2.1}$$

and its second invariant $\dot{\varepsilon}$ as

$$\dot{\varepsilon} = (\dot{\varepsilon}_{ij}\dot{\varepsilon}_{ji}/2)^{1/2}, \tag{2.2}$$

where summation over repeated indices is implied. The most commonly used model rheology for ice relates the deviatoric stress tensor $\boldsymbol{\tau}$ to $\dot{\boldsymbol{\varepsilon}}$ as (see Paterson, 1994, chapter 5)

$$\dot{\boldsymbol{\varepsilon}} = A\tau^{n-1}\boldsymbol{\tau}, \tag{2.3}$$

where A is a temperature-dependent rate factor, $n > 1$ is a constant and τ is the second invariant of $\boldsymbol{\tau}$,

$$\tau = (\tau_{ij}\tau_{ji}/2)^{1/2}. \tag{2.4}$$

The stress tensor $\boldsymbol{\sigma}$ may thus be expressed as

$$\sigma_{ij} = \tau_{ij} - p\delta_{ij} = A^{-1/n}\dot{\varepsilon}^{1/n-1}\dot{\varepsilon}_{ij} - p\delta_{ij}, \tag{2.5}$$

where p denotes pressure and δ_{ij} is the Kronecker delta. Typical values for the exponent n lie between 1.8 and 5, with $n = 3$ a popular choice.

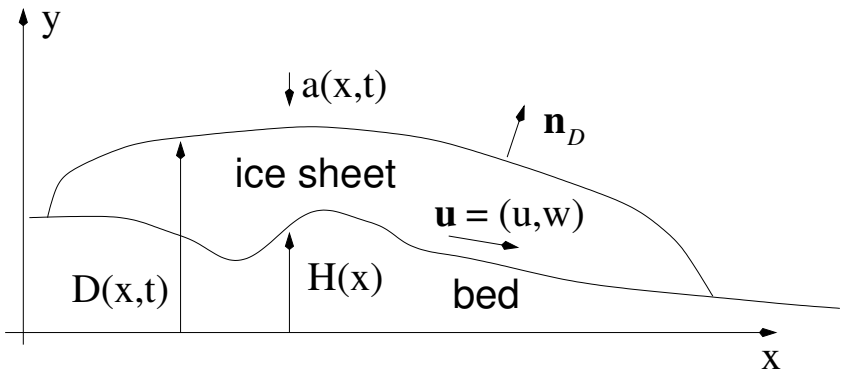

Figure 2.1: Geometry of the ice sheet flow problem.

Numerous modifications have been proposed to the simple relationship (2.5), which is commonly known as Glen's law. For instance, various authors (e.g. Hutter, 1981; Fowler, 1981) have pointed out that (2.5) implies a viscosity η of the form

$$\eta = A^{-1/n}\dot{e}^{1/n-1}/2, \tag{2.6}$$

which becomes infinite when $\dot{e}$ vanishes, and various alternatives which ensure a finite viscosity at vanishing strain rate have been suggested. More recently, increasing recognition has been given to the fact that ice can develop an induced anisotropy when stressed over sufficiently long time scales, appropriate to the oldest ice in the Antarctic and Greenland ice sheets (e.g. Svendsen and Hutter, 1996). Such behaviour clearly cannot be described by a simple viscous relationship of the form (2.5).

Simple models for ice sheet and glacier flow generally ignore such complications, and often consider only the isothermal case, where A is a constant. We adopt this approach here, and also restrict ourselves to ice sheet flow in two dimensions. The geometry of the problem is illustrated in fig. 2.1.

Since the typical Reynolds number of a glacier or ice sheet is $\lesssim 10^{-13}$ (Fowler and Larson, 1978), one can safely ignore inertial terms in the equations for momentum conservation, and thus stress tensor $\boldsymbol{\sigma}$ and velocity field $\mathbf{u} = (u, v)$ satisfy the slow flow field equations for momentum and mass conservation,

$$\nabla \cdot \boldsymbol{\sigma} - \rho g \mathbf{j} = \mathbf{0}, \tag{2.7}$$

$$\nabla \cdot \mathbf{u} = 0, \tag{2.8}$$

where ρ is ice density, g acceleration due to gravity and $\mathbf{j}$ is the y-unit vector. In addition, $\boldsymbol{\sigma}$ and $\mathbf{u}$ are related through Glen's law (2.5) with constant A. If the glacier

or ice sheet is frozen to the bed, then appropriate boundary conditions at the base $y = H(x)$ are that there is no slip. Hence

$$\mathbf{u} = \mathbf{0} \qquad \text{on } y = H(x). \tag{2.9}$$

At the free surface $y = D(x,t)$ there is no applied traction, and so

$$\boldsymbol{\sigma}\mathbf{n}_D = \mathbf{0} \qquad \text{on } y = D(x,t), \tag{2.10}$$

where $\mathbf{n}_D$ is the unit normal to the surface,

$$\mathbf{n}_D = \frac{1}{\left(1 + \left(\frac{\partial D}{\partial x}\right)^2\right)^{1/2}} \begin{pmatrix} -\frac{\partial D}{\partial x} \\ 1 \end{pmatrix}. \tag{2.11}$$

The surface itself satisfies a kinematic boundary condition of the form

$$\frac{\partial D}{\partial t} + u\frac{\partial D}{\partial x} = v + a(x,t) \qquad \text{on } y = D(x,t), \tag{2.12}$$

where a is the rate at which ice accumulates at the surface as a result of snowfall, expressed as a velocity. Commonly, a is referred to as the accumulation rate; $a < 0$ signifies that there is a net mass loss due to melting and/or sublimation. In the discussion that follows, we take a to be prescribed externally, though a more complicated treatment would couple a model for precipitation to the ice sheet model. In its simplest form, such coupling might involve the assumption that the accumulation rate a depends on surface elevation D (Morland and Johnson, 1980), though many further complications are conceivable.

Depth-integration of (2.8), using (2.9) and (2.12), gives the alternative, integrated form of mass conservation

$$\frac{\partial D}{\partial t} + \frac{\partial Q}{\partial x} = a(x,t): \qquad Q = \int_{H(x)}^{D(x,t)} u \, \mathrm{d}y. \tag{2.13}$$

2.2 The Shallow Ice Approximation

A typical ice sheet such as the present-day Antarctic ice sheet has a thickness of one or several kilometres whilst its lateral extent is typically on the order of 1000 km. In other words, the aspect ratio of a typical ice sheet is small, and this fact can be exploited to derive a lubrication approximation to the ice sheet model presented in the previous section. This approximation is commonly referred to as the 'shallow ice approximation' in glaciology.

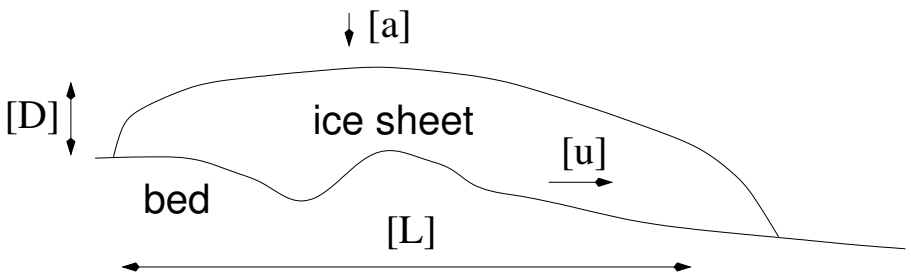

Figure 2.2: Ice sheet scales.

The following scales for the model in section 2.1 are defined (cf. fig. 2.2): $[a]$ for accumulation rate and $[L]$ for lateral extent, $[D]$ for ice thickness *and* variations in bed elevation, $[t]$ for time, $[u]$ for horizontal velocity and $[\tau]$ for deviatoric stress. We suppose that $[a]$ and $[L]$ are given as 'climatic' input. In other words, we require that the magnitude of the accumulation rate and the lateral extent of the ice sheet are known. The latter will usually be the case because the distance $[L]$ over which climatic conditions change from net snowfall to net melt is known, or because the ice sheet is supported by a continent of finite size $[L]$.

We define the remaining scales by requiring that terms in (2.13) balance,

$$[D]/[t] = [u][D]/[L] = [a], \tag{2.14}$$

so that we are dealing with the convective timescale $[t] = [L]/[u]$. Moreover, vertical deviatoric stress gradient and longitudinal pressure gradient balance,

$$[\tau]/[D] = \rho g[D]/[L], \tag{2.15}$$

and Glen's law suggests

$$[u]/[D] = 2A[\tau]^n, \tag{2.16}$$

whence we obtain

$$[D] = \left(\frac{[a][L]^{n+1}}{2A(\rho g)^n}\right)^{\frac{1}{2(n+1)}}, \qquad [u] = [a][L]/[D], \qquad [\tau] = \rho g[D]^2/[L]. \tag{2.17}$$

Typical values for the parameters in Glen's law are (Paterson, 1994, chapter 5) $n = 3$ and $A = 6{\times}10^{-24}$ Pa^{-3} s^{-1}, while for Antarctica, $[a] = 0.1$ m a^{-1}, $[L] = 3000$ km. Substituting these yields

$$[D] = 3.5\,\mathrm{km}, \qquad [u] = 10\,\mathrm{m\,a^{-1}}, \qquad [\tau] = 1.2 \times 10^5\,\mathrm{Pa},$$

which suggests that these scales are indeed realistic since $[D]$ and $[u]$ agree well with observed ice thicknesses and surface velocities in Antarctica. These scales define a single dimensionless parameter, the aspect ratio ϵ of the ice sheet, where

$$\epsilon \doteq \frac{[D]}{[L]} \approx 1.2 \times 10^{-3} \tag{2.18}$$

for the estimates given above. The fact that $\epsilon \ll 1$ will form the basis of the approximation scheme introduced below.

Equipped with these scales, we define the following dimensionless variables:

$$x = [L]x^\star, \qquad y = [D]y^\star, \qquad t = [t]t^\star, \tag{2.19}$$

$$D(x,t) = [D]D^\star(x^\star, t^\star), \qquad H(x) = [D]H^\star(x^\star), \tag{2.20}$$

$$u = [u]u^\star, \qquad v = \epsilon[u]v^\star, \qquad \dot{e} = [u]/(2[D])\dot{e}^\star, \tag{2.21}$$

$$a = [a]a^\star, \qquad Q = [u][D]Q^\star, \tag{2.22}$$

$$\tau_{xy} = [\tau]\tau^\star_{xy}, \qquad \tau_{xx} = -\tau_{yy} = \epsilon[\tau]\tau^\star_{xx} = -\epsilon[\tau]\tau^\star_{yy}, \qquad p = \rho g[D](D^\star - y^\star) + \epsilon[\tau]p^\star. \tag{2.23}$$

Dropping asterisks on the dimensionless variables, we obtain the scaled field equations

$$\frac{\partial \tau_{xy}}{\partial y} + \epsilon^2 \frac{\partial \tau_{xx}}{\partial x} - \epsilon^2 \frac{\partial p}{\partial x} - \frac{\partial D}{\partial x} = 0, \tag{2.24}$$

$$\frac{\partial \tau_{yy}}{\partial y} + \frac{\partial \tau_{xy}}{\partial x} - \frac{\partial p}{\partial y} = 0, \tag{2.25}$$

$$\frac{\partial u}{\partial x} + \frac{\partial v}{\partial y} = 0, \tag{2.26}$$

where

$$\tau_{xy} = \dot{e}^{1/n-1}\frac{\partial u}{\partial y} + \epsilon^2 \dot{e}^{1/n-1}\frac{\partial v}{\partial x}, \tag{2.27}$$

$$\tau_{xx} = 2\dot{e}^{1/n-1}\frac{\partial u}{\partial x} = -\tau_{yy}, \tag{2.28}$$

and

$$\dot{e} = \left[\left(\frac{\partial u}{\partial y}\right)^2 + \epsilon^4 \left(\frac{\partial v}{\partial x}\right)^2 + 2\epsilon^2 \left(\left(\frac{\partial u}{\partial x}\right)^2 + \left(\frac{\partial v}{\partial y}\right)^2 + \frac{\partial u}{\partial y}\frac{\partial v}{\partial x}\right)\right]^{1/2}. \tag{2.29}$$

Scaled boundary conditions at the base $y = H$ are

$$u = v = 0, \tag{2.30}$$

and at the surface $y = D$,

$$\tau_{xy} + \epsilon^2 \frac{\partial D}{\partial x}(p - \tau_{xx}) = 0, \tag{2.31}$$

$$\tau_{yy} - p - \frac{\partial D}{\partial x}\tau_{xy} = 0, \tag{2.32}$$

while equation (2.13) remains unchanged.

The Reduced Model

Ignoring terms of $O(\epsilon^2)$ on the basis that $\epsilon \ll 1$ finally gives the desired approximation,

$$\frac{\partial}{\partial y}\left(\left|\frac{\partial u}{\partial y}\right|^{1/n-1}\frac{\partial u}{\partial y}\right) = \frac{\partial D}{\partial x} \qquad \text{on } y \in (H, D), \tag{2.33}$$

$$u = 0 \qquad \text{on } y = H, \tag{2.34}$$

$$\left|\frac{\partial u}{\partial y}\right|^{1/n-1}\frac{\partial u}{\partial y} = 0 \qquad \text{on } y = D. \tag{2.35}$$

There are further equations arising from (2.25), (2.28) and (2.32) which determine v and p, but these decouple from the leading-order model. (2.33)–(2.35) can now be integrated to give ice flux:

$$Q = -\frac{1}{n+2}(D - H)^{n+2}\left|\frac{\partial D}{\partial x}\right|^{n-1}\frac{\partial D}{\partial x}, \tag{2.36}$$

and so D obeys a non-linear degenerate diffusion equation with a prescribed source term a,

$$\frac{\partial D}{\partial t} - \frac{\partial}{\partial x}\left[\frac{1}{n+2}(D - H)^{n+2}\left|\frac{\partial D}{\partial x}\right|^{n-1}\frac{\partial D}{\partial x}\right] = a(x, t). \tag{2.37}$$

Glaciers

The shallow ice approximation presented above has been derived numerous times in the glaciological literature; its principal exponents have been Morland and Johnson (1980, 1982) and Hutter (1983), while a modern perspective can be found in the review article by Fowler (2001b).

Fowler and Larson (1978) considered the analogous problem of shallow ice flow for a glacier, which essentially amounts to tilting the geometry of the problem illustrated in fig. 2.1 through a finite angle α to the vertical (see fig. 2.3). The only change to the model in section 2.1, again assuming that there is no sliding at the base of the glacier, is that the gravitational term in (2.7) now takes the form $\rho g(\sin\alpha, \cos\alpha)$.

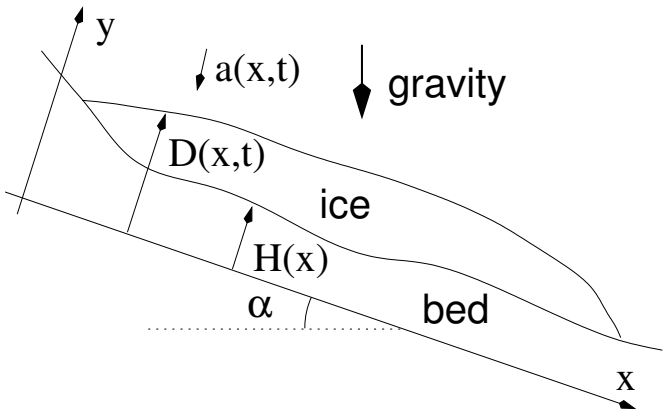

Figure 2.3: Geometry of glacier flow.

In addition to the pressure gradient caused by a change in ice surface elevation D—which is now measured relative to a 'mean' bed inclined at angle α to the horizontal—the ice flow is now also driven by a downslope component of gravity. Fowler and Larson (1978) account for this by re-defining the scale $[\tau]$ as

$$[\tau] = \rho g [D] \sin \alpha, \tag{2.38}$$

and pressure p is scaled as

$$p = \rho g \cos \alpha [D](D^\star - y^\star) + \epsilon [\tau] p^\star, \tag{2.39}$$

where ϵ is defined by (2.18), while the remaining variables are scaled as before. The finite bed slope introduces a further dimensionless parameter to the scaled model

$$\mu = \epsilon \cot \alpha. \tag{2.40}$$

If $\mu \lesssim O(1)$ and $\epsilon \ll 1$ as suggested by Fowler and Larson, then the leading-order analogue of (2.37) for glacier flow becomes

$$\frac{\partial D}{\partial t} + \frac{\partial}{\partial x}\left[\frac{1}{n+2}(D-H)^{n+2}\left(1 - \mu\frac{\partial D}{\partial x}\right)^n\right] = a(x,t). \tag{2.41}$$

In fact, Fowler and Larson go on to argue that μ becomes small for sufficiently steep glaciers and that their motion can be considered as a hyperbolic problem of the form

$$\frac{\partial D}{\partial t} + \frac{\partial}{\partial x}\frac{(D-H)^{n+2}}{n+2} = a(x,t). \tag{2.42}$$

where the neglected $O(\mu)$ diffusive term serves to smooth any shocks which arise.

A crucial feature of shallow ice models is that the gravitational 'driving stress' defined by the geometry of the ice sheet or glacier is supported locally at the bed.

In other words, the shear stress τ_b at the bed of a 'shallow' ice sheet is given by the local ice sheet geometry as

$$\tau_b = \tau_{xy}|_{y=H} = -(D-H)\frac{\partial D}{\partial x} \tag{2.43}$$

to an error of $O(\epsilon^2)$. The analogous relation for a shallow glacier is

$$\tau_b = (D-H)\left(1-\mu\frac{\partial D}{\partial x}\right). \tag{2.44}$$

Shallow ice models are commonly used to describe ice sheets and glaciers which are able to slide over their beds. This assumes implicitly that the bed is able to support a shear stress of any magnitude even when the overlying ice is no longer frozen to the bed. It is usually also assumed that this shear stress then determines the velocity at which the glacier or ice sheet slides over its bed, as discussed in section 2.3. However, as we will see in section 2.4 and chapter 3, these assumptions may not always be appropriate, and shallow ice models may need to be abandoned under certain circumstances.

A second important feature of shallow ice theories, which will become central to our discussion of subglacial cavitation in chapter 3, is that normal stress at the base of the ice is also given by the geometry of the ice sheet or glacier. For an ice sheet, we have a dimensional basal normal stress of

$$\sigma_{nn} = -\rho g[D](D^\star - H^\star) \tag{2.45}$$

to a fractional error of $O(\epsilon^2)$, while for a glacier of mean bed inclination α (cf. fig. 2.3), the equivalent expression is

$$\sigma_{nn} = -\rho g[D]\cos\alpha(D^\star - H^\star) \tag{2.46}$$

to an error of $O(\epsilon^2/\mu)$. When sliding at the base leads to local normal stress variations due to the presence of small-scale bed roughness, then the expressions (2.45)–(2.46) must be interpreted as averages over the length scale of bed roughness, as shown in appendix A.

2.3 Temperate Sliding

As the basal temperature of a glacier or ice sheet approaches the pressure melting point, a patchy film of liquid water can form at the interface between the ice and its bed, which weakens the contact between the two and is thought to allow for interfacial

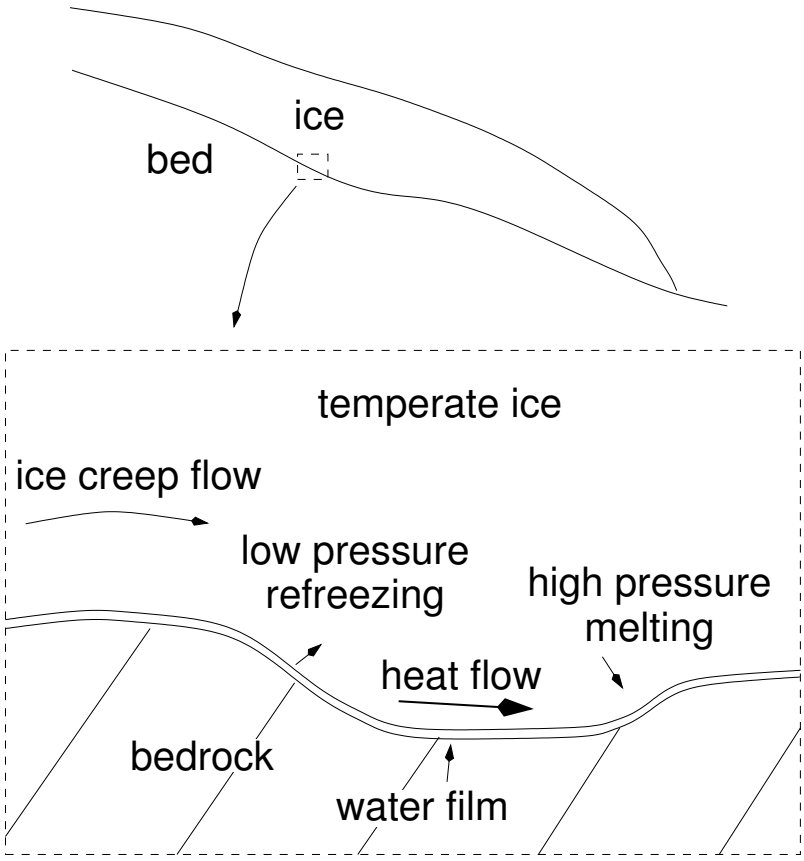

Figure 2.4: Temperate sliding. Note that the bed has small-scale irregularities which act as obstacles to ice flow.

slip (e.g. Shreve, 1984; Fowler, 1986b), and hence $\mathbf{u} = \mathbf{0}$ no longer holds at the bed. This water film is usually assumed to become continuous when the ice near the base of a glacier is temperate, i.e. at the pressure melting point throughout. Estimates for the thickness of the water film separating temperate ice from the bed are typically around 1 μm (Fowler, 1981; Paterson, 1994, chapter 7). Sheared at typical observed glacier sliding velocities of $\sim$ 10–100 m a^{-1}, a layer of water 1 μm thick supports shear stresses of around 10^{-8}–10^{-7} Pa, which may be compared with the much larger typical shear stresses of 10^5 Pa predicted for ice sheets (see the estimates after (2.17)). In other words, a continuous, thin water film at the base of a glacier or ice sheet supports insignificant amounts of shear stress and therefore allows essentially free slip.

The question which arises is not so much how sliding is possible, but how the bed of a temperate glacier opposes the gravitational driving force acting on the glacier. In the case of an undeformable and impermeable ('hard') bed, resistance to ice flow over the bed is usually assumed to arise from the presence of small-scale bed irregularities (see fig. 2.4).

There are two mechanisms by which a glacier or ice sheet can flow over a rough hard bed (Weertman, 1957). Firstly, ice can move over bed obstacles by the same process of creep deformation which gives rise to ice flux when there is no sliding. Secondly, ice can melt at the upstream end of a bed obstacle as a result of increased pressure there. This occurs because the melting point of ice anomalously decreases with increasing pressure. Hence the temperature of temperate ice drops with pressure, causing heat to flow to regions of increased pressure and ice to melt. The meltwater released then travels through the water film at the interface between ice and bedrock to the lee of the obstacle. There it refreezes as a result of reduced pressure raising the melting point (and hence causing a heat flux away from the lee of the obstacle and towards its upstream end). The effect of this process, which is known as regelation, is to allow a finite ice velocity *into* the bed at the ice-bed interface, which contributes to the net motion of the glacier.

Both sliding mechanisms cause higher normal pressures — i.e., compressive normal stresses — to be exerted on the upstream face of a bed obstacle than its downstream face, and in turn this causes a net force to be exerted by the obstacle on the basal ice in the upstream direction of the glacier. In particular, if we define $\mathbf{n}$ and $\mathbf{t}$ as the local unit normal and tangent vector to the glacier bed, respectively (fig. 2.5), then the force $\mathbf{f}$ exerted by an arc S of the bed on the glacier is

$$\mathbf{f} = -\int_S \boldsymbol{\sigma}\mathbf{n}\,\mathrm{d}s = -\int_S (\mathbf{n}\cdot\boldsymbol{\sigma}\mathbf{n})\,\mathbf{n}\,\mathrm{d}s - \int_S (\mathbf{t}\cdot\boldsymbol{\sigma}\mathbf{n})\,\mathbf{t}\,\mathrm{d}s, \tag{2.47}$$

where $\mathrm{d}s$ denotes an element of arc and $\boldsymbol{\sigma}$ is evaluated at the bed. If local shear stress $\mathbf{t}\cdot\boldsymbol{\sigma}\mathbf{n}$ at the base is negligible due to the presence of a water film, we have

$$\mathbf{f} = -\int_S (\mathbf{n}\cdot\boldsymbol{\sigma}\mathbf{n})\,\mathbf{n}\,\mathrm{d}s. \tag{2.48}$$

Suppose the mean flow direction of the glacier is aligned with the x-axis (fig. 2.4). If S denotes the portion of the bed $y = h(x)$ between $x = 0$ and $x = a$,[1] then $\mathbf{f} = (f_x, f_y)$ is given by

$$f_x = \int_0^a \sigma_{nn} h'(x)\,\mathrm{d}x, \qquad f_y = \int_0^a -\sigma_{nn}\,\mathrm{d}x, \tag{2.49}$$

where $\sigma_{nn} = (\mathbf{n}\cdot\boldsymbol{\sigma}\mathbf{n})|_{y=h(x)}$ and the prime denotes differentiation. If compressive normal stress $(-\sigma_{nn})$ is greater on the upstream side of obstacles, where local bed slope $h'(x)$ is positive, than on their downstream side, we have $f_x < 0$, and hence a net force in the upstream direction of the glacier, opposing the gravitational driving force.

[1] a is not to be confused with accumulation rate $a(x,t)$; the latter will not appear again in this thesis.

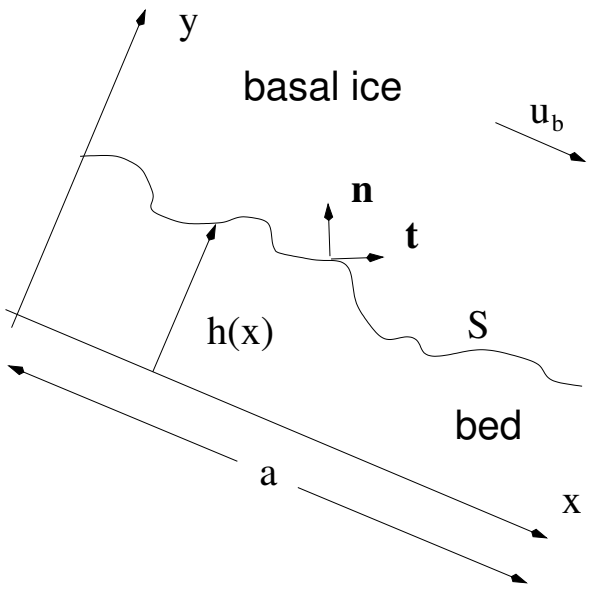

Figure 2.5: Geometry of the bed.

The stresses generated by the sliding of ice over bed obstacles increase with the velocity at which the ice slides, and hence the upstream force $-f_x$ also increases with sliding velocity. Based on the realistic premise that bed obstacles have wavelengths which are small compared with the thickness of the glacier or ice sheet, theories of hard bed sliding (e.g. Nye, 1969, 1970; Kamb, 1970; Morland, 1976a; Fowler, 1979, 1981) try to quantify an averaged 'effective' basal shear stress τ_b which arises from ice flow at some mean sliding velocity u_b over these bed obstacles. If a is a suitable averaging distance, then in the notation above one might define

$$\tau_b = -f_x/a = \frac{1}{a}\int_0^a -\sigma_{nn}h'(x)\,\mathrm{d}x, \tag{2.50}$$

where the term on the right-hand side depends on sliding velocity through σ_{nn}. When basal sliding occurs, an obvious replacement for the no-slip boundary condition (2.34) is then to impose a *sliding law* of the form

$$u = u_b = f(\tau_b) \qquad \text{on } y = H, \tag{2.51}$$

where τ_b is defined by (2.43). Sliding increases the ice flux terms in (2.37) and (2.41) by an amount $u_b(D - H)$; especially if sliding is rapid, this can be an important component of ice flux and significantly affect the evolution of an ice sheet or glacier.

Nye-Kamb Theory

A simple model for the relationship between basal sliding velocity and basal shear stress is due to Nye (1969) and Kamb (1970). These authors consider the plug flow

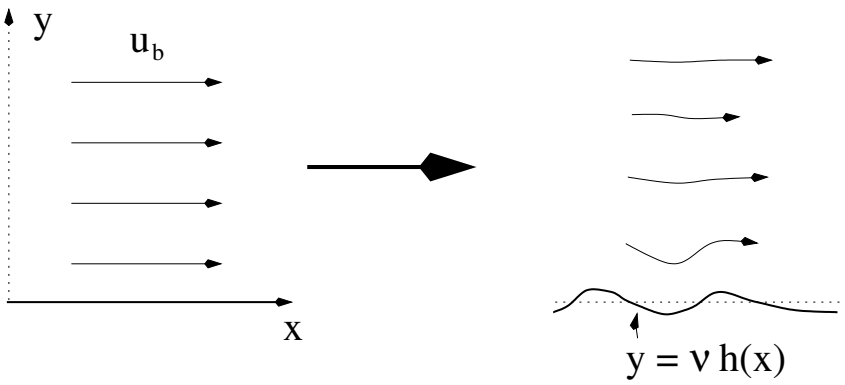

Figure 2.6: Nye's (1969) and Kamb's (1970) model

of a Newtonian fluid of infinite depth at velocity u_b over a flat surface $y = 0$ which exerts no shear stress on the fluid (cf. fig. 2.6). The surface is then perturbed by a small amount $y = \nu h(x)$, where $\nu \ll 1$, and the mean horizontal velocity at the bed is kept constant at u_b. $h(x)$ and $h'(x)$ are both assumed to be $O(1)$, thus $\nu \ll 1$ implies that perturbations to the flat surface have small slopes of $O(\nu)$.

Naïvely expanding in a regular perturbation expansion and taking terms of $O(\nu)$ yields the following field equations for the leading order velocity perturbation $\mathbf{u} = (u, v)$ and pressure perturbation p to the plug flow

$$\nabla^2 \mathbf{u} - \nabla p = \mathbf{0} \qquad y \in (0, \infty), \tag{2.52}$$

$$\nabla \cdot \mathbf{u} = 0 \qquad y \in (0, \infty), \tag{2.53}$$

in appropriate dimensionless variables. If regelation is ignored, then vanishing shear stress and normal velocity at the base require at leading order

$$v = u_b h'(x), \qquad \frac{\partial u}{\partial y} + \frac{\partial v}{\partial x} = 0 \qquad \text{on } y = 0. \tag{2.54}$$

It is, however, not clear what boundary conditions should apply at infinity, and this constitutes a major theoretical inconsistency in the model, as we will see below. Nye (1969) and Kamb (1970) simply assume that leading order perturbations vanish at infinity, and so

$$u,\, v,\, p \sim 0 \qquad \text{as } y \to \infty. \tag{2.55}$$

These equations can be solved straightforwardly using Fourier transform methods. We assume that bed is periodic with period a, and define the Fourier transform of a generic x-periodic function f with period a as

$$\hat{f}_r(y, t) = \int_0^a f(x, y, t) \exp(-ik_r x)/a \, \mathrm{d}x : \qquad k_r = \frac{2r\pi}{a}, \qquad r \in \mathbb{Z}. \tag{2.56}$$

Compressive normal stress at the bed is at leading order

$$-\sigma_{nn} = p - 2\frac{\partial v}{\partial y} \qquad \text{on } y = 0, \tag{2.57}$$

with a Fourier transform solution in terms of the bed elevation h and sliding velocity u_b given by

$$\hat{p}_r - 2\frac{\partial \hat{v}_r}{\partial y} = 2ik_r|k_r|u_b\hat{h}_r, \tag{2.58}$$

which shows that the leading-order compressive normal stress is generally greater on the upstream side of a bed obstacle than on its downstream side since, for a bed in the form of a sine wave, compressive normal stress has a phase shift of $\pi/2$ relative to the bed. Estimating the (dimensionless) effective basal shear stress by a leading-order analogue of (2.50) gives

$$\tau_b = \frac{1}{a}\int_0^a \left(p - 2\frac{\partial v}{\partial y}\right)\Big|_{y=0} h'(x)\,\mathrm{d}x = u_b \sum_{r=1}^{\infty} 4k_r^3|\hat{h}_r|^2, \tag{2.59}$$

assuming that the series on the right-hand side converges. (2.59) furnishes a sliding law which relates τ_b linearly to u_b, with a constant of proportionality dependent on the bed roughness h.

One can go on to construct the second-order corrections to the velocity and pressure fields. The important feature of the $O(\nu^2)$ correction terms is that the second-order x-velocity field has a shearing component which behaves as $\sim \nu^2\tau_b y$ at large y. This is what one would expect: If the bed supports an 'effective' shear stress then the velocity field must behave as a shearing flow at large distances from the bed. However, the same observation also shows why the Nye's and Kamb's model is not properly posed: at large $y \sim 1/\nu$, the ordering in their naïve perturbation expansion breaks down, and at $y \sim 1/\nu^2$, the shearing component becomes comparable to the unperturbed plug flow velocity. This behaviour indicates that the sliding of ice over small-scale bed obstacles is best viewed as a boundary layer to the 'outer' shearing flow of the glacier or ice sheet, which corresponds to large y in Nye's and Kamb's model.

Boundary Layer Treatment

The discussion above shows that the main difficulty in constructing a consistent theory of basal sliding lies in how to prescribe boundary conditions at 'infinity' for a flow over local bed topography. This is tantamount to the problem of coupling a mathematical description of the flow of basal ice over small-scale bed undulations to a description

of the 'bulk' flow of the glacier or ice sheet, and to the problem of defining what is meant by a sliding velocity u_b and a basal shear stress τ_b as 'seen' by the bulk flow.

A consistent formulation of the glacier sliding problem in which the bulk flow of the glacier is described by the shallow ice approximation is due to Fowler (1977, 1979, 1981), who considers the flow of ice over small-scale roughness near the bed as a boundary layer to the bulk flow of the ice. The bulk flow of the ice is described in terms of the shallow ice approximation, while the solution of the boundary layer problem provides an effective boundary condition of the form (2.51) on the bulk flow of the ice in a matching region some way above the actual physical bed. For reasons of space, we do not give the development of this theory in detail here, but a brief sketch may be found in appendix A.

Fowler's results substantiate the notion of an effective basal shear stress defined by (2.50). For small bed roughness slopes ν and ice of constant viscosity, he recovers Nye's (1969) and Kamb's (1970) leading-order model, so that the sliding law is given by (2.59). Fowler's method is, however, not limited to a Newtonian rheology, and may also be applied with some justification to beds whose roughness slopes are not small. If regelation is ignored and the ice is everywhere in contact with the bed (i.e. separated from it only by a thin film of water), Fowler's (1979; 1981) sliding law takes the general form

$$u_b = C\tau_b^n, \tag{2.60}$$

where C is a constant (or, more generally, a function of x) which depends on the geometry of the local bed roughness, and n is the exponent in Glen's law.

2.4 Deformable Beds

The assumption that basal ice rests directly on undeformable and impermeable bedrock is not always realised. In fact, around 70 % of the area glaciated during the Ice Ages is covered by soft sediments of some kind, which may have behaved very differently from hard bedrock. At least in the case of the former mid-latitude ice sheets, classical hard-bed sliding of the type considered in the previous section may therefore have been something of a rarity.

When the bed of an ice sheet consists of unfrozen soft sediment, then meltwater reaching the base of the ice can drain into the bed, rather than merely being confined to a drainage system at the interface between the ice and its bed. This may conceivably affect the process of regelation, since water generated by pressure melting no

longer needs to flow through an interfacial water film but can drain into the underlying porous sediment. More generally, the presence of pressurised meltwater at the bed has an effect on sliding through the process of cavitation described in chapter 3; hence any effect which a permeable bed has on the drainage of meltwater is likely to be reflected in the sliding behaviour of the glacier or ice sheet.

The main effect of an unfrozen deformable bed, however, occurs through the deformation of subglacial sediment or till. This was first observed directly under two glaciers in the U.S.A. and Iceland by Engelhardt and others (1978) and Boulton (1979); since then, it has been suggested that sediment deformation can contribute significantly to the basal motion (Boulton and Hindmarsh, 1987), and may in fact account for most of the observed sliding velocities of some ice streams (Blankenship and others, 1986, 1987).

As a result of the possible importance of till deformation for the large-scale behaviour of glaciers and ice sheets, the properties of till have become a focus of glaciological research (see Alley, 2000, for a review). Unfortunately, no universally accepted mathematical model for the behaviour of till has emerged from this research. Below, we review some of the basic ingredients for a continuum model of till deformation (e.g. Clarke, 1987), and point out some of the contentious issues.

Subglacial till is a granular material. As a result, it deforms more easily when contacts between individual grains are weakened by the presence of a pore fluid — liquid water in the present case — at sufficiently high pressure. In what follows, we assume that deforming till is water-saturated. If we ignore the inertial effect of momentum diffusion (Truesdell and Toupin, 1960, pp. 567–568), then the total stress field $\boldsymbol{\sigma}$ in the water-till mixture is the sum of stresses $\boldsymbol{\sigma}_e$ and $\boldsymbol{\sigma}_w$ supported by the till matrix and porewater, respectively,

$$\boldsymbol{\sigma} = \boldsymbol{\sigma}_e + \boldsymbol{\sigma}_w. \tag{2.61}$$

The stress $\boldsymbol{\sigma}_e$ supported by the till matrix is also known as effective stress. Porewater usually does not support any significant macroscopic deviatoric stresses, and we put

$$\boldsymbol{\sigma}_w = -p_w \mathbf{I}, \tag{2.62}$$

where $\mathbf{I}$ is the identity tensor (the Kronecker delta in component notation). For a slow flow, where inertial terms may be neglected, momentum conservation requires

$$\nabla \cdot \boldsymbol{\sigma} + \rho_b \mathbf{g} = \mathbf{0} \tag{2.63}$$

where $\mathbf{g}$ is the (vector-valued) acceleration due to gravity, and the bulk density ρ_b is defined in terms of the density of individual sediment grains ρ_s, the density ρ_w and porosity ϕ as

$$\rho_b = (1-\phi)\rho_s + \phi\rho_w. \tag{2.64}$$

In general, sediment grains and water are much less compressible separately than as a mixture, in which porosity ϕ may be altered. Mass conservation for the till and water may then be expressed in terms of porosity ϕ (the volume fraction occupied locally by porewater) as

$$-\frac{\partial\phi}{\partial t} + \nabla\cdot((1-\phi)\mathbf{u}) = 0 \tag{2.65}$$

$$\frac{\partial\phi}{\partial t} + \nabla\cdot(\phi\mathbf{u}) + \nabla\cdot\mathbf{q_w} = 0 \tag{2.66}$$

respectively. $\mathbf{u}$ denotes the averaged velocity field of the till matrix, and $\mathbf{q_w}$ the volume flux of water relative to it.

In order to close the model, constitutive relations for porosity ϕ, stress $\boldsymbol{\sigma}$ and flux $\mathbf{q_w}$ must be sought. $\mathbf{q_w}$ is usually assumed to obey Darcy's law,

$$\mathbf{q_w} = -\frac{k}{\eta_w}\left(\nabla p_w - \rho_w\mathbf{g}\right), \tag{2.67}$$

where permeability k depends on porosity and η_w denotes the viscosity of water. A much more contentious issue is the prescription of a rheology for till, i.e. a constitutive relation for $\boldsymbol{\sigma}$. As pointed out above, till is more easily deformed at high porewater pressures. In particular, till is more mobile when the difference between the total pressure p supported by the water-till mixture,

$$p = -\frac{1}{3}\mathrm{Tr}\,\boldsymbol{\sigma}, \tag{2.68}$$

and water pressure p_w is small. In other words, we may expect the rheology of till to depend on the *effective pressure*[2] p_e defined by

$$p_e = p - p_w. \tag{2.69}$$

Early field observations of till deformation (e.g. Boulton and Hindmarsh, 1987) suggested that a certain thickness of till directly underneath the ice deformed continuously as a shearing flow. On the basis of this observation, and due to their conceptual simplicity, viscous rheologies for till gained popularity (e.g. Alley, 1989). Boulton and

[2]A similar, but distinct definition of effective pressure is employed in chapter 3, which deals with the formation of subglacial cavities

Hindmarsh proposed a power-law relationship for incompressible till (ϕ constant) of the form

$$\dot{\boldsymbol{e}} = K\frac{\tau^{m-1}\boldsymbol{\tau}}{p_e^n}, \tag{2.70}$$

where K is a constant, $\boldsymbol{\tau} = \boldsymbol{\sigma} - p\mathbf{I}$ is the deviatoric stress tensor for the the ice-till mixture, τ its second invariant defined by equation (2.4), and $\dot{\boldsymbol{e}}$ is the strain-rate tensor for the till matrix, defined by (2.1). Since till below a certain depth is usually found to be undisturbed (see e.g. Boulton, 1987), Boulton and Hindmarsh also proposed an alternative, Herschel-Bulkley type rheology which incorporates a yield stress τ_c below which there is no deformation:

$$\dot{\boldsymbol{e}} = \begin{cases} K\frac{(\tau-\tau_c)^m}{p_e^n}\frac{\boldsymbol{\tau}}{\tau} & \tau > \tau_c, \\ \mathbf{0}, & \tau \leq \tau_c \end{cases} \tag{2.71}$$

where m, $n > 0$. τ_c is given by a Coulomb-type failure relationship

$$\tau_c = \mu p_e + C, \tag{2.72}$$

where μ is a friction coefficient and C denotes a cohesive term. The model rheologies (2.71) and (2.72) have the expected feature that deformation is facilitated when, at given shear stress τ, effective pressure is reduced. In addition, since effective pressure will generally increase with depth, (2.71) has the desirable feature that it will confine deformation to a layer of finite thickness, regardless of the thickness of till available.

Simple models for ice sliding over viscous effective-pressure dependent till in simple shear, in which water pressure is prescribed, yield sliding laws somewhat similar to those discussed in section 2.3 (e.g. Alley, 1989). In particular, τ_b is again an increasing function of u_b, but now also depends on some mean value of the effective pressure p_e (of which it is also an increasing function),

$$\tau_b = f(u_b, p_e). \tag{2.73}$$

However, more recent laboratory experiments have indicated that till may in fact not be a viscous but an elastic-plastic material with an effective pressure dependent yield criterion (e.g Iverson and others, 1998; Tulaczyk and others, 2000). In other words, yielding occurs when shear stress reaches a yield stress τ_c (usually taken to be of the form (2.72)). Below the yield stress, strains are purely elastic, while strain rates at the yield stress are given by some plastic flow rule (see e.g. Fowler and Noon, 1999). Crucially, the yield stress τ_c cannot be exceeded.

A plastic rheology for subglacial till has important consequences for the mechanics of glaciers and ice sheets overriding deformable beds with high porewater pressures:

the shear stress at the interface between ice and till cannot exceed the yield stress. This implies that shallow ice theories cannot always be applied to such glaciers or ice sheets (i.e. when driving stress τ_b defined geometrically in (2.43) or (2.44) exceeds the local yield stress at the bed), unless basal topography plays a similar role in supporting the gravitational driving stress as it does in classical hard bed sliding theory (section 2.3). If the bed is locally unable to provide sufficient resistance to balance the geometrically defined driving stress, for instance because of high porewater pressures at the bed, then tensile or 'lateral' stresses ignored in the shallow ice approximation must become comparable with shear stresses in the ice in order to balance the gravitational driving stress. This point is investigated further in Raymond (1996) and Whillans and van der Veen (1997).

One of the main criticisms of the laboratory experiments which provide most of the evidence for a plastic rheology has been the fact that they are unable to reproduce subglacial conditions. In particular, the ring-shear devices used to test the properties of till have relatively small chambers. Moderate sized clasts (rock fragments) usually jam in such devices and have to be removed from till samples prior to testing; the material whose properties are then being measured is then no longer the same as is found at the base of the ice sheet or glacier from which it was obtained (Fowler, submitted to *J. Glaciol.*).

A further difficulty in using a plastic rheology to model till deformation arises because generally one would expect effective pressure to increase with depth in the till (see Tulaczyk and others, 2000, for a discussion). In that case, the yield stress τ_c is lowest at the upper surface of the till, which is where one expects failure to occur. This is at odds with the observation of distributed strain in subglacially deformed sediments. Recently, a number of mechanisms have been proposed to explain distributed shear in plastic subglacial till, involving the occasional formation of grain bridges (Iverson and Iverson, 2001) or variations in water pressure p_w at the interface between ice and till (Tulaczyk, 1999; Tulaczyk and others, 2000).

Field measurements which could resolve the issue of till rheology unambiguously are difficult to obtain, since they usually require the effective pressure, the basal shear stress and the till strain rate to be measured simultaneously. Usually basal shear stress is badly constrained and can only be estimated using the formulae (2.43) or (2.44). When basal conditions are inhomogeneous, these formulae can, however, at best give a locally averaged basal shear stress. At worst, when shallow ice theory fails, as it must when the bed is plastic and τ_b given by (2.43) or (2.44) exceeds the local yield stress τ_c, they are simply wrong. Likewise, observations of basal porewater

pressure are usually confined to a few boreholes, and effective pressure may thus only be known in a few isolated locations. However, there are some field observations which do lend credence to an elastic-plastic till rheology, such as the measurements of elastic till deformation by Iverson and others (1999), and the measurements of drag on devices inserted into basal till and dragged through the till by the glacier Hooke and others (1997) and Fischer and others (1998).

Our purpose here is not to resolve the issue of till rheology. In part II of this thesis we will analyse a model for drumlin formation which has been proposed elsewhere (Hindmarsh, 1998b; Fowler, 2000) and which is based on the assumption of incompressible viscous till. The results of this model will then be compared with observations made of real drumlins, and agreement or otherwise of theoretical predictions with these observations may allow us to determine whether the model — and possible the choice of rheology itself — are realistic.

Part I

Glacier and Ice Sheet Sliding

Chapter 3

Subglacial Cavitation

3.1 Introduction

When the basal ice of a glacier is at the pressure melting point throughout, a water film can form at the interface between ice and bedrock. This water film supports insignificant shear stress when sheared at typical glacier sliding velocities. Classical 'hard bed' models of basal sliding therefore account for the force balance of such a glacier by supposing that irregularities on the bed generate drag. By exerting higher normal pressures on their upstream faces than their downstream faces, bed obstacles can cause a net force on the glacier in its upstream direction, which balances the gravitational driving force acting on the glacier. As the gravitational driving force increases, the variations in normal stress which generate drag must also increase. Since the mean normal stress on the bed is fixed hydrostatically, this implies that normal pressure must decrease in the lee of bed obstacles while it increases on upstream faces.

Variations in normal stress at the bed can lead to cavitation, which is unaccounted for in the sliding laws we have discussed so far (Lliboutry, 1968). Cavitation occurs once normal pressure in the lee of a bed obstacle drops to a critical *separation pressure* p_c, at which point no further decrease in normal pressure is possible. For instance, once normal pressure reaches the triple-point pressure of water, a vapour-filled cavity will start to form. Similarly, meltwater from a channelised subglacial drainage system (e.g. Paterson, 1994, chapter 6) may force its way between ice and bed if normal pressure reaches the drainage pressure, resulting in a water-filled cavity.

The extent of cavity formation depends on the size of variations in normal stress compared with the difference between mean hydrostatic pressure $\bar{p}$ at the bed and the separation pressure p_c,

$$N = \bar{p} - p_c. \tag{3.1}$$

N is usually referred to as the *effective pressure*, especially when p_c is given by the water pressure in a subglacial drainage system. The smaller the value of N, the more likely variations in normal stress are to lead to cavitation, and the more extensive cavitation will be.

One effect of cavitation is to 'drown out' elements of bed roughness. Thus, a cavity which forms in the lee of a large bed obstacle can lead to the base of the ice losing contact with smaller obstacles downstream of the large one. It is natural to suppose that this will lead to reduced resistance to flow. As a consequence, the sliding velocity of a glacier is likely to depend not only on basal shear stress τ_b, but also on effective pressure N, and the sliding law (2.51) should in fact take the form

$$u_b = f(\tau_b, N). \tag{3.2}$$

A commonly used heuristic generalisation of the sliding law (2.60) which aims to account for the drowning of bed roughness due to cavity formation is

$$u_b = C\tau_b^p N^{-q}, \tag{3.3}$$

where p, $q > 0$. This sliding law was suggested by Bindschadler (1983) on empirical grounds, and has been popularised by the theoretical treatment of Fowler (1987a) and the textbook account of Paterson (1994, chapter 5). It states qualitatively that, for a given basal shear stress τ_b, sliding velocity u_b increases when effective pressure N decreases and cavitation becomes more widespread. This is what one would expect intuitively. However, (3.3) also implies that arbitrarily high shear stresses can be supported by local bed roughness. As we shall see in the next section, this need not be the case.

3.2 A Bound on Effective Basal Shear Stress

In general, an increase in shear stress τ_b supported at the bed is achieved by increasing compressive normal stress on the upstream sides of bed obstacles, which requires a concurrent decrease in compressive normal stresses on their downstream sides. The latter may, however, be inhibited if compressive normal stress is bounded below. Iken (1981) suggested that this should lead to a bound on effective basal shear stress τ_b which depends only on effective pressure N and the geometry of the bed,

$$\tau_b \leq N \tan \beta, \tag{3.4}$$

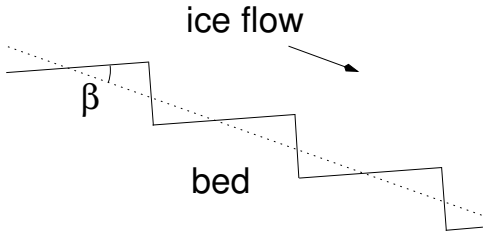

Figure 3.1: The bed considered by Iken (1981)

where β is the maximum angle between the bed and the mean flow direction. Iken's derivation, however, only applies to the periodic 'tilted staircase' geometry shown in fig. 3.1, where ice is assumed to be in contact with the bed everywhere. The generalisation of this result to other bed geometries is not immediately obvious, and may explain why sliding laws of the type (3.3) remain popular despite the fact that they conflict with Iken's bound.

Here we present a derivation of Iken's bound for more irregular beds. As suggested by Fowler (1979, 1981, see also appendix A), we suppose that the bed may be decomposed into a slowly varying smooth component H, which may be taken as constant over the bed roughness length scale, and a rapidly varying local roughness component $h(x)$. As in Iken's (1981) paper, we still require that the local roughness component $h(x)$ of the bed should be periodic with some finite period a, but there may now be many bed obstacles per period. $h(x)$ is further constrained to be piecewise continuously differentiable.

In order to construct a bound on effective basal shear stress, we consider the force exerted by the glacier bed on the overlying ice and cavity fluid (fig. 3.2). If forces on the fluid in each cavity — air, vapour or liquid water — balance and its weight may be neglected, then this is the force exerted on the base of the ice.

We require normal stress σ_{nn} at the bed to be integrable, and to satisfy

$$-\sigma_{nn} \geq p_c. \tag{3.5}$$

everywhere, where p_c is a positive constant. Since it is conceivable that not all cavities exist at the same pressure — some may be caused by water from the subglacial drainage system, others may simply be vapour-filled — p_c is a lower bound for compressive normal stress, but need not be equal to the separation pressure for any specific cavity.

The force $\mathbf{f} = (f_x, f_y)$ exerted by one period of the bed on the overlying ice and

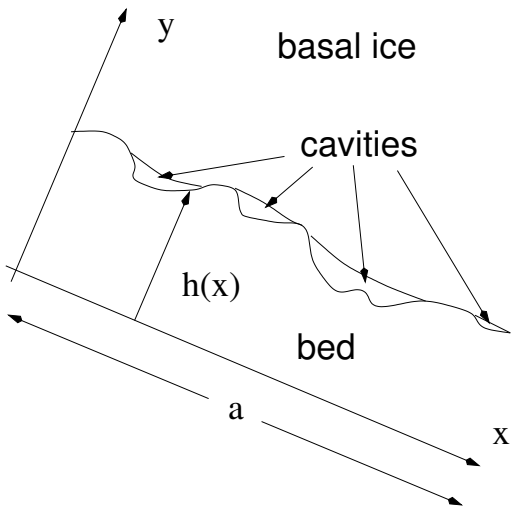

Figure 3.2: A cavitated glacier bed

cavity fluid is given by (2.49):

$$f_x = \int_0^a \sigma_{nn} h'(x)\,\mathrm{d}x, \qquad f_y = \int_0^a -\sigma_{nn}\,\mathrm{d}x. \tag{3.6}$$

Effective basal shear stress is defined as (see also (2.50) and (A.50))

$$\tau_b = -f_x/a, \tag{3.7}$$

while mean compressive normal stress $\bar{p}$ is prescribed hydrostatically (cf. (2.45)–(2.46) and (A.46)–(A.47)),

$$f_y/a = \bar{p}. \tag{3.8}$$

We define a local effective pressure $N_{loc}(x)$ as

$$N_{loc} = -\sigma_{nn} - p_c. \tag{3.9}$$

(3.5) shows that $N_{loc} \geq 0$ everywhere. Noting that h is periodic, we obtain from (3.6)–(3.8)

$$\tau_b = \frac{1}{a}\int_0^a N_{loc}(x) h'(x)\,\mathrm{d}x, \qquad N = \bar{p} - p_c = \frac{1}{a}\int_0^a N_{loc}(x)\,\mathrm{d}x. \tag{3.10}$$

Since $N_{loc}(x) \geq 0$ everywhere, (3.10) yields

$$\tau_b \leq \frac{1}{a}\int_0^a N_{loc}(x) \max\left(h'\right)\,\mathrm{d}x = N \max\left(h'(x)\right). \tag{3.11}$$

Hence τ_b satisfies Iken's bound, provided $h'(x)$ is bounded above.

The assumption that shear stress vanishes locally at the bed is essential to the derivation of this bound. It may be violated in practice, as the ice near the base of a glacier is rarely clean but usually contains varying amounts of debris which can bridge the interfacial water film (e.g. Morland, 1976b; Schweizer and Iken, 1992). Whether τ_b is still bounded when interfacial friction due to debris moving over the bed contributes to basal drag then depends on the nature of the local friction law.

It is important to realise that the derivation above does not require all cavities to form at the same separation pressure, but merely requires a lower bound p_c below which normal pressure at the bed cannot drop. Nevertheless, it will be convenient in practice to assume that all cavities are at the same pressure when we come to consider what shape a realistic sliding law should take.

3.3 The Sliding Law

The bound on τ_b above indicates the sliding law (3.3) is not viable unless the bed roughness slope $h'(x)$ is unbounded. This naturally leads to the question of what form a realistic sliding law which accounts for cavity formation should take. Attempts by Schweizer and Iken (1992) and Truffer and Iken (1998) to construct alternative sliding laws which do not violate (3.11) can at best be described as heuristic as they involve several questionable *ad hoc* assumptions about the geometry of cavities. The only properly posed model for basal sliding in the presence of cavitation is due to Fowler (1986a), who generalised Nye's (1969) and Kamb's (1970) treatment of basal sliding to include steady (time-independent) cavities.

Fowler only considered the case of a periodic bed with a single cavity per period, and found a sliding law of the form shown in fig. 3.3, where dimensionless τ_b/N is plotted against dimensionless u_b/N. The sliding law in fig. 3.3 was calculated for a (scaled) cosine-shaped bed $h(x) = \cos(x)$, such that $\max(h'(x)) = 1$. Clearly, τ_b/N calculated by Fowler (1986a) satisfies Iken's bound (3.11), though this was not pointed out in his original paper. More importantly, however, τ_b/N is not a monotonically increasing function of u_b/N, and hence u_b is no longer a single-valued function of τ_b at constant effective pressure N. Figure 3.4 shows how this multi-valuedness of the sliding law arises: at low u_b/N, when there is no cavitation or cavities are localised, τ_b/N increases linearly with u_b/N as required by Nye-Kamb theory (see section 2.3). At higher values of u_b/N, cavities grow and resistance is reduced, so that τ_b/N increases less rapidly with u_b/N. Eventually, the contact area

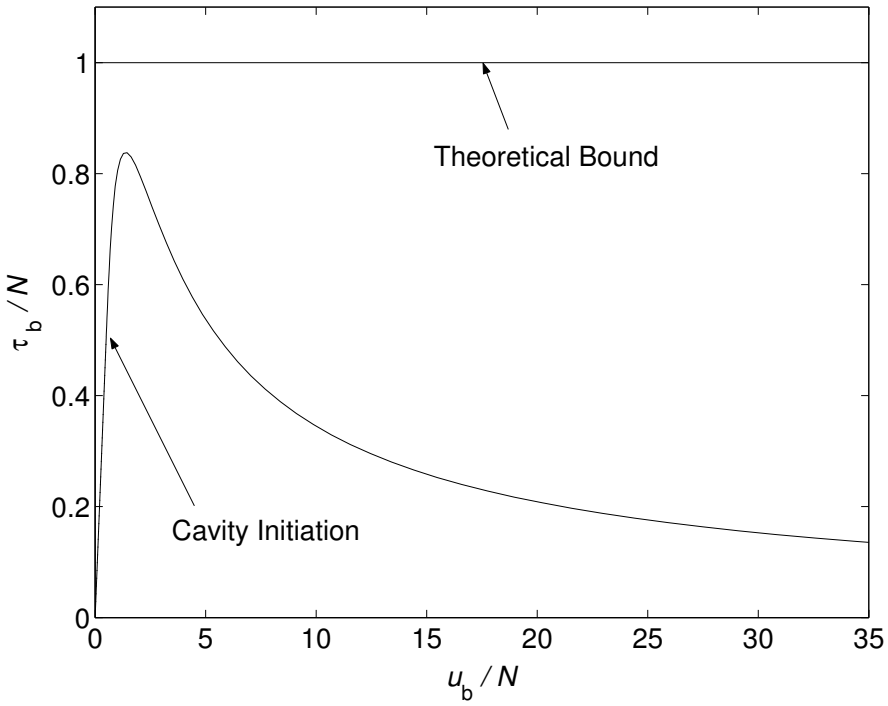

Figure 3.3: Fowler's (1986a) sliding law in the presence of cavitation for a sinusoidal bed. Note that drag decreases at high velocity owing to the 'drowning' of bed roughness shown in figure 3.4. At low sliding velocities, before cavity initiation, the sliding law follows Nye's (1969) and Kamb's (1970) linear relationship.

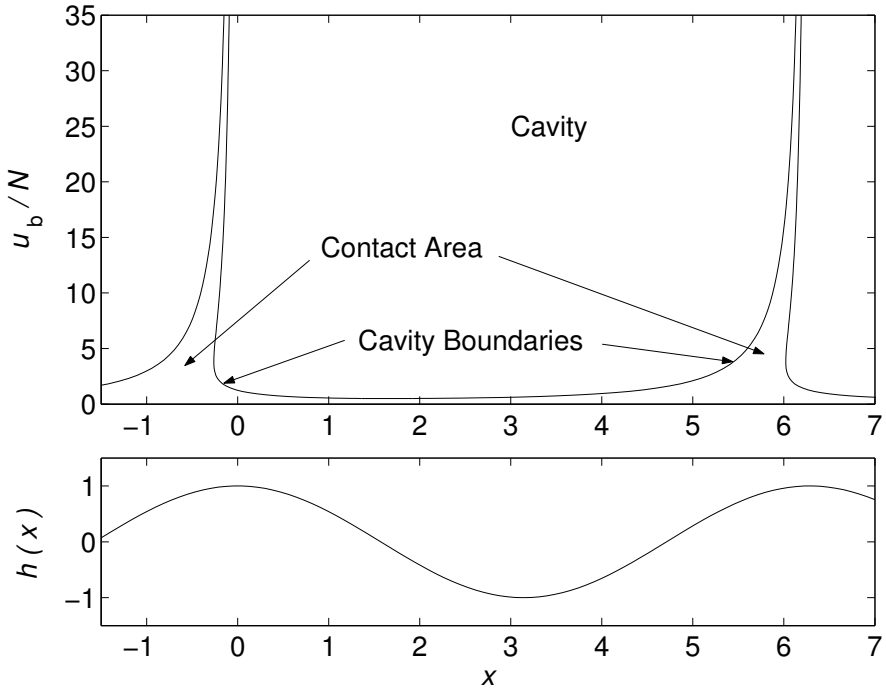

Figure 3.4: A plot of cavity boundary positions vs. u_b/N for a sinusoidal bed. The migration of the contact area towards the top of bed bumps at high velocity is evident in the top panel. This explains why τ_b/N decreases at high u_b/N.

between ice and bed shrinks and migrates to the top of the bed obstacle, where bed slope $h'(x)$ is low. Hence the drag generated starts to decrease, and so τ_b/N decreases.

Fowler (1986a) considers the multivaluedness in his sliding law as an anomaly caused by the periodicity of the bed: If the contact area on one bed obstacle migrates to the top of the obstacle and its roughness is thereby 'drowned out', then the same holds true of all other bed obstacles. For a more irregular bed, he argues, larger bumps should provide increased resistance as smaller ones are drowned out, and τ_b/N should continue to increase. This point is reiterated in Fowler (1987a), where a complicated superposition of bed obstacles of asymptotically different sizes is used to derive a sliding law of the form (3.3). Since this sliding law conflicts with Iken's bound, we are led to conclude that the superposition of bed obstacles used in Fowler (1987a) implicitly generates unbounded bed slopes.

Here we reconsider Fowler's (1986a) model and show how a solution can be derived when there is a finite number of cavities per period. This will allow us to determine the form of a realistic sliding law when bed slopes are bounded.

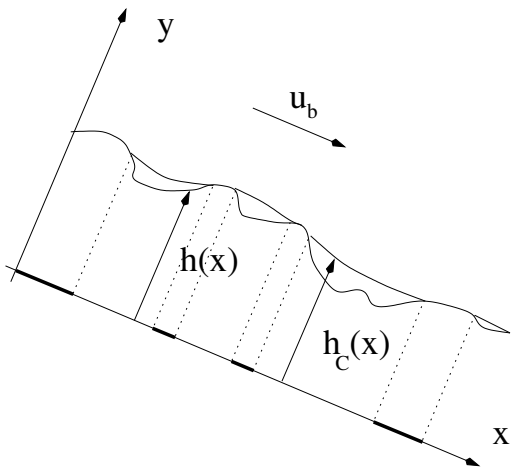

Figure 3.5: The geometry of a cavitated glacier bed. The contact areas $x \in C'$ are shown using heavy lines on the x-axis. Fowler's (1986a) model reduces the geometry of the problem to the half space $y > 0$ by assuming that bed roughness slopes are small

3.4 Fowler's Model

A formal derivation of the model based on the formulation of the sliding problem as a boundary layer (see appendix A) may be found in Fowler (1986a). As in Nye-Kamb theory (section 2.3), ice is assumed to have constant viscosity and the sliding problem is reduced to a half space geometry $y > 0$ on the basis that bed obstacles have small slopes. The bed $h(x)$ is assumed to be periodic with some period a, and cavities are assumed to be steady and to exist at some constant separation pressure p_c, so the problem is time-independent. We denote by $y = 0$, $x \in C'$ the part of the base on which ice is in contact with the bed, and while on $y = 0$, $x \in C$ the base of the ice is separated from the bed by a cavity. Where cavities exist, $h_C(x)$ will denote the height of the cavity roof (cf. fig. 3.5).

Appropriate field equations for the scaled velocity field $\mathbf{u} = (u, v)$ and pressure field p in the half space $y > 0$ are

$$\nabla^2 \mathbf{u} - \nabla p = \mathbf{0}, \tag{3.12}$$

$$\nabla \cdot \mathbf{u} = 0, \tag{3.13}$$

where a hydrostatic term has been subtracted from p.

At the base, regelation is ignored and hence vanishing normal velocity on the contact areas requires

$$v = u_b h'(x) \qquad \text{on } y = 0,\ x \in C', \tag{3.14}$$

where u_b denotes the sliding velocity, which is constant over the bed roughness scale. The unknown shape of the cavity roof $h_C(x)$ satisifies an analogous equation

$$v = u_b h_C'(x) \qquad \text{on } y = 0,\ x \in C. \tag{3.15}$$

On the cavities, compressive normal stress is equal to the separation pressure p_c, which is assumed constant for all cavities. Since a hydrostatic contribution has already been removed from p, the normal stress boundary condition on the cavity roof may be written as

$$p - 2\frac{\partial v}{\partial y} = -N \qquad \text{on } y = 0,\ x \in C, \tag{3.16}$$

where N is the (scaled) effective pressure. Furthermore, shear stress vanishes everywhere at the base,

$$\frac{\partial u}{\partial y} + \frac{\partial v}{\partial x} = 0 \qquad \text{on } y = 0. \tag{3.17}$$

Asymptotic matching with the 'outer' bulk flow gives boundary conditions

$$u,\ v,\ p \sim 0 \qquad \text{as } y \to \infty, \tag{3.18}$$

while effective basal shear stress τ_b is, at leading order,

$$\tau_b = \frac{1}{a}\int_0^a \left(p - 2\frac{\partial v}{\partial y}\right)\bigg|_{y=0} h'(x)\,\mathrm{d}x. \tag{3.19}$$

Since $h(x)$ is periodic and N constant, we can write by analogy with $(3.10)_1$,

$$\tau_b = \frac{1}{a}\int_0^a \left(p - 2\frac{\partial v}{\partial y} + N\right)\bigg|_{y=0} h'(x)\,\mathrm{d}x = \frac{1}{a}\int_0^a N_{loc}(x)h'(x)\,\mathrm{d}x. \tag{3.20}$$

From (3.16) we see that the integrand $N_{loc}(x) = (p - 2\partial w/\partial z + N)|_{y=0}$ is only non-zero on the contact areas; hence, in order to calculate the sliding law, we must determine normal stresses on C' as a function of sliding velocity u_b.

As well as the velocity and pressure fields $\mathbf{u}$ and p, the extent of cavities C is unknown *a priori*. As further constraints on the position of cavities we have the requirement that compressive normal stress cannot drop below p_c at the bed, and hence

$$N_{loc}(x) = p - 2\frac{\partial v}{\partial y} + N \geq 0 \qquad \text{on } y = 0,\ x \in C', \tag{3.21}$$

(which incidentally ensures that τ_b in (3.20) satisfies Iken's bound). Furthermore the cavity roof is above the bed

$$h_C(x) > h(x) \qquad \text{on } x \in C. \tag{3.22}$$

and we expect the base of the ice to joins the bed at the cavity end points, so that $h_C = h$ at cavity end points. Since the boundary of the ice flow domain is fixed in the present leading order problem to lie at $y = 0$ and the only unknown part of the boundary is the position of the cavity end points, the problem in hand is a free boundary problem of codimension two (see e.g. Gillow, 1998), and its particular form makes it susceptible to solution by complex variable methods (England, 1971).

3.4.1 Complex Variable Formulation

We introduce the complex variables z and $\overline{z}$ as

$$z = x + iy, \qquad \overline{z} = x - iy, \tag{3.23}$$

where i is the imaginary unit. Hence

$$\frac{\partial}{\partial x} = \frac{\partial}{\partial z} + \frac{\partial}{\partial \overline{z}}, \qquad \frac{\partial}{\partial y} = i\left(\frac{\partial}{\partial z} - \frac{\partial}{\partial \overline{z}}\right), \tag{3.24}$$

where $\partial/\partial z$ signifies the partial derivative with respect to z at constant $\overline{z}$, and $\partial/\partial\overline{z}$ is defined analogously. In the analysis below, the following relationships for a holomorphic function θ and its derivative will be used repeatedly (cf. England, 1971, section 1.3)

$$\frac{\partial}{\partial z}\overline{\theta(z)} = 0, \qquad \frac{\partial}{\partial \overline{z}}\overline{\theta(z)} = \overline{\theta'(z)}. \tag{3.25}$$

Since the flow of ice is incompressible, we define a stream function ψ such that

$$u = \frac{\partial \psi}{\partial y}, \qquad v = -\frac{\partial \psi}{\partial x}. \tag{3.26}$$

ψ satisfies the biharmonic equation

$$\nabla^4 \psi = 0, \qquad y \in (0, \infty). \tag{3.27}$$

Using (3.24), this can be re-written as

$$\frac{\partial^4 \psi}{\partial \overline{z}^2 \partial z^2} = 0, \qquad z \in S^+ \tag{3.28}$$

where we use S^+ to denote the upper half of the complex plane, $\Im(z) > 0$. We assume that ψ is at least four times continuously differentiable. Then, since S^+ is simply connected, the methods outlined in England (1971, chapter 1) allow the solution of (3.28) to be written as

$$\psi = \overline{z}\theta_1(z) + \phi_1(z) + z\overline{\theta_2(z)} + \overline{\phi_2(z)} \tag{3.29}$$

where θ_1, θ_2, ϕ_1 and ϕ_2 are holomorphic in S^+. As ψ must be real, $\psi = \left[\psi + \overline{\psi}\right]/2$, and so

$$\psi = \overline{z}\theta(z) + z\overline{\theta(z)} + \phi(z) + \overline{\phi(z)}, \tag{3.30}$$

where

$$\theta(z) = \frac{1}{2}\left[\theta_1(z) + \theta_2(z)\right], \qquad \phi = \frac{1}{2}\left[\phi_1(z) + \phi_2(z)\right]. \tag{3.31}$$

Substituting u and w defined by (3.26) in (3.12) yields, on separating x- and y-components:

$$\frac{\partial p}{\partial x} = \frac{\partial}{\partial y}\nabla^2\psi, \qquad \frac{\partial p}{\partial y} = -\frac{\partial}{\partial x}\nabla^2\psi, \tag{3.32}$$

which may be recognised as the Cauchy-Riemann relations for $p + i\nabla^2\psi$. Since the derivatives on the right-hand sides of (3.32) are continuous (this is easily seen by substituting from (3.30) for the stream function ψ and using (3.24) for the derivatives), $p + i\nabla^2\psi$ is holomorphic. From (3.24) and (3.30),

$$\nabla^2\psi = 4\frac{\partial^2\psi}{\partial\overline{z}\partial z} = 4\left[\theta'(z) + \overline{\theta'(z)}\right] \tag{3.33}$$

We define a holomorphic function $\rho(z)$ as

$$\rho(z) = p + i\nabla^2\psi - 8i\theta'(z) = p - 4i\left[\theta'(z) - \overline{\theta'(z)}\right]. \tag{3.34}$$

Since p and $4i\left[\theta'(z) - \overline{\theta'(z)}\right]$ are both real, ρ is real and must therefore be a constant, C. Hence

$$p = C + 4i\left[\theta'(z) - \overline{\theta'(z)}\right]. \tag{3.35}$$

Boundary Conditions at Infinity

ψ is unique only to within an arbitrary additive constant, and since u and v vanish at infinity, we are at liberty to put $\psi \to 0$ as $\Im(z) \to \infty$. Appropriate boundary conditions for θ and ϕ at infinity are then

$$\theta,\, \phi \to 0, \qquad \text{as } \Im(z) \to \infty. \tag{3.36}$$

Since p also vanishes at infinity, $C = 0$ and

$$p = 4i\left[\theta'(z) - \overline{\theta'(z)}\right]. \tag{3.37}$$

Boundary Conditions at the Base

On $y = 0$, $x \in C'$, vertical velocity is prescribed by (3.14),

$$v = -\frac{\partial \psi}{\partial x} = u_b h'(x). \tag{3.38}$$

Assuming both sides are differentiable,

$$\frac{\partial v}{\partial x} = -\frac{\partial^2 \psi}{\partial x^2} = u_b h''(x). \tag{3.39}$$

Using (3.24) and (3.30),

$$-\left[x\theta''(x) + x\overline{\theta''(x)} + 2\theta'(x) + 2\overline{\theta'(x)} + \phi''(x) + \overline{\phi''(x)}\right]^+ = u_b h''(x), \qquad x \in C', \tag{3.40}$$

where the superscript $^+$ indicates the fact that the boundary value is taken as z approaches the boundary from S^+, i.e. $y \to 0^+$. Similarly, equation (3.15) for the cavity roof shape yields

$$-\left[x\theta''(x) + x\overline{\theta''(x)} + 2\theta'(x) + 2\overline{\theta'(x)} + \phi''(x) + \overline{\phi''(x)}\right]^+ = u_b h_C''(x), \qquad x \in C. \tag{3.41}$$

On the cavities, normal stress is prescribed by (3.16). Substituting from (3.24), (3.30) and (3.37) yields

$$2i\left[x\theta''(x) - x\overline{\theta''(x)} + 2\theta'(x) - 2\overline{\theta'(x)} + \phi''(x) - \overline{\phi''(x)}\right]^+ = -N, \qquad x \in C. \tag{3.42}$$

Similarly, compressive normal stress on the contact areas can be calculated as

$$2i\left[x\theta''(x) - x\overline{\theta''(x)} + 2\theta'(x) - 2\overline{\theta'(x)} + \phi''(x) - \overline{\phi''(x)}\right]^+ = N_{loc}(x) - N, \qquad x \in C'. \tag{3.43}$$

Lastly, shear stress vanishes everywhere at the bed. (3.17) can be written in terms of the functions θ and ϕ as

$$\left[x\theta''(x) + x\overline{\theta''(x)} + \phi''(x) + \overline{\phi''(x)}\right]^+ = 0, \qquad x \in C \cup C'. \tag{3.44}$$

3.4.2 Formulation as a Hilbert Problem

By manipulating (3.36) and (3.40)–(3.44), the determination of the sliding law (3.20) can be reduced to the solution of a boundary value problem for a single holomorphic function. This boundary value problem takes the form of a Hilbert problem (e.g.

Muskhelishvili, 1992), which may be solved partially using standard methods; the remaining difficulty will lie in determining the position of the boundary.

We define the following holomorphic functions on S^+,

$$\Omega(z) = z\theta''(z) + 2\theta'(z) + \phi''(z), \qquad \omega(z) = z\theta''(z) + \phi''(z). \tag{3.45}$$

Their reflections $\Omega_\star$ and $\omega_\star$, defined on the lower half plane S^- are

$$\Omega_\star(z) = \overline{\Omega(\overline{z})}, \qquad \omega_\star(z) = \overline{\omega(\overline{z})}, \tag{3.46}$$

where $\Omega_\star$ and $\omega_\star$ are holomorphic on $z \in S^-$ (cf. Muskhelishvili, 1992, pp. 94–95). The boundary values of Ω satisfy

$$\overline{\Omega(x)}^+ = \lim_{y\to 0^+} \overline{\Omega(x+iy)} = \lim_{y\to 0^-} \overline{\Omega(x-iy)} = \Omega_\star^-(x), \tag{3.47}$$

where the superscript $^-$ indicates that the limit is taken as z approaches the boundary from S^-. Similarly

$$\overline{\omega(x)}^+ = \omega_\star^-(x). \tag{3.48}$$

Using these results, the boundary condition (3.40) can be rewritten as

$$-\left[x\theta''(x) + 2\theta'(x) + \phi''(x)\right]^+ - \left[\overline{x\theta''(x) + 2\theta'(x) + \phi''(x)}\right]^+ =$$

$$-\left[\Omega^+(x) + \Omega_\star^-(x)\right] = u_b h''(x) \qquad x \in C', \tag{3.49}$$

Analogously, (3.41)–(3.44) may be written as

$$-\left[\Omega^+(x) + \Omega_\star^-(x)\right] = u_b h_C''(x) \qquad x \in C, \tag{3.50}$$

$$2i\left[\Omega^+(x) - \Omega_\star^-(x)\right] = -N \qquad x \in C, \tag{3.51}$$

$$2i\left[\Omega^+(x) - \Omega_\star^-(x)\right] = N_{loc}(x) - N, \qquad x \in C', \tag{3.52}$$

$$\omega^+(x) + \omega_\star^-(x) = 0, \qquad x \in C \cup C'. \tag{3.53}$$

At infinity, (3.36) yields

$$\Omega(z) \to 0, \qquad \omega(z) \to 0 \qquad \text{as } \Im(z) \to \pm\infty. \tag{3.54}$$

Assuming that ω has no singularities at the end points of C and C' (the cavity end points), (3.53) and $(3.54)_2$ have the trivial solution $\omega(z) \equiv 0$.

It remains to determine Ω. We define

$$F(z) = \begin{cases} \left[-\Omega(z) + \frac{1}{4}iN\right]/u_b, & z \in S^+, \\ \left[-\Omega_\star(z) - \frac{1}{4}iN\right]/u_b, & z \in S^-, \end{cases}, \tag{3.55}$$

such that F is holomorphic in $S^+ \cup S^-$, and satisfies

$$F(z) = F_\star(z) = \overline{F(\overline{z})}. \tag{3.56}$$

From equations (3.49), (3.51) and (3.54), we obtain the following boundary conditions for F:

$$F^+(x) + F^-(x) = h''(x), \qquad x \in C', \tag{3.57}$$

$$F^+(x) - F^-(x) = 0, \qquad x \in C, \tag{3.58}$$

$$F(z) \to \pm\frac{iN}{4u_b} \qquad \text{as } \Im(z) \to \pm\infty. \tag{3.59}$$

From (3.58), it follows that F is continuous across C; hence F is holomorphic in the complex plane cut along C', where it satisfies (3.57). Given a solution F, the cavity roof shape may be computed from (3.50), which reads

$$h''_C(x) = F^+(x) + F^-(x) = 2F(x) \qquad x \in C. \tag{3.60}$$

Furthermore, the integrand in (3.20) can be calculated in terms of F, using (3.52),

$$N_{loc}(x) = \begin{cases} -2iu_b \left[F^+(x) - F^-(x)\right], & x \in C', \\ 0, & x \in C. \end{cases} \tag{3.61}$$

We see from (3.20) and (3.61) that the sliding law can be determined once F is known.

In order to make use of the periodicity of the problem, we define ζ and ξ by

$$\zeta = \exp\left(i2\pi z/a\right), \qquad \xi = \exp\left(i2\pi x/a\right) \tag{3.62}$$

and denote by Σ^+ the interior of the unit circle in the ζ-plane, and by Σ^- its exterior. Furthermore, let C map onto Γ in the ζ-plane and C' onto Γ'. We also define

$$G(\zeta) = F(z), \tag{3.63}$$

where $G(\zeta)$ is single-valued and hence holomorphic on $\Sigma^+ \cup \Sigma^- \cup \Gamma$ on account of (3.58) and the periodicity imposed on ψ. Defining $h_2(\xi) = h''(x)$, boundary conditions on G are:

$$G^+(\xi) + G^-(\xi) = h_2(\xi), \qquad \xi \in \Gamma', \tag{3.64}$$

$$G(0) = \frac{iN}{4u_b}, \qquad G(\infty) = -\frac{iN}{4u_b}, \tag{3.65}$$

where superscripts $^+$ and $^-$ now refer to the limit being taken as ζ approaches the boundary from Σ^+ and Σ^-, respectively. In addition to (3.64)–(3.65), a solution G must satisfy (3.56), which can be written as

$$G(\zeta) = G_\star(\zeta) = \overline{G(1/\overline{\zeta})}. \tag{3.66}$$

Note that (3.66) ensures that, if one of (3.65) is satisfied, so is the other. Finally, given a solution G, the cavity roof shape h_C can be calculated from (3.60), which now becomes

$$h_{2C}(\xi) = 2G(\xi), \qquad \xi \in \Gamma, \tag{3.67}$$

where $h_{2C}(\xi) = h_C''(x)$. The sliding law can also be calculated from (3.20) and (3.61)–(3.63):

$$\tau_b = -\frac{u_b}{\pi} \int_{\Gamma'} \frac{G^+(\xi) - G^-(\xi)}{\xi} h_1(\xi)\, \mathrm{d}\xi, \tag{3.68}$$

where $h_1(\xi) = h'(x)$.

We will assume that there are a finite number of cavities per period; the boundary Γ' then consists of a finite number of disjoint arcs of the unit circle. Under the assumptions that any singularities which G has at the endpoints of these arcs are integrable — which must be the case if normal stress in (3.61) is to be integrable — and provided $h_2(\xi)$ is Hölder continuous, the boundary value problem (3.64)–(3.65) constitutes a Hilbert problem. When the boundary Γ' is known, such problems may be solved using standard methods described in Muskhelishvili (1992, chapter 10); the difficulty here lies in determining the end points of the arcs which make up Γ' (see Muskhelishvili, 1992, chapter 13, for an account of similar codimension-two free boundary problems in the theory of two-dimensional elasticity). We describe a method of finding the positions of these endpoints next.

3.5 Method of Solution

3.5.1 Notation

Suppose that there are n cavities per bedrock period,[1] and let $x = b_j$ and $x = c_j$ denote the upstream and downstream ends of the jth cavity, respectively. Then, by the periodicity of the bed,

$$b_{j+n} = b_j + a, \qquad c_{j+n} = c_j + a. \tag{3.69}$$

As cavities must be disjoint, their end points satisfy

$$c_0 < b_1 < c_1 < \ldots < b_n < c_n, \tag{3.70}$$

where $c_0 = c_n - a$. Γ may now be written as the union of disjoint arcs Γ_j, where (cf. fig. 3.6)

$$\Gamma = \bigcup_{j=1}^{n} \Gamma_j, \qquad \Gamma_j = \left\{ \exp(i2\pi x/a) : x \in (b_j, c_j) \right\}. \tag{3.71}$$

[1] Note that n is *not* the index in Glen's law, but merely some positive integer

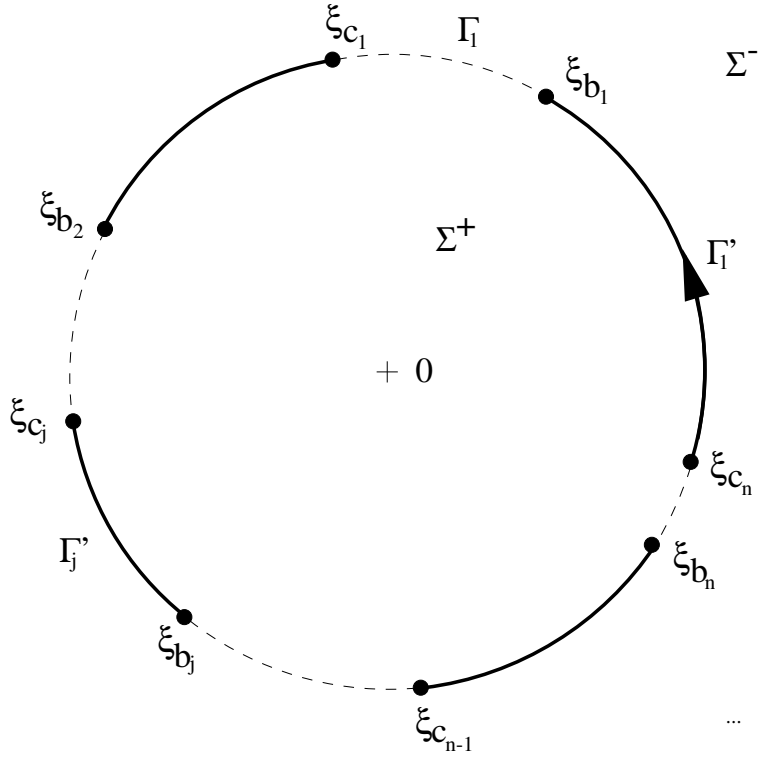

Figure 3.6: Geometry of the ζ-plane.

Similarly

$$\Gamma' = \bigcup_{j=1}^{n} \Gamma'_j, \qquad \Gamma'_j = \{\exp(i2\pi x/a) : x \in (c_{j-1}, b_j)\}\,. \tag{3.72}$$

The end points of each Γ_j will be denoted by ξ_{b_j} and ξ_{c_j}, where

$$\xi_{b_j} = \exp(i2\pi b_j/a), \qquad \xi_{c_j} = \exp(i2\pi c_j/a). \tag{3.73}$$

and ξ_{c_0} will be identified with ξ_{c_n}. Whenever integrals are taken along Γ or Γ', the integral is taken in the counterclockwise direction (i.e. with increasing x above), so that Σ^+ lies to the left of Γ and Γ'.

3.5.2 Solution Procedure

Here we consider only solutions to (3.64)–(3.65) which can be written in the form (see Muskhelishvili, 1992, chapter 10)

$$G(\zeta) = \frac{\chi(\zeta)}{2\pi i} \int_{\Gamma'} \frac{h_2(\xi)\,\mathrm{d}\xi}{\chi^+(\xi)(\xi - \zeta)} + G(\infty)\chi(\zeta). \tag{3.74}$$

where χ is of the form

$$\chi(\zeta) = \prod_{j=1}^{n} \chi_j(\zeta) : \qquad \chi_j(\zeta) = \left[\frac{\zeta - \xi_{b_j}}{\zeta - \xi_{c_{j-1}}}\right]^{1/2}, \tag{3.75}$$

and each χ_j is holomorphic in the ζ-plane cut along Γ'_j, while the branch of the root taken behaves as

$$\chi_j(\zeta) \sim 1 \qquad \text{as } \zeta \to \infty. \tag{3.76}$$

This ensures that $G(\zeta) \to G(\infty)$ as $\zeta \to \infty$.

The solution $G(\zeta)$ defined above has n integrable singularities, one at each downstream endpoint ξ_{c_j}. Other solutions to (3.64)–(3.65) are also possible, differing from (3.74)–(3.76) in the number and position of singularities of G at cavity endpoints. The reason why we persist with our present choice is that it furnishes the correct number of conditions needed to determine the positions of the cavity endpoints, as will become clearer below. In section 3.8, we further demonstrate that solutions with fewer than n endpoint singularities are not physically acceptable. Assuming that we seek the smoothest physically acceptable solution, alternatives to G defined above therefore differ from it only in the position of endpoint singularities, but not in their number. The positioning of singularities may seem arbitrary to some extent, but since there must be n singularities and we have n cavities, it is reasonable to expect that there will be one singularity per cavity, located consistently at either the downstream or upstream end of each cavity. The choice of downstream end singularities in (3.75) agrees with Fowler's (1986a) solution for a single cavity per period; high contact stresses at the downstream ends of cavities have also been suggested by Weertman and Birchfield (1982).

Having proposed that the solution of (3.64)–(3.65) should take the form (3.74)–(3.76), we now investigate how the position of the cavity endpoints $b_1, \ldots, b_n$ and $c_1, \ldots, c_n$ can be determined. Since there are $2n$ 'free' cavity endpoints, we expect $2n$ real constraints on their positions.

The Condition $G(\zeta) = G_\star(\zeta)$

The function $G(\zeta)$ defined in (3.74)–(3.76) automatically satisfies (3.64) and $(3.65)_2$, but does not necessarily satisfy $(3.65)_1$ or (3.66). As we pointed out before, (3.66) and $(3.65)_2$ together ensure that $(3.65)_1$ is satisfied, so we require simply that G defined in (3.74)–(3.76) satisfies (3.66),

$$G(\zeta) = G_\star(\zeta) = \overline{G(1/\overline{\zeta})}. \tag{3.77}$$

Note that

$$\overline{\chi(1/\overline{\zeta})} = \chi_\star(\zeta) = \prod_{j=1}^{n} \overline{\chi_j(1/\overline{\zeta})}, \tag{3.78}$$

and

$$\overline{\chi_j(1/\overline{\zeta})} = \chi_{j\star}(\zeta) = \overline{\left(\frac{1/\overline{\zeta} - \xi_{b_j}}{1/\overline{\zeta} - \xi_{c_{j-1}}}\right)^{1/2}}. \tag{3.79}$$

In order to avoid difficulties associated with different branches of the square root, we consider

$$\chi_{j\star}(\zeta)^2 = \overline{\left(\frac{1/\overline{\zeta} - \xi_{b_j}}{1/\overline{\zeta} - \xi_{c_{j-1}}}\right)} = \frac{1/\zeta - \overline{\xi_{b_j}}}{1/\zeta - \overline{\xi_{c_{j-1}}}}. \tag{3.80}$$

Since ξ_{b_j} and $\xi_{c_{j-1}}$ lie on the unit circle, $\overline{\xi_{b_j}} = 1/\xi_{b_j}$ and $\overline{\xi_{c_{j-1}}} = 1/\xi_{c_{j-1}}$. Hence

$$\chi_{j\star}(\zeta)^2 = \left(\frac{\zeta - \xi_{b_j}}{\zeta - \xi_{c_{j-1}}}\right)\left(\frac{\xi_{c_{j-1}}}{\xi_{b_j}}\right) = \frac{\chi_j(\zeta)^2}{\chi_j(0)^2}. \tag{3.81}$$

As $\chi_j(\zeta)$ is holomorphic in the complex plane cut along Γ'_j, and Γ'_j maps onto itself when $\zeta \mapsto 1/\overline{\zeta}$, $\chi_{j\star}(\zeta)$ has the same branch cuts as $\chi_j(\zeta)$. Furthermore, if $\chi_j(\zeta) \to 1$ as $\zeta \to \infty$, then $\chi_{j\star}(\zeta) = \overline{\chi_j(1/\overline{\zeta})} \to 1$ as $\zeta \to 0$. Thus the appropriate branch to take when taking the square root of both sides in (3.81) is

$$\chi_{j\star}(\zeta) = \frac{\chi_j(\zeta)}{\chi_j(0)}. \tag{3.82}$$

Hence

$$\chi_\star(\zeta) = \frac{\chi(\zeta)}{\chi(0)}. \tag{3.83}$$

Now, since $h_2(\xi)$ is real,

$$G_\star(\zeta) = \overline{G(1/\overline{\zeta})} = \frac{\overline{\chi(1/\overline{\zeta})}}{-2\pi i}\int_{\Gamma'} \frac{h_2(\xi)\,\overline{\mathrm{d}\xi}}{\overline{\chi^+(\xi)}(\overline{\xi} - 1/\zeta)} + \overline{G(\infty)}\,\overline{\chi(1/\overline{\zeta})}. \tag{3.84}$$

As $\xi = \exp(i2\pi x/a)$ lies on the unit circle, $\overline{\xi} = \exp(-i2\pi x/a) = 1/\xi$, and

$$\mathrm{d}\xi = \exp(i2\pi x/a)(i2\pi/a)\,\mathrm{d}x, \tag{3.85}$$

so

$$\overline{\mathrm{d}\xi} = \exp(-i2\pi x/a)(-i2\pi/a)\,\mathrm{d}x = -1/\xi^2\,\mathrm{d}\xi. \tag{3.86}$$

Furthermore, for $\xi \in \Gamma'$, we have that $\zeta \to \xi$ from Σ^+ as $1/\overline{\zeta} \to \xi$ from Σ^-. It follows that

$$\overline{\chi^+(\xi)} = \chi^-_\star(\xi). \tag{3.87}$$

By construction, the function χ defined in (3.75) further has the property that (cf. Muskhelishvili, 1992, chapter 10)

$$\chi^+(\xi) + \chi^-(\xi) = 0, \qquad \xi \in \Gamma'. \tag{3.88}$$

Combined with (3.83), this yields

$$\overline{\chi^+(\xi)} = \chi_\star^-(\xi) = \chi^-(\xi)/\chi(0) = -\chi^+(\xi)/\chi(0). \tag{3.89}$$

Hence, using (3.83), (3.86) and (3.89), (3.84) becomes

$$G_\star(\zeta) = \frac{\chi(\zeta)}{2\pi i}\int_{\Gamma'} \frac{h_2(\xi)}{\chi^+(\xi)}\frac{(-1/\xi^2)\,\mathrm{d}\xi}{1/\xi - 1/\zeta} + \frac{\overline{G(\infty)}}{\chi(0)}\chi(\zeta). \tag{3.90}$$

But

$$\frac{-1/\xi^2}{1/\xi - 1/\zeta} = \frac{1}{\xi - \zeta} - \frac{1}{\xi}, \tag{3.91}$$

so

$$G_\star(\zeta) = \frac{\chi(\zeta)}{2\pi}\int_{\Gamma'} \frac{h_2(\xi)\,\mathrm{d}\xi}{\chi^+(\xi)(\xi-\zeta)} + \left\{\frac{\overline{G(\infty)}}{\chi(0)} - \frac{1}{2\pi i}\int_{\Gamma'}\frac{h_2(\xi)\,\mathrm{d}\xi}{\chi^+(\xi)\xi}\right\}\chi(\zeta). \tag{3.92}$$

On comparing (3.92) and (3.74), the condition $G(\zeta) = G_\star(\zeta)$ thus reduces to

$$G(\infty) = \frac{\overline{G(\infty)}}{\chi(0)} - \frac{1}{2\pi i}\int_{\Gamma'}\frac{h_2(\xi)\,\mathrm{d}\xi}{\chi^+(\xi)\xi}. \tag{3.93}$$

With $G(\infty) = -iN/(4u_b)$, this can be rearranged to give $(3.65)_1$,

$$G(0) = \frac{\chi(0)}{2\pi i}\int_{\Gamma'}\frac{h_2(\xi)\,\mathrm{d}\xi}{\chi^+(\xi)\xi} + G(\infty)\chi(0) = \overline{G(\infty)} = \frac{iN}{4u_b}. \tag{3.94}$$

We can further show that (3.93) constitutes a single real constraint. By taking the complex conjugate of both sides of (3.93), and using similar arguments to those used above, we obtain

$$\overline{G(\infty)} = \frac{G(\infty)}{\overline{\chi(0)}} + \frac{1}{-2\pi i}\int_{\Gamma'}\frac{h_2(\xi)\,\overline{\mathrm{d}\xi}}{\overline{\chi^+(\xi)}\,\overline{\xi}} = \frac{G(\infty)}{\overline{\chi(0)}} + \frac{\chi(0)}{2\pi i}\int_{\Gamma'}\frac{h_2(\xi)\,\mathrm{d}\xi}{\chi^+(\xi)\xi} \tag{3.95}$$

Dividing both sides by $\chi(0)$ and noting that $\chi(0)\overline{\chi(0)} = 1$, we obtain again (3.93). Hence, if the real parts of the expressions on the left and right of (3.93) are equal, so are their imaginary parts; (3.93) thus constitutes a single real constraint.

The Cavity Roof

We may note that the condition

$$G_\star(\zeta) = G(\zeta)$$

ensures that $G(\xi)$ is real on $\xi \in \Gamma$, since $\xi = 1/\overline{\xi}$ there, and so $G(\xi) = \overline{G(1/\overline{\xi})} = \overline{G(\xi)}$. Hence h_{2C} in (3.67) is automatically real, as required.

Consider now the integral

$$I = \int_{\Gamma\cup\Gamma'} \frac{G^+(\xi) + G^-(\xi)}{\xi}\,\mathrm{d}\xi. \tag{3.96}$$

By construction (see the comment at the end of section 3.4.2), the boundary values of G are integrable, so I is well-defined. It is straightforward to prove that $I = 0$. To see this, consider

$$I = \int_{\Gamma\cup\Gamma'} \frac{G^+(\xi)}{\xi}\,\mathrm{d}\xi + \int_{\Gamma\cup\Gamma'} \frac{G^-(\xi)}{\xi}\,\mathrm{d}\xi. \tag{3.97}$$

The first term on the right-hand side is, by Cauchy's theorem applied to the boundary $\Gamma \cup \Gamma'$ of the simply connected region Σ^+ (the interior of the unit circle),

$$\int_{\Gamma\cup\Gamma'} \frac{G^+(\xi)}{\xi}\,\mathrm{d}\xi = 2\pi i G(0). \tag{3.98}$$

To evaluate the second term, note that $G(\zeta) - G(\infty)$ is holomorphic in the exterior region Σ^- and vanishes at infinity. Hence, by an extension of Cauchy's theorem to exterior regions (e.g Muskhelishvili, 1992, p. 63), we have

$$\int_{\Gamma\cup\Gamma'} \frac{G^-(\xi) - G(\infty)}{\xi}\,\mathrm{d}\xi = 0, \tag{3.99}$$

so that

$$\int_{\Gamma\cup\Gamma'} \frac{G^-(\xi)}{\xi}\,\mathrm{d}\xi = 2\pi i G(\infty). \tag{3.100}$$

Hence

$$I = 2\pi i[G(0) + G(\infty)] = 0, \tag{3.101}$$

by (3.65). This simplifies a rather lengthy proof to the same effect given by Fowler (1986a), who integrated explicitly the function G given by (3.74)–(3.76) with $n = 1$.

Furthermore, we have from (3.67) and bearing in mind that $\xi = \exp(i2\pi x/a)$,

$$\int_{\Gamma} \frac{G^+(\xi) + G^-(\xi)}{\xi}\,\mathrm{d}\xi = \sum_{j=1}^{n} \frac{i2\pi}{a} \int_{b_j}^{c_j} h_C''(x)\,\mathrm{d}x =$$

$$\frac{i2\pi}{a} \sum_{j=1}^{n} [h_C'(c_j) - h_C'(b_j)]. \tag{3.102}$$

Similarly, from (3.64),

$$\int_{\Gamma'} \frac{G^+(\xi) + G^-(\xi)}{\xi}\,\mathrm{d}\xi = \frac{i2\pi}{a} \sum_{j=1}^{n} [h'(b_j) - h'(c_{j-1})] =$$

$$\frac{i2\pi}{a}\sum_{j=1}^{n}[h'(b_j)-h'(c_j)], \tag{3.103}$$

where the last step (changing the index on c_j) follows from the periodicity of the bed. Hence

$$I=\frac{i2\pi}{a}\left\{\sum_{j=1}^{n}[h'(c_j)-h'_C(c_j)]+\sum_{j=1}^{n}[h'_C(b_j)-h'(b_j)]\right\}=0 \tag{3.104}$$

As discussed in section 3.4, we require $h_C = h$ at the cavity endpoints, so that the cavity roof joins the glacier bed there, i.e.

$$h_C(b_j)=h(b_j), \qquad h_C(c_j)=h(c_j), \qquad \forall\, j. \tag{3.105}$$

Furthermore, we require $h_C(x) > h(x)$ in the cavities. This implies that at the upstream ends of cavities,

$$h'_C(b_j)\geq h'(b_j), \tag{3.106}$$

while at downstream ends

$$h'_C(c_j)\leq h'(c_j). \tag{3.107}$$

Consequently, each term in square brackets in (3.104) is non-negative. $I = 0$ therefore requires that each of these terms must vanish, i.e.

$$h'(b_j)=h'_C(b_j), \qquad h'(c_j)=h'_C(c_j), \qquad \forall\, j, \tag{3.108}$$

which states that the cavity roof joins the bed tangentially at all cavity end points.

(3.67) can be written as n ordinary differential equations,

$$h''_C(x)=2G\left(\exp(i2\pi x/a)\right), \qquad x\in(b_j,c_j), \qquad j=1,\ldots,n. \tag{3.109}$$

$(3.105)_1$ and $(3.108)_1$ now provide initial conditions for each o.d.e.:

$$h_C(b_j)=h(b_j), \qquad h'_C(b_j)=h'(b_j), \qquad j=1,\ldots,n \tag{3.110}$$

$(3.105)_2$ and $(3.108)_2$ then provide further constraints on the position of the boundary points. Note that it is sufficient to impose $n-1$ of the n conditions in $(3.108)_2$, since the remaining one is automatically satisfied on account of (3.104). Integrating (3.109) thus leads to the following $2n-1$ constraints

$$h'(c_j)=h'_C(c_j)=\int_{b_j}^{c_j}2G\left(\exp(i2\pi x/a)\right)\,\mathrm{d}x+h'(b_j),$$
$$j=1,\ldots,n-1, \tag{3.111}$$

$$h(c_j) = h_C(c_j) = \int_{b_j}^{c_j} \int_{b_j}^{x} 2G\left(\exp(i2\pi x'/a)\right)\,\mathrm{d}x'\,\mathrm{d}x + h(b_j) + h'(b_j)(c_j - b_j) =$$

$$\int_{b_j}^{c_j} 2(c_j - x)G\left(\exp(i2\pi x/a)\right)\,\mathrm{d}x + h(b_j) + h'(b_j)(c_j - b_j), \qquad j = 1, \ldots, n, \quad (3.112)$$

where the last line follows by interchanging the order of integration. As discussed, G is real on $\xi \in \Gamma$, and hence (3.111)–(3.112) constitute $2n - 1$ real constraints on the position of the boundary points $b_1, \ldots, b_n$ and $c_1, \ldots, c_n$. Together with (3.93), we therefore have $2n$ real constraints, which should be sufficient to determine the endpoints of the cavities.[2]

Caveats

The conditions (3.108) are necessary in order to prevent $h_C - h$ becoming negative near the cavity endpoints, but they may not be sufficient (nor indeed are they sufficient to ensure that $h_C > h$ in each cavity away from the boundary points). Once a solution to (3.93), (3.111) and (3.112) has been calculated, it is necessary to establish *a posteriori* that the solution is physically acceptable, and results in cavity roofs for which $h_C > h$.

So far, we have assumed that the number of cavities per period is known; in general this is not the case *a priori*, and n must effectively be established by trial and error. Crucial here is the condition (3.21), which we have not used so far: Once a solution for the boundary points has been calculated, it must be checked whether the normal stress distribution on the contact areas satisfies (3.21). If (3.21) is violated, then it is likely that additional cavities must be introduced.

The last point also illustrates that the method of finding cavity end points proposed here does not guarantee a unique solution; at best, we can expect to be able to show that a solution for the position of cavity endpoints is locally unique in $2n$-dimensional $(b_1, \ldots, b_n, c_1, \ldots, c_n)$-space. If a solution is globally unique, this can only be established by other methods.

Fowler's Solution

Fowler (1986a) solved the problem considered here for $n = 1$. Although he did establish that cavity roofs should re-contact tangentially (by a more involved method than that used here, see the appendix in his paper), he did not need to use this fact to constrain the position of the cavity boundary points; the constraints (3.111) are only necessary when $n > 1$. Fowler (1986a) thus retained only the constraints (3.93)

[2]When $n = 1$, we may simply ignore (3.111), as was done in Fowler (1986a).

and (3.112) in order to determine the positions of the cavity end points. The form in which these constraints are cast in his paper is also somewhat different from that used here; in Fowler's paper, it is assumed that h can be continued analytically into an open annulus containing the unit circle, and the constraints (3.93) and (3.111) are expressed in terms of the coefficients in the Laurent expansions of h, χ and G (where the summations used are presumably truncated in order to obtain numerical results) — equation (3.93) in the present text translates into Fowler's equation (3.28), while (3.112) above is equivalent to Fowler's equation (3.29) in the case $n = 1$. Whilst Fowler's expressions allow a solution to be calculated for a single cavity per period, it is not straightforward to see how his method can be extended to the case of several cavities, and we therefore persevere with our equations (3.93), (3.111) and (3.112).

3.6 Numerical Solution

From (3.74)–(3.76), G is completely determined for a given bed $h(x)$ if the cavity endpoints and $G(\infty)$ are known. Since the position of the cavity end points is determined from the constraints (3.93), (3.111) and (3.112), which contain u_b and N only in the form $G(\infty) = iN/4u_b$, we conclude that a solution G depends on N and u_b only through $G(\infty) = iN/4u_b$. Calculating the sliding law from (3.68), we find that τ_b thus depends on u_b and N as

$$\tau_b = u_b g(u_b/N), \tag{3.113}$$

where g is some function. Equivalently

$$\tau_b = N f(u_b/N), \tag{3.114}$$

if we define $f(u_b/N) = (u_b/N)g(u_b/N)$. This was established previously by Fowler (1986a), and explains why fig. 3.3 relates τ_b/N to u_b/N.

In order to calculate the sliding law $\tau_b/N = f(u_b/N)$ for a given bed $h(x)$, we proceed as follows: At each u_b/N we first guess the number of cavities n. The constraints (3.93), (3.112) and (3.111) are then used to solve numerically for the position of cavity end points $(b_1, \ldots, b_n)$ and $(c_1, \ldots, c_n)$. If G defined for the resulting cavity end point positions by (3.74)–(3.76) is such that (3.21) and (3.22) are satisfied, then τ_b/N is calculated from (3.68); otherwise, the choice of n is altered.

3.6.1 Determination of the Cavity End Points

In order to solve the constraints (3.93), (3.111) and (3.112) numerically, we first write them in terms of real variables. Much of the necessary algebra is tedious but straightforward, and therefore omitted here. However, care must be taken when determining the sign of square roots in evaluations of χ, and we give the relevant results in appendix B.

Condition (3.93) may be written in terms of real variables as

$$\frac{1}{a}\sum_{l=1}^{n}\int_{c_{l-1}}^{b_l}\left|\prod_{j=1}^{n}\frac{\sin\left[\pi(x-c_{j-1})/a\right]}{\sin\left[\pi(x-b_j)/a\right]}\right|^{1/2}h''(x)\,\mathrm{d}x+\frac{N}{2u_b}\cos\left[\frac{\pi}{2a}\sum_{j=1}^{n}(b_j-c_{j-1})\right]=0. \tag{3.115}$$

Using (3.115), the requirement (3.111) that cavity roofs re-contact with the bed tangentially can be written as

$$\begin{aligned}\frac{1}{a}\sum_{l=1}^{n}\int_{b_p}^{c_p}\mathrm{d}y\int_{c_{l-1}}^{b_l}\mathrm{d}x\Bigg\{&\left|\prod_{k=1}^{n}\frac{\sin\left[\pi(y-b_k)/a\right]}{\sin\left[\pi(y-c_{k-1})/a\right]}\right|^{1/2}\left|\prod_{j=1}^{n}\frac{\sin\left[\pi(x-c_{j-1})/a\right]}{\sin\left[\pi(x-b_j)/a\right]}\right|^{1/2}\times\\&h''(x)\cot\left[\pi(y-x)/a\right]\Bigg\}+\\\frac{N}{2u_b}\sin\left[\frac{\pi}{2a}\sum_{j=1}^{n}(b_j-c_{j-1})\right]&\int_{b_p}^{c_p}\left|\prod_{k=1}^{n}\frac{\sin\left[\pi(y-b_k)/a\right]}{\sin\left[\pi(y-c_{k-1})/a\right]}\right|^{1/2}\mathrm{d}y+\\&h'(b_p)-h'(c_p)=0,\qquad p=1,\ldots,n-1,\end{aligned} \tag{3.116}$$

where y is now simply an integration variable and must not be interpreted as a vertical coordinate. Similarly, (3.112) can be re-written as

$$\begin{aligned}\frac{1}{a}\sum_{l=1}^{n}\int_{b_p}^{c_p}\mathrm{d}y\int_{c_{l-1}}^{b_l}\mathrm{d}x\Bigg\{&(c_p-y)\left|\prod_{k=1}^{n}\frac{\sin\left[\pi(y-b_k)/a\right]}{\sin\left[\pi(y-c_{k-1})/a\right]}\right|^{1/2}\left|\prod_{j=1}^{n}\frac{\sin\left[\pi(x-c_{j-1})/a\right]}{\sin\left[\pi(x-b_j)/a\right]}\right|^{1/2}\times\\&h''(x)\cot\left[\pi(y-x)/a\right]\Bigg\}+\\\frac{N}{2u_b}\sin\left[\frac{\pi}{2a}\sum_{j=1}^{n}(b_j-c_{j-1})\right]&\int_{b_p}^{c_p}(c_p-y)\left|\prod_{k=1}^{n}\frac{\sin\left[\pi(y-b_k)/a\right]}{\sin\left[\pi(y-c_{k-1})/a\right]}\right|^{1/2}\mathrm{d}y+\\&h'(b_p)(c_p-b_p)+h(b_p)-h(c_p)=0,\qquad p=1,\ldots,n.\end{aligned} \tag{3.117}$$

The non-linear equations (3.115)–(3.117) for $b_1,\ldots,b_n$ and $c_1,\ldots,c_n$ are solved numerically for a given bed $h(x)$ and at given u_b/N using a backtracking line search modification of Newton's method (see Dennis and Schnabel, 1996, chapter 6).[3]

[3]Note that $c_{j-1}=c_0$ for $j=1$ appears in (3.115)–(3.117); $c_0=c_n-a$ must be used here.

At each iteration step, the left-hand sides of (3.115)–(3.117) and their partial derivatives with respect to $b_1, \ldots, b_n$ and $c_1, \ldots, c_n$ are calculated numerically as follows: First, we change integration variables in (3.115)–(3.117) from x and y to x' and y', where

$$y = (c_p - b_p)y' + b_p, \qquad x = (b_l - c_{l-1})x' + c_{l-1},$$

such that all integrals are taken over the interval $(0, 1)$. Analytical expressions for the partial derivatives of the left-hand sides of (3.115)–(3.117) may then be derived by direct differentiation; we do not give these here for reasons of space. Since many of the integrands in (3.115)–(3.117) have weak singularities at the boundaries of the domains of integration, we apply a further change of variable (cf. Atkinson, 1989, pp. 306–307)

$$x' = \frac{\int_0^u \exp\left(\frac{-c}{u'(1-u')}\right) \mathrm{d}u'}{\int_0^1 \exp\left(\frac{-c}{u'(1-u')}\right) \mathrm{d}u'},$$

$$y' = \frac{\int_0^v \exp\left(\frac{-c}{v'(1-v')}\right) \mathrm{d}v'}{\int_0^1 \exp\left(\frac{-c}{v'(1-v')}\right) \mathrm{d}v'},$$

where $c = 0.25$ is used. Cubature is then carried out by separation of variables (Isaacson and Keller, 1966, section 7.3). Integration with respect to u is performed using 96-point Gauss-Legendre quadrature since these integrals involve $h''(x)$ — which is highly oscillatory when there are many bed obstacles per period — while integrals with respect to v are evaluated using 32-point Gauss-Legendre quadrature, as these integrals do not involve $h''(x)$.

3.6.2 The Cavity Roof and Effective Basal Shear Stress

Once a solution for the cavity boundary points $b_1, \ldots, b_n$ and $c_1, \ldots, c_n$ has been established, it remains to calculate the cavity roof shape and the normal stress distribution on the contact areas. Integrating (3.109) twice and using (3.110) as well as (3.115), the cavity roof shape is

$$h_C(x_0) = \frac{1}{a} \sum_{l=1}^{n} \int_{b_p}^{x_0} \mathrm{d}y \int_{c_{l-1}}^{b_l} \mathrm{d}x \left\{ (x_0 - y) \left| \prod_{k=1}^{n} \frac{\sin\left[\pi(y - b_k)/a\right]}{\sin\left[\pi(y - c_{k-1})/a\right]} \right|^{1/2} \times \right.$$

$$\left. \left| \prod_{j=1}^{n} \frac{\sin\left[\pi(x - c_{j-1})/a\right]}{\sin\left[\pi(x - b_j)/a\right]} \right|^{1/2} h''(x) \cot\left[\pi(y - x)/a\right] \right\} +$$

$$\frac{N}{2u_b}\sin\left[\frac{\pi}{2a}\sum_{j=1}^{n}(b_j-c_{j-1})\right]\int_{b_p}^{x_0}(x_0-y)\left|\prod_{k=1}^{n}\frac{\sin\left[\pi(y-b_k)/a\right]}{\sin\left[\pi(y-c_{k-1})/a\right]}\right|^{1/2}\mathrm{d}y+$$
$$h'(b_p)(x_0-b_p)+h(b_p),\qquad x_0\in(b_p,c_p) \tag{3.118}$$

Normal stress on the contact areas is evaluated from (3.61) and (3.63). We find, using (3.88) and Plemelj's formulae (Muskhelishvili, 1992, p. 42) to evaluate the boundary values of G on Γ',

$$N_{loc}(x)=-2iu_b\left[F^+(x)-F^-(x)\right]=-2iu_b\left[G^+(\xi)-G^-(\xi)\right]=$$
$$-4iu_bG(\infty)\chi^+(\xi)-\frac{2u_b\chi^+(\xi)}{\pi}\fint_{\Gamma'}\frac{h_2(\xi')\,\mathrm{d}\xi'}{\chi^+(\xi')(\xi'-\xi)},\qquad \xi\in\Gamma', \tag{3.119}$$

where $\fint$ stands for the principal value integral. Adapting the approach found in Muskhelishvili (1992, p. 27) and using (3.115), this may be written as

$$\frac{N_{loc}(x)}{N}=\left|\prod_{k=1}^{n}\frac{\sin\left[\pi(x-b_k)/a\right]}{\sin\left[\pi(x-c_{k-1})/a\right]}\right|^{1/2}\sin\left[\frac{\pi}{2a}\sum_{j=1}^{n}(b_j-c_{j-1})\right]+$$
$$\frac{2u_b}{aN}\int_{c_{p-1}}^{b_p}\left\{h''(y)\left|\prod_{j=1}^{n}\frac{\sin\left[\pi(x-b_j)/a\right]}{\sin\left[\pi(x-c_{j-1})/a\right]}\right|^{1/2}\left|\prod_{k=1}^{n}\frac{\sin\left[\pi(y-c_{k-1})/a\right]}{\sin\left[\pi(y-b_k)/a\right]}\right|^{1/2}-\right.$$
$$\left.h''(x)\right\}\cot\left[\pi(x-y)/a\right]\,\mathrm{d}y-\frac{2u_b}{\pi N}\log\left|\frac{\sin\left[\pi(x-b_p)/a\right]}{\sin\left[\pi(x-c_{p-1})/a\right]}\right|+$$
$$\frac{2u_b}{aN}\left|\prod_{j=1}^{n}\frac{\sin\left[\pi(x-b_j)/a\right]}{\sin\left[\pi(x-c_{j-1})/a\right]}\right|^{1/2}\sum_{\substack{q=1\\q\neq p}}^{n}\int_{c_q-1}^{b_q}h''(y)\left|\prod_{k=1}^{n}\frac{\sin\left[\pi(y-c_{k-1})/a\right]}{\sin\left[\pi(y-b_k)/a\right]}\right|^{1/2}\mathrm{d}y,$$
$$x\in(c_{p-1},b_p). \tag{3.120}$$

(3.118)–(3.120) are evaluated numerically using methods analogous to those used to calculate the left-hand sides of (3.115)–(3.117) at each iteration step in the calculation of $b_1,\ldots,b_n,c_1,\ldots,c_n$. Special care must be taken with the first integrand in (3.120), which may have integrable singularities not only at the end points of the range of integration, but also at $x=y$. For computational purposes, the first integral in (3.120) is therefore split into integrals over (c_{p-1},x) and (x,b_p), and a similar change of variables as before is applied to each of these integrals to eliminate weak end point singularities.

Provided $h_C(x)>h(x)$ and $N_{loc}(x)>0$ at all points where they are evaluated, the effective basal shear stress

$$\frac{\tau_b}{N}=\frac{1}{a}\sum_{p=1}^{n}\int_{c_{p-1}}^{b_p}\frac{N_{loc}(x)}{N}h'(x)\,\mathrm{d}x \tag{3.121}$$

is then computed numerically using a similar change of variable as before to eliminate end point singularities, followed by 96-point Gauss-Legendre quadrature.

3.6.3 Numerical Checks

The numerical method outlined above was implemented in MATLAB using quadrature nodes and weights taken from Abramowitz and Stegun (1972). In order to check the performance of the code, the following tests were successfully carried out:

- Only $n-1$ of the n conditions $(3.108)_2$ stating that cavity roofs re-contact tangentially are imposed in (3.116); an obvious check is therefore to test whether the remaining condition is also satisfied, as required by (3.104).
- Equation $(3.10)_2$, $\int_0^a N_{loc}(x)\,\mathrm{d}x/a = N$ must hold.
- Iken's bound (3.11) must be satisfied
- Doubling the value of the period a used whilst not altering the shape of the bed should result in the same solution, with the cavity endpoints repeated.
- For simple beds with a single cavity per period, the solutions computed by Fowler (1986a) should be reproduced.
- At low u_b/N, when there is only localised cavitation, we expect basal shear stress to be given approximately by Nye's and Kamb's relation (2.59).
- The solutions obtained must not depend on the number of quadrature nodes; this was established by using 64-point Gauss-Legendre quadrature instead of 32- and 96-point quadrature, and worked adequately except for highly oscillatory $h''(x)$ and low n.

3.6.4 Calculating the Sliding Law

The simplest strategy in constructing the sliding law is to establish the value of u_b/N at which Nye's and Kamb's solution breaks down in the sense that $N_{loc} \geq 0$ is violated. A cavity then forms around the location where $N_{loc} \geq 0$ is violated, and b_1 and c_1 can be calculated using the procedure in section 3.6.2. τ_b/N can then be calculated. u_b/N is subsequently increased, and the new cavity endpoints are computed, using the solutions for the previous value of u_b/N as initial guesses. This procedure is repeated until $N_{loc}(x) \geq 0$ is violated again, and a new cavity is introduced. The same procedure, albeit with an increased number of cavities, is then followed again.

bed no.	a	α	r_{max}	$\max(h'(x))$
1	20π	6.25	30	1.57
2	20π	1.56	30	1.51
3	20π	1.56	30	1.38
4	20π	1.56	30	1.73
5	20π	0.39	30	1.74

Table 3.1: Parameters for the beds shown in figures 3.7–3.9

3.7 Results

For simple periodic beds with a single cavity per period, Fowler's (1986a) results are reproduced by our method. In fact, figures 3.3 and 3.4 in the present text, which were calculated using the method proposed here, may be compared with Fowler's figures 3 and 5; these figures clearly agree.

Since our aim here is to calculate sliding laws for more realistic beds, we need to quantify what constitutes a 'realistic' glacier bed. Benoist (1979) measured the roughness of a glacier bed and calculated its Fourier spectrum for a range of wavelengths between 3.5 and 40 cm. For wavelengths in this range, he concludes that bed Fourier coefficients $\hat{h}_r$ (see equation (2.56) with $f = h(x)$) behave as $|\hat{h}_r|^2 \propto k_r^{-2.4}$ and so $|\hat{h}_r| \propto k_r^{-1.2}$. However, a periodic bed defined by

$$h(x) = \sum_{r=-\infty}^{\infty} \hat{h}_r \exp(ik_r x) : \qquad k_r = \frac{2\pi r}{a}, \tag{3.122}$$

with $|\hat{h}_r| \sim k_r^{-1.2}$ as $r \to \infty$ cannot be twice Hölder continuously differentiable, as required by our solution of the Hilbert problem (3.64)–(3.65). For the purpose of our model, we are thus forced to discount beds with small-scale roughness of the type suggested by Benoist. The alternative suggestion of Lliboutry (1979), namely that realistic glacier beds should be 'Gaussian' in the sense that both h and h' have Gaussian distributions, also cannot be implemented here as it implies that both bed bump heights and bed slopes are unbounded. Instead, we opt for a Gaussian Fourier spectrum, i.e. $\hat{h}_r$ takes the form

$$\hat{h}_r = \begin{cases} 0 & r > r_{max}, \\ (\alpha_r + i\beta_r)K \exp(-\alpha(k_r - k^*)^2) & r_{max} \geq r > 0, \\ \overline{\hat{h}_{-r}} & r < 0, \end{cases} \tag{3.123}$$

where r_{max} is some upper cut-off, α_r and β_r are random numbers between $-1/2$ and $1/2$, K is a normalising constant which is independent of r, α is a positive number and k^* some 'dominant' wavenumber. Large α correspond to a very regular, nearly

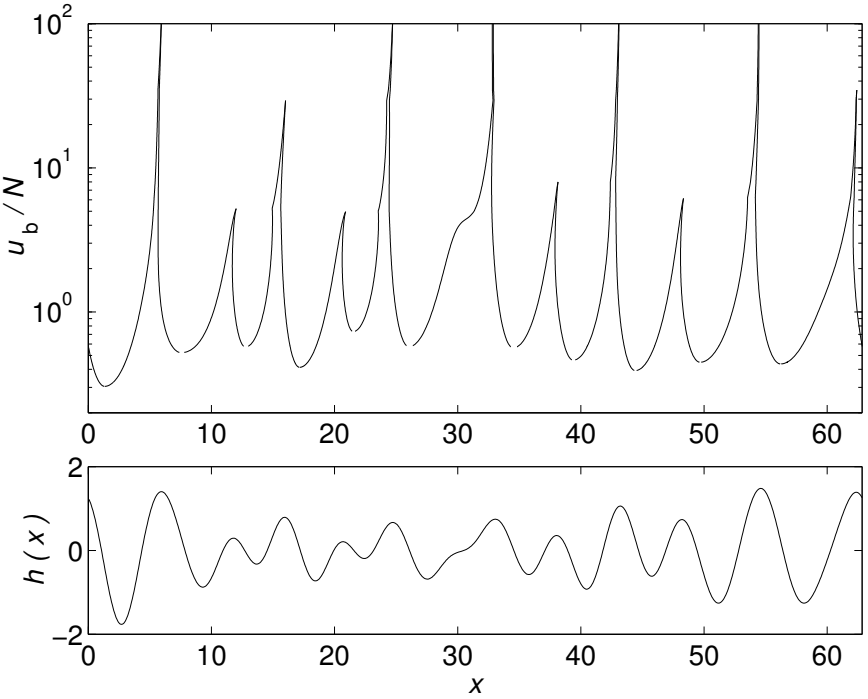

Figure 3.7: The top panel shows a plot of cavity boundary positions vs. u_b/N (by analogy with figure 3.4) for bed 1, which is shown in the bottom panel. Bed 1 has $\alpha = 6.25$. Note the logarithmic scale for u_b/N in the top panel.

sinusoidal bed for which we may expect sliding laws similar to those calculated previously by Fowler (1986a). As α is decreased, the bed becomes increasingly irregular, which corresponds to a more realistic glacier bed.

In order to facilitate comparison between different beds, K is chosen such that the Nye-Kamb roughness coefficient (see equation (2.59)) is $\sum_{r=1}^{\infty} 4|\hat{h}_r|^2 k_r^3 = 1$ for each bed, as is also the case for a sinusoidal bed. We also fix $k^* = 1$ for each bed, so that the period of the bed a is an integer multiple of the dominant wavelength $\lambda^* \doteq 2\pi/k^* = 2\pi$.

The bottom panels of figures 3.7—3.9 show three of the randomly generated beds for which sliding laws were calculated. The relevant parameter values can be found in table 3.1. The upper panels in figures 3.7—3.9 show how the position of the cavity boundaries changes with u_b/N as was previously done in figure 3.4; as was the case for a sinusoidal bed, the contact areas between ice and bed shrink and migrate to the top of bed obstacles at large velocities. Neighbouring cavities also merge at large velocities.

Figure 3.10 shows the sliding laws obtained for beds 1, 4 and 5. At low values of u_b/N, τ_b/N rises more or less linearly with u_b/N as indicated by Nye-Kamb theory.

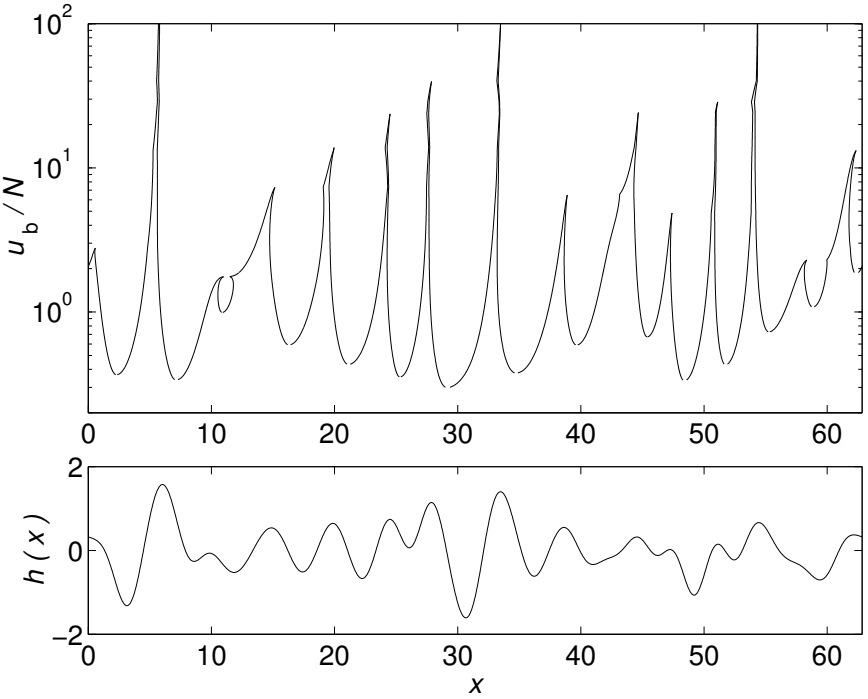

Figure 3.8: Cavity boundary position (horizontal axis) is plotted against u_b/N in the top panel for bed 4 (shown in bottom panel), which has $\alpha = 1.56$.

As cavitation becomes more widespread, the graphs of τ_b/N against u_b/N become more irregular, with a number of local maxima. Close inspection of figure 3.10 also reveals a number of discontinuities in slope, which are associated with the merging of two neighbouring cavities. However, the general trend is somewhat similar to the sliding law for a simple sinusoidal bed; τ_b/N reaches a global maximum and then starts to decrease again. This decrease is not associated with the formation of a single cavity per bed period, but with the migration of contact areas to the top of bed obstacles shown in figures 3.7–3.9 and 3.11. Near the top of bed obstacles, the bed slope is small and the resistance offered by the obstacle is therefore reduced. Notably, however, the decrease in τ_b/N is less pronounced for the more irregular beds than for the sinusoidal bed. The drowning of bed roughness is less pronounced for more irregular beds.

The main difference between the irregular beds shown in figures 3.7–3.9 and the simple sinusoidal bed is the presence of stretches of bed with relatively subdued bumps separating more prominent ones. The 'drowning' of more prominent obstacles is consequently inhibited, as panels b and c of figure 3.11 show. Nevertheless, it should be pointed out that it is not the most irregular bed for which τ_b/N decreases most slowly in fig. 3.10, where bed 4 ($\alpha = 1.56$) generates the greatest drag at high u_b/N.

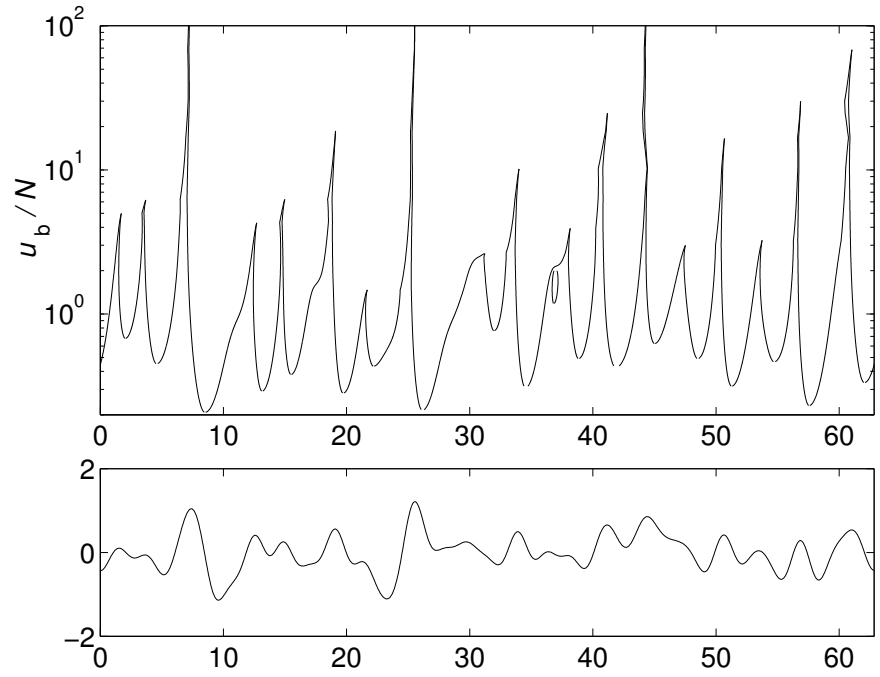

Figure 3.9: The top panel shows a plot of cavity boundary positions vs. u_b/N for bed 5 (shown in the bottom panel), which $\alpha = 0.39$.

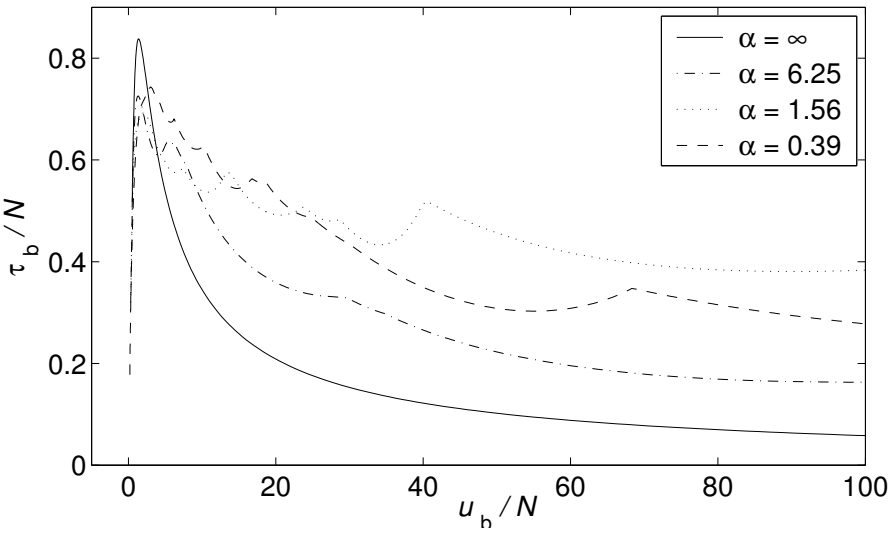

Figure 3.10: A plot showing the sliding laws for beds 1, 4 and 5 ($\alpha = 6.25$, 1.56 and 0.39, respectively). For comparison, the sliding law for a sinusoidal bed ($\alpha = \infty$) is also plotted. Each curve starts at the value of u_b/N at which cavitation first occurs. Note that the onset of cavitation occurs at a lower value of u_b/N for the most irregular bed ($\alpha = 0.39$).

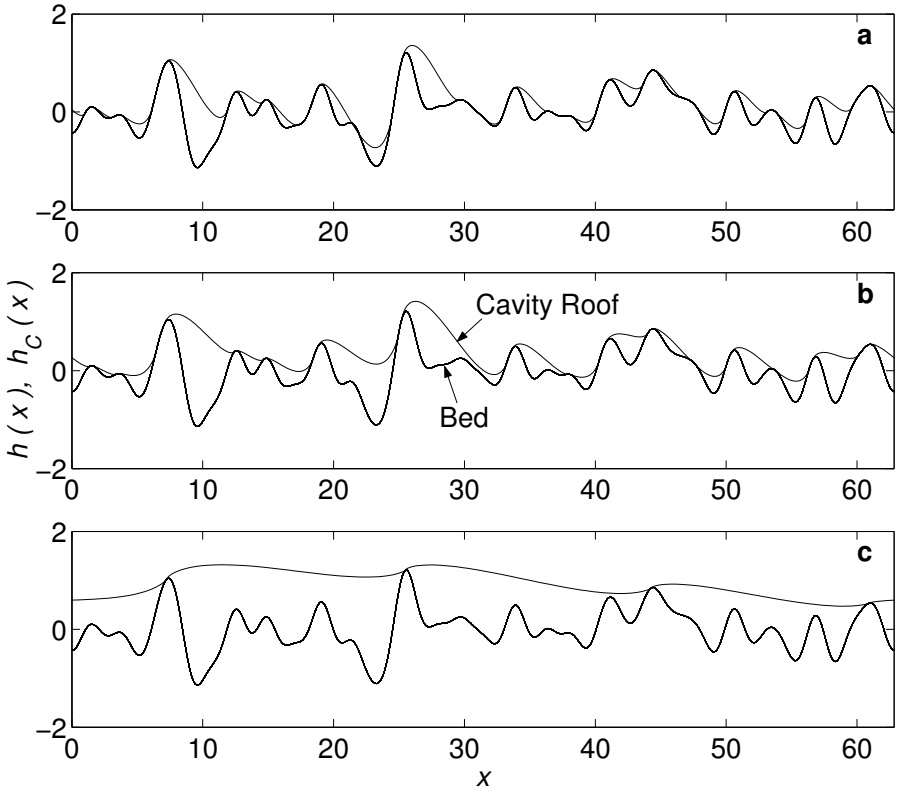

Figure 3.11: Panels a–c shows the cavity roof configuration for bed 5 at u_b/N = 1.5, 3 and 50, respectively. Note that at $u_b/N = 1.5$, τ_b/N is still increasing; this may be attributed to the fact that cavities have not yet begun to merge. At u_b/N = 3, where τ_b/N reaches its maximum (cf. fig. 3.10), the contact areas have shrunk significantly (see also fig. 3.9). At still higher velocities, cavities begin to merge and the remaining contact areas shrink and migrate towards the top of bed obstacles, where drag is reduced. However, even at $u_b/N = 50$, the contact areas on some of the more prominent bed obstacles ($x \approx 8$ and $x \approx 26$) appear to have reasonable slopes relative to the horizontal, which explains why τ_b/N drops less rapidly than for a sinusoidal bed.

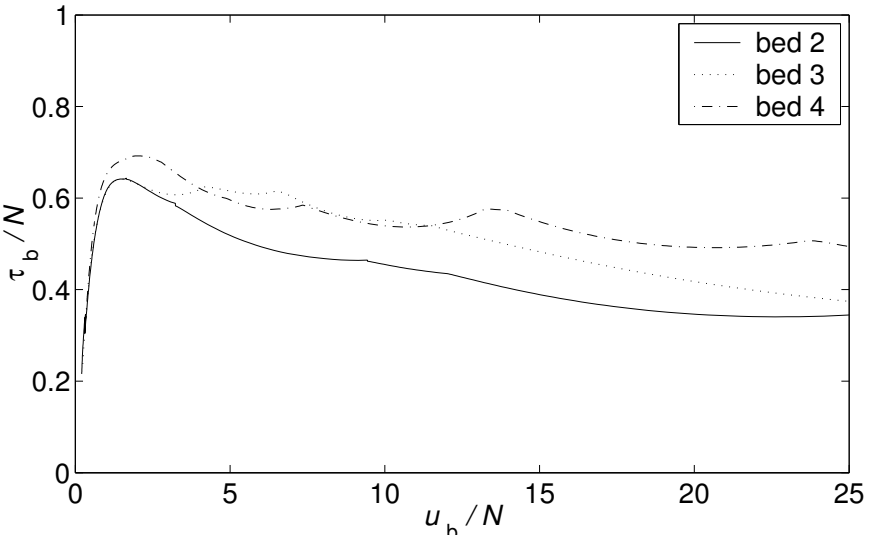

Figure 3.12: A plot showing sliding laws for beds 2, 3 and 4, all of which have $\alpha = 1.56$. Note that the different sliding laws are quantitatively quite different.

In fact, figure 3.12 shows that beds with the same parameters α and a can generate sliding laws which are quite different in detail (although qualitatively similar). It is thus difficult to associate the bed irregularity parameter α with any particular behaviour at large velocities.

In fact, it is arguable that differences in the irregularity parameter α have a greater influence at low u_b/N than high u_b/N. Figures 3.7–3.9 show that the onset of cavitation occurs at lower values of u_b/N for more irregular beds, i.e. when α is lower, and the maximum number of cavities formed is also greater. This suggests that the natural length scale for such beds is in fact shorter than $k^* = 1$. Recall that length was scaled for the more irregular beds such that the 'preferred wavenumber' $k^* = 1$ in (3.123). However, small α in (3.123) — α controls the width of the Gaussian distribution and hence the spread of wavelengths — arguably introduce more small-scale roughness than large-scale roughness into the bed. The reason for this is that each Fourier mode contributes an amount $4k_r^3|\hat{h}_r|^2$ to the Nye-Kamb roughness coefficient (cf. equation (2.59)). Consequently, the Fourier mode which contributes the most to the Nye-Kamb coefficient is likely to have k_r larger than $k^* = 1$ (for which $\hat{h}_r$ takes a maximum), and one could consider this mode as corresponding to the preferred bed wavelength. We identify this mode $k = k_{max}$ as the value of k for which

$$k^3 \exp(-2\alpha(k - k_*)^2) = k^3 \exp(-2\alpha(k-1)^2)$$

attains a maximum, $k_{max} = (1 + \sqrt{1 + 6/\alpha})/2$. Rescaling horizontal distances such

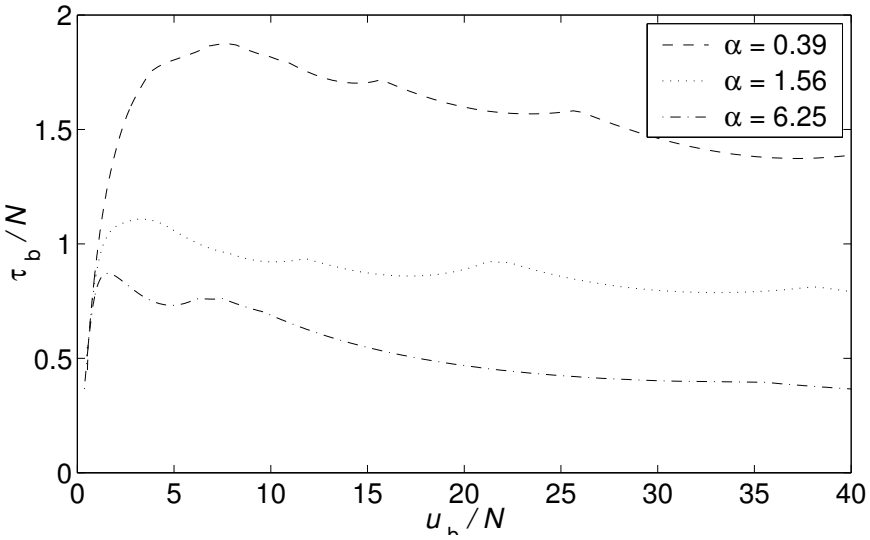

Figure 3.13: A plot showing re-scaled sliding laws for beds 1, 4 and 5, where distances and bed heights have been rescaled such that $k_{max} = 1$ and the Nye-Kamb coefficient remains at unity.

that $k_{max} = 1$, and subsequently rescaling bed height such that the Nye-Kamb coefficient remains fixed at unity changes figure 3.10 into figure 3.13.[4] This figure shows that, at small u_b/N, beds with different α behave similarly: the plots only show τ_b/N for values of u_b/N at which there is at least one cavity (the same is also true of fig. 3.10). When lengths and heights are rescaled, the onset of cavitation occurs at roughly the same value of u_b/N for all the beds with different values of α. However, the difference in behaviour at large velocities is now more pronounced. τ_b/N reaches its maximum at larger values of u_b/N for beds with lower α than for beds with higher α. The maximum value of τ_b/N has also increased for values with lower α — this may be attributed to the fact that the maximum bed slope $h'(x)$ increases under the rescaling proposed above, and that this increase is more pronounced for smaller α.

In effect, we are seeing precisely the effect anticipated by Fowler (1986a, 1987a): at low velocities, small-scale roughness (on the k_{max}-scale) provides most of the resistance, as indicated by Nye-Kamb theory. At higher velocities, larger bumps (on the k^*-scale) begin to provide more resistance. The decrease in shear stress observed here at large u_b/N is associated not with the drowning of wavelengths which provide the most drag according to Nye-Kamb theory, but with the drowning of wavelengths which contribute the greatest amplitude to the Fourier spectrum of the bed. The derivation of Fowler's (1987a) sliding law $u_b = C\tau_b^p N^{-q}$ assumes that this drown-

[4]The rescaling is $(u_b/N)_{new} = (k_{max}/k^*)^{1/2}(u_b/N)_{old}$ and $(\tau_b/N)_{new} = (k_{max}/k^*)^{1/2}(u_b/N)_{old}$.

ing of the 'dominant' wavelength in the bed 'Fourier spectrum' never occurs, i.e. that there are always obstacles with sufficiently large wavelengths *and* amplitudes for these obstacles not to be drowned.[5] Since Fowler's sliding law does not satisfy Iken's bound, this can only be possible if the superposition of bed obstacles of ever increasing wavelengths used by Fowler (1987a) leads to unbounded bed slopes. If bed slopes are to remain bounded, there must be some wavelength corresponding to a maximum bed obstacle amplitude, and correspondingly τ_b/N will be bounded. This is the case with which we have been concerned here.

3.8 Other Solutions

Here, we reconsider whether solutions to the Hilbert problem (3.64)–(3.65) which have fewer endpoint singularities than $G(\zeta)$ defined through (3.74)–(3.76) are possible. A general solution of the Hilbert problem (3.64) which has finite degree at infinity takes the form (Muskhelishvili, 1992, chapter 10)

$$G(\zeta) = \frac{\chi(\zeta)}{2\pi i} \int_{\Gamma'} \frac{h_2(\xi)\,\mathrm{d}\xi}{\chi^+(\xi)(\xi-\zeta)} + P(\zeta)\chi(\zeta), \tag{3.124}$$

where $P(\zeta)$ is an arbitrary polynomial and $\chi(\zeta)$ is defined analogously to (3.75) as

$$\chi(\zeta) = \prod_{j=1}^{n} \chi_j(\zeta). \tag{3.125}$$

However, χ_j is no longer defined by $(3.75)_2$. Instead, each χ_j and its associated index κ_j — here defined with the opposite sign convention from Muskhelishvili (1992) — must merely take one of the following four forms:

$$\chi_j(\zeta) = \begin{cases} \left(\zeta-\xi_{b_j}\right)^{1/2}\left(\zeta-\xi_{c_{j-1}}\right)^{1/2}, & \kappa_j = 1, \\ \left(\zeta-\xi_{b_j}\right)^{1/2}\left(\zeta-\xi_{c_{j-1}}\right)^{-1/2}, & \kappa_j = 0, \\ \left(\zeta-\xi_{b_j}\right)^{-1/2}\left(\zeta-\xi_{c_{j-1}}\right)^{1/2}, & \kappa_j = 0, \\ \left(\zeta-\xi_{b_j}\right)^{-1/2}\left(\zeta-\xi_{c_{j-1}}\right)^{-1/2}, & \kappa_j = -1, \end{cases} \tag{3.126}$$

where χ_j is holomorphic in the complex plane cut along Γ'_j, and the branch taken behaves as $\chi_j \sim \zeta^{\kappa_j}$ when $\zeta \to \infty$. $\chi(\zeta)$ thus defined is holomorphic in the ζ-plane cut along Γ' and behaves as $\chi \sim \zeta^{\kappa}$ when $\zeta \to \infty$, where the index κ is

$$\kappa = \sum_{j=1}^{n} \kappa_j. \tag{3.127}$$

[5] This clearly implies that the bed does not have a finite period — hence the 'Fourier spectrum' in inverted commas. A finite period is assumed here primarily in order to make the problem tractable.

In the sequel, we consider only those solutions which have $\kappa > 0$, since these have fewer cavity end point singularities (namely $n - \kappa$) than the solution (3.74)–(3.76) constructed previously. In order to approach a finite value $G(\infty)$ as $\zeta \to \infty$, such solutions must have $P(\zeta) \equiv 0$. This is, however, not sufficient to ensure that the conditions (3.65) at the origin and infinity are satisfied.

In order to impose (3.65), we require that $(3.65)_1$ and (3.66) are satisfied; as discussed before, this ensures that $(3.65)_2$ also holds.

In an analogous fashion to the derivation of (3.83) and (3.89), one can now show that

$$\chi_\star(\zeta) = \overline{\chi(1/\overline{\zeta})} = \frac{\chi(\zeta)}{\zeta^\kappa \chi(0)}, \qquad \overline{\chi^+(\xi)} = -\frac{\chi^+(\xi)}{\xi^\kappa \chi(0)}. \tag{3.128}$$

Hence, by analogy with the derivation of (3.92),

$$G_\star(\zeta) = \frac{\overline{\chi(1/\overline{\zeta})}}{-2\pi i} \int_{\Gamma'} \frac{h_2(\xi)\,\overline{\mathrm{d}\xi}}{\overline{\chi^+(\xi)}(\overline{\xi} - 1/\zeta)} = \frac{\chi(\zeta)}{2\pi i \zeta^\kappa} \int_{\Gamma'} \frac{h_2(\xi)\xi^\kappa}{\chi^+(\xi)} \frac{(-1/\xi^2)\,\mathrm{d}\xi}{1/\xi - 1/\zeta} \tag{3.129}$$

But

$$\frac{\xi^\kappa}{\zeta^\kappa}\left(\frac{-1/\xi^2}{1/\xi - 1/\zeta}\right) = \frac{(\xi/\zeta)^{\kappa-1}}{\xi - \zeta} = \begin{cases} \frac{1}{\xi-\zeta}, & \kappa = 1 \\ \frac{1}{\zeta}\sum_{r=0}^{\kappa-2}\left(\frac{\xi}{\zeta}\right)^r + \frac{1}{\xi-\zeta}, & \kappa > 1. \end{cases} \tag{3.130}$$

It follows that $G_\star(\zeta) = G(\zeta)$ is automatically satisfied when $\kappa = 1$. When $\kappa > 1$, the following additional conditions (compare also Muskhelishvili, 1992, section 84) must be imposed:

$$I_r \doteq \int_{\Gamma'} \frac{h_2(\xi)\xi^r\,\mathrm{d}\xi}{\chi^+(\xi)} = 0, \qquad r = 0, \ldots, \kappa - 2. \tag{3.131}$$

By taking the complex conjugate of I_r in (3.131), we obtain

$$\overline{I_r} = \int_{\Gamma'} \frac{h_2(\xi)\overline{\xi^r\,\mathrm{d}\xi}}{\overline{\chi^+(\xi)}} = \int_{\Gamma'} \frac{h_2(\xi)\xi^{-r}(-1/\xi^2)\,\mathrm{d}\xi}{-\chi^+(\xi)/(\chi(0)\xi^\kappa)} =$$

$$\chi(0)\int_{\Gamma'} \frac{h_2(\xi)\xi^{\kappa-r-2}\,\mathrm{d}\xi}{\chi^+(\xi)} = \chi(0) I_{\kappa-r-2} = 0, \qquad r = 0, \ldots, \kappa - 2. \tag{3.132}$$

Consequently, if the real parts of all the I_r vanish, where $r = 0, \ldots, \kappa - 2$, so do their imaginary parts. (3.131) therefore constitutes $\kappa - 1$ real constraints on $b_1, \ldots, b_n$ and $c_1, \ldots, c_n$.

In addition, we have the condition $G(0) = iN/4u_b$,

$$G(0) = \frac{\chi(0)}{2\pi i} \int_{\Gamma'} \frac{h_2(\xi)\,\mathrm{d}\xi}{\chi^+(\xi)\xi} = \frac{iN}{4u_b}, \tag{3.133}$$

which constitutes two real constraints when $\kappa > 0$, by equating real and imaginary parts.

The correct behaviour at the origin and at infinity therefore imposes $\kappa + 1$ real constraints on the cavity boundary points $b_1, \ldots, b_n$ and $c_1, \ldots, c_n$ for a solution of index $\kappa > 0$. The $2n-1$ constraints in (3.111) and (3.112) must, however, still hold as their derivation was independent of the particular solution G chosen. For $\kappa > 0$, we therefore obtain an overdetermined problem, with $2n + \kappa$ real constraints on $2n$ real variables, and in general there will be no solution. We conclude that only solutions with $\kappa \leq 0$ are, in general, possible. A physically viable solution G, which generates cavity roofs which satisfy $h_C(x) > h(x)$, must therefore have at least n cavity end point singularities.

One may wonder whether there exists some mechanism for regularisation of the stress field near a cavity endpoint at which there is a singularity in our solution. An obvious choice for such a mechanism is regelation: The high contact stresses at downstream cavity endpoints in our solution will lower the pressure melting point, and cause a heat flux towards the cavity endpoint. This will lead to an enhanced melt rate; in fact, a singularity in the stress field will lead to a singularity in the heat flux and hence in the melt rate. Since this is unphysical and contradicts the assumption that there is no ice flow into the bed and normal velocity is zero (boundary condition (3.14)), we may expect to see a small region about the contact point in which regelation cannot be ignored. We may then hope that a proper consideration of regelation in this region alleviates the melt rate and stress singularity. We do not, however, pursue this point further here.

3.9 Discussion

We have seen that Iken's (1981) bound on the basal shear stress supported by a hard bed holds for quite general bed geometries — the restriction to periodic beds is somewhat artificial, as the period of the bed may be taken to be arbitrarily long. Iken's bound presents a serious problem for classical 'shallow ice' theories for glacier and ice sheet dynamics, in which basal shear stress is prescribed by the geometry of the glacier or ice sheet. When the bed roughness of a glacier or ice sheet is too small, or when the separation pressure p_c becomes too large, the bed may not be able to support the geometrically prescribed driving stress locally. In this case, tensile stresses in the glacier or ice sheet (τ_{xx} in the notation of sections 2.1–2.2) must be comparable in magnitude to shear stresses, and we no longer have a lubrication flow.

It is worth emphasising that Iken's bound is not a sharp one, i.e. the maximum of τ_b/N will in general be less than $\max(h'(x))$. This point leads to some confusion in

the paper by Truffer and Iken (1998), who argue that τ_b/N should attain the upper bound at large velocities. Consequently, they assume that the contact area between ice and a sinusoidal bed migrates to the upstream point of inflection on the bed at high velocities ($x = 3\pi/2$ in figure 3.4), which clearly contradicts the actual solution depicted in the top panel of figure 3.4.

Similar arbitrary assumptions about the geometry of cavities abound in the glaciological literature, and they rarely lead to meaningful results, particularly when coupled with equally arbitrary assumptions about the normal stress distribution on the contact area bed between ice and bed. Thus, Schweizer and Iken (1992) assume cavities on a sinusoidal bed are symmetrical about the downstream point of inflection ($x = \pi/2$ in figure 3.4), and that normal stress on the contact area takes the shape of a truncated sinusoid (see figure 3 of their paper), with vanishing contact stress at the up- and downstream cavity endpoints. The results presented here do not support any of these assumptions; in particular, section 3.8 shows that vanishing normal stress at the both cavity endpoints is not possible. Similarly, Lliboutry (1968, 1979) assumes the cavity roofs to be straight lines. As Fowler (1986a) points out, this is not true, but appears to provide a reasonable approximation in the case of a sinusoidal bed. However, as figure 3.11 demonstrates, the assumption of straight cavity roofs becomes a bad approximation in the case of a more irregular bed. In fact, some cavity roofs in panel b of figure 3.11 have a mean upward slope, a possibility which is entirely discounted by Lliboutry (see also figure 14 of Lliboutry, 1968). Perhaps more puzzling than these arbitrary assumptions about cavity geometry — Lliboutry's (1968) approach actually predicts Fowler's (1986a) sliding law for a sinusoidal bed rather well — is the assertion found in Schweizer and Iken (1992) that a realistic sliding law should not depend on effective pressure N at all; the work presented here suggests that it certainly should, as has been shown previously by many other authors.

Most work on sliding in the presence of cavitation has focussed on simple beds with a single obstacle per period, and in particular, on sinusoidal beds (Fowler, 1986a; Schweizer and Iken, 1992; Truffer and Iken, 1998). This problem was solved — for small bed slopes — by Fowler (1986a). As explained above, the sliding laws constructed by Schweizer and Iken (1992) and Truffer and Iken (1998) are based on largely arbitrary assumptions about cavity geometry, which is why they contradict Fowler's earlier results. However, as pointed out by Lliboutry (1968, 1979, 1987) and Fowler (1986a, 1987a), the real interest lies in the effect of irregular bed topography on the sliding law, and in particular in the effect of superimposing bed obstacles with small and large wavelengths. The central question here is whether basal shear stress

(or more appropriately, τ_b/N) decreases at high sliding velocities (or u_b/N), as Fowler (1986a) found in the case of simple periodic beds (see also figures 3.3 and 3.4).

In the case of a self-similar bed composed of bed obstacles of asymptotically different sizes, Fowler (1987a) obtained a sliding law of the form (3.3),

$$u_b = C\tau_b^p N^{-q} \qquad p,\, q > 0, \tag{3.134}$$

for which τ_b continues to increase with u_b. As this sliding law contradicts Iken's bound (3.11), we are led to conclude that Fowler's superposition of bed bumps leads to unbounded bed slopes. The work presented in this chapter has been concerned with obtaining a realistic sliding law for irregular beds which have bounded slopes. To this end, we constructed a method for solving Fowler's (1986a) model directly for beds with many obstacles per bed period.

Our results indicate that basal shear stress τ_b/N increases with u_b/N at low velocities, but decreases at high velocities. This decrease occurs once obstacles with wavelengths corresponding to the maximum amplitude in the Fourier transform of the bed have become 'drowned'. The effect of bed roughness drowning is, however, less pronounced than for an irregular bed than for a simple periodic bed.

One aspect of cavity formation which has been ignored completely here is the interaction between the presence of cavities and the behaviour of the subglacial drainage system (e.g. Kamb, 1987; Fowler, 1987b). This interaction is, however, likely to be significant as the drainage system is usually assumed to control the separation pressure p_c and hence the effective pressure N which appears in the sliding law. Moreover, theories of glacier surging often assume that the subglacial drainage can switch from a channel-based subglacial drainage system to a linked cavity-based system, in which meltwater reaching the bed drains through cavities between ice and bed rather than primarily through a system of subglacial channels. A linked cavity system is then assumed to generate the high effective pressures which lead to fast sliding.

The flow of water is likely to affect the geometry of cavities and hence the sliding law because heat dissipation in the water flow will lead to melting at the cavity roof. This effect has been considered for simple bed geometries by Kamb (1987). Conversely, sliding may affect the drainage system as the extent of cavitation increases with sliding velocity (cf. fig. 3.11). If one considers drainage of water through a system of connected cavities as similar to the flow of a liquid through a porous medium, then an increase in sliding velocity should lead to an increase in 'porosity' and hence 'permeability' of the bed. These interactions are, however, badly understood at present

and form an obvious area for future research due to their importance in understanding how the bed of a glacier can balance the gravitational driving force acting on the glacier.

Chapter 4

Sliding over Large Obstacles

4.1 Introduction

The classical theory of glacier sliding over a 'hard' bed assumes that the bed obstacles which generate drag on the base of the glacier have wavelengths much shorter than the thickness of the glacier. This leads to some significant simplifications in the mathematical formulation of the sliding problem. Using Fowler's (1977; 1979; 1981) boundary layer approach, the interaction between ice flow and bed asperities can be represented in a model for the bulk flow of the glacier as boundary condition in the form of a sliding law (see also section 2.3 and appendix A).

If there is significant small-scale roughness present at the bed, then the assumption that most of the drag experienced by the ice is generated by this small-scale roughness is realistic. For instance, Nye's (1969) and Kamb's (1970) formula (2.59) indicates that short wavelengths are more likely to contribute to basal drag than large ones. In the particular case of Newtonian viscous ice flowing over a bed with small roughness slopes in the absence of cavitation, the contribution of a sinusoidal bump of fixed amplitude increases eight-fold when its wavelength is halved whilst sliding velocity is held constant.

It is, however, conceivable that small-scale roughness may be absent, or that its effect is suppressed. This may in particular be the case when the bed consists of deformable sediments rather than rigid bedrock. The drag generated by small-scale obstacles such as clasts (large rock fragments) at the ice-till interface could be reduced significantly if they are sheared along with a deforming till matrix (fig. 4.1). Likewise, the deforming till matrix itself may not generate significant resistance to flow — for instance, if it is plastic with a relatively low yield stress.

If small-scale roughness and till deformation provide insignificant resistance to flow, then one may wish to know whether drag generated by larger obstacles such as

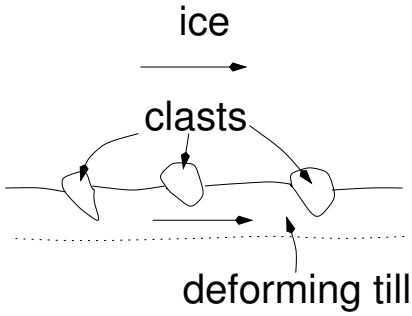

Figure 4.1: Suppression of small-scale roughness due to bed deformation.

drumlins (figs. 1.3 and 1.4) can balance the gravitational driving force acting on the ice. As the horizontal extent of a drumlin ($\sim$ 1 km) can be comparable to the typical thickness of an ice sheet, Fowler's boundary layer approach can no longer be used to study the drag generated by such obstacles and the effect of the upper free surface must be considered explicitly.

As mentioned above, one may expect long-wavelength obstacles to generate considerably less resistance to flow at any given sliding velocity than ones with short wavelengths. Consequently, if drumlin-sized bed obstacles are to generate significant drag, one may expect this to happen only at high sliding velocities. The specific case we will study in this chapter is thus the problem of an ice stream — a fast-flowing part of an ice sheet — sliding rapidly over drumlin-sized topography. For simplicity, the possibility of cavitation is again ignored. Furthermore, we consider only the case of ice of constant viscosity and bed obstacles with small slopes, as was done in the classical theories of Nye (1969) and Kamb (1970). This implies that our model will not be able to produce reliable numerical values for the drag generated by bed obstacles; for this purpose, a model using a Glen's law or similar non-linear rheology would be better suited. Our aim is thus not to give a complete answer to the question of whether drumlin-sized topography can generate significant drag on an ice stream, but to develop a first approach to the problems of how to deal with the effect of the upper, free surface of the ice on the generation of basal drag, and of how to parameterise this drag in a model for the bulk flow of the ice. Further work will be necessary to resolve the issue of whether such obstacles can actually generate significant drag at realistic sliding velocities.

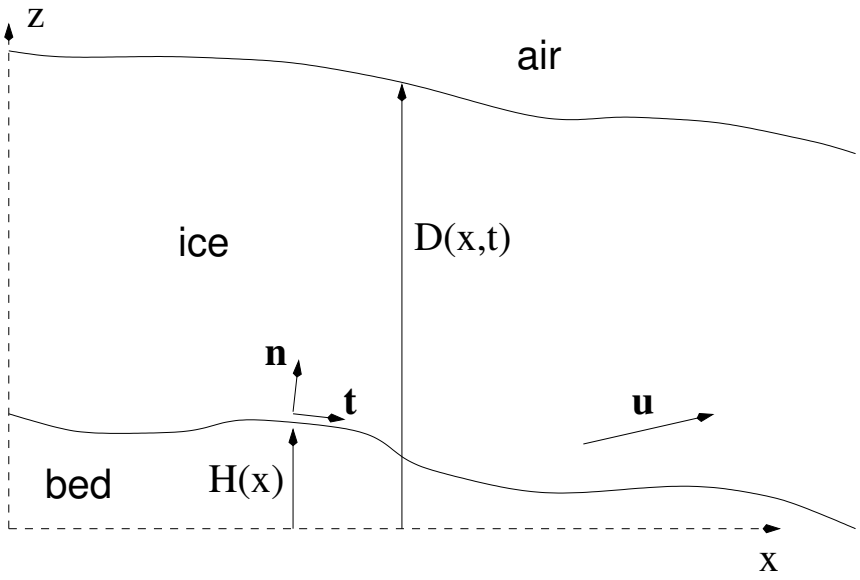

Figure 4.2: Geometry of the problem.

4.2 Model

The geometry of the problem is illustrated in figure 4.2. We consider the two-dimensional flow of Newtonian ice over a prescribed bed $z = H(x)$, while $z = D(x,t)$ denotes the upper, free surface of the ice, and a Cartesian coordinate system (x, z) with the z-axis aligned vertically upwards is used. The assumption that the bed is fixed is somewhat at odds with the notion that the bed may be deformable. However, the deforming layer of till under an ice sheet is likely to be thin. Thus, for instance, Engelhardt and Kamb (1998) estimate from field measurements that the deforming till under Ice Stream B in West Antarctica has a thickness of only 3 cm, which is insignificant compared with the height of a typical drumlin and justifies our neglect of bed deformation for the purposes of defining the domain of the ice flow.

Given viscosity η, density ρ and acceleration due to gravity g, and denoting the velocity field by $\mathbf{u} = (u, w)$, we obtain the usual slow flow equations

$$\eta \nabla^2 \mathbf{u} - \nabla p - \rho g \mathbf{k} = \mathbf{0}, \tag{4.1}$$

$$\nabla \cdot \mathbf{u} = 0, \tag{4.2}$$

where $\mathbf{k}$ is the z-unit vector. At the surface, we prescribe vanishing shear and normal stress. Writing shear and normal stress explicitly in terms of p and the derivatives of $\mathbf{u}$ and D, we require on $z = D$,

$$\frac{\eta}{1 + \left(\frac{\partial D}{\partial x}\right)^2} \left[\left(1 - \left(\frac{\partial D}{\partial x} \right)^2 \right) \left(\frac{\partial u}{\partial z} + \frac{\partial w}{\partial x} \right) + 2 \frac{\partial D}{\partial x} \left(\frac{\partial w}{\partial z} - \frac{\partial u}{\partial x} \right) \right] = 0, \tag{4.3}$$

$$p - \frac{2\eta}{1+\left(\frac{\partial D}{\partial x}\right)^2}\left[\frac{\partial w}{\partial z} + \left(\frac{\partial D}{\partial x}\right)^2 \frac{\partial u}{\partial x} - \frac{\partial D}{\partial x}\left(\frac{\partial w}{\partial x} + \frac{\partial u}{\partial z}\right)\right] = 0, \tag{4.4}$$

while the evolution of $D(x,t)$ is governed by a kinematic boundary condition (where accumulation is ignored)

$$\frac{\partial D}{\partial t} + u\frac{\partial D}{\partial x} = w \qquad \text{on } z = D. \tag{4.5}$$

At the base of the ice stream $z = H$, we suppose that there may be an applied shear stress $\tau_b(u_b, x)$ which is a function of basal sliding velocity u_b and position x,

$$\frac{\eta}{1+\left(\frac{\partial H}{\partial x}\right)^2}\left[\left(1 - \left(\frac{\partial H}{\partial x}\right)^2\right)\left(\frac{\partial u}{\partial z} + \frac{\partial w}{\partial x}\right) + 2\frac{\partial H}{\partial x}\left(\frac{\partial w}{\partial z} - \frac{\partial u}{\partial x}\right)\right] = \tau_b(u_b, x), \tag{4.6}$$

$$u_b = u\left(1 + \left(\frac{\partial H}{\partial x}\right)^2\right)^{1/2}, \qquad \text{on } z = H. \tag{4.7}$$

τ_b may arise if there is some small-scale roughness or if there is a thin deforming sediment layer with sufficient shear strength. In terms of our later analysis, we may see a non-zero τ_b as being analogous to the basal friction terms included in the classical sliding models of Morland (1976b) and Fowler (1981). For a bed with no small-scale resistance, we simply put $\tau_b = 0$. Note that u_b is the component of velocity parallel to the bed. Ignoring basal melt, velocity normal to the bed must vanish,

$$w = u\frac{\partial H}{\partial x} \qquad \text{on } z = H. \tag{4.8}$$

As in classical sliding theory (section 2.3 and appendix A), our aim here is principally to obtain a reduced model which describes how drumlin-type bed topography affects the bulk flow of the ice stream. The tool we will use to derive such a model is the technique of *homogenisation* (see e.g. Holmes, 1995, chapter 5), which is based on a multiple-scales expansion approach to dealing with structure on different length scales (the ice stream length and bed bump length scales in the present problem). In order to introduce multiple scales into the problem, we first non-dimensionalise it.

4.3 Non-Dimensionalisation

We define the following scales (see fig. 4.3): $[D]$ for the mean thickness of the ice stream, and also for the mean variation in bed elevation over the length of the ice stream,[1] $[L]$ for the length of the ice stream, $[U]$ for a typical bulk flow or 'sliding'

[1]Note that, because we scale the change in bed elevation H over the length of the ice stream $[L]$ with ice thickness $[D]$, these scalings would not apply to a steep glacier geometry (cf. section 2.2).

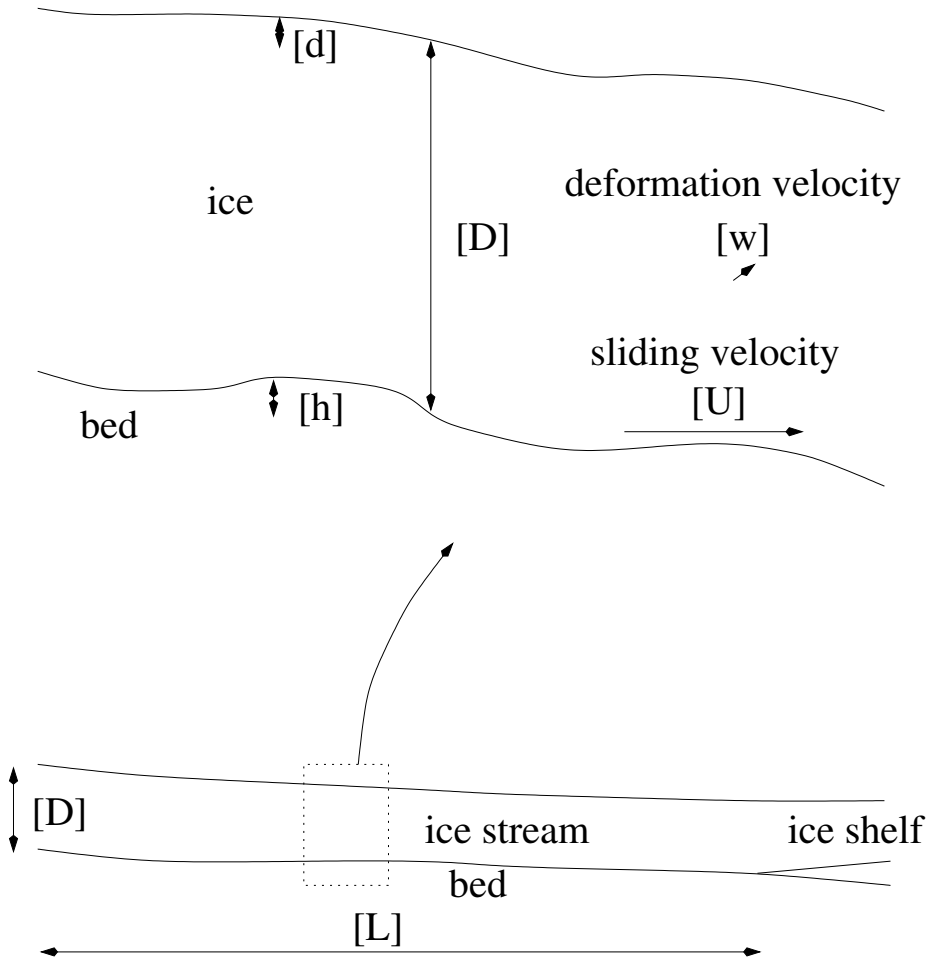

Figure 4.3: Scales for the problem of sliding over large bumps.

velocity and $[w]$ for typical velocity variations over the drumlin length scale. Note that $[U]$ and $[w]$ are distinct, and may indeed be asymptotically different. Moreover, we suppose that there are drumlins — or other bumps — of wavelength $\sim [D]$ and amplitude $[h]$ on the bed, and corresponding perturbations of height $[d]$ to the ice stream surface. We assume that these bed bumps generate most of the resistance to flow, as in the case of classical sliding with small wavelength obstacles. $[\tau]$ will denote a typical deviatoric stress, while $[\tau_d]$ is a scale for the driving stress, distinct from $[\tau]$.

As in shallow ice theory, the mean surface slope of the ice stream is assumed to be small,

$$\epsilon \doteq \frac{[D]}{[L]} \ll 1. \tag{4.9}$$

There are then two important asymptotically different horizontal length scales, $[D]$ and $[L]$. We are mostly interested in the local flow problem on the short length scale

$[D]$, as this is what controls the generation of drag due to the presence of bed bumps. However, the driving stress which causes the flow in the first place arises only because there is a mean decrease in surface elevation in the downstream direction over the length of the ice stream. One cannot therefore ignore variations on the long scale entirely, and this suggests multiply scaled horizontal coordinates and associated time variables

$$x = [L]X^\star = [D]x^\star, \tag{4.10}$$

$$t = [L]T^\star/[U] = [D]t^\star/[U]. \tag{4.11}$$

$(x^\star, t^\star)$ and $(X^\star, T^\star)$ are, of course, not independent as $(X^\star, T^\star) = \epsilon(x^\star, t^\star)$. In the limit $\epsilon \ll 1$ they will, however, be treated as independent in the context of a multiple scales expansion (e.g. Holmes, 1995). The 'inner' variables $(x^\star, t^\star)$ can be thought of as describing local variations associated with the flow over bed undulations, whereas the 'outer' ones $(X^\star, T^\star)$ describe the bulk behaviour of the ice stream. The appropriate transformation of derivatives is then

$$\frac{\partial}{\partial x} = \frac{1}{[D]}\left(\frac{\partial}{\partial x^\star} + \epsilon\frac{\partial}{\partial X^\star}\right), \tag{4.12}$$

$$\frac{\partial}{\partial t} = \frac{[U]}{[D]}\left(\frac{\partial}{\partial t^\star} + \epsilon\frac{\partial}{\partial T^\star}\right). \tag{4.13}$$

In his account of classical sliding, Fowler (1981) separated bed elevation into a smoothed bed and a local roughness component (see also appendix A). Following his example, we define a smoothed bed elevation as a running average:

$$[D]H^\star(X^\star) = \frac{1}{2X_{av}}\int_{-X_{av}}^{X_{av}} H(x+\xi)\,\mathrm{d}\xi, \tag{4.14}$$

where $[D] \ll X_{av} \ll [L]$. We assume that the smoothed bed thus defined can be considered to depend only on the outer variable $X^\star$. Of course, the smoothing introduced above is not unique, but we assume that it can be considered unique in an asymptotic sense if basal topography occurs on distinct length scales $[D]$ and $[L]$ with insignificant topography of intermediate wavelengths (see also Fowler, 1981).

It is expedient to apply a similar smoothing procedure to (4.14) to surface elevation and velocity, thus

$$[D]D^\star(X^\star, t^\star, T^\star) = \frac{1}{2X_{av}}\int_{-X_{av}}^{X_{av}} D(x+\xi, t)\,\mathrm{d}\xi, \tag{4.15}$$

$$[U]U^\star(X^\star, t^\star, T^\star) = \frac{1}{2X_{av}}\int_{-X_{av}}^{X_{av}} u(x+\xi, t)|_{z=H}\,\mathrm{d}\xi. \tag{4.16}$$

With the help of these smoothed variables, we non-dimensionalise the problem using the definitions (4.10), (4.11) and

$$z = [D]z^\star, \tag{4.17}$$

$$\mathbf{u} = \mathbf{i}[U]U^\star(X^\star, t^\star, T^\star) + \mathbf{k}\epsilon[U]\left(U^\star\frac{\partial H^\star}{\partial X^\star} - (z^\star - H^\star)\frac{\partial U^\star}{\partial X^\star}\right) + [w]\mathbf{u}^\star(x^\star, z^\star, t^\star, X^\star, T^\star), \tag{4.18}$$

$$H = [D]H^\star(X^\star) + [h]h^\star(x^\star, X^\star), \tag{4.19}$$

$$D = [D]D^\star(X^\star, t^\star, T^\star) + [d]d^\star(x^\star, t^\star, X^\star, T^\star), \tag{4.20}$$

$$\tau_b = [\tau_d]\tau_b^\star, \qquad u_b = [U]u_b^\star, \tag{4.21}$$

$$p = \rho g[D](D^\star - z^\star) - 2[\tau]\frac{\epsilon}{\nu}\frac{\partial U^\star}{\partial X^\star} + [\tau]p^\star, \tag{4.22}$$

where $\mathbf{i}$ and $\mathbf{k}$ are the x- and z-unit vectors, respectively. The decompositions of $\mathbf{u}$ and p introduced here may seem overly elaborate at first sight; they do, however, lead to some convenient simplifications later. Note that $h^\star = \{H(x) - [D]H^\star(X)\}/[h]$ may be interpreted the local bed roughness component, while $d^\star$ denotes the corresponding surface undulations, and $\mathbf{u}^\star$ denotes variations in velocity relative to a regionally smoothed velocity field.

Choice of Scales

For a given ice stream geometry, one can estimate the thickness and length scales $[D]$ and $[L]$ and the roughness scale $[h]$. It remains to define the other scales in terms of these. Clearly, by analogy with shallow ice theory, the driving stress is

$$[\tau_d] = \rho g[D]\epsilon. \tag{4.23}$$

If the aspect ratio of a typical local bed bump is defined as

$$\nu \doteq [h]/[D] \tag{4.24}$$

then the assumption that 'geometrical drag' generated by flow over bed bumps is a significant term in the force balance of the ice stream suggests that (cf. Fowler, 1981, see also equation (2.50) and the discussion leading up to equation (A.14) in appendix A)

$$[\tau] = [\tau_d]/\nu. \tag{4.25}$$

If basal bumps are shallow with $\nu \ll 1$, as will be assumed, then $[\tau] \gg [\tau_d]$ and hence deviatoric stresses in the ice will be much greater than the driving stress — this may

be contrasted with shallow ice theory (section 2.2), where deviatoric stresses in the ice scale with the driving stress. As a corollary, velocity variations on the inner length scale $[D]$ will be much greater in the present case than any shearing velocities in the ice due to the driving stress.[2] The scales $[U]$ for sliding velocity and $[w]$ for local velocity variations can be related through (4.8), which suggests we put

$$[w]/[U] = \nu. \tag{4.26}$$

But, since $[w]$ is a velocity variation over the length scale $[D]$ and $[\tau]$ is a typical deviatoric stress, and we must have

$$[\tau] = \eta[w]/[D]. \tag{4.27}$$

Combining (4.25)–(4.27) finally gives us $[U]$ and $[w]$ in terms of the ice stream geometry:

$$[w] = \frac{[\tau_d][D]}{\eta\nu}, \qquad [U] = \frac{[\tau_d][D]}{\eta\nu^2}. \tag{4.28}$$

Note that this derivation assumes that $[U]$ is determined primarily by drag due to flow over bed topography, and not by the friction law which gives shear stress at the bed as $\tau_b(u_b, x)$. In other words, the scaled basal shear stress $\tau_b^\star \sim \tau_b([U], x)/[\tau_d]$ must be $O(1)$ (or small) for all x and the value of $[U]$ calculated here.

It remains to fix $[d]$, the scale for surface perturbations. Two mechanisms affect how large surface perturbations will be. Firstly, advection in (4.5) suggests

$$[d][U]/[D] = [w] \qquad \Rightarrow \qquad [d] = \nu[D] \tag{4.29}$$

and secondly hydrostatic pressure changes in (4.4) would lead to

$$\rho g[d] = [\tau] \qquad \Rightarrow \qquad [d] = \epsilon[D]/\nu \tag{4.30}$$

For a consistent model, one should choose the smaller choice of $[d]$ above. For the present we choose (4.29), and consider later in section 4.4.2 the rescaling which may be required when $\epsilon/\nu \ll \nu$.

[2] 'Shearing velocity' is here used to refer to the velocity which arises if the ice stream flows in simple shear, with the driving stress supported locally at the base and no bed bumps present, while 'deformational velocities' refer to non-laminar velocities introduced by the presence of bed topography.

4.4 Multiple Scales Expansion

The scaled variables defined in the last section are substituted in the model in section 4.2, and the asterisks are omitted for convenience. Owing to the decompositions of the velocity field, and of bed and surface elevations, and due the introduction of multiple scales into the space and time derivatives through the expressions (4.12) and (4.13), the resulting equations are lengthy and not particularly instructive in their 'raw' form. Consequently, we do not list them here.

Instead, we proceed by noting that the dimensionless model contains two small parameters, ν and ϵ. We shall assume that $\epsilon \ll \nu \ll 1$, and construct a leading order model on this basis. This assumption is clearly realistic for most glacial bedforms with typical slopes of $\nu \approx 0.05$–0.1, which may be compared with ice stream surface slopes of $\epsilon \approx 10^{-3}$. Moreover, the restriction $\epsilon \ll \nu$ ensures that deviatoric stresses $[\tau] = [\tau_d]/\nu = \rho g[D]\epsilon/\nu$ are much smaller than hydrostatic pressures $\rho g[D]$. If this were not the case, one would expect widespread cavitation even in the absence of pressurised subglacial water, as variations in normal stress at the bed would be comparable to the mean hydrostatic pressure at the bed (cf. chapter 3).

Note that the boundaries of the ice flow domain are $z = H(X) + \nu h(x, X)$ and $z = D(X, t, T) + \nu d(x, t, X, T)$. Since $\nu \ll 1$, we expand these boundary conditions in Taylor series about $z = H$ and $z = D$ under the assumption that the velocity and pressure fields are sufficiently smooth to allow expansion to the required order. This approach can also be found in Nye (1969) and Morland (1976a,b), and allows the problem to be considered on the simpler domain $H < z < D$.

To the error in ν and ϵ indicated,[3] we obtain the following equations: Field equations become

$$\nabla^2 \mathbf{u} - \nabla p - \mathbf{i}\nu \frac{\partial D}{\partial X} = O(\epsilon^2/\nu), \qquad \text{on } z \in (H, D), \tag{4.31}$$

$$\nabla \cdot \mathbf{u} = \frac{\partial u}{\partial x} + \frac{\partial w}{\partial z} = 0, \qquad \text{on } z \in (H, D), \tag{4.32}$$

while boundary conditions (4.3)–(4.4) at the surface are

$$\frac{\partial u}{\partial z} + \frac{\partial w}{\partial x} + \nu \left[d \left(\frac{\partial^2 u}{\partial z^2} + \frac{\partial^2 w}{\partial x \partial z} \right) + 2 \frac{\partial d}{\partial x} \left(\frac{\partial w}{\partial z} - \frac{\partial u}{\partial x} \right) \right] = O(\epsilon, \nu^2) \qquad \text{on } z = D, \tag{4.33}$$

$$p - 2\frac{\partial w}{\partial z} = \frac{\nu^2}{\epsilon} d + O(\nu) \qquad \text{on } z = D. \tag{4.34}$$

[3] i.e. omitting terms of the order indicated in the scaled equations

In (4.5) $u|_{z=D+\nu d}$ and $w|_{z=D+\nu d}$ are expanded in Taylor series in νd to some order n about $z = D$, yielding[4]

$$\frac{1}{\nu}\frac{\partial D}{\partial t} + \frac{\partial d}{\partial t} + U\frac{\partial d}{\partial x} + \sum_{r=1}^{n} \frac{\nu^r d^{r-1}}{(r-1)!}\frac{\partial^{r-1}u}{\partial z^{r-1}}\frac{\partial d}{\partial x} + \frac{\epsilon}{\nu}\left(\frac{\partial D}{\partial T} + U\frac{\partial D}{\partial X}\right) =$$

$$w + \sum_{r=1}^{n} \frac{\nu^r d^r}{r!}\frac{\partial^r w}{\partial z^r} + \frac{\epsilon}{\nu}\left(U\frac{\partial H}{\partial X} - (D-H)\frac{\partial U}{\partial X}\right) + O(\epsilon, \nu^{n+1}) \qquad \text{on } z = D. \quad (4.35)$$

At the base, the shear stress relation (4.6) may now be expressed as

$$\frac{\partial u}{\partial z} + \frac{\partial w}{\partial x} + \nu\left[h\left(\frac{\partial^2 u}{\partial z^2} + \frac{\partial^2 w}{\partial x \partial z}\right) + 2\frac{\partial h}{\partial x}\left(\frac{\partial w}{\partial z} - \frac{\partial u}{\partial x}\right)\right] = \nu\tau_b + O(\epsilon, \nu^2) \qquad \text{on } z = H, \quad (4.36)$$

$$\tau_b = \tau_b(U, x, X) + O(\nu) \qquad \text{on } z = H. \quad (4.37)$$

In (4.8), we expand in a similar manner to (4.35) above,

$$w + \sum_{r=1}^{n} \frac{\nu^r h^r}{r!}\frac{\partial^r w}{\partial z^r} = U\frac{\partial h}{\partial x} + \sum_{r=1}^{n} \frac{\nu^r h^{r-1}}{(r-1)!}\frac{\partial^{r-1}u}{\partial z^{r-1}}\frac{\partial h}{\partial x} + O(\epsilon, \nu^{n+1}). \quad (4.38)$$

In order to simplify these equations and to obtain a tractable leading-order model on both inner and outer scales, we use the technique of homogenisation (e.g. Holmes, 1995, chapter 5) as described in the next section.

4.4.1 Simplification

All dependent variables other than $H(X)$, $D(X, t, T)$ and $U(X, t, T)$ are assumed to depend on both inner and outer variables, (x, t) and (X, T), respectively, which we treat as independent. As usual in multiple scales expansions, dependent variables must be bounded functions of the inner variables, x and t in our case.[5] Furthermore, we will assume that the averaging procedures (4.14)–(4.16) may, on the basis that $X_{av}/[D] \gg 1$, be re-cast as

$$\lim_{R\to\infty} \frac{1}{2R}\int_{-R}^{R} h(x, X)\,\mathrm{d}x = 0, \quad (4.39)$$

$$\lim_{R\to\infty} \frac{1}{2R}\int_{-R}^{R} d(x, t, X, T)\,\mathrm{d}x = 0, \quad (4.40)$$

$$\lim_{R\to\infty} \frac{1}{2R}\int_{-R}^{R} u(x, t, X, T)|_{z=H+\nu h}\,\mathrm{d}x = 0. \quad (4.41)$$

[4]Note that n is *not* the index in Glen's law.

[5]Strictly speaking, we require boundedness with respect to t only for t greater than some value, say $t > 0$, but not as $t \to -\infty$.

In order to simplify (4.35) and (4.38), we introduce an averaging operator as

$$\langle f \rangle = \lim_{R\to\infty} \frac{1}{2R} \int_{-R}^{R} f(x,t,z,X,T)\,\mathrm{d}x \tag{4.42}$$

for any $f(x,t,z,X,T)$ for which $\langle f \rangle$ is well-defined. Note that a more common approach to homogenisation is to suppose that the structure of the problem on the inner length scale is periodic (Holmes, 1995). In the present case, this would correspond to assuming that $h(x,X)$ and $d(x,t,X,T)$ are periodic in the inner spatial coordinate x with some period a. The averaging operator $\langle\cdot\rangle$ would then be defined as

$$\langle f \rangle = \frac{1}{a} \int_{0}^{a} f(x,t,z,X,T)\,\mathrm{d}x. \tag{4.43}$$

However, for a periodic function f, the definitions of $\langle f \rangle$ in (4.42) and (4.43) are easily seen to be equivalent. Consequently we persist here with the definition (4.42) rather than introducing an arbitrary finite period on the inner scale. This is mostly done for two reasons: Firstly, the concept of an 'averaging length' for calculating basal drag has been discussed at some length in the literature on glacier sliding (e.g. Nye, 1969; Kamb, 1970; Kamb and Echelmeyer, 1986), and our aim in retaining the limit in (4.42) is to underline that an 'averaging length' is best defined asymptotically as lying between the length scales of interest ($[D]$ and $[L]$ in the present case), rather than being assigned some arbitrary value. Secondly, the expressions (4.39)–(4.40) lend themselves in an obvious manner to defining the averaging operator through (4.42), as they now state that $\langle d \rangle = \langle h \rangle = 0$. We should also point out that an average based on (4.42) is never taken when the limit in R is not assured to exist either by assumption (as in (4.39)–(4.41)), or because dependent variables are required to be bounded in x.

The boundedness of dependent variables as functions of the inner coordinate x will be used mainly when averaging over derivatives. Consider some function $f(x,\ldots)$ which is bounded with respect to x, and which has a locally integrable x-derivative. Then

$$\left\langle \frac{\partial f}{\partial x} \right\rangle = \lim_{R\to\infty} \frac{[f]_{x=-R}^{x=R}}{2R} = 0, \tag{4.44}$$

where $[f]_{x=a}^{x=b} = f(b) - f(a)$ in the usual notation. Moreover, note that $\langle F \rangle = F$ for any F independent of x (essentially the smoothed quantities U, D and H). Armed with these properties of $\langle\cdot\rangle$, we are now ready to manipulate (4.35) and (4.38).

By averaging over both sides of (4.38), we obtain

$$\langle w \rangle + \sum_{r=1}^{n} \frac{\nu^r}{r!} \left\langle h^r \frac{\partial^r w}{\partial z^r} \right\rangle =$$

$$\left\langle U\frac{\partial h}{\partial x}\right\rangle + \sum_{r=1}^{n}\frac{\nu^r}{(r-1)!}\left\langle \frac{\partial^{r-1}u}{\partial z^{r-1}}h^{r-1}\frac{\partial h}{\partial x}\right\rangle + O(\nu^{n+1},\epsilon) \qquad \text{on } z=H. \tag{4.45}$$

By integration by parts,

$$\frac{\nu^r}{(r-1)!}\left\langle \frac{\partial^{r-1}u}{\partial z^{r-1}}h^{r-1}\frac{\partial h}{\partial x}\right\rangle = \frac{\nu^r}{r!}\left\langle \frac{\partial^{r-1}u}{\partial z^{r-1}}\frac{\partial h^r}{\partial x}\right\rangle =$$

$$\frac{\nu^r}{r!}\left(\lim_{R\to\infty}\frac{\left[\frac{\partial^{r-1}u}{\partial z^{r-1}}h^r\right]_{x=-R}^{x=R}}{2R} - \left\langle h^r\frac{\partial^r u}{\partial z^{r-1}\partial x}\right\rangle\right). \tag{4.46}$$

The first term on the right-hand side vanishes because $(\partial^{r-1}u/\partial z^{r-1})h^r$ is bounded with respect to x. Therefore, using (4.32) to rewrite $\partial u/\partial x = -\partial w/\partial z$,

$$\frac{\nu^r}{(r-1)!}\left\langle \frac{\partial^{r-1}u}{\partial z^{r-1}}h^{r-1}\frac{\partial h}{\partial x}\right\rangle = -\frac{\nu^r}{r!}\left\langle h^r\frac{\partial^r u}{\partial z^{r-1}\partial x}\right\rangle = \frac{\nu^r}{r!}\left\langle h^r\frac{\partial^r w}{\partial z^r}\right\rangle. \tag{4.47}$$

Substituting (4.47) in (4.45) and using the properties of $\langle\cdot\rangle$ listed above yields

$$\langle w\rangle = O(\nu^{n+1},\epsilon) = O(\epsilon) \qquad \text{on } z=H, \tag{4.48}$$

if, formally, an integer n exists such that $\nu^{n+1}\lesssim\epsilon$, and the expansions in (4.35) and (4.38) can be carried out to this order.

Applying $\langle\cdot\rangle$ to both sides of (4.32) and using (4.44) yields

$$\frac{\partial\langle w\rangle}{\partial z} = 0, \tag{4.49}$$

and so $\langle w\rangle = O(\epsilon)$ for all z.

In an analogous manner to the derivation of of (4.48), applying $\langle\cdot\rangle$ to both sides of (4.35) and manipulating yields

$$\frac{\partial D}{\partial t} + \epsilon\left(\frac{\partial D}{\partial T} + \frac{\partial (D-H)U}{\partial X}\right) = O(\epsilon\nu), \tag{4.50}$$

which leads to the conclusion that D depends only on the outer time variable T to $O(\epsilon)$, so $D = D(X,T)$ to $O(\epsilon)$; this is hardly surprising since one would expect the mean thickness D of the ice stream to change on the convective timescale associated with its length (and not its thickness). Moreover, we define an average over inner time analogously to the spatial average $\langle\cdot\rangle$,

$$\langle f\rangle_t = \lim_{R\to\infty}\frac{1}{R}\int_0^R f(x,t,x,X,T)\,\mathrm{d}t, \tag{4.51}$$

for any function f for which this average is well-defined. An analogue of (4.44) for time-averaging yields

$$\left\langle \frac{\partial f}{\partial t} \right\rangle_t = 0, \tag{4.52}$$

if f is bounded with respect to $t > 0$. Bearing in mind that D depends only on X and T to $O(\epsilon)$, time-averaging then reduces (4.50) to a plug-flow mass conservation equation for D,

$$\frac{\partial D}{\partial T} + \frac{\partial [(D-H)\langle U \rangle_t]}{\partial X} = O(\nu), \tag{4.53}$$

as might be expected for rapid flow in which shearing in the ice does not contribute significantly to flux (cf. equation (A.5) with large γ), and where accumulation is ignored. (4.50) substituted back in (4.35) yields the following kinematic boundary condition on the inner scale,

$$\frac{\partial d}{\partial t} + U\frac{\partial d}{\partial x} = w + O(\nu) \qquad \text{on } z = D. \tag{4.54}$$

4.4.2 Leading Order Inner Model

In the previous section, we simplified the boundary conditions on the inner scale and derived equation (4.53) for the evolution of the ice stream geometry on the outer scale. Now we are in a position to consider the outer and inner problems at leading order in ν and ϵ. Dependent variables are expanded as $\mathbf{u} = \mathbf{u}_0 + O(\nu)$, $d = d_0 + O(\nu)$ etc. On the inner scale, this yields the following leading-order (to an $O(\nu)$ error) model.

From (4.31) and (4.32),

$$\nabla^2 \mathbf{u}_0 - \nabla p_0 = \mathbf{0}, \tag{4.55}$$

$$\nabla \cdot \mathbf{u}_0 = 0, \tag{4.56}$$

on the domain $H < z < D_0$, which is an infinite strip with respect to the inner coordinates, as H and D only depend on the outer ones, X and T, to leading order.

From (4.33) and (4.34), boundary conditions are

$$\frac{\partial u_0}{\partial z} + \frac{\partial w_0}{\partial x} = 0 \qquad \text{on } z = D_0, \tag{4.57}$$

$$p_0 - 2\frac{\partial w_0}{\partial z} = \frac{\nu^2}{\epsilon} d_0 \qquad \text{on } z = D_0, \tag{4.58}$$

and from (4.54)

$$\frac{\partial d_0}{\partial t} + U_0 \frac{\partial d_0}{\partial x} = w_0 \qquad \text{on } z = D_0, \tag{4.59}$$

while from (4.36) and (4.38) one obtains

$$\frac{\partial u_0}{\partial z} + \frac{\partial w_0}{\partial x} = 0 \qquad \text{on } z = H, \tag{4.60}$$

$$w_0 = U_0 \frac{\partial h}{\partial x} \qquad \text{on } z = H. \tag{4.61}$$

Note that, to leading order, we have a non-shearing flow as indicated by the field equation (4.55) together with boundary conditions (4.57) and (4.60), which state that shear stress vanishes at the upper and lower boundaries of the domain at leading order; basal shear stress τ_b in (4.33) is a $O(\nu)$ correction. This is analogous to classical sliding with shallow bed slopes (e.g. Nye, 1969; Kamb, 1970; Fowler, 1986a), and arises because because deviatoric stresses which occur due to the flow over bed bumps are much greater than the driving stress.

We should comment at this point about the $O(\nu^2/\epsilon)$ term in (4.34) and (4.58); its retention as a possible $O(1)$ term is justified since, by virtue of $\epsilon \ll \nu$, we have $\nu^2/\epsilon \gg \nu$. Hence the $O(\nu^2/\epsilon)$ term is much greater than the $O(\nu)$ error in the leading order model. We wish to retain the term explicitly because, as will be seen in the section 4.5, it is responsible for the relaxation of surface perturbations to their steady state shape. Physically, the $O(\nu^2/\epsilon)$ term expresses the effect of increased hydrostatic pressure due to the presence of a bump at the ice surface; such increased pressure naturally leads to the bump wanting to spread under its own weight, which is why this term is responsible for the relaxation of surface bumps to their steady-state shape.

There remains the possibility that $\nu^2/\epsilon \gg 1$. In this case, the rescaling $d^{\star\star} = (\nu^2/\epsilon)d^\star$ can be considered. It is straightforward to repeat the work in sections 4.4–4.4.1 with this rescaling. One can thereby show that the rescaling introduces no new terms into the leading order model, and that the error remains of $O(\nu)$. The rescaling converts the leading-order boundary conditions (4.58) and (4.59) respectively into (again dropping asterisks)

$$p_0 - 2\frac{\partial w_0}{\partial z} = d_0 \qquad \text{on } z = D_0, \tag{4.62}$$

$$\frac{\epsilon}{\nu^2}\left(\frac{\partial d_0}{\partial t} + U_0 \frac{\partial d_0}{\partial x}\right) = w_0 \qquad \text{on } z = D_0. \tag{4.63}$$

One may then wish to ignore the $O(\epsilon/\nu^2)$ terms on the left-hand side in (4.63). As this is a singular perturbation — it ignores the time derivative in d_0 — given initial conditions may then require a boundary layer in t. However, a simpler approach than to consider this boundary layer explicitly is simply to retain the $O(\epsilon/\nu^2)$ terms in (4.63), which is equivalent to persevering with the original model, equations (4.55)–(4.61). We shall adopt this latter approach here.

4.4.3 The Sliding Velocity U_0

Given D_0 and H (which are constant with respect to the inner variables x and t), equations (4.55)–(4.61) almost constitute a closed set of equations for the variables $\mathbf{u}_0$, p_0 and d_0 in the inner coordinates x, z and t: There are two boundary conditions on each boundary for the elliptic field equations (4.55)–(4.56), namely (4.57)–(4.58) on $z = D_0$ and (4.60)–(4.61) on $z = H$, while the additional kinematic boundary condition (4.59) determines the evolution of the surface bumps d_0 given appropriate initial conditions.[6] However, it still remains to fix the sliding velocity $U_0(X, t, T)$, which appears in some of the boundary conditions. In fact, U_0 is ultimately the object of our study, as it determines the evolution of the smoothed ice stream surface D_0 on the outer scale through (4.53).

Since U_0 is independent of inner position x, we expect a constraint on U_0 which is independent of x. Simple considerations of force balance suggest that one should expect, by analogy with $(2.59)_1$, a leading order relation of the form

$$-(D_0 - H)\frac{\partial D_0}{\partial X} = \left\langle \left(p_0 - 2\frac{\partial w_0}{\partial z}\right)\Big|_{z=H} \frac{\partial h}{\partial x} \right\rangle + \left\langle \tau_b\left(U_0, x, X\right)\right\rangle, \tag{4.64}$$

where the term on the left is the mean driving stress, and the terms on the right are the mean component of normal stress in the upstream direction (the 'geometrical drag' generated by bed obstacles) and the mean basal shear stress respectively. It can, in fact, be shown in a rather convoluted manner by considering $O(\nu)$ terms in (4.31)–(4.33) and (4.36)–(4.37) in the multiple scales expansion that (4.64) is indeed correct, as we shall see below.

We expand the velocity and stress fields to $O(\nu)$ as

$$\mathbf{u} \sim \mathbf{u}_0 + \nu\mathbf{u}_1 + O(\nu^2, \epsilon), \qquad p \sim p_0 + \nu p_1 + O(\nu^2, \epsilon).$$

The field equations (4.31) and (4.32) then lead to, at $O(\nu)$,

$$\frac{\partial^2 u_1}{\partial x^2} + \frac{\partial^2 u_1}{\partial z^2} - \frac{\partial p_1}{\partial x} - \frac{\partial D_0}{\partial X} = 0, \tag{4.65}$$

$$\frac{\partial u_1}{\partial x} + \frac{\partial w_1}{\partial z} = 0, \tag{4.66}$$

where we have only listed the x-component of (4.31). Using (4.66) to re-write $\partial^2 u_1/\partial x^2 = -\partial^2 w_1/\partial z \partial x$ and subsequently integrating (4.65) with respect to z over

[6] Note that, due to the Neumann boundary conditions on u_0, equations (4.55)–(4.61) are invariant under a change of u_0 by a constant amount. In order to make the solution unique, one needs to use a leading-order version of the integral constraint (4.41).

(H, D_0) yields

$$\left(\frac{\partial u_1}{\partial z} - \frac{\partial w_1}{\partial x}\right)\Big|_{z=D_0} - \left(\frac{\partial u_1}{\partial z} - \frac{\partial w_1}{\partial x}\right)\Big|_{z=H} - \int_H^{D_0} \frac{\partial p_1}{\partial x}\,\mathrm{d}z - (D_0 - H)\frac{\partial D_0}{\partial X} = 0. \quad (4.67)$$

Taking the derivative in $\int_H^{D_0} \partial p_1/\partial x\,\mathrm{d}z$ outside the integral and applying the averaging operator $\langle\cdot\rangle$ to both sides of (4.67) leads to, by (4.44),

$$\left\langle \frac{\partial u_1}{\partial z} \right\rangle\Big|_{z=H} - \left\langle \frac{\partial u_1}{\partial z} \right\rangle\Big|_{z=D_0} = -(D_0 - H)\frac{\partial D_0}{\partial X}. \quad (4.68)$$

The right-hand side may be recognised as the driving stress which appears in (4.64). It remains to manipulate the left-hand side into a form given in terms of the leading order velocity and pressure fields, $\mathbf{u}_0$ and p_0.

To this end, we consider $O(\nu)$ terms in (4.33) and (4.36)

$$\frac{\partial u_1}{\partial z} + \frac{\partial w_1}{\partial x} + h\left(\frac{\partial^2 u_0}{\partial z^2} + \frac{\partial^2 w_0}{\partial z \partial x}\right) + 2\frac{\partial h}{\partial x}\left(\frac{\partial w_0}{\partial z} - \frac{\partial u_0}{\partial x}\right) = \tau_{b0}, \qquad \text{on } z = H, \quad (4.69)$$

$$\frac{\partial u_1}{\partial z} + \frac{\partial w_1}{\partial x} + d_0\left(\frac{\partial^2 u_0}{\partial z^2} + \frac{\partial^2 w_0}{\partial z \partial x}\right) + 2\frac{\partial d_0}{\partial x}\left(\frac{\partial w_0}{\partial z} - \frac{\partial u_0}{\partial x}\right) = 0, \qquad \text{on } z = D_0. \quad (4.70)$$

The manipulation of these two equations is very similar, and we focus therefore on (4.69). Using (4.32) to re-write $\partial u_0/\partial x = -\partial w_0/\partial z$,

$$2\frac{\partial h}{\partial x}\left(\frac{\partial w_0}{\partial z} - \frac{\partial u_0}{\partial x}\right) = 4\frac{\partial h}{\partial x}\frac{\partial w_0}{\partial z},$$

$$h\left(\frac{\partial^2 u_0}{\partial z^2} + \frac{\partial^2 w_0}{\partial z \partial x}\right) = h\left(\frac{\partial^2 u_0}{\partial z^2} + \frac{\partial^2 u_0}{\partial x^2} + 2\frac{\partial^2 w_0}{\partial z \partial x}\right).$$

But, from (4.31), $\partial^2 u_0/\partial x^2 + \partial^2 u_0/\partial z^2 = \partial p_0/\partial x$. Hence (4.69) becomes

$$\frac{\partial u_1}{\partial z} + \frac{\partial w_1}{\partial x} + h\left(\frac{\partial p_0}{\partial x} + 2\frac{\partial^2 w_0}{\partial z \partial x}\right) + 4\frac{\partial h}{\partial x}\frac{\partial w_0}{\partial z} = \tau_{b0}, \qquad \text{on } z = H \quad (4.71)$$

We apply the averaging operator $\langle\cdot\rangle$ to both sides of (4.71). Note that, by integration by parts and since h, p_0 and $\partial w_0/\partial z$ are bounded functions of the inner coordinate x,

$$\left\langle h\left(\frac{\partial p_0}{\partial x} + 2\frac{\partial^2 w_0}{\partial z \partial x}\right)\right\rangle =$$

$$\lim_{R\to\infty} \frac{\left[h\left(p_0 + 2\frac{\partial w_0}{\partial z}\right)\right]_{x=-R}^{x=R}}{2R} - \left\langle \left(p_0 + 2\frac{\partial w_0}{\partial z}\right)\frac{\partial h}{\partial x}\right\rangle = -\left\langle \left(p_0 + 2\frac{\partial w_0}{\partial z}\right)\frac{\partial h}{\partial x}\right\rangle, \quad (4.72)$$

where $[f]_{x=a}^{x=b}$ has the same meaning as before (cf. equation (4.44)). Using (4.44), averaging (4.71) thus yields

$$\left\langle \frac{\partial u_1}{\partial z} \right\rangle \Big|_{z=H} = \left\langle \left(p_0 - 2\frac{\partial w_0}{\partial z} \right) \Big|_{z=H} \frac{\partial h}{\partial x} \right\rangle + \langle \tau_{b0} \rangle \,. \tag{4.73}$$

By exact analogy with the derivation of (4.73), averaging (4.70) yields

$$\left\langle \frac{\partial u_1}{\partial z} \right\rangle \Big|_{z=D_0} = \left\langle \left(p_0 - 2\frac{\partial w_0}{\partial z} \right) \Big|_{z=D_0} \frac{\partial d_0}{\partial x} \right\rangle . \tag{4.74}$$

But, from (4.58), $p_0 - 2\partial w_0/\partial z = (\nu^2/\epsilon) d_0$ on $z = D_0$. Hence

$$\left\langle \frac{\partial u_1}{\partial z} \right\rangle \Big|_{z=D_0} = \frac{\nu^2}{\epsilon} \left\langle d_0 \frac{\partial d_0}{\partial x} \right\rangle = \frac{\nu^2}{2\epsilon} \left\langle \frac{\partial d_0^2}{\partial x} \right\rangle = 0, \tag{4.75}$$

by (4.44). Combining (4.68), (4.73), (4.75) and (4.37) finally yields the desired relation (4.64)

$$-\left(D_0 - H\right) \frac{\partial D_0}{\partial X} = \left\langle \left(p_0 - 2\frac{\partial w_0}{\partial z} \right) \Big|_{z=H} \frac{\partial h}{\partial x} \right\rangle + \langle \tau_b \left(U_0, x, X\right) \rangle \,. \tag{4.76}$$

This equation finally determines U_0. Equation (4.76) relates *mean* driving stress to *mean* sliding velocity; this is very different from shallow-ice theory where *local* driving stress determines *local* sliding velocity. Of course, it is through U_0 that the effect of local bed topography enters into the leading order 'outer problem' of determining the time-evolution of the ice stream surface D_0. Specifically, (4.53) may be written at leading order as

$$\frac{\partial D_0}{\partial T} + \frac{\partial [(D_0 - H) \langle U_0 \rangle_t]}{\partial X} = 0, \tag{4.77}$$

where $\langle \cdot \rangle_t$ denotes a time-average on the inner scale as in (4.51).

4.5 Solution of the Inner Problem

We will now concern ourselves with the inner problem at leading order, equations (4.55)–(4.61) with (4.76). The aim of doing so is to determine how the leading order sliding velocity U_0 evolves with respect to the inner time t, and therefore to determine the time-averaged sliding velocity $\langle U_0 \rangle_t$. Once $\langle U_0 \rangle_t$ can be calculated as a function of the outer ice stream surface elevation $D_0(X, T)$ and bed elevation $H(X)$, as well as their derivatives, the outer problem (4.53) can be closed. The evolution of the ice stream surface D_0 in time T can then, at least in principle, be determined.

By analogy with the case of classical sliding theory, we will refer to the desired relationship between the time-averaged sliding velocity $\langle U_0 \rangle_t$ on the one hand and driving stress $-(D-H)\frac{\partial D}{\partial X}$ and ice thickness $D-H$ on the other as a 'sliding law'. However, classical sliding theory generates a sliding law as a boundary condition for the bulk flow a glacier or ice sheet, relating shear stress and sliding velocity at the bed. This is no longer the case here: Our sliding law is simply a prescription for the bulk flow velocity $\langle U_0 \rangle_t$ (and hence for the ice flux $(D-H)\langle U \rangle_t$) in terms of driving stress and ice thickness.

One of the main benefits of the results of section 4.4 is that the free boundary problem for the ice stream surface is reduced to a fixed boundary problem on the inner scale. The surface perturbation d_0 appears as a variable in the boundary conditions of the ice flow problem, but does not affect the position of the boundary $z = D_0$ at leading order. The domain of the leading order inner ice flow problem is the strip $H < z < D_0$, where H and D_0 are independent of the inner coordinates x and t.

For simplicity, we omit the subscripts $\cdot_0$ as well as the outer variables (X, T) where this does not lead to ambiguity. As a convenient shorthand, we also denote the mean thickness of the ice and the driving stress by

$$S = D - H, \qquad \tau_d = -(D-H)\frac{\partial D}{\partial X},$$

respectively. To facilitate matters further, we assume that the bed and the ice stream surface are periodic in x with some period a. A partial solution of the inner problem can then be derived in Fourier transform space. We define the Fourier transform of a function $f(x, z, t)$ which is periodic in x with period a as

$$\hat{f}_r(z,t) = \int_0^a f(x,z,t)\exp(-ik_r x)/a \,\mathrm{d}x; \qquad k_r = \frac{2r\pi}{a}, \qquad r \in \mathbb{Z}.$$

By introducing a stream function ψ such that $u = \partial\psi/\partial z$ and $w = -\partial\psi/\partial x$, the field equation (4.56) is satisfied automatically. The stream function ψ itself satisfies the biharmonic equation,

$$\nabla^4 \psi = 0. \tag{4.78}$$

Taking the Fourier transform, we find that $\hat{\psi}_r$ satisfies the ordinary differential equation

$$\left(\frac{\mathrm{d}^2}{\mathrm{d}z^2} - k_r^2\right)^2 \hat{\psi}_r = 0, \tag{4.79}$$

with general solution

$$\hat{\psi}_r = (A_1 z + B_1)\exp(-ik_r z) + (A_2 z + B_2)\exp(ik_r z). \tag{4.80}$$

Substituting for u in the x-component of (4.55) and taking the Fourier transform yields $\hat{p}_r$ as

$$\hat{p}_r = -2ik_r \left[A_1 \exp(-k_r z) + A_2 \exp(k_r z)\right]. \tag{4.81}$$

The coefficients A_1, B_1, A_2 and B_2 can then be determined in terms of U, $\hat{h}_r$ and $\hat{d}_r$ by taking the Fourier transforms of (4.57)–(4.58) and (4.60)–(4.61) and substituting for $\hat{p}_r$ and $\hat{\psi}_r$. This yields four linear equations for the unknowns A_1, B_1, A_2 and B_2, which may be solved straightforwardly.

However, the sliding velocity U and surface perturbation $\hat{d}_r$ must still be determined themselves using (4.64) and the kinematic boundary condition (4.59). We take the Fourier transform of (4.59) and substitute for $\hat{w}_r$ in terms of A_1, B_1, A_2 and B_2, which are themselves functions of U, $\hat{h}_r$ and $\hat{d}_r$ as explained above. This yields the following equation for the evolution of bumps d on the ice stream surface

$$\left(\frac{\mathrm{d}}{\mathrm{d}t} + ik_r U + \frac{\nu^2}{2\epsilon}\frac{\sinh^2(k_r S)}{k_r\left[\sinh(k_r S)\cosh(k_r S) + k_r S\right]}\right)\hat{d}_r =$$

$$\frac{k_r S\cosh(k_r S) + \sinh(k_r S)}{\sinh(k_r S)\cosh(k_r S) + k_r S} ik_r U \hat{h}_r. \tag{4.82}$$

Equation (4.64) becomes in terms of Fourier coefficients

$$\tau_d = \sum_{r=1}^{\infty} 4k_r^3 \frac{\sinh^2(k_r S) - (k_r S)^2}{k_r S + \cosh(k_r S)\sinh(k_r S)} |\hat{h}_r|^2 U +$$

$$\sum_{r=1}^{\infty} 2\frac{\nu^2}{\epsilon} k_r \frac{\sinh(k_r S) + k_r S\cosh(k_r S)}{k_r S + \cosh(k_r S)\sinh(k_r S)} \Im\left(\hat{d}_r \overline{\hat{h}_r}\right) + \frac{1}{a}\int_0^a \tau_b(U, x)\,\mathrm{d}x. \tag{4.83}$$

where the overbar denotes complex conjugation, $\Im$ stands for imaginary part and we assume that the series converge, as in classical Nye-Kamb theory.

For large ice thicknesses $S \to \infty$, it is straightforward to see that $[\sinh^2(k_r S) - (k_r S)^2]/[k_r S + \cosh(k_r S)\sinh(k_r S)]$ tends to unity exponentially for fixed k_r, while $k_r[\sinh(k_r S) + k_r S\cosh(k_r S)]/[S^2\{k_r S + \cosh(k_r S)\sinh(k_r S)\}]$ vanishes at an exponential rate. Hence the right-hand side of (4.83) replicates the classical Nye-Kamb formula (2.59) for large ice thicknesses, as may be expected.

The evolution equation (4.82) for the height d of bumps on the ice stream surface can be interpreted as follows: The first term on the left-hand side describes the change of surface perturbations with time, while the second is an advection term. The third term on the left-hand side is a damping term which leads to the decay of surface perturbations due to increased hydrostatic pressure — note that the coefficient of $\hat{d}_r$ in this term is always positive when ice thickness S is positive. The term on the

right-hand side is a source term which represents how well basal perturbations are 'transmitted' to the surface. Notably, (4.82) is not a linear equation as U depends on the $\hat{d}_r$ through (4.83). A simple analytical solution is therefore not available, and the sliding velocity U is not simply proportional to the driving stress τ_d. This represents a notable departure from classical sliding with shallow bed bumps and a constant viscosity, where τ_b is related linearly to u_b through (2.59).

4.5.1 Sinusoidal Beds: A Phase Plane Analysis

A solution of (4.82)–(4.83) for a general bed appears prohibitive, and one may expect to have to truncate the series in (4.83) at some level to obtain a finite system of coupled ordinary differential equations. Such a truncation corresponds to a bed composed of a finite number of sinusoids with different wavelengths. Below, we consider only the simplest case of a sinusoidal bed with unit amplitude and no interfacial friction ($\tau_b \equiv 0$), as this provides some useful insights into the possible behaviour of solutions of the inner problem and how they affect the outer problem.

For a sinusoidal bed, only terms with $r = 1$ contribute to the sums in (4.83). Consequently, in order to determine how the sliding velocity U evolves with time t, we need only consider the evolution equation (4.82) with Fourier index $r = 1$. By suitably choosing the origin on the x-axis, we can put $h_1 = 0.5$, while an appropriate choice of scale $[D]$ ensures that $k_1 = 1$, and $[L]$ may be picked such that $\nu^2/\epsilon = 1$. $\hat{d}_1$ then satisfies

$$\left(\frac{\mathrm{d}}{\mathrm{d}t} + iU + F_1(S)\right)\hat{d}_1 = iF_2(S)U, \tag{4.84}$$

where

$$\tau_d = G_1(S)U + G_2(S)\Im(\hat{d}_1), \tag{4.85}$$

and

$$F_1(S) = \frac{\sinh^2 S}{2(\sinh S\cosh S + S)}, \qquad F_2(S) = \frac{S\cosh S + \sinh S}{2(\sinh S\cosh S + S)},$$
$$G_1(S) = \frac{\sinh^2 S - S^2}{\sinh S\cosh S + S}, \qquad G_2(S) = \frac{S\cosh S + \sinh S}{\sinh S\cosh S + S}. \tag{4.86}$$

Since the ice stream thickness S must be positive, the functions $F_1(S)$, $F_2(S)$, $G_1(S)$ and $G_2(S)$ are also positive. Note that, since the ice stream thickness S and driving stress τ_d do not depend on inner time t, τ_d, F_1, F_2, G_1 and G_2 can be treated as constants when solving (4.84)–(4.85).

Writing $\hat{d}_1 = \alpha + i\beta$ with α and β real, the sliding velocity U can be obtained from (4.85) as

$$U = \frac{\tau_d - G_2\beta}{G_1}. \tag{4.87}$$

Substituting for U and separating real and imaginary parts, we obtain from (4.84) the two coupled ordinary differential equations for α and β:

$$\frac{\mathrm{d}\alpha}{\mathrm{d}t} = -F_1\alpha + \frac{\tau_d - G_2\beta}{G_1}\beta, \tag{4.88}$$

$$\frac{\mathrm{d}\beta}{\mathrm{d}t} = (F_2 - \alpha)\frac{\tau_d - G_2\beta}{G_1} - F_1\beta. \tag{4.89}$$

Our ultimate aim is to determine the time-averaged sliding velocity $\langle U \rangle_t$ as a function of the driving stress τ_d and ice thickness S, which enters into (4.88)–(4.89) through the parameters F_1, F_2, G_1 and G_2. Recall that $\langle U \rangle_t$ is defined as a limit through (4.51):

$$\langle U \rangle_t = \lim_{R\to\infty} \frac{1}{R}\int_0^R U(t)\,\mathrm{d}t, \tag{4.90}$$

where we have again omitted outer coordinates from our notation. It is obvious from this definition that transients in time t do not affect the value of $\langle U \rangle_t$. In particular, if $U(t)$ approaches a limit at large times, then $\langle U \rangle_t = \lim_{t\to\infty} U$. We therefore wish to determine the behaviour of U at large times t for a given choice of τ_d, F_1, F_2, G_1 and G_2.

As U depends on β through (4.87), this is equivalent to the problem of determining β at large t. In particular, if (α, β) approaches a steady-state solution (a critical point in the (α, β)-phase plane) at large t, then the time-averaged sliding velocity $\langle U \rangle_t$ will take the value of U at that critical point, evaluated from from (4.87). Therefore, steady-state solutions or critical points of (4.88)–(4.89) and their stability are of particular interest.[7]

It is straightforward to establish that critical points (α_0, β_0) of (4.88)–(4.89) satisfy

$$\alpha_0 = \frac{\tau_d - G_2\beta_0}{F_1 G_1}\beta_0 = F_2 - \frac{G_1 F_1 \beta_0}{\tau_d - G_2\beta_0}, \tag{4.91}$$

$$f(\beta_0) \doteq G_2^2\beta_0^3 - 2\tau_d G_2\beta_0^2 + [\tau_d^2 + F_1G_1(F_1G_1 + F_2G_2)]\beta_0 - F_1G_1F_2\tau_d = 0. \tag{4.92}$$

Excluding the possibility of repeated roots, the cubic $f(\beta)$ in (4.92) can have either one or three real roots, corresponding to one or three real values of U through (4.87). Depending on the number of the corresponding critical points which are stable, it is

[7] We do not investigate the possibility of limit cycles and of solutions (α, β) which diverge at large t here, even though the former would lead to a well-defined time average $\langle U \rangle_t$.

therefore possible that $\langle U \rangle_t$ can take several different values for given F_1, F_2, G_1, G_2 and τ_d. In other words, the time-averaged sliding velocity $\langle U \rangle_t$ may be a multiply-valued function of ice thickness S and driving stress τ_d.

Position and Stability of Critical Points

In the analysis of the critical points that follows, we will assume that τ_d is positive. In the case of $\tau_d < 0$, a simple change of variables $\tau_d' = -\tau_d$ and $\beta' = -\beta$ recovers (4.88)–(4.89) with τ_d and β replaced by τ_d' and β', respectively, where τ_d' is then positive. Hence the restriction $\tau_d > 0$ does not affect the generality of our results.

We begin by showing that real solutions β_0 of (4.92) must lie in the interval $(0, G_2/\tau_d)$. To this end, consider the first derivative of the cubic $f(\beta)$ defined in (4.92):

$$f'(\beta) = 3G_2^2\beta^2 - 4\tau_d G_2\beta + \tau_d^2 + F_1G_1(F_1G_1 + F_2G_2) =$$
$$(3G_2\beta - \tau_d)(G_2\beta - \tau_d) + F_1G_1(F_1G_1 + F_2G_2). \tag{4.93}$$

Clearly $f'(\beta) > 0$ if $\beta \leq 0$ or $\beta \geq \tau_d/G_2$. Also

$$f(0) = -F_1G_1F_2\tau_d < 0, \qquad f(\tau_d/G_2) = F_1^2G_1^2 > 0. \tag{4.94}$$

Hence $f(\beta) < 0$ when $\beta \leq 0$, and $f(\beta) > 0$ when $\beta \geq \tau_d/G_2$. Consequently, real roots β_0 of (4.92) must lie in $(0, \tau_d/G_2)$. Incidentally, this ensures that velocities U evaluated from (4.87) at a critical point lie in the range $(0, \tau_d/G_1)$. Hence a positive driving stress generates a positive sliding velocity, as may be expected.

We proceed by analysing the stability of a given critical point (α_0, β_0). The Jacobian of the right-hand side of (4.88)–(4.89) evaluated at (α_0, β_0) is

$$J = \begin{pmatrix} -F_1 & (\tau_d - 2G_2\beta_0)/G_1 \\ -(\tau_d - G_2\beta_0)/G_1 & -F_1 - (F_2 - \alpha_0)G_2/G_1 \end{pmatrix}. \tag{4.95}$$

Its eigenvalues λ satisfy the quadratic

$$\lambda^2 + [2F_1 + (F_2 - \alpha_0)G_2/G_1]\,\lambda + F_1\,[2F_1 + (F_2 - \alpha_0)G_2/G_1] +$$
$$(\tau_d - G_2\beta_0)(\tau_d - 2G_2\beta_0)/G_1^2 = 0. \tag{4.96}$$

If the critical point (α_0, β_0) is to be asymptotically stable, then both roots of (4.96) must have negative real parts. By considering roots of a general quadratic $\lambda^2 + b\lambda + c = 0$ with real coefficients b and c, it is straightforward to see that this is the case if and only if b and c are both positive, i.e. if and only if the coefficients of λ^1 and λ^0 on

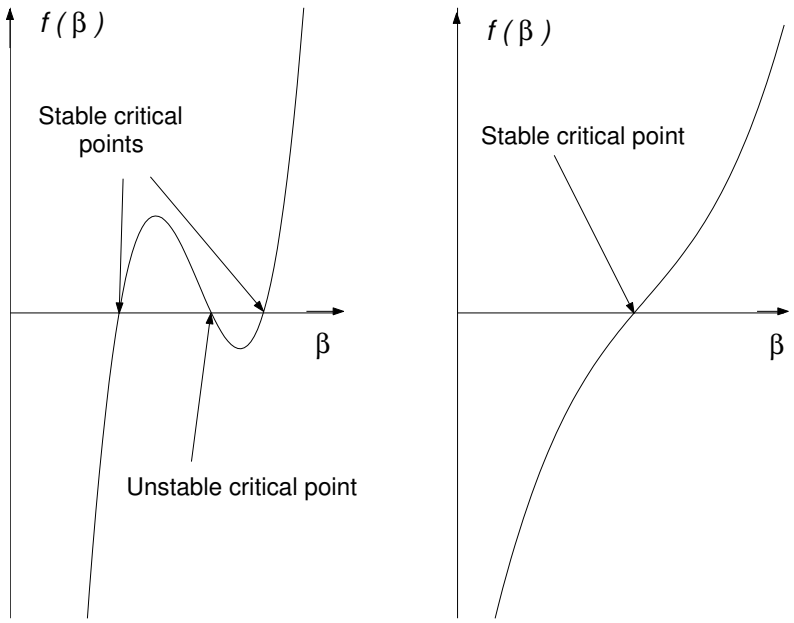

Figure 4.4: The slope of the cubic $f(\beta)$ at roots β_0, and the stability of the corresponding critical point.

the left-hand side of (4.96) are both positive. Conversely, if one or both of these coefficients is negative, then the critical point is unstable.

Using $(4.91)_2$, the first of the requirements for stability, that the coefficient of λ^1 be positive, can be expressed as

$$2F_1 + (F_2 - \alpha_0)G_2/G_1 = 2F_1 + \frac{G_2 F_1 \beta_0}{\tau_d - G_2\beta_0} > 0. \tag{4.97}$$

As we showed above, β_0 must lie in $(0, \tau_d/G_2)$, thus ensuring that this inequality is automatically satisfied.

By re-writing the coefficient of λ^0 in (4.96) and using $(4.91)_2$, the second requirement for stability can be expressed as

$$3G_2^2\beta_0^2 - 4\tau_d G_2\beta_0 + \tau_d^2 + F_1G_1(F_1G_1 + F_2G_2) > 0. \tag{4.98}$$

The left-hand side of this inequality may be recognised as $f'(\beta_0)$, where $f(\beta)$ is the cubic defined in (4.92) and the prime denotes differentiation. Above, we showed that $f'(\beta)$ is positive for large β. There are then two possible cases, illustrated in fig 4.4: If there is a single real root of (4.92), then it corresponds to a stable critical point. If there are three real roots, then two of them (the smallest and the largest) are stable, and the other unstable. Hence, where the cubic equation (4.92) for β_0 has three

roots, two of them correspond to stable critical points. These stable critical points, in turn, correspond to two possible values for $\langle U \rangle_t$. Which of these two values is taken depends on the initial conditions imposed on the ice stream surface bumps d on the local (drumlin) length scale.

The Sliding Law

Having established which critical points of (4.88)–(4.89) are stable, we now wish to investigate how the values of U corresponding to stable critical points depend on driving stress τ_d and ice thickness S.[8] Steady-state solutions of (4.84)–(4.85) yield the following relationship between τ_d and U,

$$\tau_d = G_1 U + \frac{F_1 F_2 G_2 U}{F_1^2 + U^2}. \tag{4.99}$$

This can be re-written as a cubic in U, which may again have one or three real roots, corresponding to one or three real roots of (4.92). The results above on the stability of the fixed points combined with equation (4.87) relating β to U show that, when there are three roots for U, only the largest and smallest ones corresponds to a stable fixed point. When there is only one root of (4.99), it must automatically correspond to a stable fixed point.

This observation finally allows us to construct figure 4.5, where we plot U against τ_d for various choices of S. Where U is multi-valued, the unstable branch of U is shown as a dotted line, while solid lines denote stable branches. Clearly, U is a multi-valued function of driving stress τ_d at sufficiently low values of ice thickness S, as anticipated. In fact, it can be shown from (4.99) and using the definitions (4.86) that this multi-valuedness occurs only for values of $S < 1.1621$. We should reiterate that the multiple-valuedness of the 'sliding law' does not appear in classical sliding theory in the absence of cavitation (section 2.3), as classical sliding theory corresponds to $S \gg 1$ in the present notation. The multi-valued sliding law is thus intrinsically linked with the effect of the upper, free surface of the ice stream on the drag generated by bed obstacles.

If U were a single-valued, increasing function of driving stress $\tau_d = -(D-H)\frac{\partial D}{\partial X}$ at given ice thickness $S = (D-H)$, then the outer problem,

$$\frac{\partial D}{\partial T} + \frac{\partial (D-H)U}{\partial X} = 0, \tag{4.100}$$

[8]Note that, since we are considering values of U evaluated at stable critical points, U in this section can be interpreted as $\langle U \rangle_t$, where we leave out the averaging operator for simplicity.

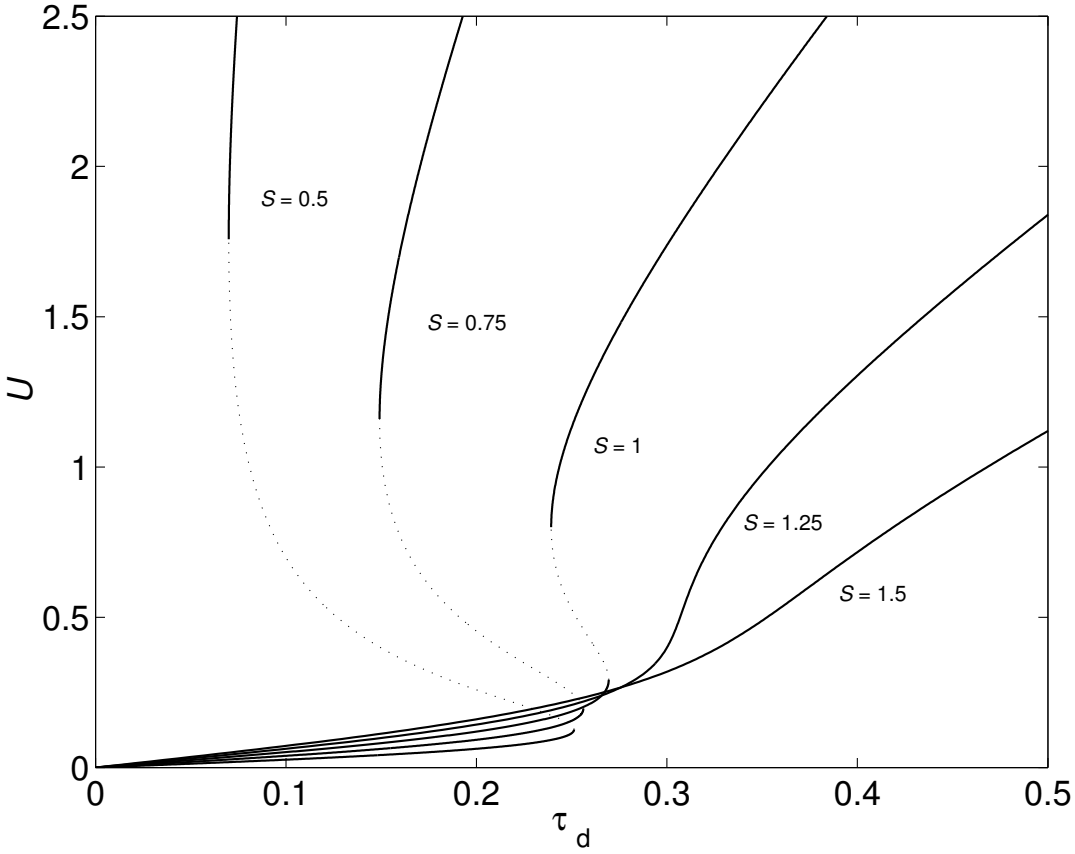

Figure 4.5: Sliding law for sliding over sinusoidal bumps with wavelengths comparable to ice thickness. $S = D - H$ denotes dimensionless ice thickness, scaled such that the period of bed bumps is 2π, while $\tau_d = -(D - H)\frac{\partial D}{\partial X}$ is the driving stress. U denotes the sliding velocity evaluated at critical points of (4.88)–(4.89), here plotted as a function of τ_d at various values of S. A solid line corresponds to stable critical points, while a broken line indicates unstable critical points. Note that the sliding law is multi-valued for $S = 0.5$, 0.75 and 1. Note also that velocities on the 'fast branch' appear to increase as ice thickness is decreased. This presumably occurs because basal obstacles become progressively less effective at generating drag when their wavelengths become large compared with ice thickness.

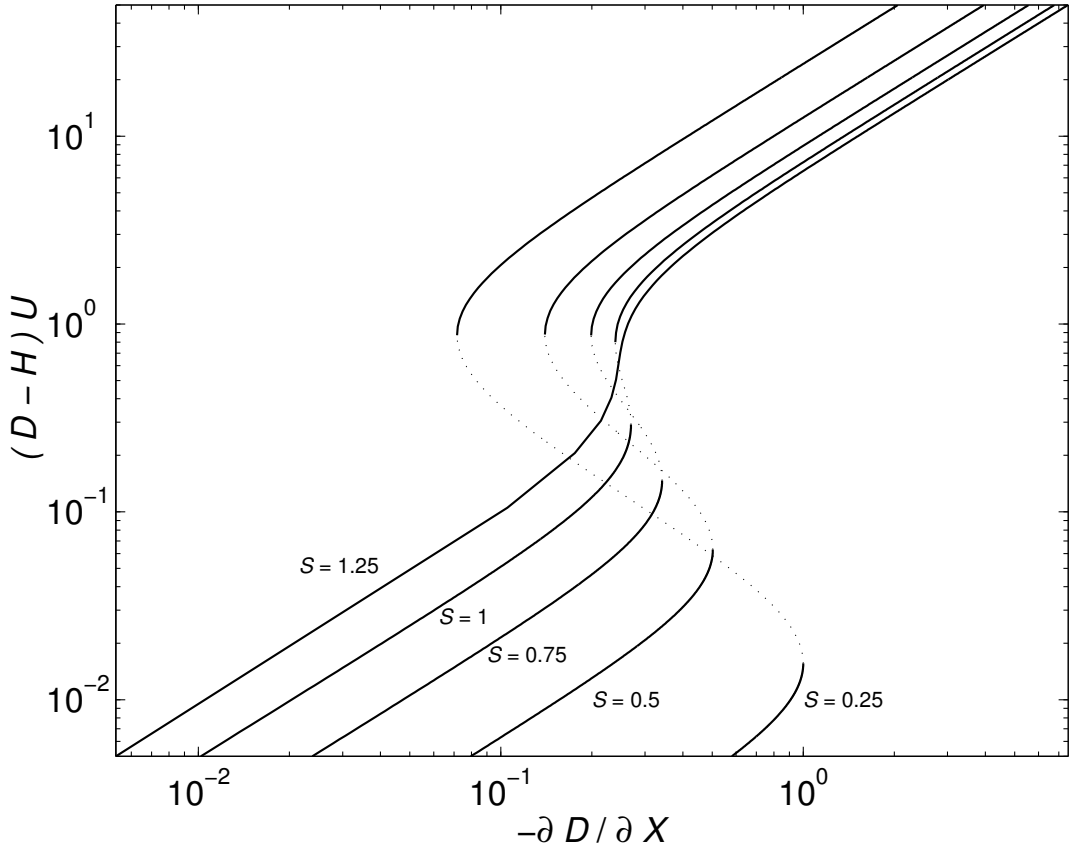

Figure 4.6: Ice flux $(D - H)U = SU$ plotted against (negative) surface slope $-\partial D/\partial X = \tau_d/S$ at various fixed values of S indicated (note the logarithmic scales). As expected, flux is a multi-valued function of surface slope and ice thickness — dotted lines indicate an unstable branch as before. Interestingly, on the fast branches, flux appears to increase at fixed surface slope when ice thickness S is decreased; the opposite is the case for shallow ice theory (cf. equation (2.36)).

would correspond to a nonlinear diffusion equation for ice thickness D, not unlike that obtained from shallow ice theory (see section 2.2, in particular equation (2.37)). Clearly, the multi-valuedness of U represents a significant complication to this picture. We are not able to give an answer here to the question of how the multi-valuedness of the sliding law could affect the dynamics of an ice stream, but this question represents an obvious direction for future research. One may, for instance, wish to investigate whether a multiply-valued sliding law could explain some kind of surging behaviour associated with transitions from a slow to a fast branch of the sliding law. This possibility has been explored previously for glaciers by Fowler (1987b).

A second, curious feature of the of the sliding law constructed here is worth mentioning. In figure 4.6, ice flux $(D - H)U = SU$ is plotted against surface slope

$-\frac{\partial D}{\partial X} = \tau_d/S$ at various fixed values of ice thickness S as indicated. The most notable feature of this plot is that flux appears to increase for a given surface slope as ice thickness S decreases, at least when the 'fast' branch of the flux curve is selected. This differs markedly from shallow ice theory, where flux increases with ice thickness (see equation (2.36)).

A flux which increases with surface slope and decreases with thickness may have a significant effect on surface profiles: Suppose, for instance, that an ice stream with a flat, horizontal bed carries a constant ice flux over some distance in the downstream direction. This might be the case if the ice stream is locally in steady state and there is insignificant accumulation. As the ice stream thins in the downstream direction, a constant flux then requires the surface slope to decrease in the downstream direction. If flux were an increasing function of ice thickness and surface slope, the opposite would be true: A constant flux would then require a steepening of the surface slope as the ice stream thins in the downstream direction.

Typical ice sheets have convex profiles, with the surface slope steepening near the margins. This is clearly in agreement with the predictions of shallow ice theory, where flux decreases with ice thickness. Conversely, ice streams — particularly ones draining into ice shelves — often have concave profiles, with surface slopes decreasing in the downstream direction (Paterson, 1994, chapter 12). It is tempting to suggest that our sliding law could explain this observation. However, in the absence of any concrete evidence that drag due bed obstacles of the type considered here could indeed be responsible for controlling the motion of ice streams (in the sense that they could produce sufficient drag to balance the driving stress at typical, observed flow velocities), this would be pure conjecture.

Finally, we should point out that flux determined by our sliding law does not decrease indefinitely with ice thickness. At large ice thicknesses S, the bulk flow velocity is governed by Nye's (1969) and Kamb's (1970) formula (2.59). In other words, for large S, U is proportional to the driving stress $-S\frac{\partial D}{\partial X}$, and hence flux is proportional to $-S^2\frac{\partial D}{\partial X}$, so flux increases again with S. The anomalous behaviour of flux increasing with decreasing ice thickness thus occurs only when ice thickness is comparable with the wavelengths of the bed obstacles which control drag on the ice stream.

4.6 Discussion

In this chapter, we have presented a discussion of how to deal with the effect of bed obstacles on the flow of an ice stream when the wavelength of these obstacles is comparable to the thickness of ice. To this end, a multiple scales expansion technique was used. This allowed the derivation of an 'inner' problem describing the generation of drag by these basal obstacles; the analogous formulation in classical sliding theory, where bed bumps are assumed to have wavelengths much smaller than the thickness of ice, is Fowler's (1977; 1979; 1981) boundary layer. In the case of a sinusoidal bed, we were able to generate from the inner problem a 'sliding law', relating smoothed ice thickness, smoothed ice surface slope and a time-averaged bulk flow velocity, all of which depend only on the outer variables X and T, and thus to derive a closed 'outer' problem.

The most important feature of this sliding law is that the time-averaged bulk flow velocity $\langle U \rangle_t$ is multi-valued at certain values of driving stress and ice thickness. The precise effect of such a multi-valued sliding law on the dynamics of an ice stream was, however, not discussed and is left for future work.

Whilst this multi-valuedness of the sliding law is an interesting feature, it is not at all clear yet whether obstacles which have wavelengths comparable to ice thickness and realistic amplitudes — comparable to those of drumlins found in deglaciated areas — can indeed generate sufficient drag at realistic sliding velocities to balance the driving stress acting on a typical ice stream. If this is not the case, then the sliding law constructed here has little relevance to real ice streams, and other mechanisms than flow over large obstacles must be responsible for the force balance of a typical ice stream, for instance the lateral shear stresses considered by Raymond (1996). In order to resolve this issue, a more realistic model of ice flow over large obstacles, for instance one in which the rheology of ice is described by Glen's law, must be considered.

Part II

Drumlin Formation

Chapter 5

Hindmarsh's Model

5.1 Introduction

In this part of the thesis, we analyse a particular theory for bedform formation which has been put forward by Hindmarsh (1998a) and studied further by Fowler (2000). There are many other hypotheses for the formation mechanisms of drumlins and similar landforms (Gravenor, 1953; Smalley and Unwin, 1968; Shaw and Freschauf, 1973; Boulton, 1979, 1987; Shaw, 1983; Shaw and Kvill, 1984), which we do not consider in detail here, though we will discuss them further in section 6.4.

Hindmarsh and Fowler's model is based on the concept that drumlins — and indeed, other 'streamlined' subglacial bedforms such as flutes and Rogen moraines — are the result of an instability in the laminar flow of ice over a deformable substrate. The instability mechanism may be summed up as follows: ice flows over a bump on the bed. As in classical hard bed sliding (section 2.3), this leads to a greater compressive normal stress on the upstream face of the bump than on its downstream face. This increases effective pressure in the till upstream of the bump and makes the underlying till less mobile. However, by contrast with classical hard bed sliding, there is no free slip at the interface between ice and bed. Instead it is assumed that there is no significant slip between ice and till and that the basal velocity of the ice is given by shearing in the till. Consequently, to compensate for the underlying till becoming less mobile upstream of the bump, shear stress becomes concentrated there. In turn, increased shear stress causes a higher till flux at the upstream side of the bump compared with the downstream side. More till flows into the bump than out, causing it to grow.

Hindmarsh (1998b) and Fowler (2000) envision that this instability leads to the evolution of bumps of a regular appearance on the interface between the ice and the substrate. Hindmarsh and Fowler formulated their model only in two dimensions,

and were thus unable to make statements about the formation of three-dimensional bedforms such as drumlins; in effect, they could only predict the formation of Rogen moraines. Here, we will consider the extension of their model to three dimensions from the outset. Furthermore, Hindmarsh and Fowler considered only the linear stability of the laminar flow of ice over till. In this thesis, we go on to construct a simplified nonlinear model which may then be solved numerically.

The substrate (or till) is modelled by Hindmarsh (1998b) and Fowler (2000) as an incompressible viscous material whose viscosity depends on effective pressure. As described in section 2.4, this choice of till rheology is not uncontroversial. Here, we persist with a viscous rheology and investigate the effect of changing various rheological parameters which make the viscous rheology more or less similar to a plastic rheology (in particular, we investigate the effect of changing the exponents m and n in the Boulton-Hindmarsh rheology (2.70)).

We should also point out that the assumptions behind Hindmarsh and Fowler's model do not agree with the model of sliding over drumlin-type topography in chapter 4, where drumlins were considered as stationary obstacles. In the present model, drumlins must be able to deform as this is the very process by which they are assumed to evolve. Moreover, the sliding model in chapter 4 assumed that drumlins provide significant 'geometrical' resistance in the same way that small-scale roughness on a hard bed is thought to provide resistance (see section 2.3). By contrast, the present drumlin formation model assumes that the driving stress acting on the ice sheet is balanced by shear stress *at* the bed. This shear stress, in turn, causes the subglacial till layer to deform.

5.2 The Model

We consider the incompressible three-dimensional flow of ice of constant viscosity η over an incompressible viscous till substrate. Let (x, y, z) denote a set of Cartesian coordinates, with the z-axis aligned vertically upwards and the x-axis aligned with the mean flow direction, as shown in figure 5.1. The interface between ice and till will be denoted by $z = s(x, y, t)$, and we suppose that there is no mean bed inclination[1]. We further chose the origin of our coordinate system such that the mean of s is zero. We also assume that the deformable till is underlain by an undeformable substratum at a depth $z = -d$.

[1]In other words, we assume that the ice flow in question is that of an ice sheet, as is appropriate for drumlins, see section 1.2.

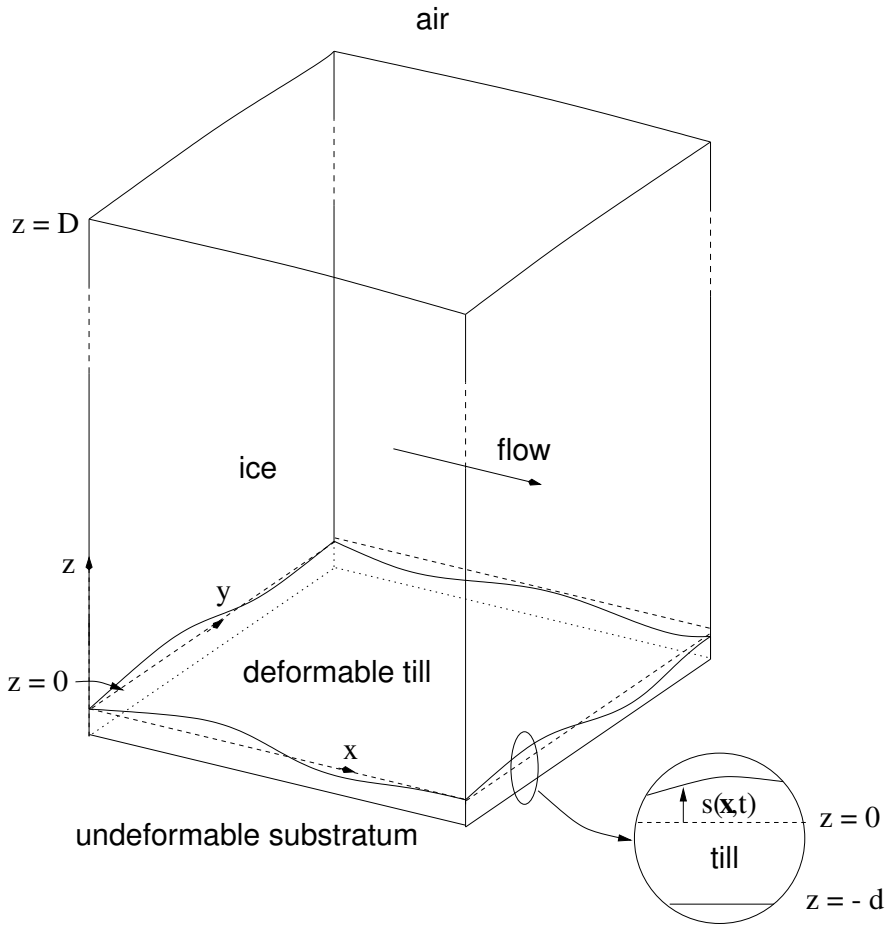

Figure 5.1: Geometry of the problem

Let $\mathbf{u} = (u, v, w)$ and $\boldsymbol{\sigma} = \boldsymbol{\tau} - p\mathbf{I}$ denote velocity and stress fields, respectively, where $\mathbf{u}$ has to be interpreted as the velocity field of the till matrix in $-d < z < s(x, y, t)$ (cf. section 2.4). For $z > s(x, y, t)$, we obtain the usual slow-flow equations

$$\eta\nabla^2\mathbf{u} - \nabla p - \rho_i g\mathbf{k} = \mathbf{0}, \tag{5.1}$$

$$\nabla \cdot \mathbf{u} = 0, \tag{5.2}$$

where ρ_i denotes the density of ice and $\mathbf{k}$ is the z-unit vector. In the till, $-d < z < s(x, y, t)$, we have

$$\nabla \cdot \boldsymbol{\tau} - \nabla p - \rho_b g\mathbf{k} = \mathbf{0}, \tag{5.3}$$

$$\nabla \cdot \mathbf{u} = 0, \tag{5.4}$$

where ρ_b is the bulk density of till, defined by (2.64). To complement (5.3), we define the rheology of till by a viscous relationship of the form

$$\dot{\boldsymbol{\epsilon}} = F(\tau, p_e)\boldsymbol{\tau}/\tau, \qquad \text{on } -d < z < s \tag{5.5}$$

where $\dot{\boldsymbol{\epsilon}}$ is the strain rate tensor, defined in terms of the derivatives of $\mathbf{u}$ by (2.1), τ is the second invariant of the deviatoric stress tensor $\boldsymbol{\tau}$ defined by (2.4) and p_e is the effective pressure defined by (2.69) as

$$p_e = p - p_w, \tag{5.6}$$

where p_w is porewater pressure. As we will see later, the dependence of till rheology on effective pressure is crucial to Hindmarsh's (1998b) and Fowler's (2000) instability model. We follow these two authors in *prescribing* the water pressure in the till rather than modelling it, and put

$$p_w = p_c - \rho_w g z, \tag{5.7}$$

where ρ_w is the density of water and p_c is a constant prescribed by some subglacial hydraulic system (e.g. Walder and Fowler, 1994). We may understand this prescription as follows: at some elevation (which we may take to be $z = 0$), the bed is connected to the subglacial hydraulic system, and water pressure at that elevation is equal to the channel pressure p_c. Above and below this level, water pressure is controlled hydrostatically (which gives zero flux in Darcy's law, (2.67)).[2]

[2]This prescription of porewater pressure differs fundamentally from that in Thorsteinsson and Raymond (2000). These authors assume that porewater pressure in till is determined by diffusion through the till, where hydraulic diffusivity is typically very low — Thorsteinsson and Raymond quote values of the diffusion coefficient of 10^{-7} m^2 s^{-1}. Hence, for a 100 m long bedform, porewater pressure diffusion would take on the order of 3000 years to equilibrate, which is long compared with the instability timescale in our model (the convective timescale for the bedform length, typically on the order of years to decades for ice which is able to slide). The prescription of p_w used here is therefore only feasible if water can flow along the interface between ice and water as well as through the till itself.

As boundary conditions, we prescribe the following: at the base of the till, there is no slip and so

$$\mathbf{u} = \mathbf{0} \qquad \text{on } z = -d. \tag{5.8}$$

At the ice-till interface, normal and shear stresses must match. Noting that the stress tensor $\boldsymbol{\sigma} = 2\eta\dot{\boldsymbol{\epsilon}} - p\mathbf{I}$ in the ice, we express this boundary condition as

$$[\boldsymbol{\sigma}\mathbf{n}]^+_- = \mathbf{0} \qquad \text{on } z = s(x, y, t) \tag{5.9}$$

where the notation $[\,]^+_-$ denotes the difference of the bracketed expression above and below the interface, i.e.

$$\boldsymbol{\sigma}^+ = \lim_{z \to s^+} \boldsymbol{\sigma}, \qquad \boldsymbol{\sigma}^- = \lim_{z \to s^-} \boldsymbol{\sigma}, \qquad [\boldsymbol{\sigma}\mathbf{n}]^+_- = \left(\boldsymbol{\sigma}^+ - \boldsymbol{\sigma}^-\right)\mathbf{n}. \tag{5.10}$$

$\mathbf{n}$ is the unit normal to the interface

$$\mathbf{n} = \frac{\mathbf{k} - \nabla_{\mathbf{x}} s}{\left(1 + |\nabla_{\mathbf{x}} s|^2\right)^{1/2}}, \tag{5.11}$$

where we use the notation $\nabla_{\mathbf{x}} = (\frac{\partial}{\partial x}, \frac{\partial}{\partial y}, 0)$.

Furthermore, we suppose that there is no slip between ice and till at the interface, so

$$[\mathbf{u}]^+_- = \mathbf{0} \qquad \text{on } z = s(x, y, t). \tag{5.12}$$

This is likely to be wrong in practice (in the sense that there probably will be some slip given by a variant of a hard-bed sliding law), but as we will find later, this is unlikely to be of any consequence. $s(x, y, t)$ itself satisfies a kinematic boundary condition

$$\frac{\partial s}{\partial t} + u\frac{\partial s}{\partial x} + v\frac{\partial s}{\partial y} = w \qquad \text{on } z = s(x, y, t), \tag{5.13}$$

where we ignore any entrainment or deposition of till from the ice. By depth integration of (5.4), (5.13) can be reduced to the form

$$\frac{\partial s}{\partial t} + \nabla_{\mathbf{x}} \cdot \mathbf{q} = 0 : \qquad \mathbf{q} = (q_x, q_y) = \int_{-d}^{s(x,y,t)} (u, v)\,\mathrm{d}z. \tag{5.14}$$

It remains to fix boundary conditions at some upper boundary for the ice. We could proceed as in chapter 4 and consider the upper surface of the ice explicitly. As in Hindmarsh's (1998b) and Fowler's (2000) papers, we eschew the greater generality of this approach and assume that the instability length scale to be derived below is much smaller than the ice thickness D (cf. fig. 5.1). By analogy with Fowler (2000), we assume that this allows us to prescribe boundary conditions of the form

$$\eta\frac{\partial u}{\partial z} \sim \bar{\tau}, \qquad \eta\frac{\partial v}{\partial y} \sim 0, \qquad p - \rho_i g(D - z) \sim 0, \qquad \text{as } z \to \infty, \tag{5.15}$$

where $\bar{\tau}$ is some applied 'driving' stress in the x-direction. Fowler (1979, 1981) has shown how such boundary conditions can in principle arise in the classical theory of hard-bed sliding as a result of asymptotic matching between a basal ice flow over local topography and an outer flow describing the bulk motion of the ice sheet (see also appendix A). Here, we do not attempt to derive the boundary conditions (5.15) by a matching procedure, but simply use them by analogy with the case of classical sliding.

In addition to the boundary conditions above, we also demand for definiteness that the bed s and velocity and stress fields be periodic in both x- and y-directions with some arbitrary periods a_x and a_y, respectively.

The model which we have set out so far is the basically the same (though written in 3-D) as those in Hindmarsh (1998b) and Fowler (2000); these two authors pre-empt the subsequent development of the theory somewhat by assuming that (5.3) can be integrated as a simple shearing flow. Such a reduction is clearly desirable as the full free-boundary problem for coupled ice-till flow above is rather complicated and it is difficult to see exactly how the instability mechanism works. A numerical solution of the full model is also likely to be an onerous task.

We will outline the approximation behind the reduction of the till flow problem to a simple shearing flow in more detail below. As a first step, we identify relevant scales and non-dimensionalise the model.

5.3 Non-Dimensionalisation

We choose the following scales: $[s]$ for variations in ice-till interface elevation, $[x]$ as the horizontal length scale associated with the instability, $[t]$ as the corresponding time scale, $[u_b]$ for till shearing ('sliding') velocity, $[q]$ for till flux, $[w]$ for velocity variations in the ice, $[\tau]$ for deviatoric stresses and $[p_e]$ for effective pressure.

Crucial to the instability model is the interaction between the geometry and movement of the interface s and velocity variations in the ice, which, in turn, cause stress variations. The latter then affect the till flux and hence can lead to the growth of relief, as described in section 5.1. We assume therefore that all terms in (5.13) and hence in (5.14) balance, and so

$$[s]/[t] = [u_b][s]/[x] = [w] = [q]/[x]. \tag{5.16}$$

For a limited thickness of available till and a distributed shearing profile in the till, we may also put from $(5.14)_2$

$$[q] = [u_b]d. \tag{5.17}$$

As we will see later, this may need to be amended when the till rheology in (5.5) is highly non-linear, or when the available till is very thick. For now, we may see that (5.16)–(5.17) imply $[s] = d$.

A typical effective pressure $\bar{p}_e$ may be defined as

$$\bar{p}_e = \rho_i g D - p_c. \tag{5.18}$$

We will assume that this is comparable to the driving stress $\bar{\tau}$; if $\bar{p}_e$ were much larger than the driving stress $\bar{\tau}$ — for instance as a result of drainage pressure p_c being too low — we would not expect any significant till deformation to occur. In particular, if till does have a yield stress of the form (2.72) with $\mu = O(1)$, then there will be no till deformation unless $\bar{\tau}/\bar{p}_e = O(1)$. Consequently, we assume that deviatoric stresses in the ice and till, as well as effective pressure, scale with $\bar{\tau}$. But a typical deviatoric stress $[\tau]$ in the ice can be related to a typical strain rate[3] $[w]/[x]$ through the viscosity of ice, and so we put

$$[\tau] = \eta[w]/[x] = \bar{\tau} = [p_e]. \tag{5.19}$$

Furthermore, we anticipate that the till deforms in approximately simple shear, and define the till velocity scale $[u_b]$ as

$$[u_b] = \int_{-d}^{0} 2F(\bar{\tau}, \bar{p}_e - (\rho_b - \rho_w)z)\,\mathrm{d}z, \tag{5.20}$$

where F defines the viscous rheology of till in (5.5). This definition of $[u_b]$ may not seem entirely straightforward at first sight, but it does ensure that the dimensionless velocity of the ice-till interface is unity when the bed is flat everywhere, i.e. when $s \equiv 0$.

(5.16)–(5.20) define eight scale relations for the eight scales we have defined. The horizontal instability length scale $[x]$ can be expressed as

$$[x] = (\eta d[u_b]/\bar{\tau})^{1/2} \tag{5.21}$$

where the till shearing velocity $[u_b]$ is given by (5.20). Crucial to our reduction of the till flow to a simple shearing flow will be the assumption that it is a shallow flow, and hence that

$$\nu \doteq \frac{d}{[x]} = \frac{[w]}{[u_b]} \ll 1 \tag{5.22}$$

[3] $[w]/[x]$ corresponds to the strain rate induced in the ice by flow over bed bumps, which generates the instability.

We can ascertain that this is likely to be the case by inserting a few typical values for $\bar{\tau}$, η and d into (5.21). Using[4] $\bar{\tau} = 5{\times}10^4$ Pa, $\eta = 3{\times}10^{13}$ Pa s, $d = 10$ m,

$$\bar{\tau}d/\eta = 1.7 \times 10^{-8}\,\mathrm{m\,s^{-1}} = 0.5\,\mathrm{m\,a^{-1}}$$

Hence it should suffice to have $[u_b] \gg 0.5$ m a^{-1} in order to ensure that ν is small. This is likely to be the case when till deformation is the case, but one should bear in mind that it is difficult to provide a reliable value for the till shearing velocity scale $[u_b]$ — and hence for the length scale $[x]$ — partly because till rheology is badly constrained (see section 2.4).[5] The obvious temptation to tune $[u_b]$ so as to produce a desired value for the bedform length scale $[x]$ must therefore be resisted. Nevertheless, it should be pointed out that it is possible to obtain reasonable values of $[x]$ for reasonable choices of $[u_b]$: for a relatively fast sliding velocity $[u_b] = 100$ m a^{-1}, (5.21) together with the estimates above yields a length scale

$$[x] = 140\,\mathrm{m},$$

which, although quite short, could be seen as a realistic length scale for a subglacial bedform.

We may further note from (5.22) that a shallow bed implies that till shearing or 'sliding' velocities $[u_b]$ are much larger than velocity variations $[w]$ in the ice. This is also the case in classical hard bed sliding with small bed slopes (see appendix (A)). It will therefore come as no surprise that the reduced model derived in section 5.4 bears strong similarities with the equations encountered in classical sliding theory. The main difference between the present model and classical hard bed sliding is that no solution exists in classical hard bed sliding theory when the bed is flat, whereas in the present case, a flat bed corresponds to a simple shearing flow in both, ice and till.

Since we expect the geometry of the till flow to be shallow as a consequence of $\nu \ll 1$, but the geometry of the ice flow not to be shallow, we scale vertical coordinates, velocity and stress fields differently for $z < s$ and $z > s$. Dimensionless horizontal coordinates and time and surface elevation are defined globally

$$(x, y) = [x](x^\star, y^\star), \qquad t^\star = [t]t^\star, \qquad s = [s]s^\star. \tag{5.23}$$

[4]The value of the viscosity η used here is obtained by substituting $\bar{\tau} = 5{\times}10^4$ Pa in the Glen's law estimate $\eta = 1/(2A\bar{\tau}^{n-1})$ with $n = 3$ and $A = 6{\times}10^{-24}$ Pa^{-3} s^{-1}.

[5]The equivalent of saying that $[u_b]$ is badly constrained is to say that the constant K in the Boulton-Hindmarsh rheologies (2.71)–(2.72) is badly constrained. As pointed out by Hooke and others (1997), the data fitting performed by Boulton and Hindmarsh (1987) cannot be taken to provide reliable data regarding rheological parameters.

For the till flow $-d < z < s$, we define the following scaled variables:

$$z = dZ^\star, \qquad (u, v) = [u_b](U^\star, V^\star), \qquad w = [w]W^\star, \qquad \mathbf{q} = [q]\mathbf{q}^\star, \tag{5.24}$$

$$p = [p_e]p_e^\star + p_w, \qquad \tau = [\tau]\tau^\star, \qquad F(\tau, p_e) = ([u_b]/2d)F^\star(\tau^\star, p_e^\star) \tag{5.25}$$

$$\tau_{xz} = [\tau]\tau_{xz}^\star, \qquad \tau_{yz} = [\tau]\tau_{yz}^\star, \tag{5.26}$$

$$\tau_{xy} = \nu[\tau]\tau_{xy}, \qquad \tau_{xx} = \nu[\tau]\tau_{xx}^\star, \qquad \tau_{yy} = \nu[\tau]\tau_{yy}^\star, \qquad \tau_{zz} = \nu[\tau]\tau_{zz}^\star \tag{5.27}$$

For the ice flow, $z > s$, we first define a 'sliding' component $\bar{\mathbf{U}}^\star$ of the velocity field (see also chapter 4 and appendix A) as

$$[u_b]\bar{\mathbf{U}}^\star(t^\star) = \frac{1}{a_x a_y}\int_0^{a_x}\int_0^{a_y}(u, v)|_{z=s(x,y,t)}\,\mathrm{d}y\,\mathrm{d}x. \tag{5.28}$$

This allows us to write

$$z = [x]z^\star, \tag{5.29}$$

$$\mathbf{u} = [u_b]\bar{\mathbf{U}}^\star + [w](\mathbf{u}^\star + \mathbf{i}z), \qquad p = \rho_i g(D - z) + [\tau]p^\star, \tag{5.30}$$

where $\mathbf{i}$ is the x-unit vector. The decomposition of velocity in (5.30) is somewhat elaborate, but does lead to simplifications later: $\bar{\mathbf{U}}^\star$ can be thought of as a sliding component, $\mathbf{i}z$ is a shearing term which accounts for the shear stress applied at infinity, and $\mathbf{u}^\star = (u^\star, v^\star, w^\star)$ denotes the residual term describing non-laminar velocity variations. We should emphasise that the sliding component $\bar{\mathbf{U}}^\star$ depends on time t, but not on position (x, y, z).

The scaled model contains four dimensionless parameters, ν defined in (5.22), and

$$\bar{N}^\star = \frac{\bar{p}_e}{\bar{\tau}}, \qquad \alpha = \frac{(\rho_b - \rho_w)gd}{\bar{\tau}}, \qquad \beta = \frac{(\rho_w - \rho_i)gd}{\bar{\tau}}. \tag{5.31}$$

As stated previously, we will assume that $\nu \ll 1$ and $\bar{N}^\star = O(1)$. For the typical values of $\bar{\tau} = 5{\times}10^4$ Pa, $d = 10$ m, and for densities $\rho_b = 2000$ kg m^{-3}, $\rho_w = 1000$ kg m^{-3}, $\rho_i = 900$ kg m^{-3}, we obtain

$$\alpha = 1, \qquad \beta = 0.1.$$

We see that we may realistically treat α as an $O(1)$ parameter; we will also retain β for the time being (though Fowler (2000) effectively sets $\beta = 0$, see comments after his equation (31)). We may note that

$$\beta = \frac{\rho_w - \rho_i}{\rho_b - \rho_w}\alpha. \tag{5.32}$$

With the typical densities above, we have $\beta = 0.1\alpha$, i.e. β will always be small compared with α. Physically, α can be interpreted as measuring the hydrostatic increase in effective pressure with depth in the till, compared with stress variations at the ice-till interface. β measures the hydrostatic increase in effective pressure at the ice-till interface due to increases in the elevation of the interface.

5.3.1 Scaled Equations

Omitting asterisks, we obtain the following field equations for the ice flow

$$\nabla^2 \mathbf{u} - \nabla p = \mathbf{0} \qquad \text{on } z \in (\nu s, \infty), \tag{5.33}$$

$$\nabla \cdot \mathbf{u} = 0 \qquad \text{on } z \in (\nu s, \infty). \tag{5.34}$$

For the till $-1 < Z < s$, we obtain

$$\frac{\partial \tau_{xz}}{\partial Z} + \nu^2 \frac{\partial \tau_{xy}}{\partial y} + \nu^2 \frac{\partial \tau_{xx}}{\partial x} - \nu \frac{\partial p_e}{\partial x} = 0, \tag{5.35}$$

$$\frac{\partial \tau_{yz}}{\partial Z} + \nu^2 \frac{\partial \tau_{xy}}{\partial x} + \nu^2 \frac{\partial \tau_{yy}}{\partial y} - \nu \frac{\partial p_e}{\partial y} = 0, \tag{5.36}$$

$$\nu \frac{\partial \tau_{zz}}{\partial Z} + \nu \frac{\partial \tau_{xz}}{\partial x} + \nu \frac{\partial \tau_{yz}}{\partial y} - \frac{\partial p_e}{\partial Z} - \alpha = 0, \tag{5.37}$$

$$\frac{\partial U}{\partial x} + \frac{\partial V}{\partial y} + \frac{\partial W}{\partial Z} = 0, \tag{5.38}$$

where

$$\frac{\partial U}{\partial Z} + \nu^2 \frac{\partial W}{\partial x} = F(\tau, p_e)\tau_{xz}/\tau, \qquad \frac{\partial V}{\partial Z} + \nu^2 \frac{\partial W}{\partial y} = F(\tau, p_e)\tau_{yz}/\tau,$$

$$\frac{\partial U}{\partial y} + \frac{\partial V}{\partial x} = F(\tau, p_e)\tau_{xy}/\tau, \qquad 2\frac{\partial U}{\partial x} = F(\tau, p_e)\tau_{xx}/\tau, \tag{5.39}$$

$$2\frac{\partial V}{\partial y} = F(\tau, p_e)\tau_{yy}/\tau, \qquad 2\frac{\partial W}{\partial Z} = F(\tau, p_e)\tau_{zz}/\tau, \tag{5.40}$$

and

$$\tau = \left[\tau_{xz}^2 + \tau_{yz}^2 + \nu^2 \left(\tau_{xx}^2 + \tau_{yy}^2 + \tau_{zz}^2 + 2\tau_{xy}^2\right)/2\right]^{1/2}. \tag{5.41}$$

Boundary conditions may be written as follows: At the base of the till $Z = -1$, velocity vanishes

$$(U, V, W) = \mathbf{0}. \tag{5.42}$$

At the ice-till interface $z = \nu s$, $Z = s$, stresses match as required by (5.9),

$$\tau_{xz} + \nu^2 \left[\frac{\partial s}{\partial x}(p_e - \tau_{xx}) - \frac{\partial s}{\partial y}\tau_{xy}\right] =$$

$$1 + \frac{\partial u}{\partial z} + \frac{\partial w}{\partial x} + \nu \left[\frac{\partial s}{\partial x}\left(p - 2\frac{\partial w}{\partial z}\right) - \frac{\partial s}{\partial y}\left(\frac{\partial u}{\partial y} + \frac{\partial v}{\partial x}\right)\right], \tag{5.43}$$

$$\tau_{yz} + \nu^2 \left[\frac{\partial s}{\partial y}(p_e - \tau_{yy}) - \frac{\partial s}{\partial x}\tau_{xy}\right] =$$

$$\frac{\partial v}{\partial z} + \frac{\partial w}{\partial y} + \nu\left[\frac{\partial s}{\partial y}\left(p - 2\frac{\partial w}{\partial z}\right) - \frac{\partial s}{\partial x}\left(\frac{\partial u}{\partial y} + \frac{\partial v}{\partial x}\right)\right], \tag{5.44}$$

$$-p_e + \bar{N} + \beta s + \nu\left[\tau_{zz} - \frac{\partial s}{\partial x}\tau_{xz} - \frac{\partial s}{\partial y}\tau_{yz}\right] =$$

$$-p + 2\frac{\partial w}{\partial z} - \nu\left[\frac{\partial s}{\partial x}\left(\frac{\partial u}{\partial z} + \frac{\partial w}{\partial x}\right) + \frac{\partial s}{\partial y}\left(\frac{\partial v}{\partial z} + \frac{\partial w}{\partial y}\right)\right]. \tag{5.45}$$

Velocities also match at the interface, and so

$$(U, V) = \bar{\mathbf{U}} + \nu(u, v), \qquad W = w, \qquad \text{on } z = \nu s,\ Z = s. \tag{5.46}$$

The interface itself evolves according to (5.13), which is re-cast in dimensionless terms as

$$\frac{\partial s}{\partial t} + U\frac{\partial s}{\partial x} + V\frac{\partial s}{\partial y} = W, \qquad \text{on } Z = s, \tag{5.47}$$

while the depth-integrated form (5.14) becomes

$$\frac{\partial s}{\partial t} + \nabla_{\mathbf{x}} \cdot \mathbf{q} = 0 : \qquad \mathbf{q} = \int_{-1}^{s} (U, V)\, \mathrm{d}Z. \tag{5.48}$$

Boundary conditions at infinity for the ice flow are

$$\frac{\partial u}{\partial z} \sim 0, \qquad \frac{\partial v}{\partial z} \sim 0, \qquad p \sim 0, \qquad \text{as } z \to \infty. \tag{5.49}$$

In the next section, we construct a reduced model by ignoring terms of $O(\nu)$ on the basis that $\nu \ll 1$. This not only reduces the till flow problem to a simple shearing flow which can be integrated straightforwardly, but also simplifies the ice flow problem somewhat, a fact overlooked by Hindmarsh (1998b) and Fowler (2000).

5.4 A Reduced Model

We proceed by ignoring terms of $O(\nu)$ in the scaled equations (5.33)–(5.49). In view of the *ad hoc* approximations made by Fowler (2000), it is not immediately obvious that the model which we obtain is still consistent with Fowler's formulation. As we will see later, the dispersion relation obtained from a linear stability analysis of our model agrees with that obtained by Fowler, and hence we can be confident that the reduced model below is indeed consistent with Fowler's model and captures the same instability mechanism. Comparison with Hindmarsh's (1998b) results is more difficult because Hindmarsh performs a linear stability analysis on his model numerically. We will return to this point below.

The advantage of our approach over Hindmarsh's and Fowler's is that we are able to carry out approximations consistently, without the need to make *ad hoc* assumptions. Furthermore, by ignoring terms of $O(\nu)$ throughout, we are able to show that the assumption of a shallow bed, which is crucial to the reduction of the till flow to a simple shearing flow, also simplifies the ice flow problem. This ultimately allows us to study a simplified nonlinear problem.

The first observation to make is that the ice flow domain is reduced at leading order to the half space $z > 0$. Field equations take the form

$$\nabla^2 \mathbf{u} - \nabla p = \mathbf{0}, \qquad \text{on } z \in (0, \infty), \tag{5.50}$$

$$\nabla \cdot \mathbf{u} = 0, \qquad \text{on } z \in (0, \infty). \tag{5.51}$$

The till flow reduces to a simple shearing flow as explained before, i.e.

$$\frac{\partial \tau_{xz}}{\partial Z} = \frac{\partial \tau_{yz}}{\partial Z} = 0, \qquad \text{on } Z \in (-1, s), \tag{5.52}$$

$$\frac{\partial p_e}{\partial Z} = -\alpha, \qquad \text{on } Z \in (-1, s). \tag{5.53}$$

We omit the mass conservation equation (5.38) here as it has already been used to derive (5.48) and will no longer be needed in our leading-order model. The relationship (5.39)–(5.41) between strain rate and deviatoric stress may now be approximated as

$$\frac{\partial U}{\partial Z} = F(\tau, p_e)\tau_{xz}/\tau, \qquad \frac{\partial V}{\partial Z} = F(\tau, p_e)\tau_{yz}/\tau, \qquad \tau = \left(\tau_{xz}^2 + \tau_{yz}^2\right)^{1/2}. \tag{5.54}$$

Boundary conditions at the base of the till are

$$U = V = 0, \qquad \text{on } Z = -1 \tag{5.55}$$

where we again omit the corresponding relation for W as it is no longer needed. Stress continuity at the ice-till interface becomes

$$\tau_{xz} = 1 + \frac{\partial u}{\partial z} + \frac{\partial w}{\partial x}, \qquad \tau_{yz} = \frac{\partial v}{\partial z} + \frac{\partial w}{\partial y}, \qquad p_e = \bar{N} + \beta s + p - 2\frac{\partial w}{\partial Z}, \qquad \text{on } Z = s,\ z = 0. \tag{5.56}$$

Continuity of velocity at the interface (5.46) may be expressed as, using (5.47) and (5.48),

$$(U, V) = \bar{\mathbf{U}}(t), \qquad w = \bar{\mathbf{U}} \cdot \nabla_{\mathbf{x}} s - \nabla_{\mathbf{x}} \cdot \mathbf{q}, \qquad \text{on } Z = s,\ z = 0, \tag{5.57}$$

where we have stated explicitly that the sliding velocity $\bar{\mathbf{U}}$ does not depend on position (x, y). Till flux $\mathbf{q}$ satisfies

$$\mathbf{q} = \int_{-1}^{s} (U, V)\, \mathrm{d}Z, \tag{5.58}$$

and the ice-till interface s evolves as

$$\frac{\partial s}{\partial t} + \nabla_{\mathbf{x}} \cdot \mathbf{q} = 0. \tag{5.59}$$

Furthermore, boundary conditions at infinity for the ice flow are

$$\frac{\partial u}{\partial z} \sim 0, \qquad \frac{\partial v}{\partial z} \sim 0, \qquad p \sim 0, \qquad \text{as } z \to \infty. \tag{5.60}$$

In the following two sections 5.4.1 and 5.4.2 we consider how the till and ice flow problems can be simplified further.

5.4.1 Till Flow

If we define a two-dimensional interfacial shear stress vector $\boldsymbol{\tau_b}$ and effective pressure[6] N as

$$\boldsymbol{\tau_b} = \left(1 + \frac{\partial u}{\partial z} + \frac{\partial w}{\partial x}, \frac{\partial v}{\partial z} + \frac{\partial w}{\partial y}\right), \qquad \text{on } z = 0, \tag{5.61}$$

$$N = \bar{N} + \beta s + p - 2\frac{\partial w}{\partial z}, \qquad \text{on } z = 0, \tag{5.62}$$

then the till flow problem (5.52)–(5.56) may be integrated to give

$$p_e = N + \alpha(s - z), \tag{5.63}$$

$$(U, V) = \frac{\boldsymbol{\tau_b}}{|\boldsymbol{\tau_b}|} \int_{-1}^{Z} F\left(|\boldsymbol{\tau_b}|, N + \alpha(s - Z')\right) \mathrm{d}Z'. \tag{5.64}$$

For simplicity, we will in future put $|\boldsymbol{\tau_b}| = (\tau_{xz}^2 + \tau_{yz}^2)^{1/2} = \tau_b$. (5.64) allows us to write continuity of horizontal velocity components at the interface, equation (5.57), as

$$\bar{\mathbf{U}} = (U, V)|_{Z=s} = \frac{\boldsymbol{\tau_b}}{\tau_b} \int_{-1}^{s} F(\tau_b, N + \alpha(s - Z'))\, \mathrm{d}Z' =$$

$$\frac{\boldsymbol{\tau_b}}{\tau_b} \int_{0}^{1+s} F(\tau_b, N + \alpha\xi)\, \mathrm{d}\xi \doteq u_b(\tau_b, N, s)\boldsymbol{\tau_b}/\tau_b, \tag{5.65}$$

where $\xi = s - Z'$ and the sliding velocity u_b is defined by the last equality,

$$u_b(\tau_b, N, s) = \int_{0}^{1+s} F(\tau_b, N + \alpha\xi)\, \mathrm{d}\xi. \tag{5.66}$$

Note that our choice of scale $[u_b]$ in (5.20) ensures that the dimensionless velocity at the ice-till interface in simple shear is $u_b(1, \bar{N}, 0) = 1$.

[6] Note that N is now a *local* effective pressure; the equivalent in chapter 3 would be $N_{loc}(x)$. We omit the subscript $_{loc}$ for simplicity here.

Similarly, till flux can be calculated from (5.64) and (5.58) as

$$\mathbf{q} = \frac{\boldsymbol{\tau_b}}{\tau_b} \int_{-1}^{s} \int_{-1}^{Z''} F(\tau_b, N + \alpha(s - Z')\,\mathrm{d}Z'\,\mathrm{d}Z'' = \frac{\boldsymbol{\tau_b}}{\tau_b} \int_{1+s}^{0} \int_{1+s}^{\xi} F(\tau_b, N + \alpha\zeta)\,\mathrm{d}\zeta\,\mathrm{d}\xi$$

$$= \frac{\boldsymbol{\tau_b}}{\tau_b} \int_{0}^{1+s} \xi F(\tau_b, N + \alpha\xi)\,\mathrm{d}\xi \doteq q_b(\tau_b, N, s)\boldsymbol{\tau_b}/\tau_b, \tag{5.67}$$

where $\xi = s - Z''$ and $\zeta = s - Z'$. The penultimate equality follows by exchanging the order of integration, whilst the last equality defines the till flux $q_b(\tau_b, N, s)$,

$$q_b(\tau_b, N, s) = \int_{0}^{1+s} \xi F(\tau_b, N + \alpha\xi)\,\mathrm{d}\xi. \tag{5.68}$$

For a given bed $s(x, y, t)$ and small bed slopes $\nu \ll 1$, the till flow problem can thus be solved explicitly once the interfacial shear stress $\boldsymbol{\tau_b}$ and effective pressure N are known. In particular, we are able to derive expressions (5.66) and (5.68) for the sliding velocity u_b and till flux q_b.[7] Note that u_b depends on the same variables τ_b and N as the sliding velocity obtained from classical hard-bed sliding models (see section 2.3 and chapter 3). We may thus suppose that if there is slip at ice-till interface which is controlled by the same processes which control sliding over hard beds, then the reduced model for coupled ice-till flow should not change significantly. In the case of interfacial slip at a rate $u_s(\tau_b, N)$, we would expect simply to change the definition of u_b above to

$$u_b(\tau_b, N, s) = u_s(\tau_b, N) + \int_{0}^{1+s} F(\tau_b, N + \alpha\xi)\,\mathrm{d}\xi. \tag{5.69}$$

Having obtained expressions for till flux and sliding velocity, our aim is ultimately to solve the evolution equation (5.59), which requires us to determine $\mathbf{q}$ for a given bed s; hence we need to find $\boldsymbol{\tau_b}$ and N for a given bed s. This is achieved by solving the ice flow problem.

5.4.2 Ice Flow

The ice flow is described by the elliptic field equations (5.50)–(5.51) together with boundary conditions (5.57) and (5.60). Using the definitions and results in section 5.4.1 above, these can be written as

$$\nabla^2\mathbf{u} - \nabla p = \mathbf{0}, \qquad \text{on } z \in (0, \infty) \tag{5.70}$$

[7] Such expressions for sliding velocity and till flux as functions of basal shear stress, effective pressure and till thickness have been derived before (e.g. Alley, 1989); what is new here is that we have derived the approximation underlying the assumption of a simple shearing flow — Hindmarsh's (1998b) 'hydrostatic thin till approximation' — in a way which treats the ice flow problem consistently.

$$nabla \cdot \mathbf{u} = 0 \qquad \text{on } z \in (0, \infty) \tag{5.71}$$

$$w = \bar{\mathbf{U}} \cdot \nabla_{\mathbf{x}} s - \nabla_{\mathbf{x}} \cdot \mathbf{q}, \qquad u_b(\tau_b, N, s)\boldsymbol{\tau_b}/\tau_b = \bar{\mathbf{U}}(t), \qquad \text{on } z = 0, \tag{5.72}$$

$$\frac{\partial u}{\partial z} \sim 0, \qquad \frac{\partial v}{\partial z} \sim 0, \qquad p \sim 0, \qquad \text{as } z \to \infty, \tag{5.73}$$

where

$$\boldsymbol{\tau_b} = \left(1 + \frac{\partial u}{\partial z} + \frac{\partial w}{\partial x}, \frac{\partial v}{\partial z} + \frac{\partial w}{\partial y}\right), \qquad \tau_b = |\boldsymbol{\tau_b}|, \qquad \text{on } z = 0, \tag{5.74}$$

$$N = \bar{N} + \beta s + p - 2\frac{\partial w}{\partial z}, \qquad \text{on } z = 0, \tag{5.75}$$

$$\mathbf{q} = q_b(\tau_b, N, s)\boldsymbol{\tau_b}/\tau_b. \tag{5.76}$$

We may compare the present model with the classical Nye-Kamb model for hard bed sliding (section 2.3). The field equations are identical (though the version of Nye-Kamb theory written down in section 2.3 is two-dimensional, whilst we are dealing with three dimensions here), and boundary conditions (5.73) at infinity are equivalent to (2.55).[8]

The boundary condition $(5.72)_1$ is similar to $(2.54)_1$; the novelty here is that the bed is able to evolve and that this leads to the term $-\nabla_{\mathbf{x}} \cdot \mathbf{q}$ appearing. This represents a significant complication compared with the 'classical' model as $\mathbf{q}$ is a function, defined in terms of till rheology by (5.67), of $\boldsymbol{\tau_b}$ and N defined in (5.74)–(5.75); $(5.72)_1$ is thus a nonlinear boundary condition relating shear stress, normal stress and the vertical velocity component w on the boundary.

Boundary condition $(5.72)_2$ is the equivalent of $(2.54)_2$, though we again see a significant complication. Whilst local shear stress at the bed vanishes in Nye-Kamb theory, it is here constrained such that the sliding velocity $u_b(\tau_b, N, s)\boldsymbol{\tau_b}/\tau_b$ is everywhere equal to a value $\bar{\mathbf{U}}(t)$ which does not depend on position (x, y) but may change with time and is unknown *a priori*. This boundary condition arises because the velocity with which the bulk of the ice moves scales with $[u_b]$, which is much larger than the typical velocity variations $[w]$ in the ice. Consequently, the velocity with which ice at the interface moves is approximately independent of position (i.e. $\bar{\mathbf{U}}(t)$ is a function of time only), and this forces the stress field at the interface to adjust such that $u_b\boldsymbol{\tau_b}/\tau_b$ is independent of position.

[8]This requires some careful examination; the Neumann conditions $(5.73)_{1,2}$ state merely that u and v should approach constant values as $z \to \infty$. In order to conclude that the Dirichlet conditions $u, v \sim 0$ hold, we need to use the definition of $\bar{\mathbf{U}}$ in (5.28), which requires $\int_0^{a_x}\int_0^{a_y}(u, v)\,\mathrm{d}y\,\mathrm{d}x/(a_x a_y) = 0$ on $z = 0$ in our leading-order model. This is sufficient to fix $u, v \sim 0$ as $z \to \infty$.

The Sliding Velocity $\bar{\mathbf{U}}$

The value of the sliding velocity $\bar{\mathbf{U}}(t)$ may be constrained by momentum conservation in much the same way as the sliding velocity in Nye-Kamb theory is constrained by equation (2.59). We integrate (5.70) over the domain[9] $0 < x < a_x$, $0 < y < a_y$, $0 < z < R$ and apply the divergence theorem. Since the stress field is required to be periodic, contributions to the surface integral from the side boundaries $x = 0$, a_x and $y = 0$, a_y vanish. Letting $R \to \infty$ and using boundary conditions (5.73) yields

$$\frac{1}{a_x a_y}\int_0^{a_x}\int_0^{a_x} \frac{\partial u}{\partial z} + \frac{\partial w}{\partial x}\,\mathrm{d}y\,\mathrm{d}x = \frac{1}{a_x a_y}\int_0^{a_x}\int_0^{a_x} \frac{\partial v}{\partial z} + \frac{\partial w}{\partial y}\,\mathrm{d}y\,\mathrm{d}x = 0, \tag{5.77}$$

$$\frac{1}{a_x a_y}\int_0^{a_x}\int_0^{a_x} p - 2\frac{\partial w}{\partial z}\,\mathrm{d}y\,\mathrm{d}x = 0. \tag{5.78}$$

Using the definitions of $\boldsymbol{\tau_b}$ and N in (5.61)–(5.62), and assuming that the mean of s is fixed at zero, we have

$$\frac{1}{a_x a_y}\int_0^{a_x}\int_0^{a_x} \boldsymbol{\tau_b}\,\mathrm{d}y\,\mathrm{d}x = \mathbf{i}, \qquad \frac{1}{a_x a_y}\int_0^{a_x}\int_0^{a_x} N\,\mathrm{d}y\,\mathrm{d}x = \bar{N}, \tag{5.79}$$

i.e. the mean shear stress at the bed is simply the driving stress applied at infinity and the mean effective pressure at the bed is $\bar{N}$.

We assume that $u_b(\tau_b, N, s) = \bar{U}$ can be inverted to give $\tau_b = \tau(\bar{U}, N, s)$. Then $(5.72)_2$ can be rewritten as

$$\boldsymbol{\tau_b} = \tau(\bar{U}, N, s)\bar{\mathbf{U}}/\bar{U}, \tag{5.80}$$

where $\bar{U} = |\bar{\mathbf{U}}|$. (5.79) then yields

$$\mathbf{i} = \frac{1}{a_x a_y}\int_0^{a_x}\int_0^{a_x} \boldsymbol{\tau_b}\,\mathrm{d}y\,\mathrm{d}x = \frac{\bar{\mathbf{U}}/\bar{U}}{a_x a_y}\int_0^{a_x}\int_0^{a_x} \tau(\bar{U}, N, s)\,\mathrm{d}y\,\mathrm{d}x, \tag{5.81}$$

since $\bar{\mathbf{U}}$ is independent of position (x, y). This integral constraint fixes the sliding velocity $\bar{\mathbf{U}}$. From (5.81) it further follows that $\bar{\mathbf{U}}$ is parallel to $\mathbf{i}$. In other words, the y-component of $\bar{\mathbf{U}}$ vanishes,

$$\bar{\mathbf{U}} = (\bar{U}, 0). \tag{5.82}$$

Since $\bar{\mathbf{U}}(t)$ is constant at any fixed time t, this is what one would expect from a simple symmetry argument: a component of sliding velocity $\bar{\mathbf{U}}$ transverse to the shear stress applied at infinity (see (5.15)) would indicate the existence of a preferred transverse direction, but no such direction can exist.

From (5.80), (5.82) in addition implies that there is no transverse component of the shear stress $\boldsymbol{\tau_b}$, and consequently no transverse till flux,

$$\boldsymbol{\tau_b} = (\tau_b, 0), \qquad \mathbf{q} = (q, 0). \tag{5.83}$$

[9] By a_x, a_y we now denote the scaled periods.

Simplified Boundary Conditions

The results above allow us to rewrite the boundary conditions (5.72) and (5.74)–(5.76) for the ice flow problem somewhat. Since we have already inverted $(5.72)_2$ to give shear stress τ_b as a function of $\bar{U}$, N and s (see (5.80)), we can also re-write flux q as a function of $\bar{U}$, N and s by substituting for τ_b in $q_b(\tau_b, N, s)$. Thus,

$$q = q_b(\tau(\bar{U}, N, s), N, s) \doteq Q(\bar{U}, N, s), \tag{5.84}$$

and we may now think of s, $\bar{U}$ and N as the 'principal' dependent variables for which we wish to solve. Boundary conditions at the base of the ice may now be written as

$$w = \bar{U}\frac{\partial s}{\partial x} - \frac{\partial q}{\partial x}, \qquad \frac{\partial u}{\partial z} + \frac{\partial w}{\partial x} = \tau(\bar{U}, N, s) - 1, \qquad \frac{\partial v}{\partial z} + \frac{\partial w}{\partial y} = 0, \qquad \text{on } z = 0, \tag{5.85}$$

where

$$N = \bar{N} + \beta s + p - 2\frac{\partial w}{\partial z} \qquad \text{on } z = 0, \tag{5.86}$$

$$q = Q(\bar{U}, N, s). \tag{5.87}$$

Furthermore, we may note that the evolution equation (5.59) reduces to

$$\frac{\partial s}{\partial t} + \frac{\partial q}{\partial x} = 0. \tag{5.88}$$

Thus, although the model is formulated in three dimensions, we see that there is a strongly preferred direction, namely the downstream direction.

Comparison with Hindmarsh's Model

Hindmarsh (1998b) assumed implicitly that the simplifications of the till flow equations which lead to the result in section 5.4.1 above are valid. His treatment of the ice flow problem, however, differs somewhat from ours as he does not implement the 'thin till' approximation ($\nu \ll 1$) consistently.

The linearisations performed by Hindmarsh for his stability analysis result in the same field equations as above, and boundary conditions $(5.85)_1$ and (5.86) above are also reproduced as Hindmarsh's equations (7b) and (10). His linearised model differs mostly from a linearised version of ours because he does not reproduce our boundary condition $(5.85)_2$; instead, he allows variations in the horizontal velocity component u to enter into his equivalent of this boundary condition (equation (8) of his paper). Hence τ_b in his model is no longer constrained such that $u_b(\tau_b, N, s)$ is constant in space. This is equivalent to changing our original boundary condition $(5.72)_2$ to

$$u_b(\tau_b, N, s)\boldsymbol{\tau_b}/\tau_b = \bar{\mathbf{U}}(t) + \nu(u, v), \qquad \text{on } z = 0. \tag{5.89}$$

Retaining the term $\nu(u, v)$ on the right-hand side is likely to lead to different results from the ones obtained here. In particular, the reduction of the boundary conditions performed above is not possible if $\nu(u, v)$ is retained in boundary condition $(5.72)_2$. However, these differences are likely to be insignificant when ν is small. Furthermore, Fowler (2000) also retains the term $\nu(u, v)$ (or more precisely, νu, since Fowler works in two dimensions, see equation (27) of his paper), and we will see later that our model captures the instability mechanism of Fowler's paper; we can thus be confident that we also capture the instability mechanism proposed by Hindmarsh (1998b).

5.4.3 Fourier Transform Solution

The reduction of the domain of the ice flow to the half-space $z > 0$ allows a partial solution to the ice flow problem to be obtained in Fourier transform space. The result will be an equation relating the Fourier coefficients of effective pressure N to the Fourier coefficients of the bed s and the flux q. This equation will be used in section 5.5 to consider how the bed instability occurs, and in section 5.6 to construct a simplified nonlinear model.

We define the Fourier transform of any generic function $f(x, y, z, t)$ which is periodic in the x- and y-directions with periods a_x and a_y as

$$\hat{f}_{nm}(z,t) = \frac{1}{a_x a_y} \int_0^{a_x} \int_0^{a_y} f(x,y,z,t) \exp\left(-ik_{x(n)}x - ik_{y(m)}y\right) \,\mathrm{d}y \,\mathrm{d}x :$$

$$k_{x(n)} = \frac{2\pi n}{a_x}, \qquad k_{y(m)} = \frac{2\pi m}{a_y}, \qquad n,\, m \in \mathbb{Z}. \tag{5.90}$$

Taking curl curl of both sides of (5.70) and using (5.71), we find that the velocity field $\mathbf{u}$ satisfies the biharmonic equation component-wise,

$$\nabla^4 \mathbf{u} = \mathbf{0}, \tag{5.91}$$

while taking the divergence of (5.70) and using (5.71) yields Laplace's equation for p,

$$\nabla^2 p = 0. \tag{5.92}$$

Taking the Fourier transforms of these equations yields the following ordinary differential equations for the Fourier coefficients of $\mathbf{u}$ and p,

$$\left(\frac{\mathrm{d}^2}{\mathrm{d}z^2} - k^2\right)^2 \hat{\mathbf{u}}_{nm} = \mathbf{0}, \tag{5.93}$$

$$\left(\frac{\mathrm{d}^2}{\mathrm{d}z^2} - k^2\right) \hat{p}_{nm} = 0, \tag{5.94}$$

where

$$k = \sqrt{k_{x(n)}^2 + k_{y(m)}^2}. \tag{5.95}$$

The general solutions to these o.d.e.s which are bounded at infinity as required by the boundary conditions (5.73) are

$$\hat{\mathbf{u}}_{nm} = (A_1 z + B_1, A_2 z + B_2, A_3 z + B_3) \exp(-kz), \tag{5.96}$$

$$\hat{p}_{nm} = A \exp(-kz). \tag{5.97}$$

It remains to determine the seven coefficients $A, A_1, A_2, A_3, B_1, B_2$ and B_3. Taking the Fourier transforms of the field equations (5.70) and (5.71) and substituting the general solutions (5.96) and (5.97) for the Fourier coefficients of $\mathbf{u}$ and p yields four linearly independent equations for $A, A_1, A_2, A_3, B_1, B_2$ and B_3. Taking the Fourier coefficients of boundary conditions (5.85) while treating $\bar{U}$, q and τ as known yields a further three equations. There are now a sufficient number of equations to determine the coefficients $A, A_1, A_2, A_3, B_1, B_2$ and B_3 in terms of $\bar{U}$ and the Fourier coefficients of s, q and τ.

Of course, even if the bed shape $s(x, y, t)$ is known — for instance at some fixed time t — the sliding velocity $\bar{U}$ and the Fourier coefficients of q and τ are not known *a priori*, but are determined through the nonlinear boundary condition (5.86). We take the Fourier transform of (5.86) and substitute for $\hat{\mathbf{u}}_{nm}$ and $\hat{p}_{nm}$ to find the desired relation

$$\hat{N}_{nm} = \beta \hat{s}_{nm} + 2ik_{x(n)}k \left(\bar{U}\hat{s}_{nm} - \hat{q}_{nm}\right), \qquad (n, m) \neq (0, 0). \tag{5.98}$$

The conversion of (5.86) to an integral equation, which may be solved in conjunction with (5.79) to determine $\bar{U}$ and N (and hence τ and q) for a given bed s, is discussed in section 5.6. Once $\bar{U}$ and N are known, we can then in principle solve for $\mathbf{u}$ and p in the ice flow domain, for instance by using the Fourier transform approach above to determine A, A_1, A_2, A_3, B_1, B_2 and B_3.

(5.98) may be compared with the corresponding relation (2.58) in two-dimensional Nye-Kamb theory. Putting β and flux q to zero, $\beta = \hat{q}_{nm} = 0$, and recognising that $k_{y(m)} = 0$ in two dimensions, so that $k = |k_{x(n)}|$, we see that (5.98) reduces to the classical expression as required.

5.5 Linear Stability Analysis

We are now ready to study the instability mechanism proposed by Hindmarsh (1998b) and Fowler (2000) in more detail. We consider first how small perturbations to the

steady-state solution $s \equiv 0$, $\bar{U} = 1$, $N \equiv \bar{N}$ evolve. These perturbations are expressed as

$$s = \varepsilon s'(x, y, t), \qquad N = \bar{N} + \varepsilon N'(x, y, t),$$
$$q = Q(1, \bar{N}, 0) + \varepsilon q'(x, y, t), \qquad \bar{U} = 1 + \varepsilon \bar{U}'(t), \tag{5.99}$$

where $\varepsilon \ll 1$.

Substituting in the evolution equation (5.88) yields

$$\frac{\partial s'}{\partial t} + \frac{\partial q'}{\partial x} = 0. \tag{5.100}$$

Linearising equation (5.87) for the till flux leads to

$$q' = Q_U \bar{U}' + Q_N N' + Q_s s', \tag{5.101}$$

where Q_U, Q_N and Q_s are constants defined by

$$Q_U = \frac{\partial Q}{\partial \bar{U}}(1, \bar{N}, 0), \qquad Q_N = \frac{\partial Q}{\partial N}(1, \bar{N}, 0), \qquad Q_s = \frac{\partial Q}{\partial s}(1, \bar{N}, 0). \tag{5.102}$$

Linearisation of the constraint (5.81) leads to

$$\frac{1}{a_x a_y} \int_0^{a_x} \int_0^{a_y} \left(\tau_U \bar{U}' + \tau_N N' + \tau_s s' \right) \mathrm{d}y \, \mathrm{d}x = 0, \tag{5.103}$$

where the constants τ_U, τ_N and τ_s are defined analogously to Q_U, Q_N and Q_s as the partial derivatives of $\tau(\bar{U}, N, s)$ evaluated at $\bar{U} = 1$, $s = 0$ and $N = \bar{N}$. In the formulation of the model, we have already required that s has zero mean, and so

$$\frac{1}{a_x a_y} \int_0^{a_x} \int_0^{a_y} s' \, \mathrm{d}y \, \mathrm{d}x = 0. \tag{5.104}$$

Equation $(5.79)_2$ further states that N' must have zero mean. Since $\bar{U}'$ is independent of position, (5.103) therefore yields

$$\bar{U}' = 0, \tag{5.105}$$

i.e. the sliding velocity perturbation is of $O(\varepsilon^2)$ and can be neglected here. This reduces (5.101) to

$$q' = Q_N N' + Q_s s'. \tag{5.106}$$

We require a further relation between s', q' and N', which is furnished by the solution of the ice flow problem. Specifically, if one considers modes of the form

$$s' = \hat{s} \exp(\sigma t + i k_x x + i k_y y), \qquad q' = \hat{q} \exp(\sigma t + i k_x x + i k_y y),$$

$$N' = \hat{N} \exp(\sigma t + ik_x x + ik_y y), \tag{5.107}$$

such a relation is provided by linearising (5.98),

$$\hat{N} = \beta \hat{s} + 2ik_x k(\hat{s} - \hat{q}), \tag{5.108}$$

where

$$k = \sqrt{k_x^2 + k_y^2}. \tag{5.109}$$

In terms of these modes, (5.100) and (5.106) may also be re-written as

$$\sigma \hat{s} + ik_x \hat{q} = 0, \tag{5.110}$$

$$\hat{q} = Q_N \hat{N} + Q_s \hat{s}. \tag{5.111}$$

Equations (5.108)–(5.111) constitute a straightforward algebraic eigenvalue problem for σ with solution

$$\sigma = -ik_x \frac{Q_s + \beta Q_N + 2ik_x k Q_N}{1 + 2ik_x k Q_N}. \tag{5.112}$$

Hence the growth rate may be expressed as

$$\Re(\sigma) = \frac{2Q_N(1 - Q_s - \beta Q_N)k_x^2 k}{1 + 4Q_N^2 k_x^2 k^2}, \tag{5.113}$$

while the downstream phase velocity is

$$-\Im(\sigma)/k_x = \frac{Q_s + \beta Q_N + 4Q_N^2 k^2 k_x^2}{1 + 4Q_N^2 k_x^2 k^2}. \tag{5.114}$$

Turning to expression (5.113) for the growth rate, we obtain the instability criterion

$$Q_N(1 - Q_s - \beta Q_N) > 0. \tag{5.115}$$

The first thing to note is that the bed is neutrally stable ($\Re(\sigma) = 0$) if the flux Q does not depend on effective pressure, i.e. if $Q_N = 0$. As stated in the introduction, the instability mechanism relies on the dependence of till rheology on effective pressure.

If (5.115) is satisfied, then all wavelengths become unstable. We wish to establish which wavelengths grow fastest, as this may indicate roughly what shape (i.e. what length-to-width ratio) the evolved instability is likely to have. By writing $k_x = k\cos\theta$, one can express the growth rate as

$$\Re(\sigma) = \frac{2Q_N(1 - Q_s - \beta Q_N)k^3 \cos^2\theta}{1 + 4Q_N^2 k^4 \cos^2\theta}. \tag{5.116}$$

Then

$$\frac{\partial \Re(\sigma)}{\partial \theta} = \frac{-4Q_N(1 - Q_s - \beta Q_N)k^3 \cos\theta \sin\theta}{(1 + 4Q_N^2 k^4 \cos^2\theta)^2}. \tag{5.117}$$

Thus $\Re(\sigma)$ has stationary values at $\theta = 0,\ \pi/2,\ \pi,\ 3\pi/2$. However, when $\theta = \pi/2$ or $3\pi/2$, we have $\Re(\sigma) = 0$. Maximum positive growth rates therefore occur for $\theta = 0,\ \pi$, and therefore at $k_y = k\sin\theta = 0$. The steady state has no transverse instabilities, and rolls (or Rogen moraine) grow fastest when the instability occurs. This is not surprising since there is no transverse till flux at leading order. It does, however, suggest that the mechanism proposed by Hindmarsh (1998b) and Fowler (2000) cannot explain the origin of drumlins, but at best that of Rogen moraines.

Having noted that the maximum growth rate corresponds to zero transverse wavenumber, one may finally compute the wavevector of the fastest growing mode as

$$(k_x, k_y)_{max} = \left(\pm \left[\frac{\sqrt{3}}{2|Q_N|} \right]^{1/2}, 0 \right). \tag{5.118}$$

In principle, one could now calculate the fastest growing wavelength $\lambda_{max} = 2\pi/k_{max}$ for various rheologies and parameter choices. We do not do so here for the following reason: In order to re-dimensionalise our results, λ_{max} would have to be multiplied by the length scale $[x]$ defined in (5.21). As explained in section 5.3, $[x]$ is not well constrained by experimental data because the till shearing velocity $[u_b]$ is not well constrained. Dimensional bedform wavelengths predicted on the basis of (5.118) and (5.21) are therefore not particularly meaningful as they can be 'tuned' very easily simply by changing $[u_b]$. We will, however, return to (5.118) when we consider the effect of changing various model parameters in sections 5.7.1 and 5.7.2.

5.5.1 Comparison with Fowler's Results

The next thing we wish to do is to show that the dispersion relation (5.112) agrees with that obtained by Fowler (2000) — it is much more difficult to establish whether our reduced model still agrees with that of Hindmarsh (1998b), since the latter author performed a linear stability analysis numerically.

Fowler (2000) did not invert $u_b(\tau_b, N, s) = \bar{U}$ to find $\tau_b = \tau(\bar{U}, N, s)$ and hence did not express q as a function of $\bar{U}$, N and s. His dispersion relation, equations (36)–(37) of his paper, thus contains derivatives of $u_b(\tau_b, N, s)$ and $q(\tau_b, N, s)$ rather than the coefficients Q_N and Q_s defined above. Applying the chain rule to $Q(\bar{U}, N, s) = q_b(\tau(\bar{U}, N, s), N, s)$,

$$\frac{\partial Q}{\partial N} = \frac{\partial q_b}{\partial N} + \frac{\partial q_b}{\partial \tau_b}\frac{\partial \tau}{\partial N}, \tag{5.119}$$

$$\frac{\partial Q}{\partial s} = \frac{\partial q_b}{\partial s} + \frac{\partial q_b}{\partial \tau_b}\frac{\partial \tau}{\partial s}. \tag{5.120}$$

To eliminate the partial derivatives of τ in favour of derivatives of u_b, we use the chain rule on $u_b(\tau(\bar{U}, N, s), N, s) = \bar{U}$, and find

$$\frac{\partial \tau}{\partial N} = -\frac{\partial u_b}{\partial N} \Big/ \frac{\partial u_b}{\partial \tau_b}, \tag{5.121}$$

$$\frac{\partial \tau}{\partial s} = -\frac{\partial u_b}{\partial s} \Big/ \frac{\partial u_b}{\partial \tau_b}. \tag{5.122}$$

By analogy with Fowler's notation, we define

$$u_\tau = \frac{\partial u_b}{\partial \tau_b}(1, \bar{N}, 0), \qquad u_N = \frac{\partial u_b}{\partial N}(1, \bar{N}, 0), \qquad u_s = \frac{\partial u_b}{\partial s}(1, \bar{N}, s),$$

$$q_\tau = \frac{\partial q_b}{\partial \tau_b}(1, \bar{N}, 0), \qquad q_N = \frac{\partial q_b}{\partial N}(1, \bar{N}, 0), \qquad q_s = \frac{\partial q_b}{\partial s}(1, \bar{N}, s). \tag{5.123}$$

Using the results above, Q_N and Q_s may be expressed as

$$Q_N = q_N - q_\tau u_N / u_\tau, \qquad Q_s = q_s - q_\tau u_s / u_\tau. \tag{5.124}$$

This allows the dispersion relation (5.113)–(5.114) to be re-written as

$$\Re(\sigma) = \frac{2[u_\tau - (q_s u_\tau - u_s q_\tau) - (q_N u_\tau - q_\tau u_N)\beta](q_N u_\tau - q_\tau u_N) k_x^2 k}{u_\tau^2 + 4(q_N u_\tau - q_\tau u_N)^2 k_x^2 k^2} \tag{5.125}$$

$$-\Im(\sigma)/k_x = \frac{4(q_N u_\tau - q_\tau u_N)^2 k_x^2 k^2 + [(q_s u_\tau - u_s q_\tau) + (q_N u_\tau - q_\tau u_N)\beta]\, u_\tau}{u_\tau^2 + 4(q_s u_\tau - u_s q_\tau)^2 k_x^2 k^2} \tag{5.126}$$

If we restrict the model to two dimensions by setting $k = |k_x|$ and further put $\beta = 0$ as is done in Fowler's (2000) paper, then (5.125)–(5.126) agree with Fowler's (dimensional) relations (36) and (37) provided we recognise that Fowler's dimensional mean velocity $\bar{u}$ corresponds to unity here, and provided we approximate $1 + 2\mu u_\tau k \approx 2\mu u_\tau k$ in Fowler's dispersion relations (36) and (37). In fact, Fowler himself uses this approximation to derive his simplified growth rate (52), which is of the same form as (5.125) here.

We can thus be confident that our reduced model captures the same instability mechanism as Fowler (2000), and that the scalings chosen in section 5.3 and the subsequent leading-order reduction are appropriate.

5.5.2 The Instability Criterion

The change of coefficients from Q_s and Q_N to u_τ, u_N, etc. performed above is not only useful for demonstrating that our results agree with those of Fowler (2000), but

also allows us to simplify the instability criterion (5.115) for many viscous rheologies using the formulae (5.66) and (5.68). From (5.66), (5.68) and (5.123) one obtains

$$q_s = u_s = F(1, \bar{N} + \alpha), \tag{5.127}$$

$$u_N = \int_0^1 F_{p_e}(1, \bar{N} + \alpha\xi)\,\mathrm{d}\xi, \qquad q_N = \int_0^1 \xi F_{p_e}(1, \bar{N} + \alpha\xi)\,\mathrm{d}\xi, \tag{5.128}$$

$$u_\tau = \int_0^1 F_\tau(1, \bar{N} + \alpha\xi)\,\mathrm{d}\xi, \qquad q_\tau = \int_0^1 \xi F_\tau(1, \bar{N} + \alpha\xi)\,\mathrm{d}\xi, \tag{5.129}$$

where

$$F_{p_e}(\tau, p_e) = \frac{\partial F}{\partial p_e}, \qquad F_\tau(\tau, p_e) = \frac{\partial F}{\partial \tau}. \tag{5.130}$$

Recall that the instability criterion (5.115) is

$$Q_N(1 - Q_s - \beta Q_N) > 0. \tag{5.131}$$

We now examine both factors, $1 - Q_s - \beta Q_N$ and Q_N, in turn.

The Term $1 - Q_s - \beta Q_N$

We expect shearing in the till to increase with shear stress τ and to decrease with effective pressure p_e, so we require the rheology $F(\tau, p_e)$ to satisfy

$$F_{p_e} < 0, \qquad F_\tau > 0. \tag{5.132}$$

It follows that u_s, q_s, u_τ, $q_\tau > 0$ and u_N, $q_N < 0$. Hence

$$1 - Q_s = 1 - q_s + q_\tau u_s/u_\tau > 1 - q_s.$$

But, since $1 = u_b(1, \bar{N}, 0) = \int_0^1 F(1, \bar{N} + \alpha\xi)\,\mathrm{d}\xi$,

$$1 - q_s = \int_0^1 F(1, \bar{N} + \alpha\xi)\,\mathrm{d}\xi - F(1, \bar{N} + \alpha) =$$

$$\int_0^1 F(1, \bar{N} + \alpha\xi) - F(1, \bar{N} + \alpha)\,\mathrm{d}\xi. \tag{5.133}$$

Since $\partial F/\partial p_e < 0$, it follows that

$$F(1, \bar{N} + \alpha\xi) - F(1, \bar{N} + \alpha) > 0, \qquad \xi \in [0, 1), \tag{5.134}$$

and hence

$$1 - Q_s > 1 - q_s > 0. \tag{5.135}$$

Since β is inherently positive (see definition (5.31)), the factor $1-Q_s-\beta Q_N$ is positive unless $Q_N > (1-Q_s)/\beta > 0$. Hence the instability criterion (5.131) becomes

$$0 < Q_N < (1-Q_s)/\beta. \tag{5.136}$$

The second condition, $Q_N < (1-Q_s)/\beta$ is likely to be less important as β is generally small — in fact, Fowler (2000) sets $\beta = 0$, so (5.136) is satisfied provided $Q_N > 0$. By contrast, the first condition, $Q_N > 0$, is crucial.

The Term Q_N

By (5.124), Q_N may be expressed as

$$Q_N = q_N - q_\tau u_N/u_\tau. \tag{5.137}$$

We wish to investigate under what circumstances $Q_N > 0$. Since $u_\tau > 0$, this is equivalent to

$$q_N u_\tau - q_\tau u_N > 0. \tag{5.138}$$

Simple model rheologies for till which have been proposed elsewhere include Boulton and Hindmarsh's (1987) power law

$$F(\tau, p_e) = K\frac{\tau^m}{p_e^n}, \qquad m,\, n > 0 \tag{5.139}$$

and an exponential rheology (Kamb, 1991; Fowler, 2000)

$$F(\tau, p_e) = A\exp(\mu\tau/p_e). \tag{5.140}$$

Both of these can be expressed in the form

$$F(\tau, p_e) = f\left(\frac{\tau^\gamma}{p_e}\right), \tag{5.141}$$

where $\gamma > 0$ and f is some function such that

$$f(\zeta),\ f'(\zeta) > 0, \qquad \text{when } \zeta > 0. \tag{5.142}$$

For rheologies of this type one can show that (5.138) always holds.

Specifically, we have from (5.128)–(5.130) with (5.141)

$$u_\tau = \int_0^1 \frac{\gamma}{\bar{N}+\alpha\xi} f'\left(\frac{1}{\bar{N}+\alpha\xi}\right)\,\mathrm{d}\xi, \tag{5.143}$$

$$q_N = \int_0^1 -\frac{\xi}{(\bar{N}+\alpha\xi)^2} f'\left(\frac{1}{\bar{N}+\alpha\xi}\right)\,\mathrm{d}\xi, \tag{5.144}$$

$$u_N = \int_0^1 -\frac{1}{(\bar{N}+\alpha\xi)^2} f'\left(\frac{1}{\bar{N}+\alpha\xi}\right)\,\mathrm{d}\xi, \tag{5.145}$$

$$q_\tau = \int_0^1 \frac{\gamma\xi}{\bar{N}+\alpha\xi} f'\left(\frac{1}{\bar{N}+\alpha\xi}\right)\,\mathrm{d}\xi. \tag{5.146}$$

For simplicity of notation, we define a function $h(\xi)$ as

$$h(\xi) = \frac{1}{(\bar{N} + \alpha\xi)^2} f'\left(\frac{1}{\bar{N} + \alpha\xi}\right). \tag{5.147}$$

From (5.142), we may note that $h(\xi) > 0$ when $\xi \in [0, 1]$. $q_N u_\tau - q_\tau u_N$ may now be expressed as

$$q_N u_\tau - q_\tau u_N = \gamma \left(\int_0^1 h(\xi)\,\mathrm{d}\xi \int_0^1 \xi(\bar{N} + \alpha\xi) h(\xi)\,\mathrm{d}\xi - \int_0^1 \xi h(\xi)\,\mathrm{d}\xi \int_0^1 (\bar{N} + \alpha\xi) h(\xi)\,\mathrm{d}\xi \right) =$$

$$\gamma\alpha \left(\int_0^1 h(\xi)\,\mathrm{d}\xi \int_0^1 \xi^2 h(\xi)\,\mathrm{d}\xi - \left(\int_0^1 \xi h(\xi)\,\mathrm{d}\xi \right)^2 \right) =$$

$$\frac{\gamma\alpha}{\langle h \rangle} \int_0^1 \left[\langle h \rangle\, \xi - \langle h\xi \rangle \right]^2 h(\xi)\,\mathrm{d}\xi, \tag{5.148}$$

where

$$\langle h \rangle = \int_0^1 h(\xi')\,\mathrm{d}\xi', \qquad \langle h\xi \rangle = \int_0^1 h(\xi')\xi'\,\mathrm{d}\xi'. \tag{5.149}$$

Since $h(\xi) > 0$, α, $\gamma > 0$, it follows that $q_N u_\tau - q_\tau u_N > 0$ and hence

$$Q_N > 0 \tag{5.150}$$

for rheologies of the type (5.141).

A Simple Instability Criterion

On account of (5.135) and (5.150), the instability criterion (5.131) for rheologies of the type (5.141) thus reduces to the simple requirement that

$$\beta < (1 - Q_s)/Q_N. \tag{5.151}$$

Since β is usually small, we expect this criterion to be satisfied under fairly general circumstances. Interestingly, Fowler (2000) uses an exponential rheology (5.140) in his model and finds a region in parameter space where the bed is stable despite setting $\beta = 0$. This may be attributed to the approximation made in equation (13) of his paper, which means that the rheology used by Fowler in the remainder of his paper is no longer of the form (5.141).

Example: Boulton-Hindmarsh Rheologies

Equation (5.151) provides a simple instability criterion for rheologies of the form (5.141). As we pointed out, β is generally small (see comments on page 110), and one may wonder if there are realistic values of β for which the instability criterion (5.151) is not satisfied. To this end, we calculate $(1-Q_s)/Q_N$ for various parameter choices when Q is defined by a Boulton-Hindmarsh rheology. For such a rheology, the function $F(\tau, p_e)$ is defined by

$$F(\tau, p_e) = K\frac{\tau^m}{p_e^n}, \qquad m,\, n > 0, \tag{5.152}$$

where the normalisation constant K must satisfy $u_b(1, \bar{N}, 0) = \int_0^1 F(1, \bar{N}+\alpha\xi)\,\mathrm{d}\xi = 1$, i.e.

$$\int_0^1 K\frac{1}{\bar{N}+\alpha\xi}\,\mathrm{d}\xi = 1. \tag{5.153}$$

$Q(\bar{U}, N, s)$ can be calculated explicitly as

$$Q(\bar{U}, N, s) = \frac{\bar{U}(N/\alpha)}{n-2}\left[1 - \frac{(n-1)(1+s)(N/\alpha)^{n-2}}{(N/\alpha+1+s)^{n-1} - (N/\alpha)^{n-1}}\right], \tag{5.154}$$

provided $n \neq 1,\, 2$. Note that Q does not depend on the exponent m, and depends on N and α only through N/α. Analytical expressions for Q_N and Q_s can be derived,

$$\alpha Q_N = \frac{Q(1, \bar{N}, 0)}{(\bar{N}/\alpha)} -$$

$$\frac{(n-1)(\bar{N}/\alpha)^{n-2}\left[(\bar{N}/\alpha)^{n-1} - (\bar{N}/\alpha+1)^{n-1} + (n-1)(\bar{N}/\alpha+1)^{n-2}\right]}{(n-2)\left[(\bar{N}/\alpha+1)^{n-1} - (\bar{N}/\alpha)^{n-1}\right]^2}, \tag{5.155}$$

$$Q_s = \frac{(n-1)(\bar{N}/\alpha)^{n}\left[(n-1)(\bar{N}/\alpha+1)^{n-2} - (\bar{N}/\alpha+1)^{n-1} + (\bar{N}/\alpha)^{n-1}\right]}{(n-2)\left[(\bar{N}/\alpha+1)^{n-1} - (\bar{N}/\alpha)^{n-1}\right]^2}. \tag{5.156}$$

These allow the critical value of

$$\beta_c = (1-Q_s)/Q_N \tag{5.157}$$

to be calculated. From (5.154)–(5.156), it follows that β_c/α is a function of $\bar{N}/\alpha$ and n only. Figure 5.2 therefore shows plots of β_c/α against $\bar{N}/\alpha$ at various values of n.

The discussion on page 110 indicates that we generally expect $\beta \approx 0.1\alpha$, so $\beta/\alpha \approx 0.1$. Figure 5.2 indicates that $\beta_c/\alpha \lesssim 0.1$, and hence stability, are only achieved for low values of $n \lesssim 2$ and at very low values of $\bar{N}/\alpha$. Such low values of $\bar{N}/\alpha$ correspond either to very deep till (and hence large α, see (5.31)), or very low mean effective

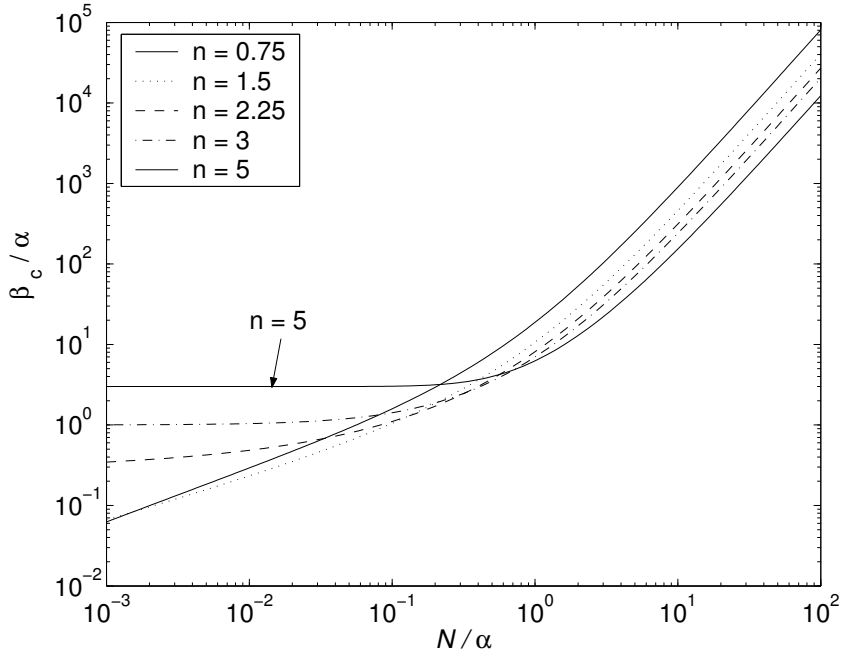

Figure 5.2: A plot of β_c/α against $\bar{N}/\alpha$ at various values of the exponent n for Boulton-Hindmarsh rheologies (5.152). Note the logarithmic scales.

pressures $\bar{N}$, i.e. when the ice sheet is close to flotation. The latter possibility may be discounted as the model is unlikely to apply to an ice sheet which is close to flotation. As we will see in section 5.7.1, rheologies with low n cannot account for deformation structures typically seen in thick subglacial sediment layers. The combination of low n and very low $\bar{N}/\alpha$ is therefore not physically realistic, and we expect the instability criterion to be satisfied by all reasonable choices of parameters n, $\bar{N}$ and α.

5.5.3 The Mechanics of the Instability

Here, we reconsider briefly how the instability mechanism works. Ignoring complications due to finite values of β, we have seen that instability essentially requires

$$Q_N > 0,$$

i.e. till flux must increase when the interface velocity is held constant and effective pressure N is increased. It is straightforward to see how this will lead to instability: The presence of a bump on the bed leads to higher compressive normal stresses being exerted by the ice on the bed upstream of the bump than downstream.[10] These

[10]This is analogous to the case of classical sliding, where these higher compressive normal stresses lead to resistance to flow, see section 2.3.

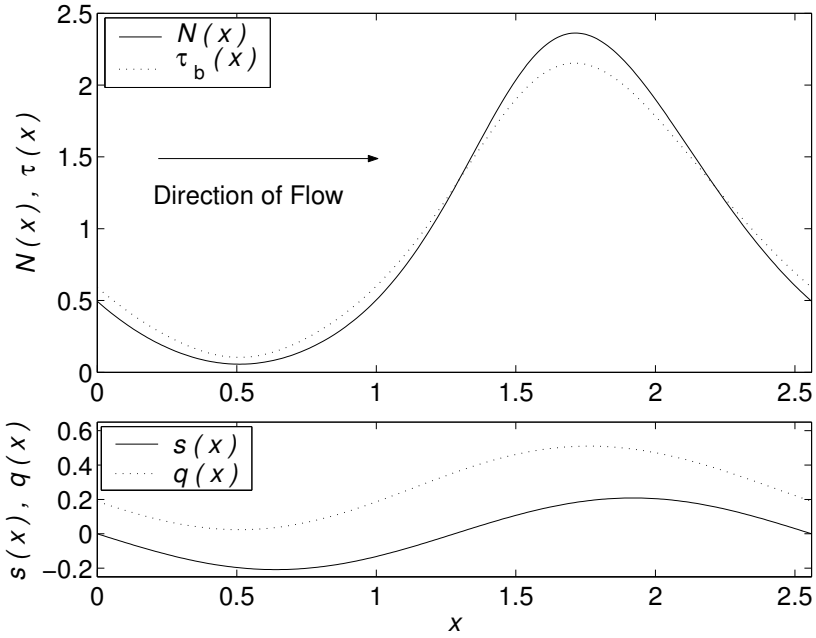

Figure 5.3: The bottom panel shows a sinusoidal bed (solid line) with period $a = 2.5595$. The dotted line shows the corresponding till flux for parameter choices $\bar{N} = 1$, $\alpha = 1$, $\beta = 0.5$ and $m = n = 5$, calculated using the numerical method described in section 5.6.1. The value of a above corresponds to the fastest growing wavelength for these parameter choices. Note that flux q decreases across the top of the bed bump, causing it to grow. The reason for this phase lead is shown in the top panel: the solid line shows the corresponding effective pressure N, and the dotted line the interfacial shear stress τ_b. Note that both, N and τ_b, are greater on the upstream side of the bedform than its downstream side. High effective pressures upstream of the top of the bed bump should lead to flux increasing across the top of the bed bump, which would cause it to decay. It is therefore the increased shear stress upstream of the bump which leads to greater flux into the bump than out, thereby causing it to grow.

compressive normal stresses lead to increased effective pressure upstream of the bed bump. At the same time, the interfacial velocity $\bar{U}$ is held constant in space. If this leads to till flux increasing where effective pressure increases, then till flux will be greater upstream of the bed bump than downstream. More till flows into the bump than out, causing it to grow.

However, the effect of holding interfacial shear stress τ_b constant whilst increasing effective pressure N is always to reduce till flux — this corresponds to q_N being negative. The fact that $\bar{U}$ is approximately constant in space is therefore crucial to the instability mechanism. It forces the shear stress τ_b to become concentrated where the bed is made stiffer by higher effective pressure. This concentration of shear stress is the mechanism by which flux increases where effective pressure is higher.

In the instability criterion $Q_N > 0$, where $Q_N = q_N - q_\tau u_N/q_\tau$, the effect of till stiffening when effective pressure is raised is represented by $q_N < 0$, while the effect of shear stress concentrating where till becomes stiffer is represented by $-q_\tau u_N/q_\tau > 0$. This illustrates the two competing effects — till stiffening tends to decrease till flux while shear stress concentration tends to increase it. As was shown in section 5.5.2 the latter effect dominates over the former for many rheologies, and causes the instability.

Having established that an instability can occur, we wish to investigate how the bed evolves once bed perturbations reach finite size. To this end, we construct and solve a simplified nonlinear model.

5.6 A Simplified Nonlinear Model

The analysis in section 5.5 has indicated that the instability proposed by Hindmarsh (1998b) and Fowler (2000) is inherently two-dimensional, that is, the fastest growing perturbations have zero transverse wavenumber. Consequently, we will restrict ourselves to two dimensions (i.e. to the (x, z)-plane) in the further development of the model.

We suppose that the transverse velocity component vanishes, $v = 0$, and that all dependent variables are independent of the transverse coordinate y. Furthermore, we drop the subscript $_x$ from the period a_x and from the downstream wavenumber $k_{x(n)}$ defined in section 5.4.3. In order to restrict the results of that section to two dimensions, we simply set the transverse wavenumber $k_{y(m)}$ to zero by setting $m = 0$, and drop the index $_m$ on the Fourier components for simplicity. (5.98) then becomes

$$N_n = \beta s_n + 2ik_n|k_n|(\bar{U}s_n - q_n), \qquad n \neq 0. \tag{5.158}$$

Here

$$N_n = \int_0^a N(x,t)\exp(-ik_n x)/a\,\mathrm{d}x : \qquad k_n = \frac{2n\pi}{a}, \qquad n \in \mathbb{Z}, \tag{5.159}$$

and s_n and q_n are defined analogously. (5.158) may be re-arranged to give

$$q_n - \bar{U}s_n + \beta\frac{i}{2k_n|k_n|}s_n - \frac{i}{2k_n|k_n|}N_n = 0, \qquad n \neq 0. \tag{5.160}$$

We invert $q = Q(\bar{U}, N, s)$ to obtain

$$N = \hat{N}(\bar{U}, q, s). \tag{5.161}$$

Multiplying both sides of (5.160) by $\exp(ik_n x)$, summing over $n \neq 0$ and applying the convolution theorem yields a non-linear integral equation for $q(x,t)$

$$q(x,t) - q_0(t) - U(t)s(x,t) + \beta \int_0^a K(x-y)s(y)\,\mathrm{d}y - \int_0^a K(x-y)N(y)\,\mathrm{d}y = 0, \quad (5.162)$$

where $N(y) = \hat{N}(\bar{U}, q(y), s(y))$,

$$K(x) = \sum_{n=-\infty,\, n\neq 0}^{\infty} K_n \exp(ik_n x), \qquad K_n = \frac{i}{2k_n|k_n|a}, \quad (5.163)$$

and y must be understood as a dummy integration variable rather than a transverse coordinate. q_0 is simply the $n = 0$ Fourier component of q, i.e. the mean flux,[11] while s_0 does not appear in this equation because we require the mean of bed elevation to be zero.

(5.162) is a non-linear integral equation of Hammerstein type for the flux $q(x,t)$. Note that time t appears in (5.162) merely as a parameter: in order to solve for the time evolution of the bed, one has to solve the evolution equation (5.88). (5.162) can be thought of as fixing the flux in terms of the bed shape $s(x,t)$ at any given time t. In addition to $q(x,t)$, (5.162) contains the sliding velocity $\bar{U}(t)$ and mean flux $q_0(t)$ as further unknowns. At fixed time t, $\bar{U}(t)$ and $q_0(t)$ are constants, but their values are not known *a priori*. We thus expect two further constraints to be satisfied by a solution of (5.162). Such constraints are provided by the integrated momentum conservation equations (5.79). These can be written as

$$\int_0^a \left[\hat{N}(\bar{U}, q, s) - \bar{N}\right] \mathrm{d}x = 0, \quad (5.164)$$

and, substituting $N = \hat{N}(\bar{U}, q, s)$ in $\tau_b = \tau(\bar{U}, N, s)$ to give $\tau_b = \hat{\tau}_b(\bar{U}, q, s)$,

$$\int_0^a \left[\hat{\tau}_b(\bar{U}, q, s) - 1\right] \mathrm{d}x = 0. \quad (5.165)$$

The coupled integral equations (5.162) and (5.164)–(5.165) should, in principle, be sufficient to determine the flux q and sliding velocity $\bar{U}$ given a bed $s(x,t)$. s itself evolves according to the evolution equation (5.88),

$$\frac{\partial s}{\partial t} + \frac{\partial q}{\partial x} = 0. \quad (5.166)$$

Before proceeding to solve these equations numerically, we should point out that we have painted a very different picture from that envisioned by Hindmarsh (1998a):

[11] Note that integrating (5.162) automatically gives $\int_0^a q\,\mathrm{d}y/a = q_0$ since K has zero mean.

In this paper, till flux $q_b(\tau_b, N, s)$ is modelled as depending primarily on till thickness s, while its dependence on N and τ_b is largely ignored: N is taken to be determined hydrostatically, while τ_b is assumed to be given in terms of ice sheet geometry by a shallow-ice formula (2.43). The evolution equation (5.166) is then hyperbolic and shocks may form, but no growth occurs. On the length scales relevant to Hindmarsh's (1998b) and Fowler's (2000) instability model, these assumptions clearly break down, as τ_b and N are related in some non-local manner to s through the integral equation (5.162) — that is, they are not simply functions of local till thickness. In fact, as we will find in sections 5.7.1 and 5.7.2, the explicit s-dependence of the till flux is of secondary importance, and can be neglected for many parameter choices of α and n. That is to say, q can often be treated as a function of shear stress τ_b and effective pressure N alone.

5.6.1 Numerical Solution

Since we have imposed periodic boundary conditions, an obvious approach to solving the evolution equation (5.166) is a spectral discretisation in x. We use a collocation method (e.g. Trefethen, 2000) with $2n_0$ gridpoints. This allows (5.166) to be semi-discretised as

$$\frac{\partial s_n}{\partial t} + ik_n q_n = 0, \qquad n = -n_0 + 1, -n_0 + 2, \ldots, n_0 - 1, \tag{5.167}$$

where the wavenumber k_n is defined as before,

$$k_n = \frac{2n\pi}{a}. \tag{5.168}$$

s_n and q_n are the discrete Fourier transforms of s and q evaluated at at the gridpoints $x_j = (j-1)a/(2n_0)$, i.e.

$$s_n(t) = \frac{1}{2n_0}\sum_{j=1}^{2n_0} s(x_j, t)\exp(-ik_n x_j), \qquad q_n(t) = \frac{1}{2n_0}\sum_{j=1}^{2n_0} q(x_j, t)\exp(-ik_n x_j). \tag{5.169}$$

A numerical approximation $\tilde{s}$ to the solution s may be obtained by interpolating trigonometrically between the gridpoints,

$$\tilde{s}(x, t) = \sum_{j=-n_0+1}^{n_0-1} s_n(t)\exp(ik_n x). \tag{5.170}$$

Time is discretised using a second-order Runge-Kutta method with time step Δt. The numerical approximation to s_n at time $r\Delta t$ will be denoted by s_n^r and the

corresponding trigonometric interpolant defined in (5.170) will be denoted by $\tilde{s}^r$. Let q^r denote a solution of the coupled integral equations (5.162) and (5.164)–(5.165) for $s = \tilde{s}^r$. The time-stepping scheme can then be expressed as

$$s_n^{r+1/2} = s_n^r + ik_n q_n^r \Delta t/2, \tag{5.171}$$

$$s_n^{r+1} = s_n^r + ik_n \left(q_n^r + q_n^{r+1/2}\right) \Delta t/2, \tag{5.172}$$

where $q^{r+1/2}$ is a solution of the integral equations (5.162) and (5.164)–(5.165) for $s = \tilde{s}^{r+1/2}$, where $\tilde{s}^{r+1/2}$ is defined in terms of $s_n^{r+1/2}$ through (5.170).

In order to implement this time-stepping scheme, the coupled integral equations (5.162) and (5.164)–(5.165) must be solved for given bed shapes $\tilde{s}^r$ and $\tilde{s}^{r+1/2}$.

Solution of the Integral Equations

The nonlinear integral equations (5.162) and (5.164)–(5.165) solved for a given bed s using a Newton-Kantorovič iteration scheme (Rall, 1969; Miel, 1990, see also appendix C). Omitting time dependence, the integral equations may be written in operator form as

$$T(q, q_0, \bar{U}) \doteq$$
$$\left(q(x) - q_0 - \bar{U}s(x) + \beta \int_0^a K(x-y)s(y)\,\mathrm{d}y - \int_0^a K(x-y)N(y)\,\mathrm{d}y,\right.$$
$$\left.\int_0^a N(x) - \bar{N}\,\mathrm{d}x, \int_0^a \tau_b(x) - 1\,\mathrm{d}x\right) = 0, \tag{5.173}$$

where N and τ are functions of $\bar{U}$, q and s. Let the jth iterate be denoted by $(q^j, q_0^j, \bar{U}^j)$ (note that superscripts here no longer denote time discretisation). Each iteration step then takes the form

$$\begin{aligned} q^{j+1} &= q^j + \Delta q^j, \\ q_0^{j+1} &= q_0^j + \Delta q_0^j, \\ \bar{U}^{j+1} &= \bar{U}^j + \Delta \bar{U}^j, \end{aligned} \tag{5.174}$$

where the increments Δq^j, ΔU^j and Δq_0^j are defined in terms of the jth iterate by

$$T'_{(q^j, q_0^j, \bar{U}^j)} \left(\Delta q^j, \Delta q_0^j, \Delta \bar{U}^j\right) = -T(q^j, q_0^j, \bar{U}^j). \tag{5.175}$$

Here, T' denotes the Fréchet derivative[12] of the operator T at $(q^j, q_0^j, \bar{U}^j)$. Dropping superscripts ^{j},

$$T'_{(q,q_0,\bar{U})}(\Delta q, \Delta q_0, \Delta \bar{U}) = \Big(\Delta q(x) - \Delta q_0 - \Delta \bar{U} s(x) -$$

[12]To be precise, on would have to specify a Banach space in which the derivative is defined, see appendix C.

$$\int_0^a K(x-y)\left[\left.\frac{\partial\hat{N}}{\partial q}\right|_{q(y),q_0,\bar{U}}\Delta q(y)+\left.\frac{\partial\hat{N}}{\partial\bar{U}}\right|_{q(y),q_0,\bar{U}}\Delta\bar{U}\right]\mathrm{d}y,$$

$$\int_0^a\left.\frac{\partial\hat{N}}{\partial q}\right|_{q(y),q_0,\bar{U}}\Delta q(y)+\left.\frac{\partial\hat{N}}{\partial\bar{U}}\right|_{q(y),q_0,\bar{U}}\Delta\bar{U}\,\mathrm{d}y,$$

$$\int_0^a\left.\frac{\partial\hat{\tau}_b}{\partial q}\right|_{q(y),q_0,\bar{U}}\Delta q(y)+\left.\frac{\partial\hat{\tau}_b}{\partial\bar{U}}\right|_{q(y),q_0,\bar{U}}\Delta\bar{U}\,\mathrm{d}y\Bigg). \tag{5.176}$$

Thus, each iteration step amounts to the solution of a Fredholm integral equation of the second kind (the first 'component' of the three-component equation (5.175)) coupled with two linear equations for Δq_0 and $\Delta\bar{U}$ (the second and third 'components').

Since K is defined by a Fourier series from (5.163), we use a degenerate kernel approximation to solve the linear integral equations (5.175) (Atkinson, 1997, chapter 2, see also appendix C). Thus $K(x)$ is approximated by the finite sum

$$K_{r_0}(x-y)=\sum_{r=-r_0}^{r_0}K_r\exp(ik_rx)\exp(-ik_ry). \tag{5.177}$$

For brevity in notation, we define $\phi_r(x)=\exp(ik_rx)$. The Fredholm integral equation (the first component of (5.175)) with K replaced by K_{r_0} can be written as

$$\Delta q(x)=-f_1(x)+\Delta q_0+\Delta\bar{U}s(x)+\sum_{r=-r_0}^{r_0}K_r\int_0^a\frac{\partial\hat{N}}{\partial\bar{U}}(y)\phi_{-r}(y)\,\mathrm{d}y\,\phi_r(x)\Delta\bar{U}+$$

$$\sum_{r=-r_0}^{r_0}\int_0^a K_r\frac{\partial\hat{N}}{\partial q}(y)\phi_{-r}(y)\Delta q(y)\,\mathrm{d}y\,\phi_r(x), \tag{5.178}$$

where f_1 is the first 'component' of $T(q,q_0,\bar{U})$,

$$f_1(x)=q(x)-q_0-\bar{U}s(x)+\beta\int_0^a K(x-y)s(y)\,\mathrm{d}y-\int_0^a K(x-y)N(y)\,\mathrm{d}y. \tag{5.179}$$

An approximation to $\Delta q(y)$ can thus be calculated once the right-hand side of (5.178) is known. f_1 is known in principle from the previous iteration, as is $\int(\partial\hat{N}/\partial\bar{U})(y)\phi_{-r}(y)\,\mathrm{d}y$. It remains to determine the $2r_0+3$ constants Δq_0, $\Delta\bar{U}$ and γ_r, where γ_r is defined by

$$\gamma_r=\int_0^a K_r\frac{\partial\hat{N}}{\partial q}(y)\phi_{-r}(y)\Delta q(y)\,\mathrm{d}y,\qquad r=-r_0,\ldots,r_0. \tag{5.180}$$

Following the usual solution procedure for degenerate kernels, $2r_0+1$ linear equations for these constants can be obtained by multiplying both sides of (5.178) by $K_r\frac{\partial\hat{N}}{\partial q}\phi_{-r}$ and integrating. We simplify our notation by dropping the limits of summation

(sums over r will be over $-r_0, \ldots, r_0$) and integration (over $[0, a]$). We also omit the integration variable y as all integrands are functions of y only. Thus, for example, $\int(\phi_r \partial\hat{N}/\partial\bar{U})$ is to be interpreted as $\int_0^a \phi_r(y)\partial\hat{N}/\partial\bar{U}(y)\,\mathrm{d}y$. The relevant equations are then

$$\sum_r \left[\delta_{pr} - K_p \int \left(\phi_{r-p}\frac{\partial\hat{N}}{\partial q}\right)\right]\gamma_r - K_p \int \left(\phi_{-p}\frac{\partial\hat{N}}{\partial q}\right)\Delta q_0 -$$

$$\left[F_p \int \left(\phi_{-p}\frac{\partial\hat{N}}{\partial q}s\right) + \sum_r K_p K_r \int \left(\phi_{r-p}\frac{\partial\hat{N}}{\partial q}\right)\int \left(\phi_r \frac{\partial\hat{N}}{\partial\bar{U}}\right)\right]\Delta\bar{U} =$$

$$-K_p \int \left(\phi_{-p}\frac{\partial\hat{N}}{\partial q}f_1\right), \qquad p = -r_0, \ldots, r_0 \tag{5.181}$$

where δ_{pr} is the Kronecker delta. A further two equations are obtained by substituting Δq from (5.178) into the second and third components of (5.175):

$$\sum_r \int \left(\phi_r \frac{\partial\hat{N}}{\partial q}\right)\gamma_r + \int \left(\frac{\partial\hat{N}}{\partial q}\right)\Delta q_0 +$$

$$\left[\int \left(\frac{\partial\hat{N}}{\partial\bar{U}} + \frac{\partial\hat{N}}{\partial q}s\right) + \sum_r K_r \int \left(\phi_r\frac{\partial\hat{N}}{\partial q}\right)\int \left(\phi_r\frac{\partial\hat{N}}{\partial\bar{U}}\right)\right]\Delta\bar{U} = \int \left(f_1\frac{\partial\hat{N}}{\partial q}\right) - f_2, \tag{5.182}$$

$$\sum_r \int \left(\phi_r \frac{\partial\hat{\tau}_b}{\partial q}\right)\gamma_r + \int \left(\frac{\partial\hat{\tau}_b}{\partial q}\right)\Delta q_0 +$$

$$\left[\int \left(\frac{\partial\hat{\tau}_b}{\partial\bar{U}} + \frac{\partial\hat{\tau}_b}{\partial q}s\right) + \sum_r K_r \int \left(\phi_r\frac{\partial\hat{\tau}_b}{\partial q}\right)\int \left(\phi_r\frac{\partial\hat{\tau}_b}{\partial\bar{U}}\right)\right]\Delta\bar{U} = \int \left(f_1\frac{\partial\hat{\tau}_b}{\partial q}\right) - f_2, \tag{5.183}$$

where f_2 and f_3 are the second and third components of $T(q, q_0, \bar{U})$, respectively,

$$f_2 = \int_0^a \hat{N}(\bar{U}, q(y), s) - \bar{N}\,\mathrm{d}y, \tag{5.184}$$

$$f_3 = \int_0^a \hat{\tau}_b(\bar{U}, q(y), s) - 1\,\mathrm{d}y. \tag{5.185}$$

The coefficients in these equations have to be calculated numerically using the previous iterate. Note that, since s is periodic with period a, and the initial guess for q is chosen to be periodic, every iterate of q and hence all the integrands above are periodic. An appropriate choice of quadrature rule is therefore the composite trapezium rule (e.g Atkinson, 1989, pp. 285–289) with n_{int} grid points, where $n_{int} \gg r_0$.[13]

[13]Typically, $n_{int} = 8 \times r_0$ was used.

Once the coefficients have been calculated, equations (5.181)–(5.183) can be solved by Gaussian elimination. Δq can then be recovered from (5.178), where f_1 and $\int(\phi_{-r}\partial\hat{N}/\partial\bar{U})$ are evaluated from the previous iterate using the composite trapezium rule as above. Convergence can be tested for by evaluating $T(q, q_0, \bar{U})$ numerically for the new iterate, again using the composite trapezium rule.

The Functions $\hat{N}(\bar{U}, q, s)$ and $\hat{\tau}_b(\bar{U}, q, s)$

So far, we have only stated that $q = Q(\bar{U}, N, s)$ is inverted to find $N = \hat{N}(\bar{U}, q, s)$ and hence $\tau_b = \hat{\tau}_b(\bar{U}, q, s)$. In the simulations carried out, a Boulton-Hindmarsh rheology (5.152) was used to define $Q(\bar{U}, N, s)$ and $\tau(\bar{U}, N, s)$:

$$Q(\bar{U}, N, s) = \frac{\bar{U}(N/\alpha)}{n-2}\left[1 - \frac{(n-1)(1+s)(N/\alpha)^{n-2}}{(N/\alpha+1+s)^{n-1} - (N/\alpha)^{n-1}}\right], \tag{5.186}$$

$$\tau(\bar{U}, N, s) = \left[\bar{U}\frac{(\bar{N}/\alpha+1)^{n-1} - (\bar{N}/\alpha)^{n-1}}{(\bar{N}/\alpha+1)^{n-1}(\bar{N}/\alpha)^{n-1}}\frac{(N/\alpha+1+s))^{n-1}(N/\alpha)^{n-1}}{(N/\alpha+1+s)^{n-1} - (N/\alpha)^{n-1}}\right]^{1/m}. \tag{5.187}$$

Figure 5.4 shows plots of Q and τ_b against N for $\bar{N} = \alpha = \bar{U} = 1$, $s = 0$ and at various values of $m = n$. As the figure indicates, $q = Q(\bar{U}, N, s)$ is a monotonically increasing function of N and hence the inversion $N = \hat{N}(\bar{U}, q, s)$, where it exists, is single-valued. Note that Q and τ are both positive as required and are only defined for positive N and $\bar{U}$. Hence $\hat{N}(\bar{U}, q, s)$ only exists for $\bar{U} > 0$ and $q > 0$. It is further possible to show that $Q(\bar{U}, N, s) < \bar{U}(1+s)/2$ — this is evident in the top panel of figure 5.4, where Q does not exceed $\bar{U}(1+s)/2 = \frac{1}{2}$ — so $\hat{N}(\bar{U}, q, s)$ only exists for $q < \bar{U}(1+s)/2$.

In general, the inversion of Q can only be carried out numerically,[14] which is achieved using a Newton iteration scheme. The partial derivatives appearing in equations (5.178) and (5.181)–(5.183) can then be calculated from the derivatives of Q and τ defined above using the formulae

$$\frac{\partial\hat{N}}{\partial q} = 1/\frac{\partial Q}{\partial N}, \qquad \frac{\partial\hat{N}}{\partial\bar{U}} = -\frac{\partial Q}{\partial\bar{U}}/\frac{\partial Q}{\partial N},$$

$$\frac{\partial\hat{\tau}_b}{\partial q} = \frac{\partial\tau}{\partial N}\frac{\partial N}{\partial q}, \qquad \frac{\partial\hat{\tau}_b}{\partial\bar{U}} = \frac{\partial\tau}{\partial\bar{U}} + \frac{\partial\tau}{\partial N}\frac{\partial N}{\partial\bar{U}}. \tag{5.188}$$

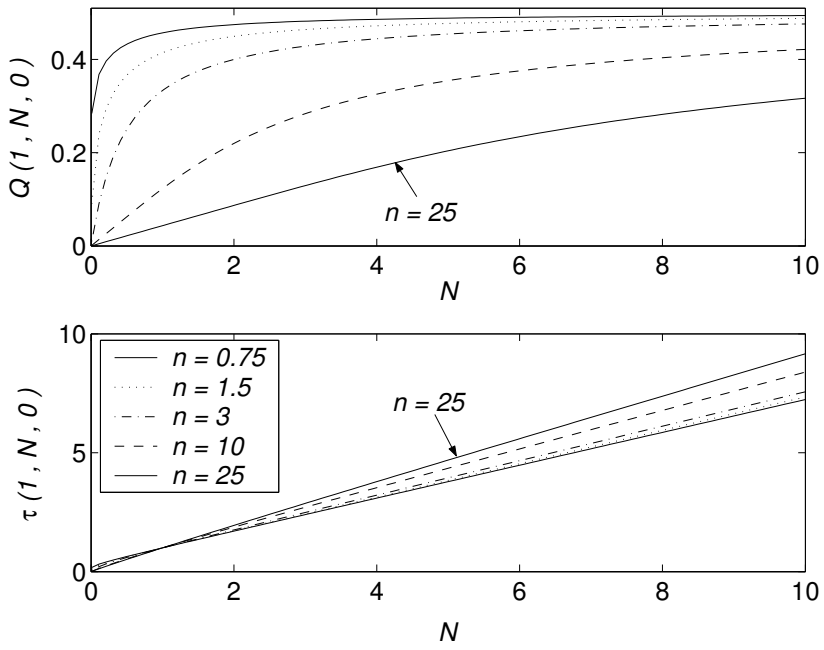

Figure 5.4: The top panel shows till flux Q at $\bar{N} = \alpha = \bar{U} = 1$ and $s = 0$ as a function of N and at various values of the exponent n. The bottom panel shows τ_b for the same parameter choices as a function of N and at various values of n. Note that we have set $m = n$. The key in the lower panel, relating line type to exponent n, is also valid for the upper panel.

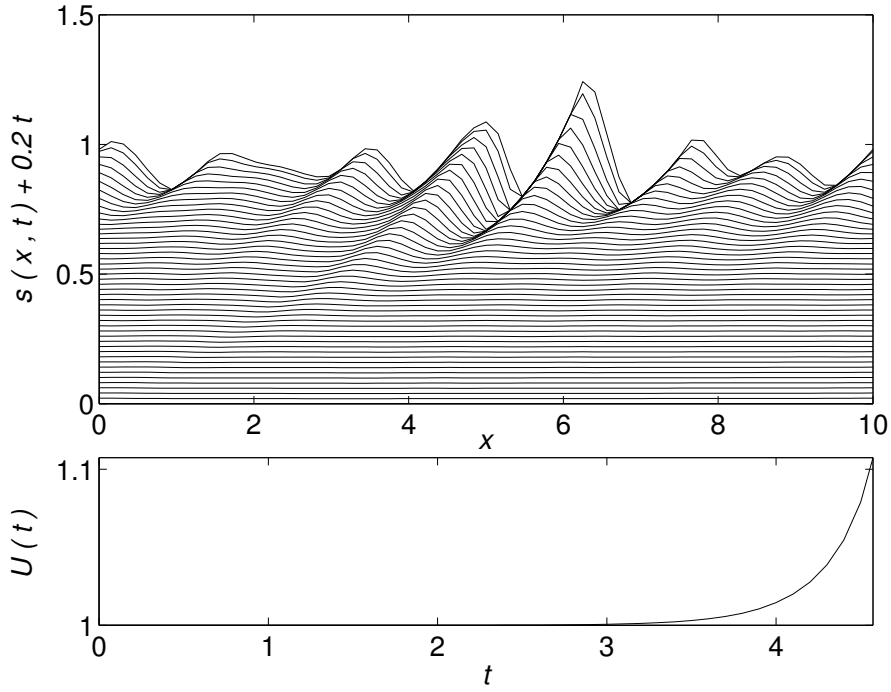

Figure 5.5: Numerical solution of the nonlinear bedform evolution model with parameters $m = n = 3$, $\alpha = 5$, $\beta = 0.5$, $\bar{N} = 3$ and $a = 10$. The top panel shows solutions $s(x, t)$ at various times t plotted against x. For ease of viewing, these solutions are staggered, so that the plot actually shows $s + 0.2t$. The bottom panel shows $\bar{U}(t)$ plotted against t. Note that $\bar{U}$ increases with time, which may seem counterintuitive. The simulation was stopped when effective pressure reached zero in the lee of the largest bedform.

5.7 Results

Figure 5.5 shows a typical result of one of the numerical simulations, carried out with randomised initial conditions. The top panel shows the solution s at against x, staggered with increasing time t for ease of viewing. The instability is evident from this figure: The initially nearly flat bed evolves regular waves of growing amplitude. The bottom panel shows the sliding velocity $\bar{U}$ plotted against time. A curious result here is that $\bar{U}$ increases as the bed develops irregularities. This can be attributed to the fact that $\bar{U}$ is not determined by the 'geometrical' resistance of the bed which determines sliding velocity in classical hard-bed sliding (section 2.3) — this is a higher-order effect here and therefore ignored in the leading order model — but by the rheological properties of till through equation (5.165).

The main feature of figure 5.5 is that the simulation stops although no steady or travelling wave solution has been attained. Figure 5.6 shows the reason for this: Once the bed bumps have reached a sufficient size, the variations in normal stress due to the flow of ice over them become sufficiently large to cause effective pressure N to go to zero. As in the classical hard-bed case, the ice then separates from the bed and a cavity forms. The model formulated here cannot take account of cavitation and consequently breaks down, and the simulation stops.

Cavitation was observed in all the simulations carried out. It appears therefore that the nonlinearity in $\hat{N}(\bar{U}, q, s)$ and $\hat{\tau}_b(\bar{U}, q, s)$ is insufficient to lead to bounded growth and the evolution of a steady or travelling wave pattern of bedforms. We consider the reformulation of the model for the case of cavitation in chapter 6. However, as a solution of the full nonlinear model in the presence of cavitation turns out to be prohibitive, we will only study a special limit of the Boulton-Hindmarsh rheology in that chapter.

Before doing so we wish to study the effect of varying the various model parameters on the results obtained so far, in the hope that this will provide some further insights.

5.7.1 Deep Sediment Layers

As mentioned in the review of the geological literature on drumlins in section 1.2, many drumlins have a stratified core which has not undergone significant deformation. The question which we wish to address here is whether the present model can be reconciled with this observation.

[14] A notable exception is $n = 3$, for which $N = \alpha(1+s)q/[\bar{U}(1+s) - 2q]$.

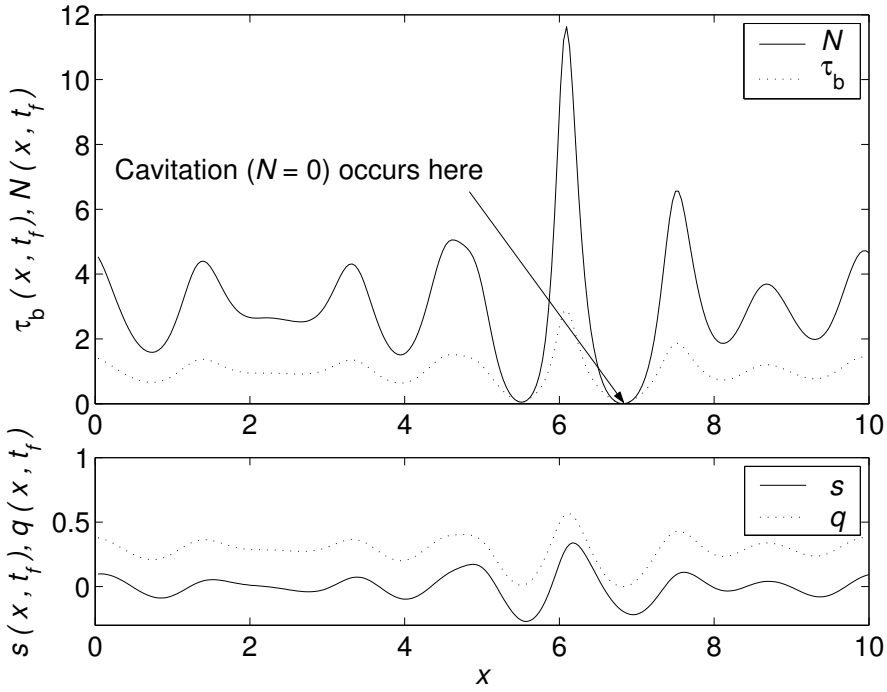

Figure 5.6: The bottom panel shows the bed shape (here smoothed by trigonometric interpolation) and till flux at the end of the simulation shown in figure 5.5. The top panel shows effective pressure N and shear stress τ_b at the end of the simulation. Note that effective pressure N, and hence shear stress τ_b and flux q, reach zero in the lee of the largest bedforms. This indicates an incipient cavity. Note that till flux decreases across the top of the largest bedform, which demonstrates that it is still growing when cavitation first occurs.

Typically, till deformation is observed to be limited to a certain thickness below the ice-till interface (see section 2.4). If one wishes to construct a model for drumlin formation by till deformation which accounts for stratified cores, then this deforming thickness must correspond to the till sheath usually found on drumlins (see section 1.2), and must be considerably smaller than the height of the drumlin itself.

The model formulated in section 5.2 assumes that deforming till is underlain at some fixed depth $z = -d$ by an undeformable substratum. The instability mechanism therefore ostensibly leads to variations in the thickness of deforming till — $d + s(x, t)$ in dimensional terms — but it does not appear to affect the underlying, potentially stratified substratum. The interface between unstratified till and undeformable substratum remains at $z = -d$.

An obvious modification of the model which allows the interface between till and substratum to evolve is to endow till with a yield stress $\tau_c = \mu p_e + C$ (cf. equation (2.72)), below which no deformation occurs. Such a yield stress can in principle be included in the model if $F(\tau, p_e)$ is defined by a Herschel-Bulkley model for till (2.71). It is, however, possible to gain some insight into the evolution of a till layer underlain by an 'undeformable' substratum using the simpler Boulton-Hindmarsh rheology (2.70) adopted here. The reason for this is that till deformation remains concentrated near the ice-till interface for appropriate choices of the exponent n, regardless of the thickness of the till. If till deformation is sufficiently concentrated near the top of the till, then one can consider the lower parts of the 'deforming' till to be essentially undisturbed, as total strain there remains small over times of $O(1)$. The boundary between till and stratified sediment then no longer needs to lie at $z = -d$. Rather, there will be a more gradual change from highly deformed material near the ice-till interface to virtually undeformed — and hence potentially stratified — material near $z = -d$.

To see how deformation is concentrated near the top of the deforming till layer, note that the mean thickness of the deformable layer in the model is d, which enters into the reduced model through the parameters $\alpha = (\rho_b - \rho_w)gd/\bar{\tau}$ and $\beta = (\rho_w - \rho_i)\alpha/(\rho_b - \rho_w)$, so thick till corresponds to large α. Figure 5.7 shows profiles of till velocity $U(Z)$ versus depth Z (cf. equation (5.64)) for Boulton-Hindmarsh rheologies with different exponents n at parameter values $\tau_b = 1$, $N = \bar{N} = 1$, $s = 0$ and $\alpha = 10$, which corresponds to p_e increasing to over ten times the driving stress at the bottom of the deformable till. Dimensionally, $\alpha = 10$ with $\bar{\tau} = 10^5$ Pa and $\rho_b - \rho_w = 1000$ kg m^{-3} corresponds to $d = 100$ m. It is evident from figure 5.7 that deformation is concentrated near the top of the till for $n = 2.25$ and larger. For such

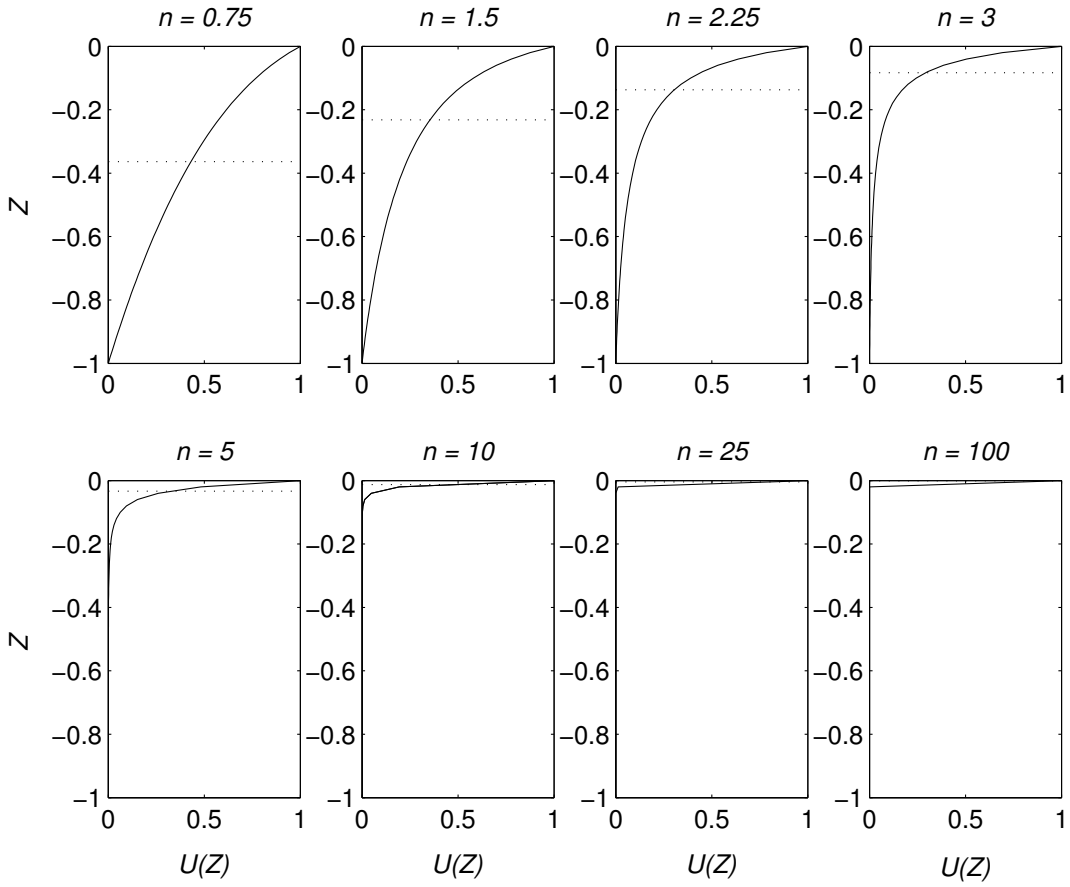

Figure 5.7: Horizontal velocity $U(Z)$ is plotted on the horizontal axis against depth in the till on the vertical axis for a variety of parameter choices n. In all cases, $\tau = 1$, $N = \bar{N}$, $s = 0$ and $\alpha = 10$; dimensionally this roughly corresponds to a till thickness of 100 m. The dotted lines are at $Z = -q/\bar{U}$, and thus show the 'effective thickness' of the deforming till defined in the text.

rheologies the deeper parts of the till are essentially undeformed (although there is no sharp boundary between deformed and undeformed material as there would be for a Herschel-Bulkley material). By contrast, deformation is not obviously concentrated near the ice-till surface when $n = 1.5$ or less.

To obtain a measure of the depth to which thick deformable sediment is significantly sheared, one can consider the ratio of dimensional flux to dimensional surface velocity,

$$d_{eff} \doteq q/u|_{z=s} = d \times q^\star/\bar{U}^\star = \frac{\alpha q^\star}{(\rho_b - \rho_w)g\bar{U}^\star}, \tag{5.189}$$

where q and $u|_{z=s}$ are dimensional while their starred equivalents are dimensionless. d_{eff} is the *dimensional* thickness of till which would generate flux q if it moved at a uniform velocity $u|_{z=s}$. Examination of the dimensionless $Q(\bar{U}, N, s)$ defined in (5.186) shows that

$$\alpha Q(\bar{U}, N, s)/\bar{U} \sim \begin{cases} N/(n-2) & n > 2, \\ (n-1)(1+s)^{2-n}N^{n-1}\alpha^{2-n}/(2-n) & 1 < n < 2 \\ (1-n)(1+s)\alpha/(2-n) & 0 < n < 1. \end{cases} \tag{5.190}$$

as $\alpha \to \infty$ while N, $s = O(1)$. Hence $\alpha q^\star/\bar{U}^\star$ in (5.189) approaches a finite limit $N/(n-2)$ when $n > 2$ and $\alpha \to \infty$; this corresponds to the dimensional deformation thickness d_{eff} approaching a finite limit,

$$d_{eff} \to \frac{p_e|_{z=s}}{(n-2)(\rho_b - \rho_w)}, \tag{5.191}$$

as $d \to \infty$ and when $n > 2$, where $p_e|z = s$ is the dimensional interfacial shear stress. For $n < 2$, the deformation thickness d_{eff} continues to increase with d. This is clearly in agreement with figure 5.7. Till deformation is concentrated near the top of the till only for $n > 2$. Since deformation of real subglacial sediment is generally observed to be confined to a relatively narrow layer near the ice-till interface (e.g. Boulton and Hindmarsh, 1987), we conclude that power-law rheologies (2.70) can only be viable when $n > 2$ (although a model which does incorporate a yield stress may be preferable, as the boundary between deformed and undeformed material is usually fairly sharp in real subglacial sediments). In the rest of this thesis, we therefore only consider the case $n > 2$.

Evolution of Bedforms in Deep Sediment

If the bedform evolution model studied here is to be successful at predicting stratified drumlin cores, then the height of the evolved bedform must be considerably larger

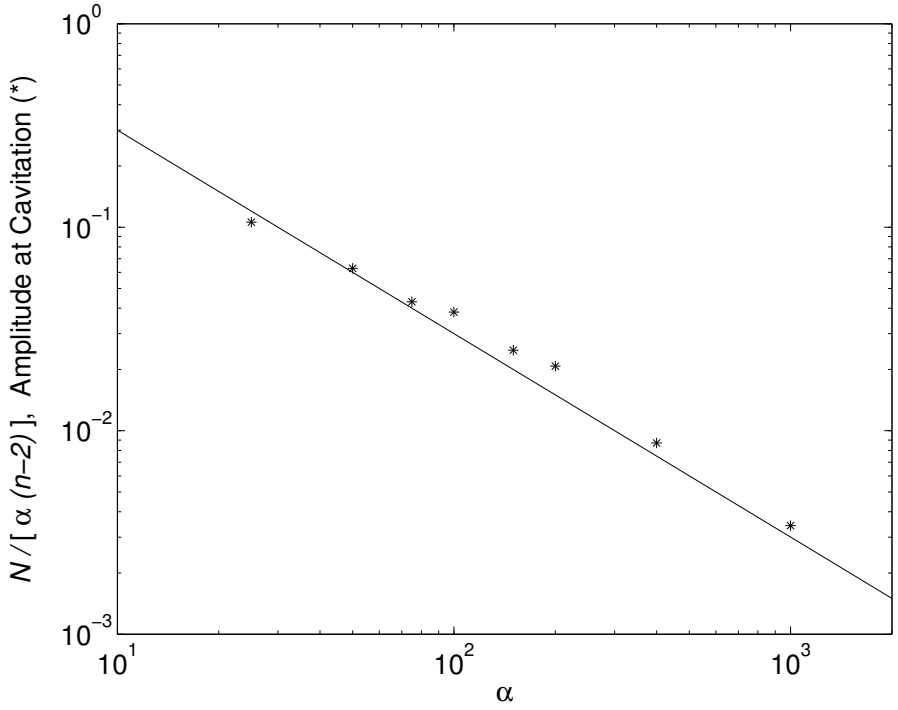

Figure 5.8: Each star denotes the maximum value of $s(x)$ attained at the final time step before cavitation during a simulation of the nonlinear model with parameter values $\bar{N} = 3$, $m = n = 3$, $\beta = 0.1\alpha$ and at the value of α shown on the horizontal axis. The solid line is a plot of $\bar{d}_{eff}/d = \bar{N}/[\alpha(n-2)]$ against α.

than the thickness of the effectively deforming till, and hence must be considerably larger than d_{eff} provided $d \gg d_{eff}$.[15] In dimensionless terms, this corresponds to dimensionless s being much larger than $d_{eff}/d \sim N/[\alpha(n-2)]$.

The main difficulty here is that we are not yet able to make any definitive statements about the fully evolved bedform as our model breaks down at cavitation. One can, however, hope that cavitation eventually leads to bounded growth, and that the height of the evolved bedforms is comparable to their height when cavitation first occurs. In this spirit, we compare the dimensionless height of bedforms at cavitation with d_{eff}/d — or more precisely, with $\bar{d}_{eff}/d$, where $\bar{d}_{eff} = \bar{N}d/[\alpha(n-2)]$ is the mean of d_{eff} over the bed when d is large.

Figure 5.8 shows the maximum value of $s(x)$ attained at the final time step before cavitation in a series of simulations in which $m = n = 3$, $\bar{N} = 3$, $\beta = 0.1\alpha$, and α is varied. Each maximum value of s is plotted as a point against the corresponding α, and the solid line is a plot of $\bar{d}_{eff}/d = \bar{N}/[\alpha(n-2)] = 3/\alpha$ against α (note the

[15]Since the evolved bedform cannot be much larger than the mean thickness of available sediment d, the evolved bedform in our model cannot be much larger than d_{eff} when $d \sim d_{eff}$

logarithmic scales). Although the maximum value of s is generally slightly larger than $3/\alpha$, the difference is not large and importantly, the maximum amplitude attained decreases at the same rate as $3/\alpha$. At least at cavitation, the height of the bedform is comparable to the effectively deforming thickness of till.

These results suggest that the dimensionless bed elevation $s^\star$ — the asterisk is reintroduced for definiteness — should be rescaled as $s^{\star\star} = (d/\bar{d}_{eff})s^\star = [(n-2)\alpha/\bar{N}]s^\star$ when α is large. In other words, the scale for the *dimensional* bed height s should no longer be d but $\bar{d}_{eff} = d \times \bar{N}/[\alpha(n-2)]$. The reason for this is presumably that the flux scale $[q]$ was chosen as $[u_b]d$ in equation (5.17) (see section 5.3); as the discussion above shows, when d is large a more appropriate scale is

$$[q] = [u_b]\bar{d}_{eff} = \frac{[u_b]\bar{p}_e}{(n-2)(\rho_b - \rho_w)g}, \tag{5.192}$$

where $\bar{p}_e = \rho_i g D - p_c$. The rescaling indicated here then follows straightforwardly from (5.16), which states amongst other things that

$$[s] = [q]/[u_b], \tag{5.193}$$

i.e. the instability amplitude scale $[s]$ is inherently equal to the effective thickness of deforming till. In addition to the change in scale $[s]$, $[x]$ also needs to be changed as the scale relations (5.16) and (5.19)–(5.20) with $[q]$ defined by (5.192) rather than (5.17) yield

$$[x] = (\eta[q]/\bar{\tau})^{1/2} = (\bar{d}_{eff}/d)^{1/2}(\eta[u_b]d/\bar{\tau})^{1/2} \tag{5.194}$$

The appropriate rescaling for $\alpha \gg 1$ is thus $x^{\star\star} = (d/\bar{d}_{eff})^{1/2}x^\star = [(n-2)\alpha/\bar{N}]^{1/2}x^\star$. This can be confirmed by considering the wavelength of the fastest growing mode in the linear stability analysis: Equations (5.154)–(5.155) show that Q_N behaves as

$$Q_N \sim \frac{1}{\alpha(n-2)}, \qquad \text{as } \alpha \to \infty,\ \bar{N} = O(1). \tag{5.195}$$

Calculating the fastest growing wavelength λ_{max} from (5.118) as

$$\lambda_{max} = \frac{2\pi}{k_{max}} = 2\pi\left[\frac{2Q_N}{\sqrt{3}}\right]^{1/2} \sim 2\pi\left[\frac{2}{\sqrt{3}(n-2)\alpha}\right]^{1/2}, \tag{5.196}$$

we see that the instability length scale behaves as predicted when $\bar{N} = O(1)$ and $\alpha \gg 1$.

The results above indicate that the scale relations (5.192)–(5.193) are appropriate and hence that the instability amplitude scale is equal to the thickness of effectively

deforming till. The model therefore seems unlikely to produce stratified cores. Combined with the earlier result, that the model is unable to predict three-dimensional instabilities in the limit $\nu \ll 1$, our results so far provide a strong indication that Hindmarsh's (1998b) and Fowler's (2000) models may not be appropriate descriptions of drumlin formation. However, we cannot make any definitive statements yet as we still need to model the evolution of the predicted bedforms after cavitation.

5.7.2 The Plastic Limit

Laboratory studies of till typically indicate that till behaves as a plastic material (Kamb, 1991; Iverson and others, 1998; Iverson and Iverson, 2001, see also section 2.4). In other words, experiments indicate that till deforms irreversibly when a yield stress τ_c is reached, but this stress also cannot be exceeded. In a viscous rheology of the Boulton-Hindmarsh type (2.70), such behaviour can be accommodated approximately if the exponents m and n are allowed to become large simultaneously (see also Kamb, 1991; Hooke and others, 1997). Specifically, consider $\tau(\bar{U}, N, s)$ for a Boulton-Hindmarsh rheology, which may be re-written from (5.187) as

$$\tau(\bar{U}, N, s) =$$

$$\bar{U}^{1/m} \left(\frac{N}{\bar{N}}\right)^{(n-1)/m} \left[1 - \left(\frac{\bar{N}/\alpha}{\bar{N}/\alpha + 1}\right)^{n-1}\right]^{1/m} \left[1 - \left(\frac{N/\alpha}{N/\alpha + 1 + s}\right)^{n-1}\right]^{-1/m}. \tag{5.197}$$

When $m \sim n \to \infty$ and N, $\bar{N}$, α, $s = O(1)$, the terms in square brackets tend to unity. Consequently

$$\tau(\bar{U}, N, s) \sim \bar{U}^{1/m} \left(\frac{N}{\bar{N}}\right)^{(n-1)/m} \left[1 + O\left(\frac{1}{m} M^{n-1}\right)\right], \tag{5.198}$$

where

$$M = \max\left(\frac{\bar{N}/\alpha}{\bar{N}/\alpha + 1}, \frac{N/\alpha}{N/\alpha + 1 + s}\right) < 1 \tag{5.199}$$

since $N > 0$ and $1 + s > 0$ if the till is not to be pinched out. Since $m \sim n$, the exponent of $N/\bar{N}$ behaves as $(n-1)/m \sim 1$. Hence

$$\tau \sim \bar{U}^{1/m} \frac{N}{\bar{N}}. \tag{5.200}$$

Thus τ is proportional to N at leading order, as would be the case for a Coulomb failure criterion (2.72) with zero cohesive term, and depends only weakly on $\bar{U}$ — in the perfectly plastic case, τ is entirely independent of $\bar{U}$.

The plastic limit $m \sim n \gg 1$ may therefore represent the physically most realistic type of viscous rheology, as it corresponds most closely to experimental results. In order to understand how the present bedform model is affected when the exponents m and n become large, we consider the till flux $Q(\bar{U}, N, s)$ defined in (5.186), which can be expressed as

$$Q(\bar{U}, N, s) =$$
$$\frac{\bar{U}N}{\alpha(n-2)} + \frac{\bar{U}(n-1)(1+s)}{(n-2)} \left(\frac{N/\alpha}{N/\alpha + 1 + s} \right)^{n-1} \left[1 - \left(\frac{N/\alpha}{N/\alpha + 1 + s} \right)^{n-1} \right] \quad (5.201)$$

For $\bar{U},\ N, s, \alpha = O(1)$, the first term on the right-hand side behaves as $O(1/n)$, while the second behaves as $O(M^n)$, where $M < 1$ is defined in (5.199) above. Hence the second term tends to zero exponentially, while the first tends to zero algebraically, i.e. more slowly. Consequently

$$Q \sim \frac{\bar{U}N}{\alpha(n-2)} \left[1 + O\left(nM^n\right) \right]. \quad (5.202)$$

The leading-order expression for $Q \sim \bar{U}N/[\alpha(n-2)]$ is familiar from section 5.7.1, equation (5.190). It shows that flux behaves as $1/n$ when the exponent n becomes large (see also Alley and others, 1997). In other words, the thickness of the deforming layer decreases as $1/n$. Such a decrease is also evident in figure (5.7), where deformation becomes increasingly concentrated at the top of the till as n is increased. As in section 5.7.1, we expect that the bed amplitude at cavitation scales with the effective thickness of deforming till, and this is confirmed in figure 5.9. Hence the dimensional bed amplitude at cavitation scales with $\bar{d}_{eff}$ as in section 5.7.1, where

$$\bar{d}_{eff} = \frac{\bar{p}_e}{(n-2)(\rho_b - \rho_w)}.$$

It is worth calculating d_{eff} for some reasonable values of effective pressure $\bar{p}_e$ and densities ρ_b and ρ_w. When $\bar{p}_e = 10^5$ Pa, $\rho_b - \rho_w = 1000$ kg m^{-3} and $g = 10$ m s^{-2},

$$\bar{d}_{eff} = \frac{10}{n-2} \text{ metres}. \quad (5.203)$$

Thus, even at a moderately low value of $n = 10$, one expects cavitation to occur when bedforms have reached a typical height of only about 1 m; this is much smaller than the heights of real bedforms, which are on the order of tens of metres. The present model for bedform evolution can therefore only explain the observed sizes of bedforms if n is not too large and if there is considerable further growth after cavitation.

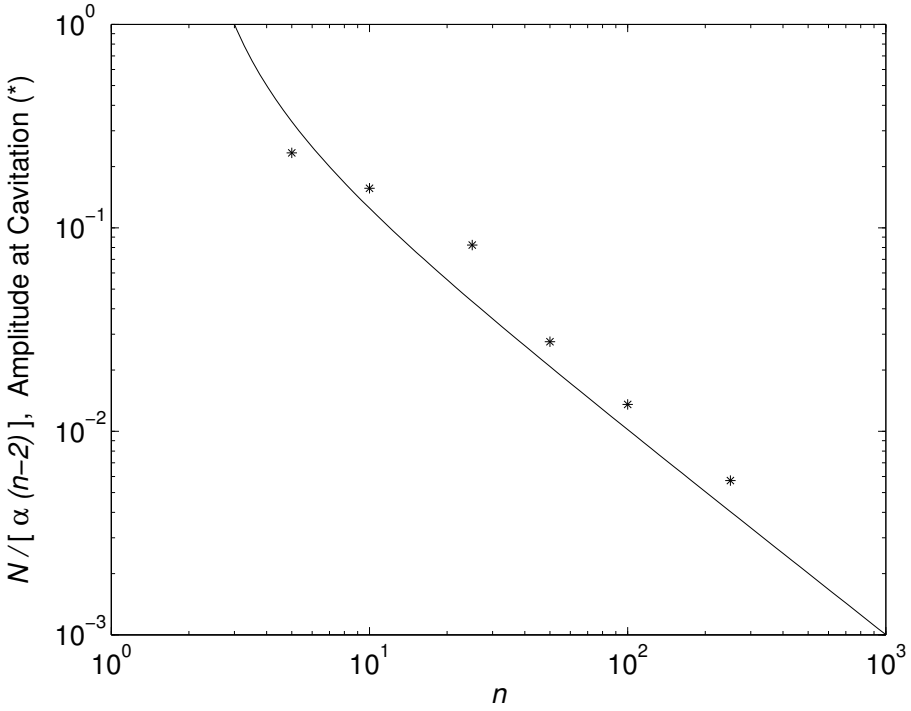

Figure 5.9: Each star denotes the maximum value of $s(x)$ attained at the final time step before cavitation during a simulation of the nonlinear model with parameter values $\bar{N} = 1$, $\alpha = 1$, $\beta = 0.1\alpha$, $m = n$ and at the value of n shown on the horizontal axis. The solid line is a plot of $\bar{d}_{eff}/d = \bar{N}/[\alpha(n-2)]$ against n. Note that the maximum amplitude at cavitation clearly scales with $\bar{N}/[\alpha(n-2)]$.

A Quasi-Linear Model

The leading order expression for Q in (5.202) is linear in N — this linearity is evident in the top panel of figure 5.4, where the plot of Q against N for $n = 25$ is almost a straight line for moderate values of N. It turns out that this allows the model to be simplified further if we also choose $m = n - 1$. In that case, (5.197) yields τ as

$$\tau \sim \bar{U}^{1/(n-1)} \frac{N}{\bar{N}} \left[1 + O(M^n/n)\right]. \tag{5.204}$$

Integrating both sides over one period of the bed and using the integral constraints (5.164) and (5.165) on N and τ yields

$$\frac{1}{a}\int_0^a \tau(x,t)\,\mathrm{d}x = 1 = \bar{U}(t)^{1/(n-1)} \frac{1}{a}\int_0^a \frac{N(x,t)}{\bar{N}} \left[1 + O(M^n/n)\right]\,\mathrm{d}x =$$

$$\bar{U}(t)^{1/(n-1)} \left[1 + O(M^n/n)\right], \tag{5.205}$$

and hence

$$\bar{U}(t) = 1 + O(M^n). \tag{5.206}$$

By setting $\bar{U} = 1$, Q in (5.202) becomes linear,[16]

$$Q = \frac{N}{\alpha(n-2)}. \tag{5.207}$$

Substituting $\bar{U} = 1$ and $N = \alpha(n-2)q$ renders the integral equation (5.162) linear. In essence, we obtain a linear model in q and s; this is, however, only valid provided $N > 0$ everywhere on the bed and hence provided no cavities form. If growth occurs in this linear model — which it must because $Q_N = 1/[\alpha(n-2)] > 0$ — then growth must be unbounded, at least until cavitation occurs. However, once cavities are formed, the presence of cavity boundary points introduces a new nonlinearity into the model, which may ultimately lead to bounded growth. In chapter 6, we return to investigate this point further.

We conclude by noting that an analytical solution based on the linearisation $\bar{U} = 1$, $Q = \alpha(n-2)N$, where $N > 0$, is readily available from the linear stability analysis in section 5.5; one simply needs to set $Q_s = 0$ and $Q_N = \alpha(n-2)$. This analytical solution may be compared with a numerical solutio.n for the full nonlinear model. Results are shown in figure 5.10 Clearly, the analytical and numerical solutions for s are almost indistinguishable.

[16]Setting $\bar{U} = 1$ assumes that effective pressure $N(x)$ does remain bounded uniformly for large exponents n, so that M does not approach unity for large n.

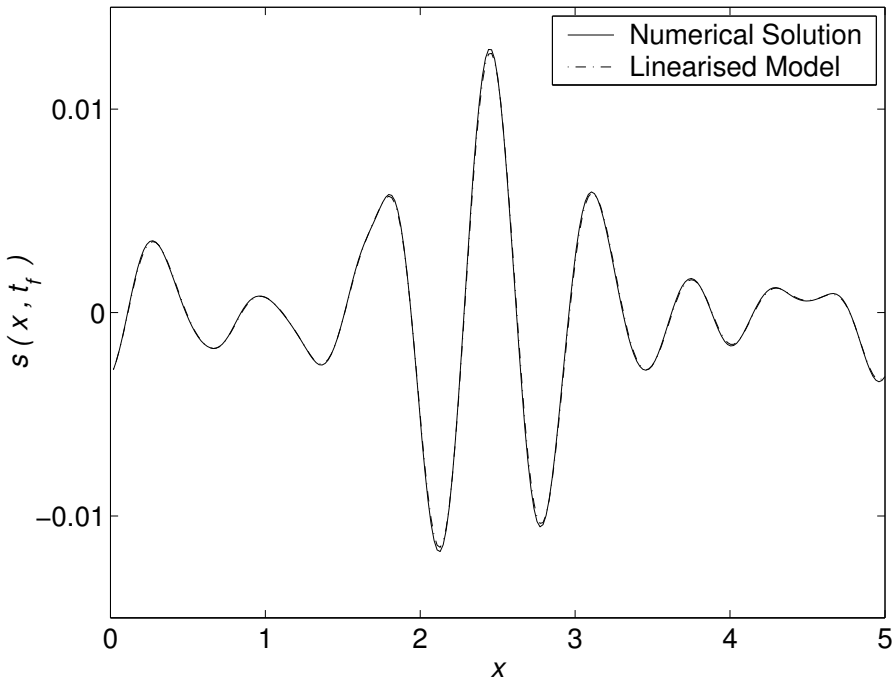

Figure 5.10: The solid line shows the shape of the bed at the final time step in a simulation with parameter values $n = 100$, $m = 99$, $\bar{N} = 1$, $\alpha = 1$. The dot-dashed line shows the shape of the bed calculated for the same initial conditions and at the same value of t using the linearised rheology (5.207). Note that the sliding velocity $\bar{U}(t)$ calculated numerically stayed at unity within numerical error during the numerical simulation.

5.8 Discussion

In this chapter, we constructed a simplified model which encapsulates the essence of the instability mechanism proposed by Hindmarsh (1998b) and Fowler (2000) to explain the formation of subglacial bedforms. The mechanics of the instability were analysed and it was shown that the flow of ice over a bump on a deformable bed can lead to a combination of changes in interfacial effective pressure and shear stress which cause the bump to grow.

Our analysis also shows that the instability is inherently two-dimensional, at least in our leading-order model. This suggests that the mechanism proposed by Hindmarsh and Fowler may not be able to explain the formation of three-dimensional features such as drumlins, but only that of Rogen moraines.

Numerical solutions of the reduced nonlinear model constructed in section 5.6 show that the instability is not quenched before cavitation sets in. One may therefore suspect that, if the growth of the predicted bedforms is to be bounded, the formation of cavities must provide some kind of mechanism for this to happen. Specifically, we expect the appearance of cavity boundary points to introduce additional nonlinearities into the model which ultimately lead to bounded growth.

In sections 5.7.1 and 5.7.2, the effect of changing the thickness of the available deformable sediment and of changing the rheological exponents m and n was addressed. The central result here was that, when cavitation first occurs, the height of the bedform is comparable to the 'effectively deforming' thickness of the till layer, defined as the dimensional ratio of till flux to surface velocity. At least at cavitation, the bedforms predicted by Hindmarsh and Fowler's model do not have stratified cores.

A further result of section 5.7.2 is that till flux may be linearised for quasi-plastic rheologies which have large exponents $n \gg 1$ and $m = n - 1$. This will be used again in chapter 6, where we address how to modify the model to allow for cavitation.

Chapter 6

Cavitation on Deformable Beds

6.1 Introduction

The bedform evolution model described in chapter 5 may be summed up as follows: The interface between ice and till $s(x,t)$ evolves according to an integrated mass-conservation equation for the till,

$$\frac{\partial s}{\partial t} + \frac{\partial q}{\partial x} = 0. \tag{6.1}$$

The till flux q is a function of the till thickness, and hence of s, but crucially, it is also a function of shear stress τ_b and effective pressure N at the ice-till boundary. τ_b and N are determined by a solution of the ice flow equations, in which they appear in the boundary conditions.

In this section, we consider how these boundary conditions change when there are cavities present. The resulting model is then analysed in the later sections of this chapter. However, owing to the complexity of the full time-dependent model, we only establish the existence of travelling wave solutions for cavitated beds in section 6.3. A full analysis of the time-dependent model for cavitated beds is left for future work. Although we are therefore unable to discuss the actual evolution of bedforms after cavitation, we may hope that they will ultimately form travelling waves of the type constructed here.

As in the later sections of chapter 5, we restrict ourselves to two dimensions. For later convenience — as we will wish to use z to denote the complex variable $z = x+iy$ — the vertical axis will be re-labelled as the y-axis, and v rather than w will denote the vertical component of velocity. One further simplification will be introduced from the outset: we set $\beta = 0$, which is tantamount to saying that ice and water have the same density. This is, of course, not strictly true, but as we stated before, β is generally small, and requiring it to vanish does not affect the instability mechanism

significantly (see section 5.5.2). Furthermore, setting $\beta = 0$ simplifies some of the analysis which follows.

Recall that the ice flow equations for the model without cavities may be written, with the above changes of notation, as (cf. section 5.4.2)

$$\nabla^2 \mathbf{u} - \nabla p = \mathbf{0} \qquad \text{on } y \in (0, \infty), \tag{6.2}$$

$$\nabla \cdot \mathbf{u} = 0 \qquad \text{on } y \in (0, \infty), \tag{6.3}$$

where $\mathbf{u} = (u, v)$ is the reduced velocity field and p the pressure field. Boundary conditions at infinity are

$$\frac{\partial u}{\partial y} \sim 0, \qquad p \sim 0 \qquad \text{as } y \to \infty. \tag{6.4}$$

At the base of the ice, boundary conditions are

$$v = \bar{U}\frac{\partial s}{\partial x} - \frac{\partial q}{\partial x}, \qquad \frac{\partial u}{\partial y} + \frac{\partial v}{\partial x} = \tau_b - 1 \qquad \text{on } y = 0, \tag{6.5}$$

where $\bar{U}(t)$ is a mean sliding velocity which is independent of position and τ_b is interfacial shear stress.

The interfacial shear stress is related to sliding velocity $\bar{U}$ through some 'sliding law' which arises as a result of shearing in the till,

$$\bar{U} = u_b(\tau_b, N, s), \tag{6.6}$$

where interfacial effective pressure N is defined as — bearing in mind that $\beta = 0$ —

$$N = \bar{N} + p - 2\frac{\partial v}{\partial y} \qquad \text{on } y = 0. \tag{6.7}$$

Here we choose to express the relationship between $\bar{U}$ and τ_b in the form widely used in chapter 5,

$$\tau_b = \tau(\bar{U}, N, s), \tag{6.8}$$

which results from inverting (6.6). The sliding velocity $\bar{U}$ can then in principle be determined by the integrated momentum conservation equation

$$\int_0^a \left[\tau(\bar{U}, N, s) - 1\right] \, \mathrm{d}x = 0, \tag{6.9}$$

where a is the period of the bed. Till flux q can be expressed in various ways, for instance one can set $q = q_b(\tau_b, N, s)$. Here we choose to write

$$q = Q(\bar{U}, N, s). \tag{6.10}$$

When cavities are present, we still expect the boundary conditions above to hold on the contact areas, although the integrated momentum conservation equation (6.9) will clearly no longer hold. In line with the notation in chapter 3, we denote these contact areas by $y = 0$, $x \in C'$, whilst cavities are denoted by $y = 0$, $x \in C$ (as before, we require the bed to be periodic with period a, and there to be a finite number of cavities per period). On a cavity roof, compressive normal stress must be equal to the water pressure. In terms of the leading order model constructed in chapter 5, this corresponds to zero effective pressure N on the cavitated parts of the bed,

$$\bar{N} + p - 2\frac{\partial v}{\partial y} = N = 0 \qquad \text{on } y = 0,\ x \in C. \tag{6.11}$$

Furthermore, the cavity fluid is unlikely to support any significant shear stress at a cavity roof. This corresponds to vanishing interfacial shear stress τ_b at a cavity roof, so

$$\frac{\partial u}{\partial y} + \frac{\partial v}{\partial x} = \tau_b - 1 = -1 \qquad \text{on } y = 0,\ x \in C. \tag{6.12}$$

The cavity roof $s_C(x,t)$ — the notation $s(x,t)$ will continue to be reserved for the top surface of the till — can be expected to satisfy a kinematic boundary condition of the leading order form

$$\frac{\partial s_C}{\partial t} + \bar{U}\frac{\partial s_C}{\partial x} = v \qquad \text{on } y = 0,\ x \in C. \tag{6.13}$$

Since the ice is decoupled from the bed where a cavity is present, we expect zero till flux on $x \in C$, and hence

$$\frac{\partial s}{\partial t} = 0 \qquad \text{on } x \in C. \tag{6.14}$$

The boundary conditions (6.11)–(6.13) on the cavitated parts of the bed, together with (6.5) and (6.7) on the contact areas, yield a mixed boundary value problem for the ice flow which is very similar to the ice flow problem for hard-bed sliding discussed in chapter 3. We discuss a strategy for solving this boundary value problem next.

6.2 Complex Variable Formulation

The ice flow problem (6.2)–(6.14), where the boundary conditions (6.5) and (6.7) hold only on the contact areas, is analogous to the ice flow problem considered for hard bed sliding in the presence of cavitation in section 3.4. For instance, the vertical velocity boundary condition $(6.5)_1$ corresponds to (3.14), with the additional complication that the flux $q(x,t)$ is not known *a priori* even if the shape of the bed $s(x,t)$ is known at some time t. Similarly, the normal stress boundary condition (6.11) corresponds

to (3.16), with minor changes in notation. The main difference between the models arises because shear stress vanishes everywhere at the bed in classical sliding theory, whereas in the present model, 'shear stress' $\partial u/\partial y + \partial v/\partial x$ is non-zero at the bed through boundary conditions $(6.5)_2$ and (6.12).[1] Likewise, the sliding velocities — $\bar{U}(t)$ here and u_b in chapter 3 — are determined differently. $\bar{U}$ is determined through the till shearing sliding law $\tau_b = \tau(\bar{U}, N, s)$, whereas u_b in chapter 3 is determined by the geometrical drag exerted by bed obstacles on the ice through (3.20). Despite these differences, the similarity between the two problems is obvious.

As a result of the close analogy between the two problems, we do not develop the complex variable formulation in the same detail as in sections 3.4.1 and 3.4.2; the reader is encouraged to refer back to these sections.

A stream function ψ is again defined such that

$$u = \frac{\partial \psi}{\partial y}, \qquad v = -\frac{\partial \psi}{\partial x}. \tag{6.15}$$

The complex variables z and $\overline{z}$ are defined as before

$$z = x + iy, \qquad \overline{z} = x - iy, \tag{6.16}$$

and the stream function ψ can be expressed in terms of these as[2]

$$\psi = \overline{z}\theta(z) + z\overline{\theta(z)} + \phi(z) + \overline{\phi(z)}, \qquad z \in S^+, \tag{6.17}$$

where S^+ denotes the upper half of the complex plane and $\theta(z)$ and $\phi(z)$ are holomorphic on S^+. We can require the stream function to vanish at infinity, and hence θ and ϕ to satisfy

$$\theta, \phi \to 0 \qquad \text{as } \Im(z) \to \infty. \tag{6.18}$$

Pressure p also vanishes at infinity and is therefore given by

$$p = 4i\left[\theta'(z) - \overline{\theta'(z)}\right]. \tag{6.19}$$

By analogy with (3.40) and (3.41), boundary conditions $(6.5)_1$ and (6.13) can be expressed in terms of θ and ϕ as

$$-\left[x\theta''(x) + x\overline{\theta''(x)} + 2\theta'(x) + 2\overline{\theta'(x)} + \phi''(x) + \overline{\phi''(x)}\right]^+$$

[1] We put 'shear stress' in inverted commas because the total shear stress at the bed is $\tau_b = \partial u/\partial y + \partial v/\partial x + 1$ owing to the decomposition of the velocity field in (5.28). τ_b does, of course, vanish on the cavitated parts of the bed.

[2] Note that the boundary conditions are time-dependent. Consequently the stream function will depend on t. This explicit time dependence of θ and ϕ, and later F, f, G and g is omitted in our notation.

$$= \begin{cases} \bar{U}\dfrac{\partial^2 s}{\partial x^2} - \dfrac{\partial^2 q}{\partial x^2} & \in C', \\ \dfrac{\partial^2 s_C}{\partial x \partial t} + \bar{U}\dfrac{\partial^2 s_C}{\partial x^2} & x \in C, \end{cases} \tag{6.20}$$

where the superscript $^+$ again refers to the limit being taken as z approaches the boundary from S^+. The effective pressure boundary conditions (6.7) and (6.11) can be written by analogy with (3.42) and (3.44) as

$$2i\left[x\theta''(x) - x\overline{\theta''(x)} + 2\theta'(x) - 2\overline{\theta'(x)} + \phi''(x) - \overline{\phi''(x)}\right]^+ = \begin{cases} N(x,t) - \bar{N} & x \in C', \\ -\bar{N} & x \in C. \end{cases} \tag{6.21}$$

Lastly, the shear stress boundary conditions $(6.5)_2$ and (6.12) become

$$\left[x\theta''(x) + x\overline{\theta''(x)} + \phi''(x) + \overline{\phi''(x)}\right]^+ = \begin{cases} \tau_b(x,t) - 1 & x \in C', \\ -1 & x \in C. \end{cases} \tag{6.22}$$

6.2.1 Reformulation as a Hilbert Problem

As in section 3.4.2, the boundary value problem (6.20)–(6.22) can be re-written as a Hilbert problem. We define two functions $F(z)$ and $f(z)$ as

$$F(z) = \begin{cases} z\theta''(z) + 2\theta'(z) + \phi''(z) & z \in S^+, \\ \overline{\overline{z}\theta''(\overline{z}) + 2\theta'(\overline{z}) + \phi''(\overline{z})} & z \in S^-, \end{cases} \qquad f(z) = \begin{cases} z\theta''(z) + \phi''(z) & z \in S^+, \\ \overline{-\overline{z}\theta''(\overline{z}) - \phi''(\overline{z})} & z \in S^-, \end{cases} \tag{6.23}$$

where S^- is the lower half of the z-plane. $F(z)$ and $f(z)$ are holomorphic in S^- as well as S^+ by the Schwarz reflection principle. The boundary conditions (6.20)—(6.22) may be re-written in terms of F and f as

$$-\left[F^+(x) + F^-(x)\right] = \begin{cases} \bar{U}\dfrac{\partial^2 s}{\partial x^2} - \dfrac{\partial^2 q}{\partial x^2} & x \in C', \\ \dfrac{\partial^2 s_C}{\partial x \partial t} + \bar{U}\dfrac{\partial^2 s_C}{\partial x^2} & x \in C, \end{cases} \tag{6.24}$$

$$2i\left[F^+(x) - F^-(x)\right] = \begin{cases} N(x,t) - \bar{N} & x \in C', \\ -\bar{N} & x \in C, \end{cases} \tag{6.25}$$

$$f^+(x) - f^-(x) = \begin{cases} \tau_b(x,t) - 1 & x \in C', \\ -1 & x \in C, \end{cases} \tag{6.26}$$

where the superscript $^-$ denotes the limit taken as z approaches the x-axis from below. Note that F and f loosely speaking correspond to Ω and ω in section 3.4.2,

respectively. By contrast with ω, f is not identically equal to zero owing to the presence of non-zero interfacial shear stress. Boundary conditions at infinity are

$$F(z),\, f(z) \to 0 \qquad \text{as } \Im(z) \to \pm\infty. \tag{6.27}$$

In order to exploit the periodicity of the bed, we transform again to the ζ-plane, where

$$\zeta = \exp\left(\frac{i2\pi z}{a}\right), \qquad \xi = \exp\left(\frac{i2\pi x}{a}\right). \tag{6.28}$$

Functions $G(\zeta)$ and $g(\zeta)$ are defined by

$$G(\zeta) = F(z), \qquad g(\zeta) = f(z). \tag{6.29}$$

Since $F(z) = \overline{F(\overline{z})}$ and $f(z) = -\overline{f(\overline{z})}$, G and g satisfy

$$G(\zeta) = G_\star(\zeta) \doteq \overline{G(1/\overline{\zeta})}, \qquad g(\zeta) = -g_\star(\zeta) \doteq -\overline{g(1/\overline{\zeta})}. \tag{6.30}$$

Boundary conditions on G and g become,

$$-\left[G^+(\xi) + G^-(\xi)\right] = \begin{cases} \bar{U}\dfrac{\partial^2 s}{\partial x^2} - \dfrac{\partial^2 q}{\partial x^2} & \xi \in \Gamma', \\ \dfrac{\partial^2 s_C}{\partial x \partial t} + \bar{U}\dfrac{\partial^2 s_C}{\partial x^2} & \xi \in \Gamma, \end{cases} \tag{6.31}$$

$$2i\left[G^+(\xi) - G^-(\xi)\right] = \begin{cases} N(x,t) - \bar{N} & \xi \in \Gamma', \\ -\bar{N} & \xi \in \Gamma, \end{cases} \tag{6.32}$$

$$g^+(\xi) - g^-(\xi) = \begin{cases} \tau_b(x,t) - 1 & \xi \in \Gamma', \\ -1 & \xi \in \Gamma, \end{cases} \tag{6.33}$$

where C maps onto Γ and C' onto Γ' when $x \mapsto \xi$; note that the closure of $\Gamma \cup \Gamma'$ is the unit circle as before (see also figure 3.6). As in chapter 3, we use the superscripts $^+$ and $^-$ to denote limits being taken as ζ approaches the unit circle from the interior and exterior, respectively. Boundary conditions (6.27) at infinity now become

$$G(0) = G(\infty) = 0, \qquad g(0) = g(\infty) = 0. \tag{6.34}$$

In the next section, we discuss how to solve the Hilbert problems (6.31)–(6.32) and (6.33). There are some crucial differences from the development in section 3.5. By contrast with the case of a hard bed, the right-hand side of (6.31) is not known *a priori* on $\xi \in \Gamma'$ even if $s(x,t)$ is known at some time t, as $q(x,t)$ forms part of the solution. This complication leads to a different approach from that taken in

section 3.5 which recovers an integral equation analogous to (5.162). Crucially, the presence of the term $-\partial^2 q/\partial x^2$ on the right-hand side of (6.31) also alleviates the stress singularity which invariably occurs in sliding over hard beds in the presence of cavitation (see section 3.8).

6.2.2 Solution of the Hilbert Problems

We assume that $N(x,t)$ and $\tau_b(x,t)$ are Hölder continuous in x on the closure of C'. Below, a tilde will indicate a change of independent variables from x to ξ in these functions, i.e.

$$\tilde{N}(\xi,t) = N(x,t), \qquad \tilde{\tau}_b(\xi,t) = \tau_b(x,t). \tag{6.35}$$

Solutions to (6.32) and (6.33) which vanish at infinity can be written as (cf. Muskhelishvili, 1992, pp. 65–66)

$$G(\zeta) = -\frac{1}{4\pi}\int_{\Gamma'} \frac{\tilde{N}(\xi,t)\,\mathrm{d}\xi}{\xi-\zeta} + \frac{1}{4\pi}\int_{\Gamma\cup\Gamma'} \frac{\bar{N}\,\mathrm{d}\xi}{\xi-\zeta}, \tag{6.36}$$

$$g(\zeta) = \frac{1}{2\pi i}\int_{\Gamma'} \frac{\tilde{\tau}_b(\xi,t)\,\mathrm{d}\xi}{\xi-\zeta} - \frac{1}{2\pi i}\int_{\Gamma\cup\Gamma'} \frac{\mathrm{d}\xi}{\xi-\zeta}, \tag{6.37}$$

where integrals along Γ and Γ' are taken in the anti-clockwise direction (i.e. with increasing x). Clearly, G and g satisfy $G(\infty) = g(\infty) = 0$. In order to impose conditions (6.34) at the origin, we impose the conditions (6.30). Using $\overline{\mathrm{d}\xi} = -1/\xi^2\,\mathrm{d}\xi$, $G_\star(\zeta)$ and $g_\star(\zeta)$ are

$$G_\star(\zeta) = -\frac{1}{4\pi}\int_{\Gamma'} \tilde{N}(\xi,t)\left[\frac{1}{\xi-\zeta}-\frac{1}{\xi}\right]\mathrm{d}\xi + \frac{1}{4\pi}\int_{\Gamma\cup\Gamma'} \bar{N}\left[\frac{1}{\xi-\zeta}-\frac{1}{\xi}\right]\mathrm{d}\xi, \tag{6.38}$$

$$g_\star(\zeta) = -\frac{1}{2\pi i}\int_{\Gamma'} \tilde{\tau}_b(\xi,t)\left[\frac{1}{\xi-\zeta}-\frac{1}{\xi}\right]\mathrm{d}\xi + \frac{1}{2\pi i}\int_{\Gamma\cup\Gamma'} \left[\frac{1}{\xi-\zeta}-\frac{1}{\xi}\right]\mathrm{d}\xi, \tag{6.39}$$

and so (6.30) amounts to

$$\int_{\Gamma'} \frac{\tilde{N}(\xi,t)\,\mathrm{d}\xi}{\xi} - \int_{\Gamma\cup\Gamma'} \frac{\bar{N}\,\mathrm{d}\xi}{\xi} = 0, \qquad \int_{\Gamma'} \frac{\tilde{\tau}_b(\xi,t)\,\mathrm{d}\xi}{\xi} - \int_{\Gamma\cup\Gamma'} \frac{\mathrm{d}\xi}{\xi} = 0, \tag{6.40}$$

which can readily be recognised as the equivalents of the integrated momentum conservation equations (5.164) and (5.165).

Equations (6.36) and (6.37) provide solutions for $G(\zeta)$ and $g(\zeta)$ in terms of $N(x,t)$ and $\tau_b(x,t)$. The latter are, of course, not known *a priori* but must be established as part of the solution. Substitution of $G(\zeta)$ from (6.36) and using Plemelj's formulae (Muskhelishvili, 1992, p. 42) in (6.31) yields

$$\frac{\partial^2}{\partial x^2}\left(\bar{U}s - q\right) = \frac{1}{2\pi}\fint_{\Gamma'} \frac{\tilde{N}(\xi',t)\,\mathrm{d}\xi'}{\xi'-\xi} - \frac{1}{2\pi}\fint_{\Gamma\cup\Gamma'} \frac{\bar{N}\,\mathrm{d}\xi'}{\xi'-\xi} =$$

$$\frac{1}{2\pi}\left[\fint_{\Gamma'}\frac{\tilde{N}(\xi',t)\,\mathrm{d}\xi'}{\xi'-\xi}+i\pi\bar{N}\right]\qquad \xi\in\Gamma', \tag{6.41}$$

where the left-hand side is evaluated at some x such that $\xi=\exp(i2\pi x/a)$. Thus $q(x,t)$ and $\bar{U}(t)$ are related to $s(x,t)$ by a singular integro-differential equation if $q=Q(\bar{U},N,s)$ is again inverted to give $N=\hat{N}(\bar{U},q,s)$. In addition, they must satisfy the integral constraints (6.40). Once q and $\bar{U}$ have been determined from these equations, $\tau_b=\hat{\tau}_b(\bar{U},q,s)$ and $N=\hat{N}(\bar{U},q,s)$ can be calculated on the contact areas and hence $G(\zeta)$ and $g(\zeta)$ can be determined. In particular, once $N(x,t)$ is known on the contact areas, the evolution of the cavity roof $s_C(x,t)$ can be determined. From (6.31) and (6.36), we have

$$\frac{\partial}{\partial x}\left(\frac{\partial s_C}{\partial t}+\bar{U}\frac{\partial s_C}{\partial x}\right)=\frac{1}{2\pi}\left[\int_{\Gamma'}\frac{\tilde{N}(\xi',t)\,\mathrm{d}\xi'}{\xi'-\xi}+i\pi\bar{N}\right]\qquad \xi\in\Gamma. \tag{6.42}$$

Next, we demonstrate that solutions $q(x,t)$ and $\bar{U}(t)$ of the integro-differential equation (6.41) coupled with the constraints (6.40) must satisfy a nonlinear integral equation similar to (5.162). For simplicity, we restrict ourselves to the case of a single cavity per period. Given the regular appearance of evolving bedforms before cavitation (see figure 5.5) the restriction to a single cavity per period is not unrealistic if the period a is close to the fastest growing wavelength predicted by linear stability analysis (section 5.5). Let the end points of one cavity be $x=b(t)$ and $x=c(t)+a$, where $c<b<c+a$. Then

$$\Gamma'=\left\{\exp(i2\pi x/a):x\in(c,b)\right\},$$

$$\Gamma=\left\{\exp(i2\pi x/a):x\in(b,c+a)\right\}. \tag{6.43}$$

Reduction to an Integral Equation

Note that, if $\tilde{N}(\xi,t)$ is Hölder continuous on the closure of Γ', then the boundary values of $G(\zeta)$ defined by (6.36) are integrable on Γ and Γ'. We can thus integrate (6.41) as an initial value problem with as yet undetermined initial conditions at $x=c$.

First, we re-write (6.41) in terms of real variables. Using (6.40), we find

$$\left.\frac{\partial^2(\bar{U}s-q)}{\partial x^2}\right|_{x=x'}=\frac{1}{2a}\fint_c^b N(x'')\cot(\pi(x'-x'')/a)\,\mathrm{d}x'',\qquad x\in(c,b). \tag{6.44}$$

If both sides of (6.41) are integrated with respect to x' over (c,X),

$$\left.\frac{\partial(\bar{U}s-q)}{\partial x}\right|_{x=X}=\left.\frac{\partial(\bar{U}s-q)}{\partial x}\right|_{x=c}-\frac{1}{2a}\int_c^X\fint_c^b N(x'')\cot(\pi(x''-x')/a)\,\mathrm{d}x''\,\mathrm{d}x'. \tag{6.45}$$

By the Poincaré-Bertrand formula (Muskhelishvili, 1992, pp. 56–60), the order of integration on the right-hand side can be interchanged (since only one integral is singular). Hence

$$\left.\frac{\partial(\bar{U}s-q)}{\partial x}\right|_{x=X} = \left.\frac{\partial(\bar{U}s-q)}{\partial x}\right|_{x=c} - \frac{1}{2\pi}\int_c^b \log\left|\frac{\sin\left[\pi(x''-X)/a\right]}{\sin\left[\pi(x''-c)/a\right]}\right| N(x'',t)\,\mathrm{d}x''. \tag{6.46}$$

For later reference, note that the equation (6.42) for the cavity roof can similarly be simplified. Integrating over $x \in (X, c+a)$, where $b < X < c+a$, yields straightforwardly (as none of the integrals involved are singular)

$$\left(\frac{\partial s_C}{\partial t} + \bar{U}\frac{\partial s_C}{\partial x}\right)\Bigg|_{x=X} = \left(\frac{\partial s_C}{\partial t} + \bar{U}\frac{\partial s_C}{\partial x}\right)\Bigg|_{x=c+a} - \frac{1}{2\pi}\int_c^b \log\left|\frac{\sin\left[\pi(x'-X)/a\right]}{\sin\left[\pi(x'-c)/a\right]}\right| N(x')\,\mathrm{d}x'. \tag{6.47}$$

Returning to the problem of determining $q(x,t)$, we integrate (6.46) once more, and obtain the desired integral equation

$$\bar{U}(t)s(x,t) - q(x,t) = \left(\bar{U}s-q\right)|_{x=c} + \left.\frac{\partial(\bar{U}s-q)}{\partial x}\right|_{x=c}(x-c) - \frac{1}{2\pi}\int_c^b \left[\int_c^x \log\left|\frac{\sin\left[\pi(x''-x')/a\right]}{\sin\left[\pi(x''-c)/a\right]}\right| \mathrm{d}x'\right] N(x'',t)\,\mathrm{d}x'', \qquad x \in (c,b). \tag{6.48}$$

Hence solutions $q(x,t)$ and $\bar{U}(t)$ of the integro-differential equation (6.41) coupled with the constraints (6.40) must satisfy the integral equation (6.48) with $N(x'',t) = \hat{N}(\bar{U}(t), q(x'',t), s(x'',t))$. The somewhat more technical issue of the conditions under which a solution of (6.48) also satisfies (6.44) is addressed in appendix C, where we also show how (6.48) can be reduced to the integral equation (5.162) when there are no cavities present.

Given boundary points $c(t)$ and $b(t)$ and appropriate initial conditions (in x) on $\bar{U}s - q$ and its first partial derivative with respect to x, one may expect to be able to solve the integral equation (6.48) coupled with the constraints (6.40) numerically in a manner similar to that used in section 5.6.1. This still leaves the questions of how the boundary points evolve in time, and how the initial conditions should be specified.

In the next section, we do not address these problems in their general time-dependent setting. Rather, we focus on the simpler problem of finding travelling wave solutions for cavitated beds. In other words, we take the velocity of the free points b and c to be fixed at some value V, and consider what form appropriate initial

conditions in (6.48) and (6.47) might take in that case, and how the pattern speed V and the position of the cavity endpoints is determined.

Although a solution of the full time-dependent problem is desirable, a consideration of travelling wave solutions alone can still provide us with useful information. The original non-linear model in chapter 5 did not produce an 'evolved' pattern of bedforms but broke down at cavitation. Our main aim in introducing cavities into the model is therefore to determine whether cavitation can, at least in principle, lead to the formation of an 'evolved' pattern. Since such a pattern may well take the form of travelling waves, we wish to establish whether such travelling waves exist, and if they do, what shape they take.

6.3 Travelling Wave Solutions

Let

$$\eta = x - Vt, \tag{6.49}$$

and suppose that $s(x,t)$, $q(x,t)$, etc. depend on x and t only through the travelling wave coordinate η, while $\bar{U}$ is constant. The cavity end points will move at speed V, and without loss of generality, we may put

$$c(t) = Vt, \qquad b(t) = b_0 + Vt, \tag{6.50}$$

where the downstream cavity endpoint position b_0 is undetermined as yet, and lies in the range $0 < b_0 < a$. Owing to the periodicity of the problem, we will only be concerned with values of η in the range $[0, a]$. The contact area in that interval corresponds to $\eta \in (0, b_0)$, while the cavity corresponds to $\eta \in (b_0, a)$.

The evolution equation (6.1) now relates bed height s and flux q as

$$-V\frac{\mathrm{d}s}{\mathrm{d}\eta} + \frac{\mathrm{d}q}{\mathrm{d}\eta} = 0 \qquad \Rightarrow \qquad q(\eta) = Vs(\eta) + \bar{q} \qquad \text{on } \eta \in (0, b_0), \tag{6.51}$$

where $\bar{q}$ is a constant. In the cavities, there is zero flux and hence the till surface elevation is constant. If, in addition, till flux and till surface elevation are continuous across at least one of the cavity end points, then

$$s(\eta) = -\bar{q}/V \qquad \text{on } \eta \in (b_0, a). \tag{6.52}$$

The constant $\bar{q}$ is constrained by the requirement that the mean of s be zero. This leads to the interpretation of $\bar{q}$ as a mean flux,

$$\frac{1}{a}\int_0^{b_0} q(\eta)\,\mathrm{d}\eta - \bar{q} = 0. \tag{6.53}$$

Note that we expect $s > -\bar{q}/V$ in the contact areas, i.e. we expect intuitively that bed height will be greater in the contact areas than in cavities. Since we must also have $q > 0$ in contact areas, we therefore seek positive pattern speeds $V > 0$ by (6.51).

On the contact areas, q and s are also related by the integral equation (6.48), which now becomes

$$\bar{U}s(\eta) - q(\eta) = \bar{U}s(0^+) - q(0^+) + \bar{U}s'(0^+) - q'(0^+) -$$
$$\frac{1}{2\pi}\int_0^{b_0}\left[\int_0^{\eta}\log\left|\frac{\sin\left[\pi(\eta''-\eta')/a\right]}{\sin\left[\pi\eta''/a\right]}\right|\,\mathrm{d}\eta'\right]N(\eta'')\,\mathrm{d}\eta'' \qquad \eta\in(0,b_0), \tag{6.54}$$

where primes on s and q denote differentiation with respect to η. The superscripts $^+$ have been introduced for definiteness, to indicate that the initial values are to be interpreted as limits taken when η approaches zero from above. This is necessary as s and q or their derivatives might conceivably be discontinuous across a cavity boundary.

Further constraints on $\bar{U}$, q and s are provided by (6.40), which now reads

$$\frac{1}{a}\int_0^{b_0}\left[N(\eta)\,\mathrm{d}\eta - \bar{N}\right]\,\mathrm{d}\eta = 0 \tag{6.55}$$

$$\frac{1}{a}\int_0^{b_0}\left[\tau_b(\eta)\,\mathrm{d}\eta - 1\right]\,\mathrm{d}\eta = 0 \tag{6.56}$$

The cavity roof $s_C(\eta)$ is given by (6.47) as

$$(\bar{U}-V)s_C'(\eta') = (\bar{U}-V)s_C'(a^-) - \frac{1}{2\pi}\int_0^{b_0}\log\left|\frac{\sin\left[\pi(\eta''-\eta')/a\right]}{\sin\left[\pi\eta''/a\right]}\right|N(\eta'')\,\mathrm{d}\eta'', \tag{6.57}$$

where the superscript $^-$ indicates the limit being taken as η approaches a from below. This may be integrated again over $\eta'\in(\eta,a)$ to give

$$(\bar{U}-V)s_C(\eta) = (\bar{U}-V)s_C(a) + (\bar{U}-V)s_C'(a)(\eta-a) +$$
$$\int_0^{b_0}\left[\frac{1}{2\pi}\int_{\eta}^{a}\log\left|\frac{\sin\left[\pi(\eta''-\eta')/a\right]}{\sin\left[\pi\eta''/a\right]}\right|\,\mathrm{d}\eta'\right]N(\eta')\,\mathrm{d}\eta'' \qquad \eta\in(b_0,a). \tag{6.58}$$

6.3.1 Jump Conditions at Cavity Boundaries

So far, we have paid little attention to what happens at the cavity boundary points. In order to prescribe physically realistic initial conditions in (6.54) and (6.58), and in order to determine the free point b_0, the behaviour of the ice and till flow near the cavity boundaries must now be re-considered.

As in the case of hard bed sliding, we expect that there will be no discontinuities in the elevation of the lower boundary of the ice, and hence that

$$s_C(a^-) = s_C(0^-) = s(0^+), \qquad s(b_0^-) = s_C(b_0^+), \tag{6.59}$$

where the superscripts $^+$ and $^-$ have the same meaning as above.

By analogy with equation (3.104) for hard beds, we can further show that

$$s_C'(a^-) - s'(0^+) = s_C'(b_0^+) - s'(b_0^-). \tag{6.60}$$

To derive (6.60), note that (6.31) becomes the following in the travelling wave model:

$$-[G^+(\xi) + G^-(\xi)] = \begin{cases} (\bar{U} - V)s''(\eta) & \xi \in \Gamma' \\ (\bar{U} - V)s_C''(\eta) & \xi \in \Gamma, \end{cases} \tag{6.61}$$

where $\xi = \exp(i2\pi(\eta + Vt)/a)$,

$$\Gamma' = \{\exp(i2\pi(\eta + Vt)/a) : \eta \in (0, b_0)\} \tag{6.62}$$

$$\Gamma = \{\exp(i2\pi(\eta + Vt)/a) : \eta \in (b_0, a)\}, \tag{6.63}$$

and the superscripts $^+$ and $^-$ retain their original meaning, indicating limits being taken as ζ approaches the unit circle from within and without, respectively. The result (6.60) then follows by integrating $[G^+(\xi) + G^-(\xi)]/\xi$ around the unit circle $\Gamma \cup \Gamma'$ and using Cauchy's theorem, by exact analogy with the derivation of (3.104).

A further physically sensible assumption is that the lower boundary of the ice has no 'kinks' or discontinuities in slope. Thus we impose

$$s_C'(a^-) = s_C'(0^-) = s'(0^+), \qquad s_C'(b_0^+) = s'(b_0^-), \tag{6.64}$$

in addition to (6.59). As (6.60) shows, it is sufficient to impose this condition at one of the cavity boundaries; it will then automatically be satisfied at the other.

Till Shocks

As we will see later, it is not possible to impose the same continuity on the till surface as we have imposed on the ice surface: There will generally be a discontinuity or shock in s, and a corresponding shock in flux q, and hence in effective pressure N, at one of the cavity boundaries. Such shocks are not unexpected: the equivalent in the theory of dune formation would be a slip face (cf. Fowler, 2001a).

The possibility of shock formation poses the question whether such a shock should be located at $\eta = 0$ or at $\eta = b_0$. A simple physical argument suggests that only a

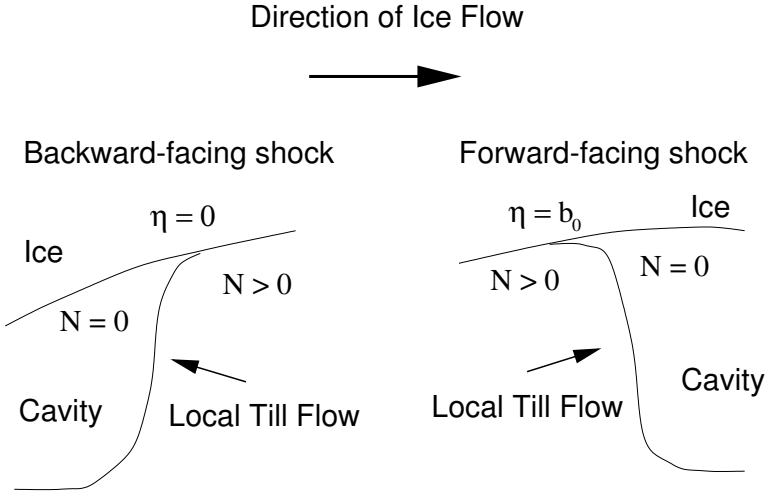

Figure 6.1: Backward- and forward-facing till shocks.

forward-facing shock at $\eta = b_0$ is possible: Locally, near the shock, till flow will no longer be the simple shearing flow that was assumed in the derivation of till flux in (5.68). Since the shock corresponds to a discontinuity in effective pressure N, pressure will be greater on the contact area side of the shock than on the cavity side. Hence there will be a significant pressure gradient driving the flow of till near the shock. Mathematically, this effect could in principle be described by an appropriate rescaling of the till-flow equations (5.35)–(5.41) near the shock. The resulting local till flow problem is likely to be complicated and we sidestep a detailed treatment here by arguing heuristically: The pressure gradient near the shock will drive till from the contact area into the cavity, i.e. forward in the positive η-direction if the shock is at $\eta = b_0$, and backwards if the shock is at $\eta = 0$ (cf. fig. 6.1). We may expect that this is the direction in which the shock front will move. However, as we are seeking travelling wave solutions with positive pattern speed, the shock front must move forward. This suggests that a backward-facing shock at $\eta = 0$ is not feasible.

Lastly, we can demonstrate that till flux and surface elevation related by (6.51) and (6.52) are consistent with the existence of a shock at one of the cavity boundaries. If mass is conserved, then such a shock moving at the pattern speed V must satisfy a jump condition of the form

$$V = \frac{[q]^+_-}{[s]^+_-} \tag{6.65}$$

where $[\,]^+_-$ denotes the difference between the right and left limits of the bracketed quantity at the shock. Suppose that there is a shock at $\eta = b_0$. By (6.51) and (6.52), we have $[q]^+_- = -q(b_0^-) = -Vs(b_0^-) - \bar{q}$ and $[s]^+_- = -\bar{q}/V - s(b_0^-)$; (6.65) is therefore automatically satisfied, regardless of the value taken by $s(b_0^-)$.

Initial Conditions

Following the argument about shock location above, we expect no shocks at the downstream cavity endpoint $\eta = 0$. Hence flux q and bed height s are continuous at $\eta = 0$,[3] and we impose

$$q(0^+) = 0, \qquad \bar{U}s(0^+) = -\bar{U}\bar{q}/V, \qquad s_C(a^-) = s(0^+). \tag{6.66}$$

In order to impose continuity in the ice surface slope $(6.64)_1$ at the downstream cavity endpoint, while requiring the cavity roof to be above the till surface in the cavity, and till flux to be positive in the contact areas, we must have

$$s_C'(a^-) = q'(0^+) = s'(0^+) = 0. \tag{6.67}$$

These initial conditions render the equation for the cavity roof as

$$(\bar{U} - V)s_C(\eta) = -\frac{(\bar{U} - V)}{V}\bar{q} +$$
$$\frac{1}{2\pi}\int_0^{b_0}\left[\int_\eta^a \log\left|\frac{\sin\left[\pi(\eta'' - \eta')/a\right]}{\sin\left[\pi\eta''/a\right]}\right| \mathrm{d}\eta'\right] N(\eta'')\,\mathrm{d}\eta'' \qquad \eta \in (b_0, a), \tag{6.68}$$

while the integral equation (6.54) now becomes

$$\bar{U}s(\eta) - q(\eta) = -\bar{U}\bar{q}/V -$$
$$\frac{1}{2\pi}\int_0^{b_0}\left[\int_0^\eta \log\left|\frac{\sin\left[\pi(\eta'' - \eta')/a\right]}{\sin\left[\pi\eta''/a\right]}\right| \mathrm{d}\eta'\right] N(\eta'')\,\mathrm{d}\eta'', \qquad \eta \in (0, b_0). \tag{6.69}$$

6.3.2 Constraints

So far, we have five equations — the integral equation (6.69), the constraints (6.53), (6.55) and (6.56), and the relation (6.51) between $q(\eta)$ and $s(\eta)$ — for the six unknowns $s(\eta)$, $q(\eta)$, $\bar{q}$, $\bar{U}$, V and b_0. One further constraint is therefore needed. Note that we have already imposed $(6.59)_1$ and $(6.64)_1$, which implies that $(6.64)_2$ must also hold. We still have to ensure that $(6.59)_2$ holds, i.e. that there is no discontinuity in the lower boundary of the ice at the upstream cavity endpoint b_0 and so

$$s(b_0^-) = s_C(b_0^+)$$

Using (6.51), (6.68) and (6.69), this constraint becomes

$$\int_0^{b_0}\left[\int_0^a \log\left|\frac{\sin\left[\pi(\eta'' - \eta')/a\right]}{\sin\left[\pi\eta''/a\right]}\right| \mathrm{d}\eta'\right] N(\eta'')\,\mathrm{d}\eta'' = 0. \tag{6.70}$$

[3]Note that, for a Boulton-Hindmarsh rheology (5.186), N vanishes when q vanishes, so continuity of q at the downstream end of a cavity also implies continuity in effective pressure.

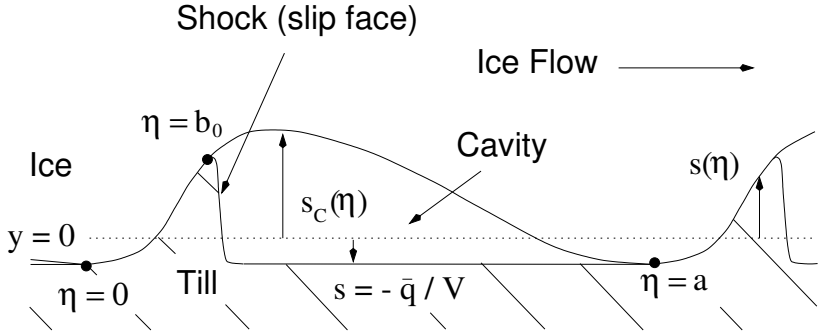

Figure 6.2: Sketch of the expected shape of travelling wave solutions.

With this additional constraint, one may expect to be able to solve the travelling wave problem for a given choice of period a, mean effective pressure $\bar{N}$ and rheological parameters which define the functions $\hat{N}(\bar{U}, q, s)$ and $\hat{\tau}_b(\bar{U}, q, s)$. There is then no guarantee that $q(b_0)$ will vanish; in general we must expect a shock at the upstream cavity endpoint. The travelling wave solutions being sought can thus be expected to have the shape indicated in figure 6.2.

Summary: The Travelling Wave Problem

The integral equation (6.70) and the constraint (6.69) can be simplified further if we write

$$\log\left|\frac{\sin\left[\pi(\eta''-\eta')/a\right]}{\sin\left[\pi\eta''/a\right]}\right| = \frac{1}{2}\left\{\log\left(4\sin^2\left[\pi(\eta''-\eta')/a\right]\right) - \log\left(4\sin^2\left[\pi\eta''/a\right]\right)\right\} \quad (6.71)$$

The integral

$$\int_0^a \log\left(4\sin^2\left[\pi(\eta''-\eta')/a\right]\right)\,\mathrm{d}\eta' = \int_0^a \log\left(4\sin^2\left[\pi y/a\right]\right)\,\mathrm{d}y$$

can be turned into $-ia/\pi$ times the integral of an appropriate branch of $\frac{1}{\zeta}\log(1-\zeta)$ taken around the unit circle (see appendix C, section C.1); the integral then vanishes by Cauchy's theorem and the constraint (6.69) reads

$$\int_0^{b_0} \log\left[4\sin^2(\pi\eta/a)\right] N(\eta)\,\mathrm{d}\eta = 0 \quad (6.72)$$

(6.71) and (6.72) together allow the integral equation (6.70) to be re-written as

$$\bar{U}s(\eta) - q(\eta) = -\bar{U}\bar{q}/V - \frac{1}{4\pi}\int_0^{b_0}\left[\int_0^{\eta}\log\left(4\sin^2\left[\pi(\eta''-\eta')/a\right]\right)\,\mathrm{d}\eta'\right] N(\eta'')\,\mathrm{d}\eta'', \quad (6.73)$$

where

$$q(\eta) = Vs(\eta) + \bar{q}, \tag{6.74}$$

and

$$\frac{1}{a}\int_0^{b_0} q(\eta)\,\mathrm{d}\eta - \bar{q} = 0, \tag{6.75}$$

$$\frac{1}{a}\int_0^{b_0} N(\eta)\,\mathrm{d}\eta - \bar{N} = 0, \tag{6.76}$$

$$\frac{1}{a}\int_0^{b_0} \tau_b(\eta)\,\mathrm{d}\eta - 1 = 0. \tag{6.77}$$

Effective pressure and basal shear stress are, of course, functions of sliding velocity $\bar{U}$, till flux q and till surface elevation s as before,

$$N = \hat{N}(\bar{U}, q, s), \qquad \tau_b = \hat{\tau}_b(\bar{U}, q, s). \tag{6.78}$$

6.3.3 Solution

A numerical solution of the travelling wave problem (6.72)–(6.78) with τ_b and N given as nonlinear functions of $\bar{U}$, q and s through the Boulton-Hindmarsh expressions (5.186) and (5.187) is faced with one serious obstacle: We are seeking solutions q which, by construction, vanish at the downstream cavity endpoint $\eta = 0$. If an iteration scheme is used to approximate q, then it is likely that one of the iterates will have negative values of q near $\eta = 0$. In general, $\hat{N}$ and $\hat{\tau}_b$ are, however, not defined for negative q (see the discussion on page 137). This is likely to cause the iteration scheme to fail. In abstract terms, the difficulty arises because we are seeking a solution which lies on the boundary of the domain of definition of the integral operators in (6.72), (6.76) and (6.77) (cf. appendix C, section C.4).

There are at least two ways of avoiding this problem: Firstly, we could choose the Boulton-Hindmarsh rheological parameters m and n such that $\hat{N}(\bar{U}, q, s)$ and $\hat{\tau}_b(\bar{U}, q, s)$ can be defined for negative q, even though this is unphysical.[4] A second, simpler approach which we adopt here is to use the quasi-linear model developed on page 150.

The Quasi-Linear Model

Recall that for large n and $m = n-1$, we could put $\bar{U} = 1$ and hence $q = N/[\alpha(n-2)]$ when there were no cavities present. It is straightforward to ascertain by analogy with the work on page 150 that $\bar{U} = 1$ still holds when the integral constraints

[4] One possible choice would be $n = 3$ and $m = 1$.

(5.164)–(5.165) are replaced by (6.76)–(6.77). Hence we may still approximate $q = N/[\alpha(n-2)]$ on the contact areas even after cavity formation.

We put $\bar{U} = 1$, $q = N/[\alpha(n-2)]$, and re-scale

$$X = \eta/a, \qquad B = b_0/a, \qquad S = \frac{\alpha(n-2)\,[Vs + \bar{q}]}{\bar{N}}, \qquad S_C = \frac{\alpha(n-2)\,[Vs_C + \bar{q}]}{\bar{N}}.$$

Defining

$$\mu = \frac{1-V}{a^2\alpha(n-2)V},$$

the travelling wave problem (6.72)–(6.77) may be re-cast as

$$\int_0^B \log\left[4\sin^2(\pi X)\right] S(X)\,\mathrm{d}X = 0, \tag{6.79}$$

$$\mu S(X) + \frac{1}{4\pi}\int_0^B \left[\int_0^X \log\left[4\sin^2(\pi(X''-X'))\right]\,\mathrm{d}X'\right] S(X'')\,\mathrm{d}X'' = 0, \tag{6.80}$$

$$\int_0^B S(X)\,\mathrm{d}X = 1, \tag{6.81}$$

while

$$\bar{q} = \frac{\bar{N}}{\alpha(n-2)}\int_0^B S(X)\,\mathrm{d}X = \frac{\bar{N}}{\alpha(n-2)}, \tag{6.82}$$

and (6.77) is satisfied automatically if (6.81) is.

At a given B, (6.80) is a linear eigenvalue problem for S with eigenvalue μ, which is a proxy for the pattern speed. (6.79) thus acts as a constraint on the unknown upstream cavity boundary B, while (6.81) simply determines the amplitude of the eigenfunction $S(X)$ — note that the determination of B and μ through (6.80) and (6.82) decouples from (6.81). Importantly, equations (6.79)–(6.81) do not contain any of the parameters $\bar{N}$, α, n or a explicitly. We are therefore seeking a set of solutions for $S(X)$, μ and B from which solutions for $s(x)$, V and b_0 can be recovered for all parameter choices simply by scaling.

Numerical Method

Since we are only interested in real eigenvalues μ in (6.80), we use the following procedure to solve (6.79)–(6.80): First, the eigenvalue problem is re-written as

$$\mu S(X) + \frac{1}{4\pi}\int_0^B \left[\int_0^{X-X''} \log\left[4\sin^2(\pi y)\right]\,\mathrm{d}y\right] S(X'')\,\mathrm{d}X'' =$$

$$\frac{1}{4\pi}\int_0^B \left[\int_0^{X''} \log\left[4\sin^2(\pi y)\right]\,\mathrm{d}y\right] S(X'')\,\mathrm{d}X''. \tag{6.83}$$

where $y = X' - X''$. The integral on the right-hand side is independent of X. If we only wish to find solutions to (6.79)–(6.80) without requiring the eigenfunction S to satisfy the normalisation condition (6.81), then we may scale S such that

$$\frac{1}{4\pi}\int_0^B \left[\int_0^X \log\left[4\sin^2(\pi y)\right]\,\mathrm{d}y\right] S(X)\,\mathrm{d}X = 1, \tag{6.84}$$

and (6.83) can be re-written as an inhomogeneous Fredholm integral equation

$$\mu S(X) + \frac{1}{4\pi}\int_0^B \left[\int_0^{X-X''} \log\left[4\sin^2(\pi y)\right]\,\mathrm{d}y\right] S(X'')\,\mathrm{d}X'' = 1. \tag{6.85}$$

Note that the kernel of the integral operator on the left-hand side is anti-symmetric, and consequently only has pure imaginary eigenvalues.[5] By the Fredholm alternative, (6.85) has a solution for any real non-zero μ. We denote this solution by $S(X;\mu,B)$. If we impose the constraints (6.79) and (6.84), then the problem of determining μ and B amounts to solving the non-linear equations

$$f_1(\mu,B) \doteq \frac{1}{4\pi}\int_0^B \left[\int_0^X \log\left[4\sin^2(\pi y)\right]\,\mathrm{d}y\right] S(X;\mu,B)\,\mathrm{d}X - 1 = 0, \tag{6.86}$$

$$f_2(\mu,B) \doteq \int_0^B \log\left[4\sin^2(\pi X)\right] S(X;\mu,B)\,\mathrm{d}X = 0. \tag{6.87}$$

Numerically, this is achieved using a backtracking line-search modification of Newton's method, where the Jacobian is approximated by finite differences (Dennis and Schnabel, 1996). In order to calculate $S(X;\mu,B)$ and hence $f_1(\mu,B)$ and $f_2(\mu,B)$ numerically for given μ and B, we use a degenerate kernel approximation (Atkinson, 1997, chapter 2): As shown in appendix C, section C.1, the kernel

$$K(x) = \frac{1}{4\pi}\int_0^x \log\left[4\sin^2(\pi y)\right]\,\mathrm{d}y \tag{6.88}$$

can be approximated uniformly by the truncated Fourier series

$$K_{n_0}(x) = \sum_{n=-n_0,n\neq 0}^{n_0} \frac{i\exp(i2n\pi x)}{8\pi^2 n|n|} \tag{6.89}$$

as $n_0 \to \infty$. Replacing $K(x)$ with $K_{n_0}(x)$, the solution of (6.85) follows the standard method for degenerate kernels (see also section 5.6.1).

[5]This is the reason why the integral on the right-hand side of (6.83) can never be zero at a solution with real μ, and hence the scaling of S to set the right-hand side of (6.83) to unity is valid.

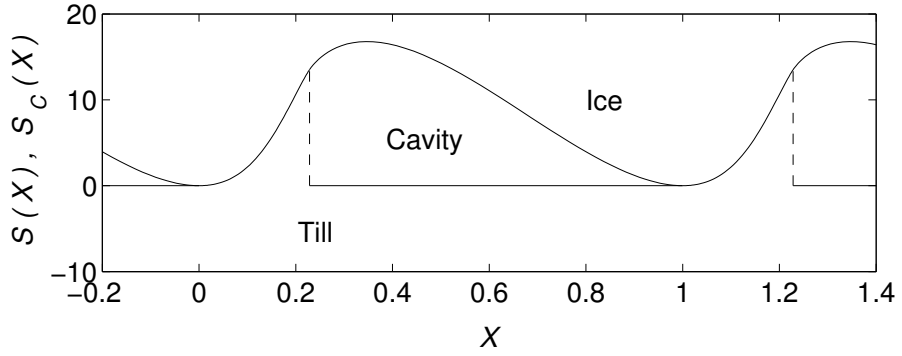

Figure 6.3: Travelling wave solutions for the quasilinear Boulton-Hindmarsh rheology $m = n - 1 \gg 1$. The broken line shows the till shock at $B = 0.2285$.

Results

From all the initial guesses chosen for μ and B, the iteration scheme always converged to the roots $\mu = 2.971\times10^{-3}$ and $B = 0.2285$. It therefore appears that there exists one simple periodic travelling wave solution with prescribed period a when the quasi-linear model of section 5.7.2 is modified to allow for the presence of cavities. This may be contrasted with the observation that growth is unbounded in the quasi-linear model if negative effective pressures are permitted and no cavities are formed. It is therefore the presence of a cavity which introduces the additional nonlinearity that allows for the existence of travelling wave solutions.

Using this solution for μ and B, $S(X)$ can be calculated by normalising the corresponding eigenfunction $S(X;\mu,B)$ using (6.81) and $S_C(X)$ can then be found using (6.68), which now becomes

$$\mu S_C(X) = \frac{1}{4\pi}\int_0^B \left[\int_X^1 \log\left(4\sin^2\left[\pi(X''-X')/a\right]\right)\,\mathrm{d}X'\right] S(X'')\,\mathrm{d}X'. \tag{6.90}$$

Figure 6.3 shows the shape of the solutions $S(X)$ and $S_C(X)$. The till in each 'bedform' is concentrated in a wedge shape, downstream of which there is an elongated cavity. Note that the till shock, shown as a broken vertical line in figure 6.3, would in practice be smoothed locally due to the presence of a significant pressure gradient near the shock.

The wavelength a can be chosen arbitrarily in our travelling wave calculation. It affects the pattern speed through

$$V = \frac{1}{1 + a^2\alpha(n-2)\mu}. \tag{6.91}$$

For $q = N/[\alpha(n-2)]$, the fastest growing wavelength computed from (5.118) is $\lambda_{max} = 2\pi\{2/[\sqrt{3}\alpha(n-2)]\}^{1/2}$. If we suppose that a is approximately equal to λ_{max},

then $a^2\alpha(n-2) \approx 8\pi^2/\sqrt{3} \approx 45.6$. With $\mu \approx 0.00297$, the pattern speed is then $V \approx 0.881$. V is thus close to, though slightly less than, the sliding velocity $\bar{U} = 1$. The travelling wave pattern thus moves at a speed close to that at which the basal ice is sliding.

It is instructive to re-dimensionalise the results for the height of travelling waves: Ignoring the fact that V is slightly smaller than unity, S and S_C are scaled here with the effective deforming till thickness $\bar{d}_{eff}$ defined in section 5.7.1. The units on the vertical axis in figure 6.3 are therefore roughly equal to the thickness of deforming till measured when the bed is flat. From (5.203), we obtain an estimate for $\bar{d}_{eff}$ as

$$\bar{d}_{eff} = \frac{10}{n-2}\,\text{metres}.$$

The numerical solution for $S(X)$ shown in figure 6.3 has a maximum height of 13.5, thus corresponding to roughly $135/(n-2)$ metres; this approximates to a reasonable height for a bedform when n takes the moderate value of 10.

While the shape of the lower boundary of the ice resembles the longitudinal profile of a drumlin — with a steeper upstream slope and a tapered downstream slope — it is important to realise that the bedform which would be observed after deglaciation is the till wedge at the upstream end of each cavity in figure 6.3. This till wedge clearly does not resemble a drumlin: Its steeper face is the downstream face, where the shock is located. It also has no stratified core, despite being considerably larger than the deformation thickness scale $\bar{d}_{eff}$: effective pressure N is concentrated on the contact area, and therefore considerably larger than the mean effective pressure $\bar{N}$ from which $\bar{d}_{eff}$ is calculated. Consequently, the local effective thickness of deforming till is considerably larger than $\bar{d}_{eff}$, ensuring that the till wedge is entirely unstratified.

6.4 Discussion

The travelling waves whose shapes have been calculated in this chapter are clearly not drumlins — they are two-dimensional, unstratified and have a longitudinal profile very unlike that of a drumlin. It is debatable whether Rogen moraines could be described successfully by the travelling wave model. Clearly, the till shock at the downstream side of the travelling wave solution would in practice be smoothed somewhat, but one would still expect to see a steep slip face. There is, however, no evidence in the literature on Rogen moraines (e.g. Lundqvist, 1969; Aario, 1977; Shaw, 1979; Fisher and Shaw, 1992) that such landforms generally have a steep down-glacier face; in fact, accounts of steep upstream faces and gentler lee slopes are quite common.

A further difficulty in trying to apply the travelling wave model developed here to Rogen moraines is that Rogen moraines often do contain sorted or stratified sediment (e.g. Shaw, 1979; Fisher and Shaw, 1992), while the till wedge here consists entirely of deformed and therefore unstratified material. Lastly, of course, there is a long-standing supposition that the formation processes of drumlins and Rogen moraines are related (Lundqvist, 1969; Aario, 1977, 1987; Fisher and Shaw, 1992), and as we mentioned above, the model being studied here seems unable to predict drumlins.

One suggestion which might remedy some of the shortcomings of the present model is that the cavities which are formed could become filled with sediment transported by a subglacial drainage system (Fowler, 2001a); stratified sediments in Rogen moraine cores would then be caused by deposition of water-borne sediment. It is unclear whether such a mechanism is realistic, and how it would affect our results. Clearly, sediment transport by the cavity fluid would interfere with the formation of the till shock at the upstream end of the cavity, and it is unclear what kind of travelling wave solution, if any, would result.

In terms of understanding the presence of undeformed sediment in the cores of subglacial bedforms, the concept of 'cavity fill' suggested by Fowler (2001a) has a further deficiency: some bedforms contain materials which were obviously not laid down underneath a glacier, but must have been in place before the bedform was generated (e.g. Schaeffer, 1969; Goldthwait, 1974; Krüger and Thomsen, 1984). Such bedforms must be erosional in origin, whereas Hindmarsh's (1998b) and Fowler's (2000) model, on the evidence presented so far, can only produce stratified sediments which are depositional in origin through cavity fill.

There is further evidence to suggest that erosional bedforms cannot be produced by sediment deformation alone. We take the Puget Sound drumlin field (figures 1.3 and 6.4) as an example (B. Hallet, University of Washington, private communication): The Puget Ice Lobe, under which this drumlin field was formed, is thought to have occupied the Puget Sound area for around 1,000 years. The stratigraphy of the drumlin field is as follows: The Puget sound area is covered fairly uniformly by a till layer 1 – 2 m thick, underlain by an undeformed massive layer of sand thought to have resulted from glacial outwash. If till deformation was thus confined to a layer 1 m thick and deforming at speeds comparable to the inferred sliding velocities of the Puget lobe — around 500 m a^{-1} — then a till flux of around 500 m^2 a^{-1} can be estimated. In fact, if there was some degree of slip at the ice-till interface, then till flux is likely to have been less than this estimate. In order to excavate 50 metre-high drumlins along the length of the ice lobe (200 km), the amount of sediment removed

from the bed of the Puget lobe, expressed as a volume per unit width of the ice lobe, must have been around 10^7 m^2. Given the estimate of till flux above, the process of till deformation would have taken about 20 thousand years to excavate that amount of sediment, which is clearly considerably longer than the estimated length of time of 1000 years during which the drumlin field must have been formed.

If till deformation is an unlikely mechanism for drumlin formation, what of the alternatives? Many early theories of drumlin formation (see Gravenor, 1953, for a review) consider 'erosion' and 'deposition' of sediment without addressing the specifics of how sediment is eroded or deposited, and are therefore of little use for modelling purposes. The later theories of Smalley and Unwin (1968) and Boulton (1987) are similar to the one we have studied in this thesis in the sense that they consider sediment deformation as responsible for shaping subglacial bedforms. A different — and controversial — school of thought has emerged in the last twenty years largely as a result of the theories of Shaw and co-workers. Shaw (1983) first proposed the notion that drumlins could be the result of large subglacial floods, which are envisaged as flowing in the form of a continuous water sheet at the base of the ice sheet. Such floods could then conceivable generate drumlins by analogy with the processes responsible for the formation of fluvial dunes (cf. Fowler, 2001a). The main criticism of this 'flood hypothesis' — which itself is re-iterated in numerous papers (e.g. Shaw and Kvill, 1984; Sharpe, 1987; Fisher and Shaw, 1992) — is the feasibility of floods on the size required to generate drumlin fields (Boulton, 1987). If a flood covering tens of thousands of square kilometres (the size of a large drumlin field) did occur under an ice sheet, one would expect the ice sheet to lift off its bed and therefore to surge. It is not clear to what extent such surges can occur without the ice sheet disintegrating partly, or whether the amount of liquid water required for such a flood can be generated and stored underneath an ice sheet. A further problem associated with Shaw's theory is the stability of the flood as a sheet flow. In general, large outburst floods or *jökullhlaups* occur through a single subglacial channel (see also Ng, 1998).

Clearly, there is currently no universally accepted theory to explain the origin of drumlins, or of any other type of streamlined bedform. Worse still, few of the theories which have been enunciated by geologists and geomorphologists over the years have ever been put in a form which might allow them to be tested at least semi-quantitatively in the manner in which we have been able to test Hindmarsh's (1998b) and Fowler's (2000) theory. Much work, especially at the modelling end, remains to be done in the study of drumlins.

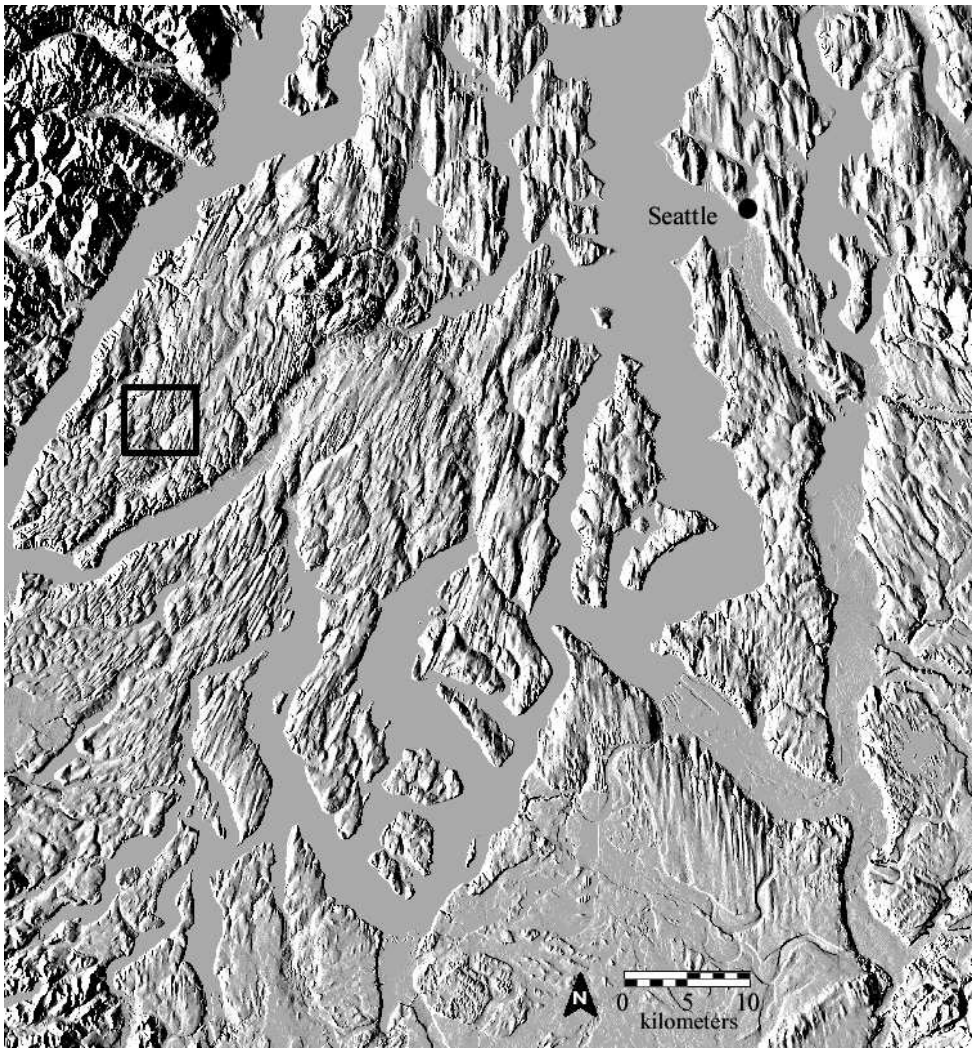

Figure 6.4: A digital elevation model of the Puget Sound drumlin field, Washington State, U.S.A. Ice flow direction is from top to bottom. A typical height for the drumlins in the Puget Sound area is 50 m, and the drumlin field extends for roughly 200 km in the North-South direction. Note that the small box on the left-hand side indicates the area enlarged in figure 1.3. Image courtesy of Ralph Haugerud, U.S. Geological Survey.

Chapter 7

Conclusions and Further Work

In this thesis, we have studied various aspects of the interactions between the flow of glaciers and ice sheets on the one hand and the underlying bedrock or soft sediment on the other. The motivation for studying such interactions broadly speaking lies in their effect on the bulk flow of the glacier or ice sheet. In particular, the surging of glaciers and the streaming behaviour of ice sheets may be controlled by processes which occur at their base.

In chapter 3 we considered the effect of cavitation on the sliding of glaciers. Cavitation has long been held to be an important factor in the surging of some glaciers (Kamb, 1987; Fowler, 1987b). The precise form of a sliding law which accounts for cavitation and thus relates sliding velocity, basal shear stress and effective pressure has, however, remained unresolved. In particular, power-laws of the form $u_b = C\tau_b^p N^{-q}$ have commonly been used to model the flow of glaciers. Such sliding laws have gained popularity despite the fact that they conflict with Iken's bound $\tau_b \leq N \max(h')$ for the shear stress supported by beds which have bounded slopes h' relative to the mean flow direction. The main object of the work in chapter 3 was thus to resolve what shape a realistic sliding law should take when there are bed bumps of many different sizes but when the bed slope remains bounded. The results obtained are not dissimilar from Fowler's (1986a) sliding law for simple periodic beds: Shear stress initially increases with velocity up to a maximum, and then decreases again as bed roughness is drowned out.

Such a sliding law suggests that models of glacier dynamics may need to take greater account of longitudinal and lateral stresses as the gravitational driving stress cannot be supported locally at the bed under all circumstances. This is especially true for fast-flowing glaciers with high basal water pressures, under which cavitation may be widespread.

In view of our results, an obvious area for future research lies in the interactions between sliding with cavitation and the subglacial drainage of meltwater: Once there is significant cavitation, the sliding law becomes very sensitive to effective pressure, and hence to subglacial water pressure. Although this fact is widely appreciated in the glaciological community, there is as yet little theoretical understanding of how basal water pressures at the bed are determined, especially when drainage occurs through a system of linked cavities rather than an isolated channel.[1] Some work in this area has been carried out by Kamb (1987), Fowler (1987a) and Humphrey (1987), but a comprehensive model coupling linked cavity drainage with the dynamics of the overlying glacier remains to be constructed.

In chapter 4, we considered how the notion of a 'sliding law' is changed when the obstacles which generate most of the drag on an ice sheet are no longer small compared with the thickness of the overlying ice, but have wavelengths comparable to it. The particular case studied is that of an ice stream with constant viscosity flowing rapidly over bed bumps with small slopes. The theory constructed is thus essentially an extension of Nye's (1969) and Kamb's (1970) classical sliding theory to the case of an ice mass of finite thickness.

One of the obvious shortcomings of the work in chapter 4 is that the theory constructed there cannot give a definitive answer to the question: Can long-wavelength obstacles such as drumlins play a significant rôle in the force balance of an ice stream, moving at realistic speeds of hundreds to thousands of metres per year? In order to settle this issue, a model which takes account of the non-linear rheology of ice would be necessary.

Our approach does, however, do two things: Firstly, it develops a framework within which the effect of basal topography on the length scale considered can be dealt with. Secondly, it illustrates that the upper, free surface of the ice stream can have a significant effect on the drag generated. In particular, it can lead to sliding velocity and hence ice flux becoming a multi-valued function of ice thickness and driving stress. How such a multi-valued relationship between ice flux, ice thickness and surface slope might affect the dynamics of an ice stream is another obvious avenue for future research.

In chapters 5 and 6, we turned our attention to a rather different aspect of the interaction between ice flow and the uderlying substrate, namely the question of how certain undulations on the ice-bed interface might be formed. Specifically, we

[1] By contrast, the hydraulics of individual subglacial channels are much better understood. See, for instance, Ng (1998).

considered in detail Hindmarsh's (1998b) and Fowler's (2000) model for the formation of subglacial bedforms. This model assumes that bedforms are generated as the result of an instability in the flow of ice over deformable, viscous till.

The assumption that bedforms have shallow slopes — which is already inherent in Hindmarsh's and Fowler's work — allows their model to be simplified significantly. In chapter 5, we were able to show that the leading-order model which arises predicts the formation of transverse rolls, which may conceivably be interpreted as Rogen moraines. However, no instability predicting the formation of three-dimensional features was found, and the model seems unable to explain the formation of drumlins.

A simplified nonlinear model for two-dimensional bed bumps was also derived and solved numerically in order to study the evolution of these bumps on the ice-till interface once they have reached finite amplitude. The results obtained indicate that these bumps invariably continue to grow until effective pressure reaches zero and cavitation is initiated. At cavitation, the amplitude of bed bumps is comparable to the ratio of till flux to till surface velocity, which may be interpreted as the 'effective' thickness of the deforming till. The bedforms predicted thus do not have stratified cores when cavitation first occurs.

In chapter 6, the problem of two-dimensional periodic travelling wave solutions of Hindmarsh's and Fowler's model, modified to take account of cavitation, was addressed. It was shown numerically that such solutions do exist, suggesting that the formation of cavities may eventually lead to bounded growth of bed bumps. However, the shape of the travelling wave solutions obtained is very dissimilar from real Rogen moraines: The travelling wave solutions constructed in chapter 6 have shocks at their downstream ends, and no internal stratification.

Taken as a whole, our analysis of Hindmarsh's (1998b) and Fowler's (2000) model for bedform formation suggests that this model is not particularly successful at explaining many of the features which subglacial bedforms typically have, such as their shapes and the occurrence of internal stratification. Unfortunately, this negative result does not indicate any obvious avenues for future theoretical research into the formation of drumlins. It can be expected the drumlin problem will only be resolved once our quantitative understanding of the subglacial environment and of the various processes controlling the transport of subglacial sediment has improved considerably.

Part III

Appendices

Appendix A

The Basal Boundary Layer

In order to formulate the glacier sliding problem more precisely, Fowler (1979, 1981) introduced a boundary layer approach to the flow of ice over basal obstacles, based on the assumption that their wavelengths are much shorter than the thickness of overlying ice. We only sketch the resulting model here with minor changes in exposition. Further details may be found in Fowler's papers and doctoral thesis (Fowler, 1977).

The basic idea behind the boundary layer treatment of basal sliding is that the 'outer' flow of the glacier or ice sheet, at some distance above the bed, is similar to the lubrication flow of the shallow-ice theories presented in section 2.2, but the no-slip boundary condition at the base is no longer applied. Instead, the 'inner' flow of basal ice over bed undulations, which is driven by shear stresses in the outer flow near the bed, leads to a non-zero sliding velocity. The two flows are described mathematically by an outer solution in terms of coordinates $(x^\star, y^\star)$ defined previously, and an inner solution in terms of local variables near the bed (cf. fig. A.1). The two solutions are then matched asymptotically in a matching region some way above the bed to produce a sliding law of the form (2.51).

In line with Fowler's work, we ignore regelation here and focus instead on sliding by viscous creep over obstacles. A simple model for the flow of a temperate ice sheet over an undeformable rough bed then consists of equations (2.7)–(2.8) and (2.10)–(2.12), while the no-slip boundary condition (2.9) is replaced by free slip at the bed,

$$\mathbf{t} \cdot \boldsymbol{\sigma} \mathbf{n} = 0 \qquad \text{on } y = H, \tag{A.1}$$

where $\mathbf{t}$ and $\mathbf{n}$ stand for the unit tangent and normal to the bed. Also, there is no flow into the bed, and hence

$$\mathbf{n} \cdot \mathbf{u} = 0 \qquad \text{on } y = H. \tag{A.2}$$

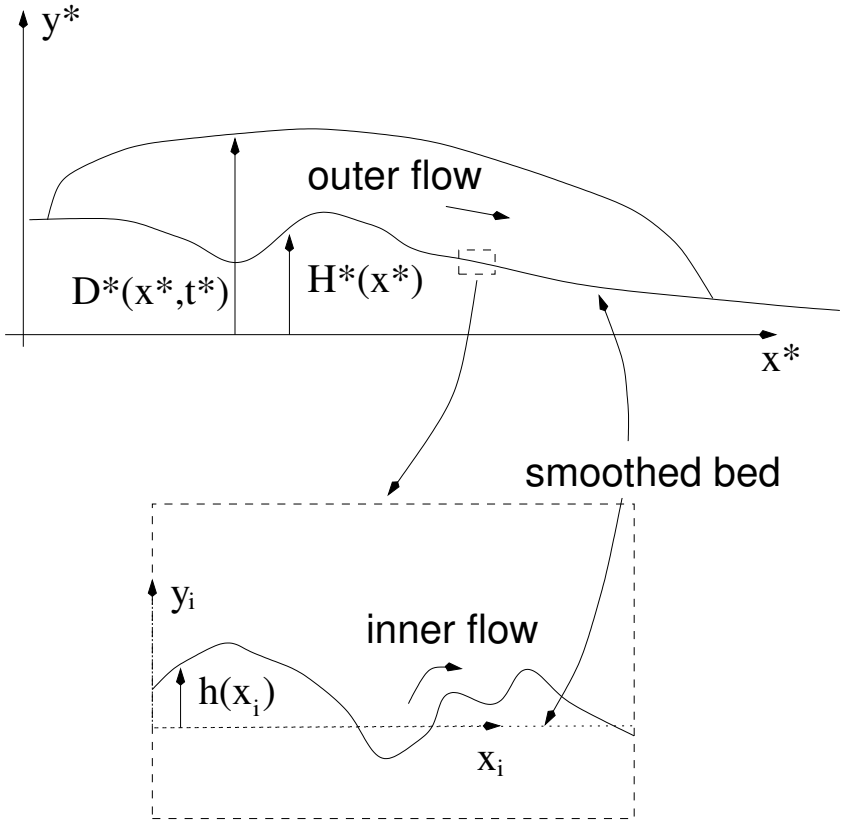

Figure A.1: Boundary layer geometry.

Outer Flow

The scales for the outer flow are the same as those used in section 2.2 for ice sheets. The treatment for glaciers proceeds analogously.

In addition, we introduce a further as yet undetermined scale $[u_b]$ for the sliding velocity and change the scaling for the velocity field from (2.19) to

$$u = [u_b]u_b^\star(x^\star, t^\star) + [u]u^\star, \qquad v = \epsilon[u_b]\frac{\partial u_b^\star}{\partial x^\star}(y^\star - H^\star) + \epsilon[u]v^\star, \tag{A.3}$$

$u_b^\star$ is a dimensionless sliding velocity, defined such that $u^\star = 0$ on $y^\star = H^\star$. As there are now small-scale bed irregularities present, $H^\star$ has to be understood as a smoothed bed, defined below in (A.9).

$[u_b]$ introduces an additional parameter, the slip ratio

$$\gamma = [u_b]/[u]. \tag{A.4}$$

The sliding problem is only of interest if there is significant sliding, and thus we assume that $O(1) \lesssim \gamma$. The reduced model in section 2.2 consisting of (2.33)–(2.35) still holds

to an error of $O(\gamma^2\epsilon^2)$ provided $\gamma \ll 1/\epsilon$, and so we assume that $O(1) \lesssim \gamma \ll \epsilon^{-1}$. Sliding then increases the ice flux in (2.36) to

$$Q = -\frac{1}{n+2}(D-H)^{n+2}\left|\frac{\partial D}{\partial x}\right|^{n-1}\frac{\partial D}{\partial x} + \gamma u_b(D-H). \tag{A.5}$$

Inner Flow

The inner flow near the bed is concerned with the problem of ice flow over bed roughness on some wavelength scale $[x]$—typically centimetres to metres—where $[x] \ll [D]$ (fig. A.1). This allows us to define a small dimensionless parameter δ which denotes the ratio of bed roughness wavelength to ice thickness,

$$\delta = [x]/[D]. \tag{A.6}$$

$\delta \ll 1$ forms the basis of the asymptotic matching procedure which allows a sliding law of the form (2.51) to be calculated.

The horizontal coordinate is rescaled with $[x]$ in the boundary layer to define

$$x_i = x/[x], \tag{A.7}$$

where the subscript $_i$ indicates 'inner' variables.[1] The assumption, made in section 2.2, that bed relief varies only on the outer length scale $[L]$ and has slopes of order $[D]/[L]$ clearly no longer holds when bed obstacles are present. In order to account for local bed roughness of amplitude $[h]$, Fowler (1979, 1981) proposes a decomposition of the bed (see fig. A.1) into a local, rough part denoted by $[h]h(x_i)$ and a smoothed part $[D]H^\star(x^\star)$ defined by a running average

$$[D]H^\star(x^\star) = \frac{1}{2X_{av}}\int_{-X_{av}}^{X_{av}} H(x+\xi)\,\mathrm{d}\xi, \tag{A.8}$$

such that[2]

$$H(x) = [D]H^\star(x^\star) + [h]h(x_i). \tag{A.9}$$

This decomposition is made formally unique by requiring that the averaging distance X_{av} should satisfy

$$[x] \ll X_{av} \ll [L],$$

[1] Strictly speaking, this introduces multiple scales into the problem, since we now have $x^\star = \delta\epsilon x_i$, and variables dependent on $x^\star$ appear in the boundary layer problem, namely $u_b^\star$ and $H^\star$ defined below.

[2] More precisely, we should take the rough part to be $[h]h(x_i, x^\star)$

and by assuming that there are no significant bed undulations of wavelengths intermediate between $[x]$ and $[L]$. The smoothed bed $H^\star$ can then be used to define a local vertical coordinate y_i as

$$y = [D]H^\star(x^\star) + [x]y_i. \tag{A.10}$$

We define local bed roughness as

$$\nu \doteq [h]/[x], \tag{A.11}$$

and assume that ν is large compared with the mean bed slope, which scales with ϵ, so $\epsilon \ll \nu$. If ice slides at some mean velocity $[u_b]$ over basal topography with local slope ν, then the boundary condition (A.2) suggests that local variations in velocity scale with $[u_i]$, where

$$[u_i] = \nu[u_b]. \tag{A.12}$$

Furthermore, Glen's law requires the balance

$$[u_i]/[x] = 2A[\tau_i]^n, \tag{A.13}$$

where $[\tau_i]$ is a scale for deviatoric stresses in the boundary layer. Since shallow ice theory requires the 'driving stress' to be supported locally — in terms of the outer coordinates — at the bed (see comment at the end of section 2.2), the effective basal shear stress τ_b in equation (2.50) scales with stresses $[\tau]$ in the outer flow, while the integrand on the right-hand side of (2.50) scales as $\nu[\tau_i]$, and so

$$[\tau_i] = [\tau]/\nu, \tag{A.14}$$

(2.16) together with (A.12)–(A.14) and gives us the sliding velocity scale $[u_b]$ in terms of the creep velocity scale $[u]$ for the outer flow and the bed roughness parameters δ and ν as

$$[u_b] = (\delta/\nu^{n+1})[u] \Rightarrow \gamma = \delta/\nu^{n+1}. \tag{A.15}$$

Since we are assuming that $1 \lesssim \gamma$, this implies that $\nu^{n+1} \lesssim \delta$ and we must formally have

$$\nu \lesssim \delta^{1/(n+1)} \ll 1$$

as $\delta \ll 1$. The assumption of small bed roughness slope ν, which underpins most analytical treatments of hard bed sliding (Nye, 1969, 1970; Kamb, 1970; Morland, 1976a,b; Fowler, 1986a), and which is used in chapter 3, is thus formally justified. However, for realistic small but finite values of $\delta \approx 0.01$ and $n = 3$, $\delta^{1/(n+1)} \approx 0.3$, and finite sliding velocities may be obtained for bed roughness slopes which cannot realistically be considered small (see also Gudmundsson, 1997).

Dimensionless Inner Model

Armed with the scales defined above we introduce dimensionless velocities and stresses in the boundary layer as

$$u = [u_b]u_b^\star + [u_i]u_i, \qquad v = [u_i]v_i \qquad \dot{e} = [u_i]/(2[x_i])\dot{e}_i, \tag{A.16}$$

$$\boldsymbol{\tau} = [\tau_i]\boldsymbol{\tau_i}, \qquad p = \rho g(D-y) + [\tau_i]p_i. \tag{A.17}$$

Omitting subscripts $_i$, we arrive at the following[3] scaled problem for the boundary layer $\nu h(x_i) < y_i \ll 1/\delta$:

$$\nabla \cdot \boldsymbol{\tau} - \nabla p = O(\nu\delta, \epsilon, \epsilon\delta/\nu), \tag{A.18}$$

$$\nabla \cdot \mathbf{u} = 0, \tag{A.19}$$

where $\mathbf{u} = (u, v)$,

$$\tau_{xy} = \tau_{yx} = \dot{e}^{1/n-1}\left(\frac{\partial u}{\partial y} + \frac{\partial v}{\partial x}\right) + O(\epsilon, \epsilon\delta/\nu), \tag{A.20}$$

$$\tau_{xx} = -\tau_{yy} = 2\dot{e}^{1/n-1}\frac{\partial u}{\partial x} + O(\epsilon, \epsilon\delta/\nu), \tag{A.21}$$

and

$$\dot{e}^2 = \left[\left(\frac{\partial u}{\partial y}\right)^2 + \left(\frac{\partial v}{\partial x}\right)^2 + 2\left(\left(\frac{\partial u}{\partial x}\right)^2 + \left(\frac{\partial v}{\partial y}\right)^2 + \frac{\partial u}{\partial y}\frac{\partial v}{\partial x}\right)\right] + O(\epsilon, \epsilon\delta/\nu). \tag{A.22}$$

Boundary conditions on $y = \nu h(x)$ are

$$v = (u_b + \nu u)\frac{\partial h}{\partial x} + O(\epsilon, \epsilon\delta/\nu), \tag{A.23}$$

$$\left(1 - \nu^2\left(\frac{\partial h}{\partial x}\right)^2\right)\left(\frac{\partial u}{\partial y} + \frac{\partial v}{\partial x}\right) + 4\nu\frac{\partial h}{\partial x}\frac{\partial v}{\partial y} = O(\epsilon, \epsilon\delta/\nu) \tag{A.24}$$

from (A.2) and (A.1), respectively.

Inner and outer solution are matched asymptotically in a matching region where $1 \ll y_i \ll 1/\delta$, $\delta \ll y^\star \ll 1$ (e.g. Holmes, 1995, chapter 2). In order to avoid ambiguity, we re-introduce asterisks on outer variables and subscripts $_i$ on inner ones and obtain

$$u_i \sim \nu^n \left.\frac{\partial u^\star}{\partial y^\star}\right|_{y^\star = H^\star} y_i + O(\delta\nu^n, \epsilon^2\gamma/\nu), \qquad p_i \sim O(\epsilon\nu),$$

[3] In the context of the implied multiple scales expansion alluded to above, we are here ignoring terms of the form $\nu\delta\frac{\partial D^\star}{\partial x^\star}$, $\epsilon\delta/\nu\frac{\partial u_b^\star}{\partial x^\star}$ and $\epsilon\frac{\partial H^\star}{\partial x^\star}\frac{\partial}{\partial z_i}$, as indicated on the right-hand side of the equations. Under the restrictions imposed on ϵ, ν and γ, we will find that the error incurred is small and may be neglected at leading order.

$$v_i \sim O(\epsilon/\gamma\nu) \qquad \text{as } y_i \to \infty, \tag{A.25}$$

where $y_i \to \infty$ is to be understood as $1 \ll y_i \ll 1/\delta$.

By assumption, we have

$$\delta \ll 1, \qquad 1 \lesssim \gamma \ll 1/\epsilon, \qquad \epsilon \ll \nu \lesssim 1, \tag{A.26}$$

where $\gamma = \delta/\nu^{n+1}$. Hence we may neglect at leading order the $O(\nu\delta, \epsilon, \epsilon\delta/\nu)$ correction terms in (A.18)–(A.24), and obtain the following leading-order boundary conditions at infinity,

$$u_i \sim \nu^n \left.\frac{\partial u^\star}{\partial y^\star}\right|_{y^\star=H^\star} y_i, \qquad v_i = 0, \qquad p_i = 0. \tag{A.27}$$

Effective Basal Shear Stress

τ_b defined by (2.43) can be expressed as

$$\tau_b = \left.\left(\frac{\partial u^\star}{\partial y^\star}\right)^{1/n}\right|_{y^\star=H^\star}, \tag{A.28}$$

and so boundary condition $(\text{A.27})_1$ yields

$$\tau_{i(xy)} \sim \nu\tau_b \qquad \text{as } y_i \to \infty. \tag{A.29}$$

We assume for definiteness that the roughness component $h(x_i)$ is periodic with some period a, and that velocity and stress fields are likewise x-periodic with period a. Consider the integral of $\boldsymbol{\tau}_i\mathbf{n} - p_i\mathbf{n}$ around the boundary of the domain shown in fig. A.2, where $\mathbf{n}$ denotes the inward pointing unit normal to the domain boundary. Applying the divergence theorem and taking the x-component of the resulting expression yields to leading order

$$\tau_b = -\frac{1}{a}\int_0^a (\mathbf{n}\cdot\boldsymbol{\tau}_i\mathbf{n} - p_i)\big|_{y_i=\nu h(x_i)} \frac{\partial h}{\partial x_i}\,\mathrm{d}x_i, \tag{A.30}$$

which is closely related to (2.50).

Solution of the Inner Problem

We have seen above that the construction of an 'effective' basal shear stress as suggested in (2.50) can be substantiated by introducing the notion of a boundary layer which describes the local flow of basal ice over a rough bed. However, the inner problem defined by (A.16)–(A.24) and (A.27) does not define τ_b as a function of u_b. To see this, suppose that (u, v) solves these equations for a given $u_b = u_{b0}$. Then

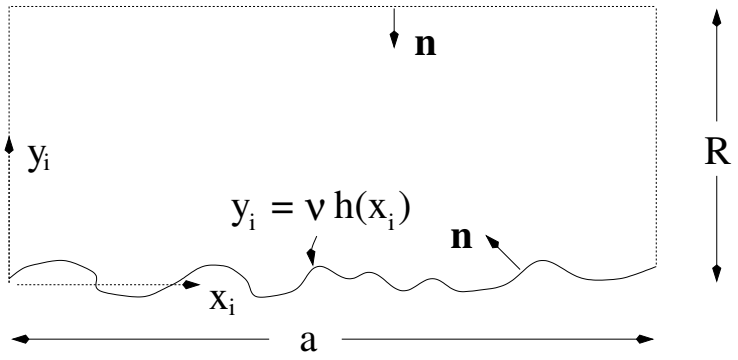

Figure A.2: Domain around which the integrals leading to (A.30) and (A.44) are taken. R is such that $1 \ll R \ll 1/\delta$.

$(u - \Delta u_b/\nu, v)$ solves the same equations for $u_b = u_{b0} + \Delta u_b$ where Δu_b is constant, and τ_b stays invariant under this transformation. Fowler (1979, 1981) attempts to resolve this apparent contradiction by using the fact that formally we must have $\nu \ll 1$. For $1 \ll y_i \ll 1/\nu^n$, $(A.27)_1$ then suggests the alternative boundary condition

$$u_i \sim 0 \qquad \text{as } y_i \to \infty,^4 \tag{A.31}$$

which is adopted in Fowler's papers. This change from Neumann to Dirichlet boundary conditions avoids the problem of multiple solutions. However, as discussed above, finite bed velocities can arise for bed roughnesses which are realistically not small (in the sense that ν^{n+1} is small but ν is not), and so Fowler (1979, 1981) retains ν as an $O(1)$ parameter in (A.23) and (A.24).

In order to calculate τ_b as a function of u_b, one can then use the following procedure: Rescale u, v, τ and p in (A.18)–(A.24) and (A.27) as

$$\mathbf{U} = (U, V) = (u, v)/u_b, \qquad \dot{E} = \dot{e}/u_b, \qquad \mathbf{T} = \boldsymbol{\tau}/u_b^{1/n}, \qquad P = p/u_b^{1/n}. \tag{A.32}$$

Bearing in mind that u_b is independent of the inner coordinates (x_i, y_i), this yields a problem in the variables $\mathbf{U}$, $\mathbf{T}$... which is independent of u_b and depends only on the geometry of basal roughness h and the roughness coefficient ν:

$$\nabla \cdot \mathbf{T} - \nabla P = 0 \tag{A.33}$$

$$\nabla \cdot \mathbf{U} = 0 \tag{A.34}$$

where

$$T_{xy} = T_{yx} = \dot{E}^{1/n-1} \left(\frac{\partial U}{\partial y} + \frac{\partial V}{\partial x} \right), \qquad T_{xx} = -T_{yy} = 2\dot{E}^{1/n-1} \frac{\partial U}{\partial x}, \tag{A.35}$$

[4] $y_i \to \infty$ is now to be understood as $1 \ll y_i \ll \min(1/\delta, 1/\nu^n)$

and

$$\dot{E} = \left[\left(\frac{\partial U}{\partial y} \right)^2 + \left(\frac{\partial V}{\partial x} \right)^2 + 2 \left(\left(\frac{\partial U}{\partial x} \right)^2 + \left(\frac{\partial V}{\partial y} \right)^2 + \frac{\partial U}{\partial y} \frac{\partial V}{\partial x} \right) \right]^{1/2}. \tag{A.36}$$

Boundary conditions at the base $y = \nu h$ are

$$V = (1 + \nu U) \frac{\partial h}{\partial x}, \tag{A.37}$$

$$\left(1 - \nu^2 \left(\frac{\partial h}{\partial x} \right)^2 \right) \left(\frac{\partial U}{\partial y} + \frac{\partial V}{\partial x} \right) + 4\nu \frac{\partial h}{\partial x} \frac{\partial V}{\partial y} = 0, \tag{A.38}$$

and at infinity

$$\mathbf{U} \sim \mathbf{0}, \qquad p \sim 0. \tag{A.39}$$

(A.30) then becomes

$$\tau_b = u_b^{1/n} \frac{1}{a} \int_0^a \left(P - \mathbf{n} \cdot \mathbf{T}\mathbf{n} \right)\big|_{y=\nu h(x)} \frac{\partial h}{\partial x} \, \mathrm{d}x \tag{A.40}$$

The integral on the right is independent of u_b as $\mathbf{T}$ and P are the solution of a problem which depends only on ν and h, and we have

$$\tau_b \propto u_b^{1/n}. \tag{A.41}$$

This result was established by Fowler (1981), who also used a variational method to show how the constant of proportionality—the integral in (A.40)—can be approximated for a given bed $h(x)$. Note that, in the context of the implied multiple scales expansion, h should depend on the outer variable $x^\star$ as well as the inner variable x_i, and thus the constant of proportionality will, in fact, be a function of outer position $x^\star$.

Finally, ignoring terms of $O(\nu)$ in (A.18)–(A.24) and setting the exponent $n = 1$ in Glen's law obtains Nye's (1969) and Kamb's (1970) leading order model (2.52)–(2.55); under the assumption of constant viscosity and small bed roughness slopes, the constant of proportionality can therefore be calculated explicitly using (2.59).

Normal Stress at the Bed

We conclude this appendix by considering the total normal stress exerted on the bed of a glacier or ice sheet which is sliding over local bed obstacles. This quantity is of interest in chapter 3, where we consider the problem of subglacial cavitation and its effect on the sliding law.

For an ice sheet, the *dimensional* normal stress at the bed $\sigma_{nn} = \mathbf{n}\cdot\boldsymbol{\sigma}\mathbf{n}|_{z=H}$, where $z = H$ denotes the actual physical bed, is

$$\sigma_{nn} = \rho g[D]\left[-D^\star + H^\star + \nu\delta h + \epsilon/\nu\,(\mathbf{n}\cdot\boldsymbol{\tau}_i\mathbf{n} - p_i)|_{z_i=\nu h}\right]. \tag{A.42}$$

For a glacier, the analogous expression is

$$\sigma_{nn} = \rho g[D]\cos\alpha\left[-D^\star + H^\star + \nu\delta h + \epsilon/(\mu\nu)\,(\mathbf{n}\cdot\boldsymbol{\tau}_i\mathbf{n} - p_i)|_{z_i=\nu h}\right]. \tag{A.43}$$

By integrating $\boldsymbol{\tau}_i\mathbf{n} - p_i\mathbf{n}$ around the domain shown in figure A.2, as was done previously to calculate τ_b, we obtain from the y-component of the resulting expression that

$$\frac{1}{a}\int_0^a (\mathbf{n}\cdot\boldsymbol{\tau}_i\mathbf{n} - p_i)|_{z_i=\nu h}\,\mathrm{d}x_i = 0. \tag{A.44}$$

Furthermore, the decomposition of the bed in (A.8) suggests that we require

$$\frac{1}{a}\int_0^a h\,\mathrm{d}x_i = 0, \tag{A.45}$$

and so the mean (over the bed roughness scale) of normal stress supported at the bed is, to leading order, given hydrostatically. For an ice sheet,

$$\frac{1}{a}\int_0^a \sigma_{nn}\,\mathrm{d}x_i = -\rho g[D]\,(D^\star - H^\star), \tag{A.46}$$

while for a glacier

$$\frac{1}{a}\int_0^a \sigma_{nn}\,\mathrm{d}x_i = -\rho g[D]\cos\alpha\,(D^\star - H^\star). \tag{A.47}$$

In a similar way, we can show that (A.30) and (2.50) are equivalent at leading order. Note that

$$\frac{1}{a}\int_0^a (-D^\star + H^\star)\frac{\partial h}{\partial x_i}\,\mathrm{d}x_i = 0, \tag{A.48}$$

since $D^\star$ and $H^\star$ are independent of the inner variable x_i (to an error of $O(\epsilon\delta)$) and h is periodic. Similarly

$$\frac{1}{a}\int_0^a h\frac{\partial h}{\partial x_i}\,\mathrm{d}x_i = [h^2/2]_{x_i=0}^{x_i=a} = 0. \tag{A.49}$$

Hence

$$\frac{1}{a}\int \sigma_{nn}\frac{\partial h}{\partial x_i}\,\mathrm{d}x_i = [\tau]\frac{-1}{a}\int_0^a (\mathbf{n}\cdot\boldsymbol{\tau}_i\mathbf{n} - p_i)|_{z_i=\nu h}\,\mathrm{d}x_i = [\tau]\tau_b, \tag{A.50}$$

as required.

Appendix B

The Argument of $\chi(0)$, $\chi^+(\xi)$

If we restrict the argument of a complex number to lie in $[0, 2\pi)$, then the argument of $\chi_j(\zeta)$, in terms of the angles shown in figure B.1, is $(\beta - \gamma)/2$. This follows straightforwardly from the definition of χ_j in (3.75) and the fact that $\chi_j(\zeta) \to 1$ as $\zeta \to \infty$ along the arrow shown. It can easily be seen by letting the point ζ coincide with the origin in figure B.1 that the argument of $\chi_j(0)$ is

$$\arg \chi_j(0) = \frac{\pi\,(b_j - c_{j-1})}{a}, \tag{B.1}$$

so that

$$\chi(0) = \exp\left(i\frac{\pi}{a} \sum_{k=1}^{n} (b_k - c_{k-1}) \right) \tag{B.2}$$

Turning now to the argument of the boundary value $\chi_j^+(\xi)$ on Γ_j', the result

$$\arg \chi_j^+(\xi) = \frac{\pi}{2} + \frac{\pi(b_j - c_{j-1})}{2a}, \qquad \xi \in \Gamma_j' \tag{B.3}$$

follows straightforwardly from elementary geometry of the circle applied to figure B.2. Similar geometrical considerations yield from figure B.3

$$\arg \chi_j^+(\xi) = \frac{\pi(b_j - c_{j-1})}{2a}, \qquad \xi \notin \Gamma_j'. \tag{B.4}$$

Straightforward algebra leads to

$$\left|\chi^+(\xi)\right| = \left| \prod_{j=1}^{n} \frac{\sin\left[\pi(x - b_j)/a\right]}{\sin\left[\pi(x - c_{j-1})/a\right]} \right|^{1/2}. \tag{B.5}$$

This, combined with the results above on the argument of $\chi_j^+(\xi)$ above yields

$$\chi^+(\xi) = \begin{cases} \left| \prod_{j=1}^{n} \frac{\sin[\pi(x-b_j)/a]}{\sin[\pi(x-c_{j-1})/a]} \right|^{1/2} i \exp\left(i\frac{\pi}{2a} \sum_{k=1}^{n} (b_k - c_{k-1}) \right), & \xi \in \Gamma', \\ \left| \prod_{j=1}^{n} \frac{\sin[\pi(x-b_j)/a]}{\sin[\pi(x-c_{j-1})/a]} \right|^{1/2} \exp\left(i\frac{\pi}{2a} \sum_{k=1}^{n} (b_k - c_{k-1}) \right), & \xi \in \Gamma. \end{cases} \tag{B.6}$$

(B.2) and (B.6) can now be used to derive (3.115)–(3.120).

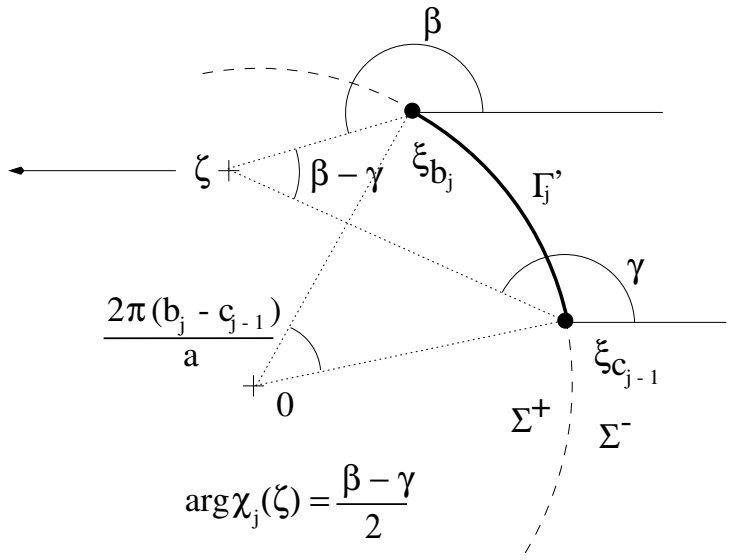

Figure B.1: Determining the argument of $\chi_j(\zeta)$

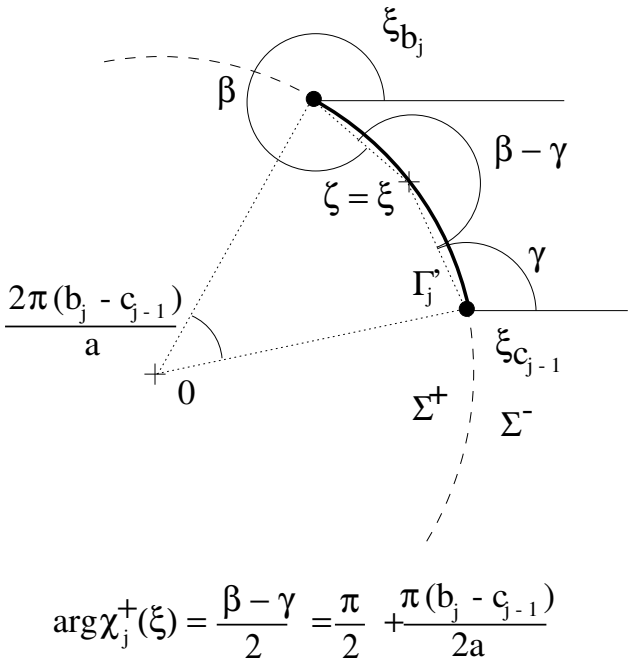

Figure B.2: The argument of $\chi_j^+(\xi)$ on Γ_j'.

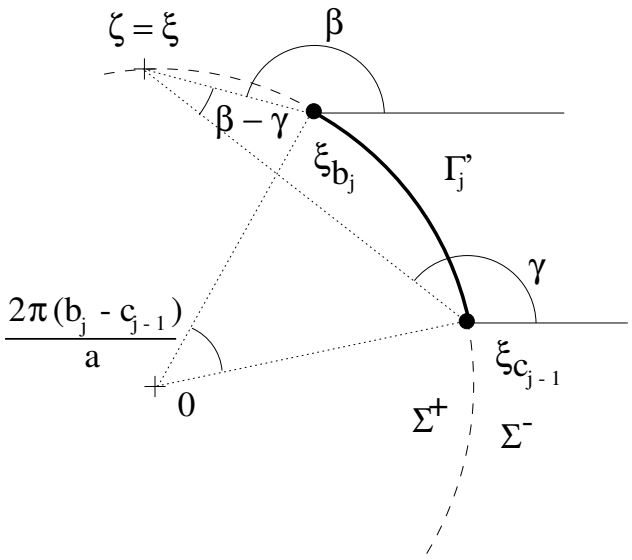

$$\arg\chi_j^+(\xi) = \frac{\beta-\gamma}{2} = \frac{\pi(b_j - c_{j-1})}{2a}$$

Figure B.3: The argument of $\chi_j^+(\xi)$ on the unit circle away from Γ_j'.

Appendix C

Numerical Solution of Integral Equations

In this appendix, we consider some technical points associated with the solution of the integral equations (5.162) and (6.48). A complete analysis of the drumlin formation model in chapters 5 and 6 is, however, not intended. In particular, we do not consider solutions of the evolution equation (5.166) at all here. Consequently, time t will generally be omitted from our notation.

As our starting point, we take the integral equation (6.48), which is here expressed as

$$\bar{U}s(x) - q(x) = \bar{U}s(c) - q(c) + \left[\bar{U}s'(c) - q'(c)\right](x-c) -$$
$$\frac{1}{4\pi}\int_c^b \left[\int_c^x \log\left(4\sin^2\left[\pi(x'-x'')/a\right]\right) - \log\left(4\sin^2\left[\pi(x''-c)/a\right]\right)\,\mathrm{d}x'\right]$$
$$\hat{N}(\bar{U}, q(x''), s(x''))\,\mathrm{d}x'', \tag{C.1}$$

where primes on s and q denote differentiation with respect to x, and N is explicitly written as a function of $\bar{U}$, q and s. We assume that $\hat{N}(\bar{U}, q, s)$ is smooth — with partial derivatives with respect to $\bar{U}$, q and s of any order required — when $\bar{U} > 0$ and $0 < q < \bar{U}(1+s)$, which is the typical domain of definition of N (see also the discussion on page 137).

The first thing we wish to do is to demonstrate that a solution $q(x)$ of (C.1) which is continuous on the closed interval $[c, b]$ satisfies the singular integro-differential equation (6.44), provided $s(x)$ is sufficiently smooth on $[c, b]$ — sufficient conditions are that $s'(x)$ is continuous on $[c, b]$ and $s''(x)$ exists on (c, b). To show this, we first need some results concerning the kernel in (C.1). We define

$$K(x) = \frac{1}{4\pi}\int_0^x \log\left[4\sin^2(\pi y/a)\right]\,\mathrm{d}y. \tag{C.2}$$

After a change of variables, $y = x' - x''$, (C.1) can then be written as

$$\bar{U}s(x) - q(x) = \bar{U}s(c) - q(c) + \left[\bar{U}s'(c) - q'(c)\right](x-c) -$$
$$\int_c^b \left[K(x-x'') + K(x''-c) - \frac{x-c}{4\pi}\log\left(4\sin^2\left[\pi(x''-c)/a\right]\right)\right]$$
$$\hat{N}(\bar{U}, q(x''), s(x''))\,\mathrm{d}x''. \tag{C.3}$$

C.1 The Kernel $K(x)$

The power series

$$\sum_{n=1}^{\infty}\frac{\zeta^{n-1}}{n} = -\frac{\log(1-\zeta)}{\zeta}$$

has radius of convergence one, and therefore converges everywhere inside the unit circle in the complex ζ-plane.[1] The series also converges pointwise on the unit circle except at $\zeta = 1$ (Apostol, 1969, p. 409). For ξ on the unit circle and $r \in (0,1)$, we have

$$\left|\sum_{n=1}^{n_0}\frac{r^{n-1}\xi^n}{n}\right| \le \sum_{n=1}^{n_0}\left|\frac{r^{n-1}\xi^n}{n}\right| = \sum_{n=1}^{n_0}\frac{r^{n-1}}{n} < \frac{\log(1-r)}{r} \tag{C.4}$$

for any finite n_0. Since $\frac{1}{r}\log(1-r)$ is integrable over $r \in (0,1)$, so is

$$\sum_{n=1}^{\infty}\frac{r^{n-1}\xi^n}{n} = -\frac{\log(1-r\xi)}{r\xi}\xi,$$

and the order of summation and integration may be interchanged by the dominated convergence theorem, i.e.

$$\int_0^1 -\frac{\log(1-r\xi)}{r\xi}\xi\,\mathrm{d}r = \sum_{n=1}^{\infty}\int_0^1\frac{(r\xi)^{n-1}}{n}\xi\,\mathrm{d}r = \sum_{n=1}^{\infty}\frac{\xi^n}{n^2}. \tag{C.5}$$

Similarly

$$\int_0^1 -\frac{\log(1-r\overline{\xi})}{r\overline{\xi}}\overline{\xi}\,\mathrm{d}r = \sum_{n=1}^{\infty}\frac{\overline{\xi}^n}{n^2}. \tag{C.6}$$

Subtracting the last two expressions and recognising that $\overline{\xi} = 1/\xi$ yields

$$\sum_{n=-\infty,\,n\neq 0}^{\infty}\frac{\xi^n}{n|n|} = \int_0^1 -\frac{\log(1-r\xi)}{r\xi}\xi\,\mathrm{d}r - \int_0^1 -\frac{\log(1-r\overline{\xi})}{r\overline{\xi}}\overline{\xi}\,\mathrm{d}r. \tag{C.7}$$

But the right-hand side is just the integral $\int -\frac{1}{\zeta}\log(1-\zeta)\,\mathrm{d}\zeta$ taken along the radial

[1] Note that the branch of the logarithm must be continuous on the interior of the unit circle with $\log(1) = 0$. At the origin, where the right-hand side is ill-defined, we may assign $\frac{1}{\zeta}\log(1-\zeta)$ its limiting value of zero.

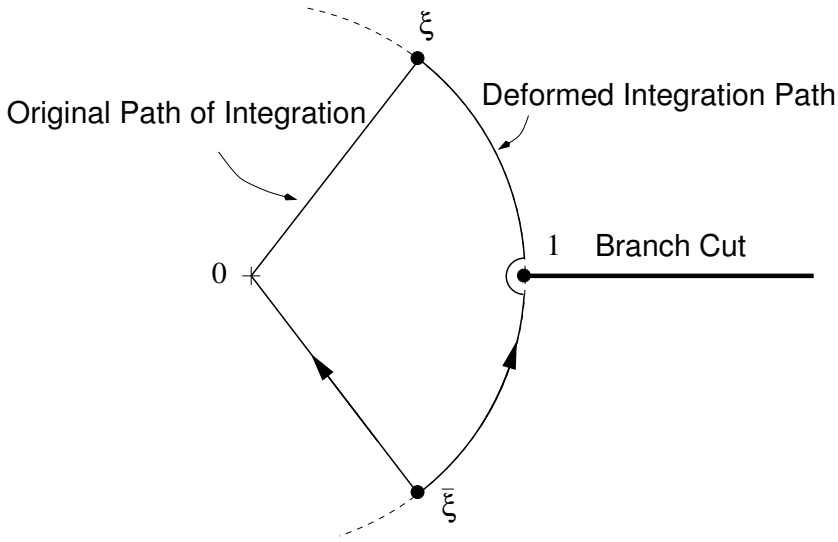

Figure C.1: Integration paths in the determination of $K(x)$.

path from $\overline{\xi}$ to ξ indicated in figure C.1. Since the integrand $-\frac{1}{\zeta}\log(1-\zeta)$ can be made holomorphic in the complex plane cut along the interval $[1,\infty)$ on the real line,[2] the curve along which the integral is taken can be deformed to lie on the unit circle, with a small indentation at the branch point $\zeta = 1$ (see figure C.1). The indentation does not contribute to the integral along the deformed curve in the limit where the radius of the indentation tends to zero. Putting $\xi = \exp(i2\pi x/a)$ as before, the integral may thus be expressed as

$$\sum_{n=-\infty,\, n\neq 0}^{\infty} \frac{\xi^n}{n|n|} = -\frac{i2\pi}{a}\int_{-x}^{x} \log\left[1-\exp(i2\pi x'/a)\right]\,\mathrm{d}x' =$$

$$-\frac{i2\pi}{a}\int_{0}^{x} \log\left[1-\exp(i2\pi x'/a)\right] + \log\left[1-\exp(-i2\pi x'/a)\right]\,\mathrm{d}x' =$$

$$-\frac{i2\pi}{a}\int_{0}^{x} \log\left[4\sin^2(\pi x'/a)\right]\,\mathrm{d}x'. \tag{C.8}$$

Consequently, the kernel K defined by (C.2) may be written as

$$K(x) = \frac{1}{4\pi}\int_{0}^{x} \log\left[4\sin^2(\pi y/a)\right]\,\mathrm{d}y = \sum_{n=-\infty,\, n\neq 0}^{\infty} \frac{i\xi^n}{8\pi^2 n|n|/a}. \tag{C.9}$$

The argument above has shown that the series on the right converges pointwise to the integral in the middle. By the Weierstrass M-test, it also converges uniformly. We may also note that the kernels $K(x)$ defined by (C.2) and (5.163) are the same, and therefore no confusion in notation arises.

[2]Note that the singularity at the origin is removable.

We are now ready to demonstrate that solutions $q(x)$ of (C.1) which are continuous on $[c,b]$ also satisfy certain differentiability requirements on $[c,b]$.

C.2 Differentiation of solutions

Suppose that $q(x)$ satisfies (C.1) for a given $s(x)$ and $\bar{U}$, and is continuous on $[c,b]$. If $s(x)$ is continuously differentiable on $[c,b]$, then we can show that the right-hand side of (C.3) can be differentiated and consequently that

$$q'(x) = \bar{U}s'(x) - \bar{U}s'(c)x + q'(c) +$$
$$\int_c^b \left\{ K'(x-x'') - \frac{1}{4\pi}\log\left(4\sin^2\left[\pi(x''-c)/a\right]\right)\right\} \hat{N}(\bar{U}, q(x''), s(x''))\,\mathrm{d}x'', \qquad \text{(C.10)}$$

where the prime on K denotes differentiation. Since $\hat{N}(\bar{U}, q(x''), s(x''))$ is continuous on $x'' \in [c,b]$ if $q(x'')$ and $s(x'')$ are continuous and lie in the domain of definition of $\hat{N}$, and since $s'(x)$ is continuous by assumption, the right-hand side of (C.10) is automatically continuous on account of the well-known properties of convolution integrals (e.g. Debnath and Mikusiński, 1999, pp. 77-79; the results presented there are easily adapted to integration over a bounded interval). Consequently $q(x)$ is continuously differentiable on $[c,b]$. In order to show (C.10) we only need to show that differentiation and integration commute when taking the derivative of the right-hand side of (C.3). In particular, we only need to show that

$$\frac{\mathrm{d}}{\mathrm{d}x}\int_c^b K(x-x'')N(x'')\,\mathrm{d}x'' = \int_c^b K'(x-x'')N(x'')\,\mathrm{d}x'', \qquad \text{(C.11)}$$

when $N(x)$ is continuous on $[c,b]$. To show this, define

$$K_{n_0}(x) = \sum_{n=-n_0,\, n\neq 0}^{n_0} \frac{i\exp(i2n\pi x/a)}{8\pi^2 n|n|/a}. \qquad \text{(C.12)}$$

Then, by the results in section C.1, $K_{n_0}(x) \to K(x)$ uniformly as $n_0 \to \infty$. Moreover, we have

$$K'_{n_0}(x) = -\sum_{n=-n_0,\, n\neq 0}^{n_0} \frac{\exp(i2n\pi x/a)}{4\pi|n|}, \qquad \text{(C.13)}$$

and $K'_{n_0}(x)$ converges pointwise to $K'(x)$ for all $x \neq 0$ as $n_0 \to \infty$. Since $\sum_{n=1}^{\infty} 1/|n|^2$ is convergent, $K'_{n_0}(x)$ also converges as a Fourier series to $K'(x)$ in the $L^2([0,a])$-norm, and hence in the $L^1([0,a])$-norm. Consider now

$$f_{n_0}(x) = \int_c^b K_{n_0}(x-x'')N(x'')\,\mathrm{d}x''. \qquad \text{(C.14)}$$

Then $f_{n_0}(x)$ is continuous and converges uniformly to $\int_c^b K(x''-x)N(x'')\,\mathrm{d}x''$ as $n_0 \to \infty$. Furthermore, since $K_{n_0}(x-x'')$ is continuously differentiable, (C.14) can be differentiated directly,

$$f'_{n_0}(x) = \int_c^b K'_{n_0}(x-x'')N(x'')\,\mathrm{d}x'', \tag{C.15}$$

and $f'_{n_0}(x)$ is continuous. Also

$$\sup_{x\in[c,b]} \left| \int_c^b K'(x-x'')N(x'')\,\mathrm{d}x'' - f'_{n_0}(x) \right| \leq$$

$$\int_c^b |K'(x-x'') - K_{n_0}(x-x'')| \sup_{x'\in[c,b]} |N(x')|\,\mathrm{d}x'' \leq$$

$$\sup_{x'\in[c,b]} |N(x')| \int_0^a |K'(y) - K_{n_0}(y)|\,\mathrm{d}y \tag{C.16}$$

by the periodicity of $K_{n_0}(x)$ and $K(x)$. Since K_{n_0} converges to K in the L^1-norm, $f'_{n_0}(x)$ therefore converges uniformly on $[c,b]$ to $\int_c^b K'(x-x'')N(x'')\,\mathrm{d}x''$. The desired result (C.11) follows by the completeness of $C^1([c,b])$, the space of continuously differentiable functions on $[c,b]$.

We can now show that $q(x)$ also satisfies the singular integro-differential equation (6.44). Define

$$K_\epsilon(x) = \begin{cases} K(x) & |x| < \epsilon, \\ 0 & \text{otherwise.} \end{cases} \tag{C.17}$$

For some given $x \in (c,b)$, choose ϵ such that $0 < \epsilon < \min(x-c, b-x)$. Equation (C.10) for $q'(x)$ may then be written as

$$q'(x) = \bar{U}s'(x) - \bar{U}s'(c)x + q'(c) +$$

$$\int_c^{x-\epsilon} K'(x-x'')N(x'')\,\mathrm{d}x'' + \int_{x+\epsilon}^b K'(x-x'')N(x'')\,\mathrm{d}x'' +$$

$$\int_c^b K'_\epsilon(x-x'')N(x'')\,\mathrm{d}x'' - \int_c^b \frac{1}{4\pi}\log\left(4\sin^2\left[\pi(x''-c)/a\right]\right)N(x'')\,\mathrm{d}x''. \tag{C.18}$$

Since $N'(x)$ is continuous on $[c,b]$,

$$\frac{\mathrm{d}}{\mathrm{d}x}\int_c^b K'_\epsilon(x-x'')N(x'')\,\mathrm{d}x'' = \int_c^b K'_\epsilon(x-x'')N'(x'')\,\mathrm{d}x''. \tag{C.19}$$

Furthermore, since $K'(x-x'')$ is continuously differentiable on $[c, x-\epsilon]$ and $[x+\epsilon, b]$, we have

$$\frac{\mathrm{d}}{\mathrm{d}x}\int_c^{x-\epsilon} K'(x-x'')N'(x'')\,\mathrm{d}x'' = \int_c^{x-\epsilon} K''(x-x'')N'(x'')\,\mathrm{d}x'' + K'(\epsilon)N'(x-\epsilon),$$

$$\frac{\mathrm{d}}{\mathrm{d}x}\int_{x+\epsilon}^{b} K'(x-x'')N(x'')\,\mathrm{d}x'' = \int_{x+\epsilon}^{b} K''(x-x'')N(x'')\,\mathrm{d}x'' - K'(-\epsilon)N'(x+\epsilon). \quad \text{(C.20)}$$

Hence, assuming $s''(x)$ exists on (c,b), differentiating both sides of (C.18) yields

$$q''(x) = \bar{U}s''(x) + \left(\int_c^{x-\epsilon} + \int_{x+\epsilon}^{b}\right) K''(x-x'')N(x'')\,\mathrm{d}x'' +$$

$$K'(\epsilon)N(x-\epsilon) - K'(-\epsilon)N(x+\epsilon) + \int_c^b K'_\epsilon(x-x'')N'(x'')\,\mathrm{d}x''. \quad \text{(C.21)}$$

The last integral vanishes as $\epsilon \to 0$. Similarly, $K'(\epsilon) = K'(-\epsilon) = \log(4\sin^2[\pi\epsilon/a])$ and $K'(\epsilon)$ diverges logarithmically as $\epsilon \to 0$. So, by the mean value theorem

$$|K'(\epsilon)N(x-\epsilon) - K'(-\epsilon)N(x+\epsilon)| = |2K'(\epsilon)N'(x+\theta\epsilon)\epsilon| \le |2K'(\epsilon)\epsilon| \sup_{x\in[c,b]} |N'(x)|, \quad \text{(C.22)}$$

where $-1 < \theta < 1$. Consequently, the first and second terms on the last line of (C.21) also vanish as $\epsilon \to \infty$, while the first integral on the right-hand side tends to a principal value integral. We obtain

$$q''(x) = \bar{U}s''(x) + \fint_c^b K''(x-x'')N(x'')\,\mathrm{d}x', \quad \text{(C.23)}$$

where $K''(x-x'') = (1/2a)\cot(\pi(x-x'')/a)$. Hence we recover (6.44).

C.3 Non-Cavitated Beds

Next, we show how (5.162) can be derived from (6.48) when there are no cavities present, i.e. when $b = c + a$. (6.48) is here written in the form (C.3),

$$\bar{U}s(x) - q(x) = \bar{U}s(c) - q(c) + \left[\bar{U}s'(c) - q'(c)\right](x-c) -$$

$$\int_c^{c+a} \left[K(x-x'') + K(x''-c) - \frac{x-c}{4\pi}\log\left(4\sin^2\left[\pi(x''-c)/a\right]\right)\right] N(x'')\,\mathrm{d}x''. \quad \text{(C.24)}$$

If (C.3) with $b = c + a$ is compared with the integral equation (5.162) obtained from a Fourier transform solution of the ice flow problem, the first thing to note is that two 'initial conditions' appear on the right-hand side of (C.3), whereas (5.162) instead contains only the mean flux $q_0(t)$. This mean flux, along with the mean sliding velocity $\bar{U}(t)$, is constrained by the integral relations (5.164)–(5.165). The equivalent for (C.3) is the statement that the choice of initial conditions and the sliding velocity $\bar{U}$ are constrained by the integral relations (6.40), which are the same as (5.164)–(5.165) when written in real variables. However, there are now three constants to

determine at fixed time t, namely $\bar{U}$, $\bar{U}s(c) - q(c)$ and $\bar{U}s'(c) - q'(c)$, rather than just $\bar{U}$ and q_0. Hence an additional constraint is required.

The obvious remedy for this is to require the solution $q(x)$ to be periodic in x, which is not the case for all choices of initial conditions. Hence we require

$$\bar{U}s(c+a) - q(c+a) = \bar{U}s(c) - q(c). \tag{C.25}$$

Setting $x = b = c + a$ in (C.24) then provides an expression for $\bar{U}s'(c) - q'(c)$. Noting that $K(x)$ is periodic with period a, and antisymmetric in x, we have $K(c+a-x'') = -K(x''-c)$, and so

$$\bar{U}s'(c) - q'(c) = -\int_c^{c+a} \frac{1}{4\pi} \log\left(4\sin^2\left[\pi(x''-c)/a\right]\right) N(x'')\,\mathrm{d}x''. \tag{C.26}$$

Substituting in (C.24) yields

$$\bar{U}s(x) - q(x) = \bar{U}s(c) - q(c) - \int_c^{c+a} \left[K(x-x'') + K(x''-c)\right] N(x'')\,\mathrm{d}x''. \tag{C.27}$$

We wish to replace $\bar{U}s(c) - q(c)$ by $q_0 = \int_c^{c+a} q(x)\,\mathrm{d}x/a$. Hence we integrate both sides of (C.27) with respect to x over $[c, c+a]$ and divide by a. Since $K(x)$ is periodic with period a as well as antisymmetric, we have $\int_c^{c+a} K(x-x'')\,\mathrm{d}x = 0$. Furthermore, by definition, the mean of s is zero, and so $\int_c^{c+a} s(x)\,\mathrm{d}x = 0$. We obtain

$$-q_0 = \bar{U}s(c) - q(c) - \int_c^{c+a} K(x''-c)N(x'')\,\mathrm{d}x''. \tag{C.28}$$

Substituting in (C.27) finally yields

$$\bar{U}s(x) - q(x) + q_0 = \int_c^{c+a} K(x-x'')N(x'')\,\mathrm{d}x'', \tag{C.29}$$

which is of the form (5.162) with $\beta = 0$, if one bears in mind that $q(x)$ and $s(x)$, and hence $N(x)$ are periodic.

C.4 Numerical Method

In section 5.6.1, a numerical method is described for solving the integral equation (5.162) coupled with the constraints (5.164)–(5.165) for a given bed $s(x)$. We are now ready to give a little theoretical background to this method. Before launching into a description, we should emphasise that we are not in a position to give a full analysis of a solution of these equations coupled with the evolution equation (5.166).

As demonstrated above, provided $s(x)$ is sufficiently smooth, continuous solutions of (5.162) satisfy the singular integro-differential equation (6.41) which arises when the elliptic ice-flow problem is solved using a complex variable method. Consequently, we restrict ourselves to seeking continuous solutions $q(x) \in C_p([0,a])$, where $C_p([0,a])$ is the space of continuous functions on the real line with period a. $C_p([0,a])$ is a Banach space with the usual sup-norm

$$||f||_\infty = \sup_{x\in[0,a]} (f(x)). \tag{C.30}$$

In solving (5.162) coupled with (5.164)–(5.165), we seek a solution of the operator equation (5.173), where $T(q, q_0, \bar{U})$ is an operator defined on a subset E of the Banach space $\mathcal{X} = C_p([0,a]) \times \mathbb{R}^2$, where $\mathcal{X}$ endowed with some suitable norm, such as

$$\big|\big|(q, q_0, \bar{U})\big|\big| = ||q||_\infty + |q| + |\bar{U}|. \tag{C.31}$$

Typically E is the set defined by $\bar{U} > 1$, $0 < q(x) < \bar{U}(1 + s(x))/2$, so E is an open subset of $\mathcal{X}$. Moreover, as the discussion in the first few sections of this appendix has shown, the range of the operator T is a subset of $\mathcal{X}$. Furthermore, T is Fréchet differentiable on E with Fréchet derivative T' given by (5.175).

An appropriate method for solving such an operator equation is a Newton-Kantorovič iteration scheme (Rall, 1969) as outlined in section 5.6.1. In principle, one can test whether sufficient conditions for the convergence of an initial guess to a locally unique solution are satisfied; these conditions are given by the Newton-Kantorovič theorem (Rall, 1969; Ortega, 1968). However, a test for convergence based on these conditions not only requires T' to be Lipschitz continuous (which it will be on any closed subset of E if $\hat{N}(\bar{U}, q, s)$ and $\hat{\tau}_b(\bar{U}, q, s)$ are sufficiently smooth), but also requires the Lipschitz constant to be estimated. As Dennis and Schnabel (1996, p. 92) point out, it is usually easier to establish empirically if a given initial guess converges than to estimate the Lipschitz constant.

At each iteration step, we use a degenerate kernel approximation to approximate T'^{-1} (cf. section 5.6.1). It is straightforward to show that this degenerate kernel approximation converges as the number of modes r_0 used tends to infinity. Specifically, if we define T'_{r_0} as the degenerate kernel approximation to T' (given by the right-hand side (5.176) with K replaced by K_{r_0}), then

$$\big|\big|(T' - T'_{r_0})(\Delta q, \Delta q_0, \Delta\bar{U})\big|\big| =$$

$$\left|\left|\int_0^a (K(x-y) - K_{r_0}(x-y)) \left(\left.\frac{\partial \hat{N}}{\partial q}\right|_{q(y),q_0,\bar{U}} \Delta q(y) + \left.\frac{\partial \hat{N}}{\partial \bar{U}}\right|_{q(y),q_0,\bar{U}} \Delta\bar{U} \right) \mathrm{d}y \right|\right|_\infty \leq$$

$$\left(\left\| \frac{\partial \hat{N}}{\partial q} \right\|_\infty ||\Delta q||_\infty + \left\| \frac{\partial \hat{N}}{\partial \bar{U}} \right\|_\infty |\bar{U}| \right) \int_0^a |K(x-y) - K_{r_0}(x-y)| \, \mathrm{d}y.$$

Since $K_{r_0}(x)$ converges uniformly to $K(x)$ by the results of section C.1, T'_{r_0} converges in norm to T'. Consequently $T'^{-1}_{r_0}$ converges in norm to T'^{-1}, if the latter exists (Atkinson, 1997, chapter 2).

References

R. Aario, 1977. Flutings, drumlins and Rogen-landforms. *Nordia*, **2**, 5–14.

R. Aario, 1987. Drumlins of Kuusamo and Rogen-ridges of Ranua, northeast Finland. In J. Menzies and J. Rose (Eds.), *Drumlin Symposium*. Balkema, Rotterdam, pp. 87–102.

M. Abramowitz and I.A. Stegun (Eds.), 1972. *Handbook of Mathematical Functions*. Dover Publications, New York.

W.C. Alden, 1905. The drumlins of southeastern Wisconsin. *U.S. Geol. Surv. bull. ser. B*, **76**, 9–46.

R.B. Alley, 1989. Water-pressure coupling of sliding and bed deformation: II. Velocity-depth profiles. *J. Glaciol.*, **35**(119), 119–129.

R.B. Alley, 2000. Continuity comes first: recent progress in understanding subglacial deformation. In A.J. Maltman, B. Hubbard, and M.J. Hambrey (Eds.), *Deformation of Glacial Materials*. Vol. **176** of *Special Publications*. Geological Society, London, pp. 171–179.

R.B. Alley, K.M. Cuffey, E.B. Evenson, J.C. Strasser, D.E. Lawson, and G.J. Larson, 1997. How glaciers entrain and transport basal sediment: physical constraints. *Quat. Sci. Revs.*, **16**(9), 1017–1038.

R.B. Alley, D.E. Lawson, E.B. Evenson, J.C. Strasser, and G.J. Larson, 1998. Glaciohydraulic supercooling: a freeze-on mechanism to create stratified, debris-rich basal ice: II. Theory. *J. Glaciol.*, **44**(148), 563–569.

T.M. Apostol, 1969. *Calculus*, 2nd Edition. Vol. **2**. Blaisdell Publishing Co., Waltham, Mass.

K.E. Atkinson, 1989. *An Introduction to Numerical Analysis*, 2nd Edition. J. Wiley & Sons, Ltd., New York.

K.E. Atkinson, 1997. *Numerical Solutions of Integral Equations of the Second Kind.* Cambridge Monographs on Computational and Applied Mathematics. Cambridge University Press, Cambridge.

J.-P. Benoist, 1979. The Spectral Power Density and Shadowing Function of Glacial Microrelief at the Decimetre Scale. *J. Glaciol.*, **23**(89), 57–66.

R. Bindschadler, 1983. The importance of pressurized subglacial water in separation and sliding at the glacier bed. *J. Glaciol.*, **29**(101), 3–19.

D.D. Blankenship, C.R. Bentley, S.T. Rooney, and R.B. Alley, 1986. Seismic measurements reveal a saturated porous layer beneath an active antarctic ice stream. *Nature*, (322), 54–57.

D.D. Blankenship, C.R. Bentley, S.T. Rooney, and R.B. Alley, 1987. Till beneath Ice Stream B. 1. Properties derived from seismic travel times. *J. Geophys. Res.*, **92**(B9), 8903–8911.

G.S. Boulton, 1974. Processes and patterns of glacial erosion. In D.R. Coates (Ed.), *Glacial Geomorphology.* Vol. **5** of *Binghampton Symposia in Geomorphology.* Allen & Unwin, London, Ch. 2, pp. 41–87.

G.S. Boulton, 1979. Processes of glacier erosion on different substrata. *J. Glaciol.*, **23**(89), 15–37.

G.S. Boulton, 1987. A theory of drumlin formation by subglacial sediment deformation. In J. Menzies and J. Rose (Eds.), *Drumlin Symposium.* Balkema, Rotterdam, pp. 25–80.

G.S. Boulton and R.C.A. Hindmarsh, 1987. Sediment deformation beneath glaciers: rheology and geological consequences. *J. Geophys. Res.*, **92**(B9), 9059–9082.

G.K.C. Clarke, 1987. Subglacial till: a physical framework for its properties and processes. *J. Geophys. Res.*, **92**(B9), 9023–9036.

D.R. Coates (Ed.), 1974. *Glacial Geomorphology.* Vol. **5** of *Binghampton Symposia in Geomorphology.* Allen & Unwin, London.

L. Debnath and J. Mikusiński, 1999. *Introduction to Hilbert Spaces with Applications.* Academic Press, San Diego.

J.E. Dennis and R.B. Schnabel, 1996. *Numerical Methods for Unconstrained Optimization and Nonlinear Equations*. Classics in Applied Mathematics. SIAM, Philadelphia.

C. Embleton and C.A.M. King, 1975. *Glacial Geomorphology*, 3rd Edition. Edward Arnold, London.

H. Engelhardt, W.D. Harrison, and B. Kamb, 1978. Basal sliding and conditions at the glacier bed as revealed by borehole photography. *J. Glaciol.*, **20**(84), 469–508.

H. Engelhardt and B. Kamb, 1998. Basal sliding of Ice Stream B. *J. Glaciol.*, **44**(147), 223–230.

A.H. England, 1971. *Complex Variable Methods in Elasticity*. J. Wiley & Sons, Ltd., London.

W. Everett, 1987. An analysis of the literature on drumlins and related streamlined forms. Master's thesis, University of London, unpublished.

N. Eyles (Ed.), 1983. *Glacial Geology*. Pergamon, Oxford.

U.H. Fischer, N.R. Iverson, B. Hanson, R.LeB. Hooke, and P. Jansson, 1998. Estimation of the hydraulic properties of subglacial till from ploughmeter measurements. *J. Glaciol.*, **44**(148), 517–522.

T.G. Fisher and J. Shaw, 1992. A depositional model for Rogen moraine, with examples from the Avalon Peninsula, Newfoundland. *Can. J. Earth. Sci.*, **29**, 669–686.

A.C. Fowler, 1977. Glacier Dynamics. D.Phil. thesis, Oxford University.

A.C. Fowler, 1979. A mathematical approach to the theory of glacier sliding. *J. Glaciol.*, **23**(89), 131– 141.

A.C. Fowler, 1981. A theoretical treatment of the sliding of glaciers in the absence of cavitation. *Phil. Trans. R. Soc. L.*, **298**(1445), 637–685.

A.C. Fowler, 1986a. A sliding law for glaciers of constant viscosity in the presence of subglacial cavitation. *Proc. R. Soc. L. Ser. A*, **407**, 147–170.

A.C. Fowler, 1986b. Subtemperate basal sliding. *J. Glaciol.*, **32**(110), 3–5.

A.C. Fowler, 1987a. Sliding with cavity formation. *J. Glaciol.*, **33**(105), 255–267.

A.C. Fowler, 1987b. A Theory of Glacier Surges. *J. Geophys. Res.*, **92**(B9), 9111–9120.

A.C. Fowler, 2000. An instability mechanism for drumlin formation. In A. Maltman, M.J. Hambrey, and B. Hubbard (Eds.), *Deformation of glacial materials*. Vol. **176** of *Spec. Pub. Geol. Soc.* The Geological Society, London, pp. 307–319.

A.C. Fowler, 2001a. Dunes and Drumlins. In N.J. Balmforth and A. Provenzale (Eds.), *Geomorphological Fluid Mechanics*. Vol. **582** of *Lecture Notes in Physics*. Springer-Verlag, Berlin, pp. 430–454.

A.C. Fowler, 2001b. Modelling the Flow of Glaciers and Ice Sheets. In B. Straughan, R. Greve, H. Ehrentraut, and Y. Wang (Eds.), *Continuum Mechanics and Applications in Geophysics and the Environment*. Springer-Verlag, Berlin, pp. 276–304.

A.C. Fowler and D.A. Larson, 1978. On the flow of polythermal glaciers. I. Model and preliminary analysis. *Proc. R. Soc. L. Ser. A.*, **363**, 217–242.

A.C. Fowler and C.G. Noon, 1999. Mathematical models of compaction, consolidation and regional groundwater flow. *Geophys. J. Int.*, **136**, 251–260.

K. Gillow, 1998. Codimension-Two Free Boundary Problems. D.Phil. thesis, Oxford University.

G. Glückert, 1973. Two large drumlin fields in central Finland. *Fennia*, **120**, 5–37.

R.P. Goldthwait, 1974. Rates of formation of glacial features in Glacier Bay, Alaska. In D.R. Coates (Ed.), *Glacial Geomorphology*. Vol. **5** of *Binghampton Symposia in Geomorphology*. Allen & Unwin, London, Ch. 6, pp. 163–185.

C.P. Gravenor, 1953. The origin of drumlins. *Am. J. Science*, **251**, 674–687.

C.P. Gravenor and W.A. Meneley, 1958. Glacial flutings in central and northern Alberta. *Am. J. Sci.*, **256**, 715–728.

G.H. Gudmundsson, 1997. Basal-flow characteristics of a non-linear flow sliding frictionless over strongly undulating bedrock. *J. Glaciol.*, **43**(143), 80–89.

D.G. Harry and A.S. Trenhaile, 1987. The morphology of the Aran drumlin field, southern Ontario, Canada. In J. Menzies and J. Rose (Eds.), *Drumlin Symposium*. Balkema, Rotterdam, pp. 161–173.

R.C.A. Hindmarsh, 1998a. Drumlinization and drumlin-forming instabilities: viscous till meachanisms. *J. Glaciol.*, **44**(147), 293–314.

R.C.A. Hindmarsh, 1998b. The stability of a viscous till sheet coupled with ice flow, considered at wavelengths less than the ice thickness. *J. Glaciol.*, **44**(146), 285–292.

M.H. Holmes, 1995. *Introduction to Perturbation Methods*. Vol. **20** of *Texts in Applied Mathematics*. Springer-Verlag, New York.

R.LeB. Hooke, B. Hanson, N.R. Iverson, P. Jansson, and U.H. Fischer, 1997. Rheology of till beneath Storglaciären, Sweden. *J. Glaciol.*, **43**(143), 172–179.

N. Humphrey, 1987. Coupling between water pressure and basal sliding in a linked-cavity hydraulic system. In E.D. Waddington and J.S. Walder (Eds.), *The Physical Basis of Ice Sheet Modelling*. Vol. **170** of *IAHS Publications*. International Association of Hydrological Sciences, Wallingford, pp. 105–119.

K. Hutter, 1981. The effect of longitudinal strain on the shear stress of an ice sheet: in defence of using stretched coordinates. *J. Glaciol.*, **27**(95), 39–56.

K. Hutter, 1983. *Theoretical Glaciology*. D. Reidel, Dordrecht.

A. Iken, 1981. The effect of subglacial water pressure on the sliding velocity of a glacier in an idealized numerical model. *J. Glaciol.*, **27**(97), 407–422.

E. Isaacson and H.B. Keller, 1966. *Analysis of Numerical Methods*. J. Wiley & Sons, Ltd., New York.

N.R. Iverson, R.W. Baker, R.LeB. Hooke, B. Hanson, and P. Jansson, 1999. Coupling between a glacier and a soft bed: I. A relation between effective pressure and local shear stress determined from till elasticity. *J. Glaciol.*, **45**(149), 31–40.

N.R. Iverson, T.S. Hooyer, and R.W. Baker, 1998. Ring-shear studies of till deformation: Coulomb-plastic behaviour and distributed shear in glacier beds. *J.Glaciol.*, **44**(148), 634–642.

N.R. Iverson and R.M. Iverson, 2001. Distributed shear of subglacial till due to Coulomb slip. *J. Glaciol.*, **47**(158), 481–488.

B. Kamb, 1970. Sliding motion of glaciers: Theory and observation. *Rev. Geophys.*, **8**(4), 673–728.

B. Kamb, 1987. Glacier Surge Mechanism Based on Linked Cavity Configuration of the Basal Water Conduit System. *J. Geophys. Res.*, **92**(B9), 9083–9100.

B. Kamb, 1991. Rheological nonlinearity and flow instability in the deforming bed mechanism of ice stream motion. *J. Geophys. Res.*, **96**(B10), 16585–16595.

B. Kamb and K.A. Echelmeyer, 1986. Stress-gradient coupling in glacier flow: I. Longitudinal averaging of the influence of ice thickness and surface slope. *J. Glaciol.*, **32**(111), 267–284.

A. Karczewski, 1987. Lithofacies variability of a drumlin in Pomerania, Poland. In J. Menzies and J. Rose (Eds.), *Drumlin Symposium*. Balkema, Rotterdam, pp. 177–184.

J. Krüger and H.H. Thomsen, 1984. Morphology, stratigraphy and genesis of small drumlins in front of the glacier Mýrdalsjökull, south Iceland. *J. Glaciol.*, **30**(104), 94–105.

L. Lliboutry, 1968. General Theory of Subglacial Cavitation and Sliding of Temperate Glaciers. *J. Glaciol.*, **7**(49), 21–58.

L. Lliboutry, 1979. Local friction laws for glaciers: critical review and new openings. *J. Glaciol.*, **23**(89), 67–96.

L. Lliboutry, 1987. Realistic, yet simple bottom boundary conditions for glaciers and ice sheets. *J. Geophys. Res.*, **92**(B9), 9101–9110.

J. Lundqvist, 1969. Problems of the so-called Rogen-moraine. *Sveriges Geologiska Undersökning Ser. C Årsbok*, **64**(5), 3–32.

J. Lundqvist, 1970. Studies of drumlin tracts in central Sweden. *Acta Geographica Lodziensia*, (24), 317–326.

J. Menzies (Ed.), 1995. *Modern Glacial Environments*. Butterworth-Heinemann, Oxford.

G. Miel, 1990. Numerical Solution on Parallel Processors of Two-Point Boundary Value Problems in Astrodynamics. In M.A. Golberg (Ed.), *Numerical Solutions of Integral Equations*. Plenum Press, New York, Ch. 4, pp. 131–182.

L.W Morland, 1976a. Glacier sliding down an inclined wavy bed. *J. Glaciol.*, **17**(77), 447–462.

L.W. Morland, 1976b. Glacier sliding down an inclined wavy bed with friction. *J. Glaciol.*, **17**(77), 463–478.

L.W. Morland and I.R. Johnson, 1980. Steady motion of ice sheets. *J. Glaciol.*, **25**(92), 229–246.

L.W. Morland and I.R. Johnson, 1982. Effects of bed inclination and topography on steady isothermal ice sheets. *J. Glaciol.*, **28**(98), 71–90.

T. Murray, 1997. Assessing Paradigm Shifts: Deformable Glacier Beds. *Quat. Sci. Revs.*, **16**(9), 995–1016.

N.I. Muskhelishvili, 1992. *Singular Integral Equations*. Dover Publications, Inc., New York, unabridged republication of 2nd edition published by P. Noordhoff, Groningen, 1953.

F.S.L. Ng, 1998. Mathematical Modelling of Subglacial Drainage and Erosion. D.Phil. thesis, Oxford University.

J.F. Nye, 1969. A calculation of the sliding of ice over a wavy surface using a Newtonian viscous approximation. *Proc. R. Soc. L. Ser.A*, **311**, 445–467.

J.F. Nye, 1970. Glacier sliding without cavitation in a linear viscous approximation. *Proc.R. Soc. L. Ser. A*, **315**, 381–403.

J.M. Ortega, 1968. The Newton-Kantorovič Theorem. *Am. Math. Monthly*, **75**(6), 658–660.

W.S.B. Paterson, 1994. *The physics of glaciers*, 3rd Edition. Pergamon, Oxford.

V.K. Prest, D.R. Grant, and V.N. Rampton, 1968. Glacial map of Canada. published by Canada Geological Survey.

L.B. Rall, 1969. *Computational Solution of Nonlinear Operator Equations*. J. Wiley & Sons, Inc., New York.

C. Raymond, 1996. Shear margins in glaciers and ice sheets. *J. Glaciol.*, **42**(140), 90–102.

I. Schaeffer, 1969. Der Drumlin von Hörmatting in Oberbayern. *Eiszeitalter u. Gegenw.*, **20**, 175–195.

J. Schweizer and A. Iken, 1992. The role of bed separation and friction in sliding over an undeformable bed. *J. Glaciol.*, **38**(128), 77–92.

D.S. Sharpe, 1987. The stratified nature of drumlins from Victoria Island and southern Ontario, Canada. In J. Menzies and J. Rose (Eds.), *Drumlin Symposium.* Balkema, Rotterdam, pp. 185–214.

J. Shaw, 1979. Genesis of the Sveg tills and Rogen moraines of central Sweden: a model of basal melt-out. *Boreas*, **8**, 409–426.

J. Shaw, 1983. Drumlin formation related to inverted melt-water erosion marks. *J. Glaciol*, **29**(103), 461–479.

J. Shaw and R.C. Freschauf, 1973. A kinematic discussion of the formation of glacial flutings. *Canadian Geographer*, **18**, 19–35.

J. Shaw and D. Kvill, 1984. A glaciofluvial origin for drumlins in the Livingston lake area, Saskatchewan. *Can. J. Earth Sci.*, **21**(12), 1442–1459.

R.L. Shreve, 1984. Glacier sliding at subfreezing temperatures. *J. Glaciol.*, **30**, 341–347.

I.J. Smalley and D.J. Unwin, 1968. The formation and shape of drumlins and their distribution and orientation in drumlin fields. *J. Glaciol.*, **7**(51), 377–390.

H.T.U. Smith, 1948. Giant glacial grooves in Northwest Canada. *Am. J. Sci.*, **246**, 503–514.

D.E. Sugden and B.S. John, 1976. *Glaciers and Landscape.* Edward Arnold, London.

B. Svendsen and K. Hutter, 1996. A continuum approach for modelling induced anisotropy in glaciers and ice sheers. *Ann. Glaciol.*, **23**, 262–269.

R.S. Tarr, 1894. The origin of drumlins. *Am. Geologist*, **13**, 393–407.

T. Thorsteinsson and C.F. Raymond, 2000. Sliding versus till deformation in the fast motion of an ice stream over viscous till. *J. Glaciol*, **45**(155), 633–640.

L.N. Trefethen, 2000. *Spectral Methods in MATLAB*. Software, Environments and Tools. SIAM, Philadelphia.

C. Truesdell and R.A. Toupin, 1960. The Classical Field Theories. In S. Flügge (Ed.), *Principles of Classical Mechanics and Field Theory*. Vol. **3** of *Handbuch der Physik*. Springer-Verlag, Berlin, Ch. 2.

M. Truffer and A. Iken, 1998. The sliding velocity over a sinusoidal bed at high water pressure. *J. Glaciol.*, **44**(147), 379–382.

S. Tulaczyk, 1999. Ice sliding over weak, fine-grained till: dependence of ice-till interactions on till granulometry. *Spec. Paper Geol. Soc. Am.*, **337**, 159–177.

S. Tulaczyk, W.B. Kamb, and H.F. Engelhardt, 2000. Basal mechanisms of Ice Stream B, West Antarctica: 1. Till mechanics. *J. Geophys. Res.*, **105**(B1), 463–481.

J.S. Walder and A.C. Fowler, 1994. Channelised subglacial drainage over a deformable bed. *J. Glaciol.*, **40**(134), 3–15.

J. Weertman, 1957. On the sliding of glaciers. *J. Glaciol.*, **3**(21), 33–38.

J. Weertman and G.E. Birchfield, 1982. Subglacial water flow under ice streams and West Antarctic ice-sheet stability. *Ann. Glaciol.*, **3**, 316–320.

I.M. Whillans and C.J. van der Veen, 1997. The role of lateral drag in the dynamics of Ice Stream B, Antarctica. *J. Glaciol.*, **43**(144), 231–237.

G.R. Whittecar and D.M. Mickelson, 1979. Composition, internal structures and an hypothesis of formation for drumlins, Waukesha County, Wisconsin, USA. *J. Glaciol.*, **22**(87), 357–371.